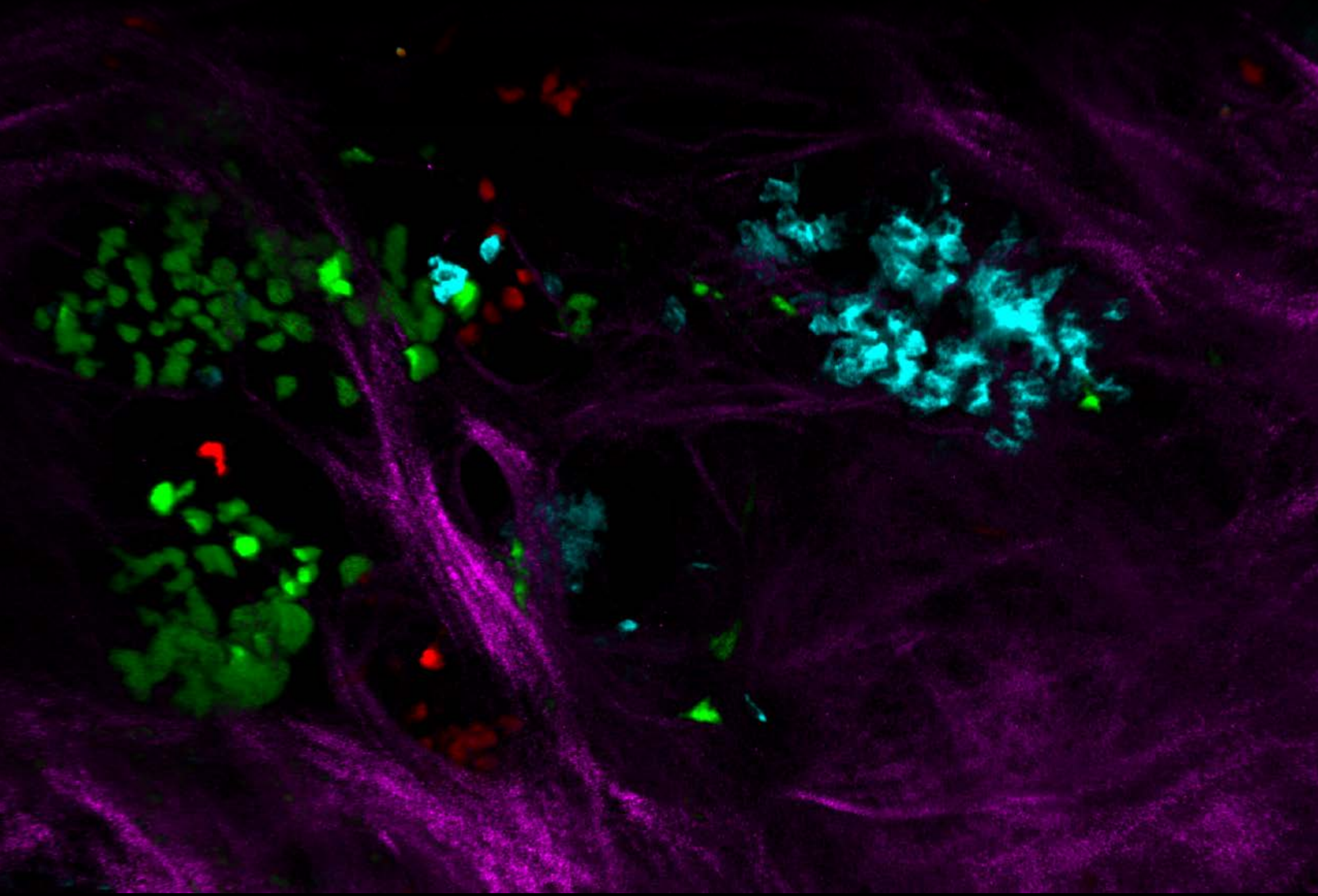

Illuminating Cancer Mechanisms through Confocal Microscopy

Article Collection

WILEY

CURRENT PROTOCOLS
A Wiley Brand

Sponsored by:
Leica
MICROSYSTEMS

Illuminating Cancer Mechanisms through Confocal Microscopy

EMILY E. FRIEBEN, PH.D., ASSOCIATE EDITOR, WILEY INTERDISCIPLINARY REVIEWS

Cancer is one of the leading causes of death worldwide, affecting millions of patients and their families every year. Despite incredible breakthroughs in cancer medicine that have led to a decline in deaths, the number of cancer patients is still expected to rise in the upcoming decades. This prediction is attributed to growth and aging of the population, maintaining lifestyle behaviors known to increase cancer risk (e.g., poor diet, smoking, physical inactivity), as well as cancer recurrence. With the projected increase in cases, there is a pressing need to develop novel, effective therapeutics. Thoroughly understanding the mechanisms and features unique to each type of cancer is essential to the success of finding new therapies. Likewise, advancements in research technology have been critical to uncovering key findings and revolutionizing cancer research.

One of the most powerful technologies used in basic cancer research is confocal microscopy. Confocal microscopy offers several advantages over conventional microscopy, such as low background noise, the ability to control the depth of field, and the capability to collect optical sections from thick specimens. With the relative ease of obtaining high-quality images from specimens prepared for conventional fluorescence microscopy, the popularity and use of confocal microscopy for cancer and biomedical research has grown extensively in recent years.

In this article collection, we highlight seven recent publications that utilize confocal microscopy to elucidate important mechanisms of cancer. First, Klimpel et al. (2020) present a series of cell-permeable peptides bearing a C-terminal CaaX motif that was based on the sequence of Ras proteins. Confocal microscopy was used to examine the cellular uptake and intracellular distribution of the CaaX-peptides. These peptides were shown to affect downstream signaling of K-Ras and promote cancer cell death, showing the potential of regulating post-translational cysteine prenylation as a therapeutic strategy. Next, Rainey et al. (2020) uncover perturbations in Src tyrosine kinase signaling that disrupt epithelial spatial organization in colorectal cancer (CRC) and are behind the transition to high-grade CRC. Confocal microscopy was utilized to study cell cortex dynamics, centrosome disposition, mitotic spindle geometry and orientation, and multicellular patterns. These studies showed that Src regulation of CRC morphogenic growth was via ezrin–centrosome engagement.

Following these articles, Stefanello et al. (2021) examine whether nuclear pore complexes (NPCs) are critical for malignant transformation, motility, and survival of non-small cell lung cancer cells. Confocal microscopy was used to visualize NPCs in the nuclear envelopes of both cancerous and non-cancer cells, as well as to examine their permeability. The authors found that malignant transformation is accompanied by an increased density of NPCs, as well as a weakening of the stringency of the NPC barrier. Their findings indicate that modulation of the NPC barrier may be a viable therapeutic strategy for suppressing a malignant phenotype or enhancing the efficacy of existing chemotherapies.

Our next two studies focus on the development of realistic, 3D *in vitro* glioma models. Barin et al. (2022) present the development of a novel cell culture system to study patient-derived glioma cells, a 3D-engineered scaffold fabricated by two-photon polymerization. Patient-derived glioma cells and established glioma cell lines successfully colonized the scaffolds. Additionally, compared to 2D cell cultures, the 3D scaffolds had a closer resemblance to the features of *in vivo* glioma cells. These findings indicated that the 3D-engineered glioma scaffolds are promising tools for understanding brain cancer as well as for screening of drugs. Sinha et al. (2023) designed a 3D poly(ethylene-glycol)-based hydrogel system to study the role of viscoelasticity on glioblastoma (GBM) cell fates and drug responses. Increasing stress relaxation was shown to promote invasive behavior, to enhance GBM proliferation, and to enhance drug sensitivity. These findings underscore the importance of viscoelasticity in *in vitro* models of GBM and their implications on GBM cell fates.

Our final two studies focus on breast cancer metastasis. Molnár et al. (2020) showed that pericytes play a critical role in the development of brain metastases. They found that brain pericytes had a chemoattractant effect on breast cancer cells. These pericytes secreted extracellular matrix proteins, which enhanced the adhesion of breast cancer cells, as well as insulin-like growth factor 2, which had a pro-proliferative effect. Together, the findings indicate that brain pericytes induce pro-metastatic effects in breast cancer. Finally, Firatligil-Yildirir et al. (2021) used two organ-on-chip platforms (invasion/chemotaxis (IC-chip) and extravasation (EX-chip)) to quantitatively analyze invasion and extravasation of breast cancer cells towards different tissues. For both platforms, the results were consistent with published clinical data, highlighting the utility of these *in vitro* tools to simulate different microenvironments and distinguish *in vivo* metastatic phenotypes.

Through the studies presented in this article collection, we hope to illustrate the utility of confocal microscopy in mechanistic cancer research. For more information regarding confocal microscopy, we encourage you to visit the Leica Microsystems STELLARIS Confocal Platform page and explore the possibilities presented there for your research.

REFERENCES:

Klimpel, A., Stillger, K., Wiederstein, J.L., Krüger, M. and Neundorf, I. (2021), Cell-permeable CaaX-peptides affect K-Ras downstream signaling and promote cell death in cancer cells. FEBS J, 288: 2911-2929. https://doi.org/10.1111/febs.15612

Rainey, L., Deevi, R.K., McClements, J., Khawaja, H., Watson, C.J., Roudier, M., Van Schaeybroeck, S. and Campbell, F.C. (2020), Fundamental control of grade-specific colorectal cancer morphology by Src regulation of ezrin–centrosome engagement. J. Pathol., 251: 310-322. https://doi.org/10.1002/path.5452

Stefanello, S. T., Luchtefeld, I., Liashkovich, I., Pethö, Z., Azzam, I., Bulk, E., Rosso, G., Döhlinger, L., Hesse, B., Oeckinghaus, A., Shahin, V., (2021), Impact of the nuclear envelope on malignant transformation, motility, and survival of lung cancer cells. Adv. Sci. 8: 2102757. https://doi.org/10.1002/advs.202102757

Barin, N., Balcioglu, H. E., de Heer, I., de Wit, M., Lamfers, M. L. M., van Royen, M. E., French, P. J., Accardo, A., (2022), 3D-Engineered scaffolds to study microtubes and localization of epidermal growth factor receptor in patient-derived glioma cells. Small 18: 2204485. https://doi.org/10.1002/smll.202204485

Sinha, S., Ayushman, M., Tong, X., Yang, F., (2022), Dynamically crosslinked poly(ethylene-glycol) hydrogels reveal a critical role of viscoelasticity in modulating glioblastoma fates and drug responses in 3D. Adv. Healthcare Mater., 12: 2202147. https://doi.org/10.1002/adhm.202202147

Molnár, K., Mészáros, Á., Fazakas, C., Kozma, M., Győri, F., Reisz, Z., Tiszlavicz, L., Farkas, A.E., Nyúl-Tóth, Á., Haskó, J., Krizbai, I.A. and Wilhelm, I. (2020), Pericyte-secreted IGF2 promotes breast cancer brain metastasis formation. Mol. Oncol., 14: 2040-2057. https://doi.org/10.1002/1878-0261.12752

Firatligil-Yildirir, B., Bati-Ayaz, G., Tahmaz, I., Bilgen, M., Pesen-Okvur, D., & Yalcin-Ozuysal, O. (2021). On-chip determination of tissue-specific metastatic potential of breast cancer cells. Biotechnol. Bioeng., 118: 3799– 3810. https://doi.org/10.1002/bit.27855

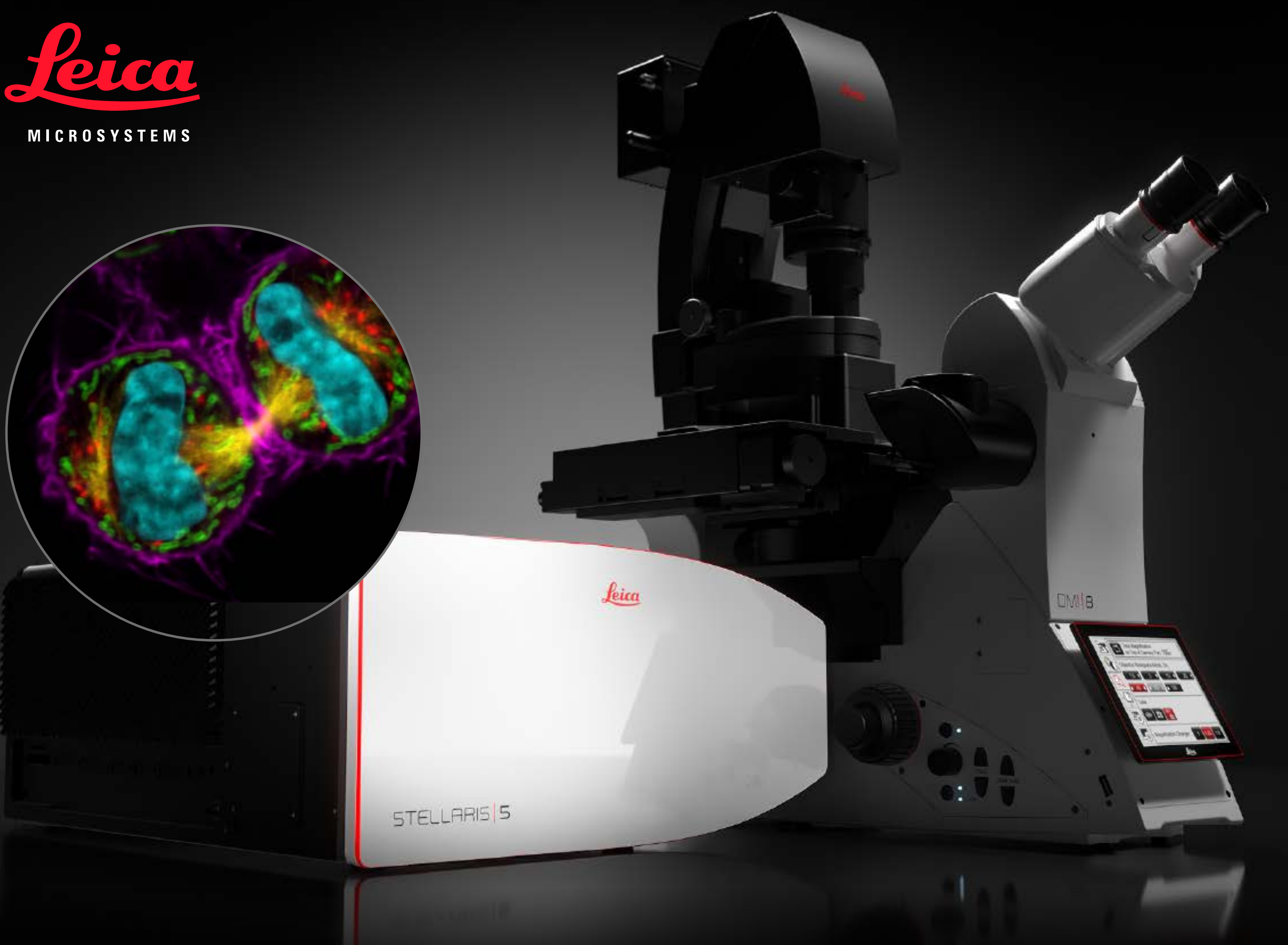
Leica
STELLARIS 5
DMi8

Content

Cover Image © Leica

The FEBS Journal

FEBS PRESS
science publishing by scientists

Cell-permeable CaaX-peptides affect K-Ras downstream signaling and promote cell death in cancer cells

Annika Klimpel[1], Katharina Stillger[1], Janica L. Wiederstein[2], Marcus Krüger[2,3] and Ines Neundorf[1]

1 Institute for Biochemistry, University of Cologne, Germany
2 Institute for Genetics, Cologne Excellence Cluster on Cellular Stress Responses in Aging-Associated Diseases (CECAD), University of Cologne, Germany
3 Center for Molecular Medicine (CMMC), University of Cologne, GermanyOpen access funding enabled and organized by ProjektDEAL.

Keywords
CaaX motif; cell-penetrating peptides; cysteine prenylation; farnesyltransferase; Ras proteins

Correspondence
I. Neundorf, Institute for Biochemistry,
University of Cologne, Zuelpicher Str. 47a,
50674 Cologne, Germany
Tel: +49 (0) 221 470 8847
E-mail: ines.neundorf@uni-koeln.de

[Correction added on 04 December 2020, after first online publication: Peer review history is not available for this article, so the peer review history statement has been removed.]

(Received 16 February 2020, revised 17 August 2020, accepted 26 October 2020)

doi:10.1111/febs.15612

Cysteine prenylation is a post-translational modification that is used by nature to control crucial biological functions of proteins, such as membrane trafficking, signal transduction, and apoptosis. It mainly occurs in eukaryotic proteins at a *C*-terminal CaaX box and is mediated by prenyltransferases. Since the discovery of prenylated proteins, various tools have been developed to study the mechanisms of prenyltransferases, as well as to visualize and to identify prenylated proteins. Herein, we introduce cell-permeable peptides bearing a *C*-terminal CaaX motif based on Ras sequences. We demonstrate that intracellular accumulation of those peptides in different cells is controlled by the presence of their CaaX motif and that they specifically interact with intracellular prenyltransferases. As proof of concept, we further highlight their utilization to alter downstream signaling of Ras proteins, particularly of K-Ras-4B, in pancreatic cancer cells. Application of this strategy holds great promise to better understand and regulate post-translational cysteine prenylation.

Introduction

Protein prenylation is an irreversible post-translational modification (PTM) found in eukaryotic cells and includes farnesylation (15-carbon body) and geranylgeranylation (20-carbon body) at a *C*-terminal CaaX box, comprising cysteine (C) and aliphatic (a) and variable (X) amino acids [1–3]. Attachment of these isoprenoids to cysteine occurs by prenyltransferases (farnesyltransferase (FTase) and geranylgeranyltransferase (GGTase)) and results in a stable thioether bond depending on the identity of the variable amino acid X (Fig. 1A) [4–7]. Subsequent steps include proteolysis to release the terminal aaX tripeptide by the endopeptidase RAS-converting enzyme 1 (RCE1) [8,9], and methylation of the free carboxylic function of the terminal cysteine residue by isoprenylcysteine carboxyl methyltransferase (ICMT) [10,11]. Cysteine prenylation has been studied extensively owing to its involvement in numerous biological processes, particularly signal

Abbreviations
CF, 5,6-carboxyfluorescein; CLSM, confocal laser scanning microscopy; CPP, cell-penetrating peptides; ER, endoplasmaic reticulum; FTase, farnesyltransferase; FTI, farnesyltransferase inhibitor; GGTase, geranylgeranyltransferase; HVR, hypervariable region; ICMT, isoprenylcysteine carboxyl methyltransferase; PDAC, pancreatic ductal adenocarcinoma; PTM, post-translational modification; RCE1, RAS-converting enzyme 1; SPPS, solid-phase peptide synthesis.

transduction pathways that regulate cell growth and proliferation [4,12]. In this respect, the activation of small GTP-binding Ras proteins, which induces the cycling between an active GTP-bound and an inactive GDP-bound state [13], is of high interest. In mammalian cells, the Ras subfamily consists of several isoforms, including HRas, N-Ras, and the splice variants K-Ras-4A and K-Ras-4B [14]. All four family members show high-sequence homology in their *N*-terminal globular domain but differ in their *C*-terminal hypervariable region (HVR) including the secondary signal and the CaaX box (Fig. 1 for HRas and K-Ras-4B) [15]. Ras proteins are important nodes in many cellular processes, such as cell proliferation, growth, survival, and intracellular signaling networks, and their dysregulation is responsible for severe malignancies [4]. In fact, RAS genes are the most commonly mutated oncogenes in cancer and roughly 20–30% of all tumors show enhanced RAS activity due to specific mutations [16,17].

For example, 90% of pancreatic carcinomas show activating K-Ras (point mutations at codon 12, 13, or 61) [20–22]. Earlier studies showed that gain-of-function mutations result in an arrest of Ras proteins in their active GTP-bound state, and oncogenic Ras is considered as a promising target for anticancer therapy.

But so far, active Ras mutants are undruggable due to the lack of suitable pockets for binding small molecule inhibitors [15,19]. An alternative targeting strategy implies interference of the post-translational processing of Ras proteins [12,23], which requires membrane association promoted by protein prenylation for initiation of downstream signaling cascades [24,25]. Early studies already highlighted that loss-of-membrane association prevents Ras mutants to induce cell transformation [26]. Initial attempts to develop pharmacological Ras inhibitors focused on FTase inhibitors (FTI) [27], but resulted in disappointing clinical trials [28]. This was partly due to the fact that K-Ras can also be a substrate for GGTase, leading to geranylgeranyl cross-prenylation and rescue of its oncogenic activity [28,29].

However, owing to its involvement in multiple biochemical pathways, many studies are still ongoing to develop tools that help to understand enzymes involved in the prenylation process and to find novel drug targets, particularly in terms of Ras function and

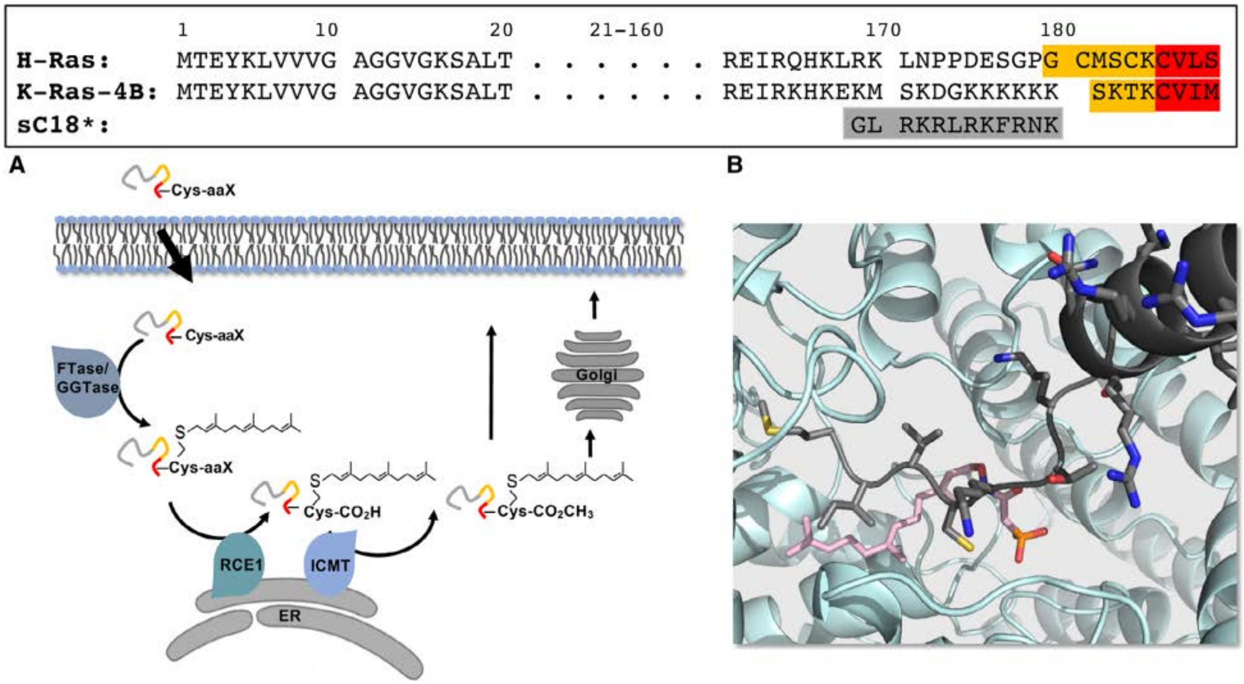

Fig. 1. Alignment of human HRas and K-Ras-4B. Protein sequences were exported from the UniPort database with the respective accession numbers P01112-1 and P01116-2 [18]. CaaX boxes: red, secondary signals: underlined, sequence of sC18*: gray. CaaX-peptides comprise a fusion of the colored sequences (see Table 1). (A) Model of CaaX-peptide processing: after cellular uptake, prenyltransferases attach an isoprenoid lipid to the Cys of the CaaX motif. Then, cleavage of the aaX tripeptide by RCE1 and methylation of the free carboxylic group by ICMT occurs. (B) Crystal structure of the FTase binding pocket with the potentially interacting CaaX-1 peptide (gray) and a farnesyl pyrophosphate analog (pink). Generated with the PDB code 1D8D using PYMOL [19].

inhibition. For instance, analogs of isoprenoid diphosphates are utilized to analyze the mechanisms of prenylation, to identify prenylated proteins, and to validate enzymatic activities of prenyltransferases [30,31]. Additionally, libraries of short peptides having free CaaX-termini were screened against substrate specificity of prenyltransferases [32]. To temporally control prenylation, caged substrates (either isoprenoids or peptides) were developed that can be released upon photolysis and were used to characterize the prenylation reaction in more details [33]. While those studies helped to get a clearer picture about structural and mechanistic features, as well as the enzymology of prenyltransferases, still much has to be learned about protein prenylation in living cells. Recently, an approach in this direction was provided by Flynn *et al.* that created a calibrated sensor for cellular FTase activity [34]. Moreover, also cell-penetrating prenylated peptides were generated as tools to study enzymatic processing and intracellular trafficking related to this PTM [35,36].

Herein, we designed cell-permeable peptides incorporating the *C*-terminal sequence of Ras proteins and investigated their impact on intracellular prenylation processes. The so-called CaaX-peptides include a cell-penetrating peptide (CPP) sequence, namely sC18* [37,38], and the CaaX boxes CVLS and CVIM, which are derived from HRas and K-Ras-4B, respectively (Fig. 1). Our results highlight that these peptides are specifically recognized by prenyltransferases (most probably FTase; Fig. 1B) based on their PTM motifs. Thus, we present an intriguing example of how the intracellular accumulation of cell-permeable peptides can be controlled. Strikingly, these novel tools induced notable downstream effects on the cellular level, particularly in cancer cells, what makes them a promising, novel concept to address Ras proteins, and their signaling cascades.

Results and Discussion

Design and synthesis of cell-permeable CaaX-peptides

Three different CaaX-peptides were designed comprising each a cell-penetrating peptide sequence at the *N* terminus, followed by the so-called secondary signal [25] and the CaaX motif (see Table 1 for sequences). In case of the K-Ras-4B-derived peptide CaaX-1, we replaced parts of the secondary signal, which is responsible for plasma membrane association in acidic regions (Fig. 1) [16,39]. In our opinion, this polybasic feature was perfectly fulfilled by the sequence of sC18*. This truncated CPP version still demonstrates cell-penetrating abilities [38,40] and was used in order to keep the general length of all peptide hybrids as short as possible. Moreover, the penultimate amino acid of the CaaX motif of HRas (CaaX-2), which is in this case a leucine, was exchanged with a glycine (yielding peptide CaaX-3). This amino acid substitution was previously shown to result in loss-of-membrane association and increased cytosolic distribution for an eGFP-CVGS construct [34]. All designed peptides were synthesized by solid-phase peptide synthesis (SPPS) using an optimized synthesis strategy (Fig. 2).

Subsequently, they were labeled with 5(6)-carboxyfluorescein (CF) or biotin, respectively, and after cleavage from the resin and purification, the amino acid sequence was substantiated by mass spectrometry. As controls, peptides having the CaaX box cysteine substituted with serine were generated (SaaX-1 and SaaX-2), since prenylation does not take place at serine [34]. In

Table 1. Names, sequences, and analytical data of investigated peptides.

Names	Descriptions	Sequences	MW_{calc} [Da]	MW_{exp} [Da]	Net charge
CaaX-1	sC18*-KRas4B(181-188)	GLRKRLRKFRNK-SKTK-CVIM-OH	2463.1	2463.6	+9
SaaX-1	sC18*-KRas4B(181-188), *C185S*	GLRKRLRKFRNK-SKTK-SVIM-OH	2447.0	2447.5	+9
CaaX-2	sC18*-HRas(181-189)	GLRKRLRKFRNK-GCMSCK-CVLS-OH	2584.2	2584.7	+8
CaaX-3	sC18*-HRas(181-189), *L188G*	GLRKRLRKFRNK-GCMSCK-CVGS-OH	2528.1	2528.5	+8
SaaX-2	sC18*-HRas(181-189), *C186S*	GLRKRLRKFRNK-GCMSCK-SVLS-OH	2568.2	2568.9	+8
sC18*	–	GLRKRLRKFRNK-NH2	1571.9	1571.4	+8
Control peptides					
sC18*-KR	sC18*-KRas4B(181-184)	GLRKRLRKFRNK-SKTK-NH2	2015.5	2015.8	+10
KR-C-1	KRas4B(181-188)	SKTK-CVIM-OH	909.2	909.1	+2
KR-S-1	K-Ras4B(181-188), *C185S*	SKTK-SVIM-OH	893.1	893.2	+2
sC18*-HR	sC18*-HRas(181-185)	GLRKRLRKFRNK-GCMSCK-NH2	2180.7	2180.7	+9
HR-C-2	HRas(181-189)	GCMSCK-CVLS-OH	1030.3	1030.9	+1
HR-C-3	HRas(181-189), *L188G*	GCMSCK-CVGS-OH	974.2	973.8	+1
HR-S-2	HRas(181-189), *C186S*	GCMSCK-CVLS-OH	1014.2	1014.0	+1

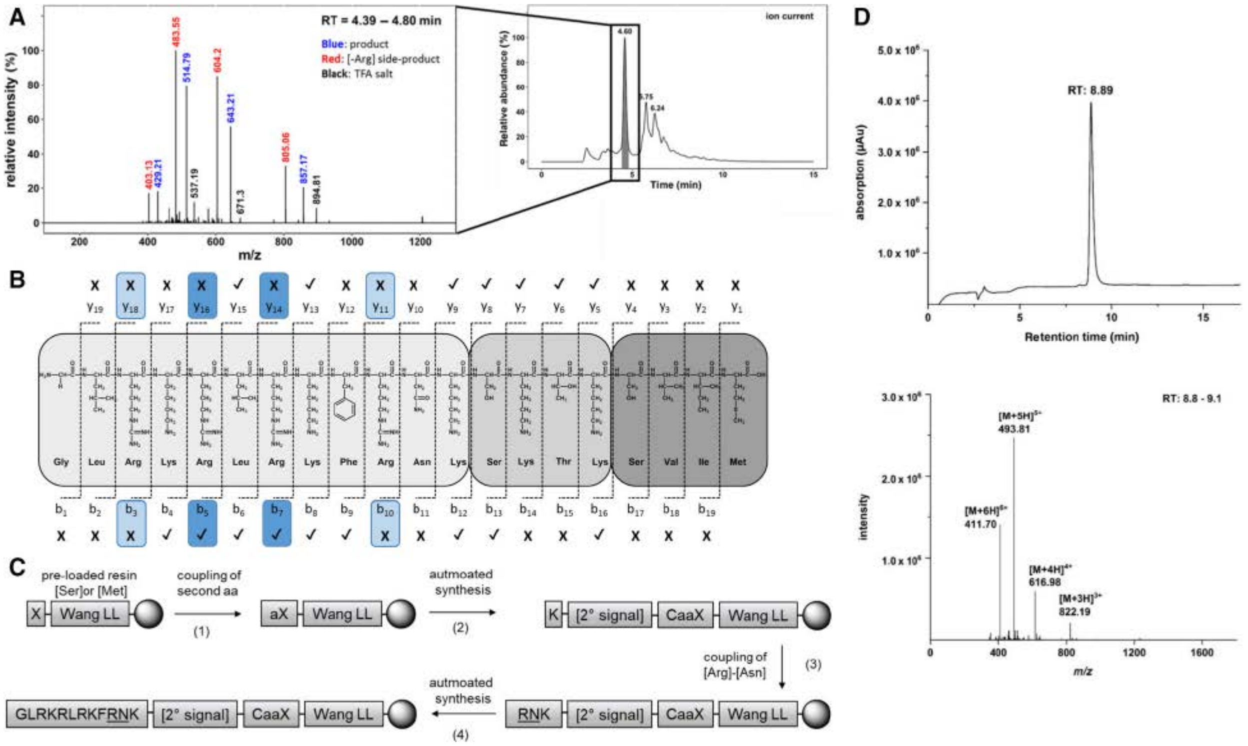

Fig. 2. Optimization of peptide synthesis strategy. (A) Exemplary ion current and mass spectrum (RT = 4.39–4.80 min) of SaaX-2 showing the [-Arg] by-product with more intensive MS signals than the desired product. The quasimolecular ions of SaaX-2 are highlighted in blue (m/z): [M + 3]3+ = 857.17, [M + 4]4+ = 643.21, [M + 5]5+ = 514.79, [M + 6]6+ = 429.21. Quasimolecular ions belonging to [-Arg] by-product are marked in red. Signals beside product signals in black belong to a TFA-adduct of SaaX-2. Similar problems occurred when synthesizing the other CaaX/SaaX-peptides. (B) Fragmentation pattern of SaaX-1 obtained by LC-MS2. Y-ions for fragments resulting from bond cleavage next to Arg residues were not detectable, but the b-ions b5 and b7 were obtained (✓ = detected; x = not detected). For verification of these results and to determine whether the first or the last arginine of the sequence was missing, a further fragmented synthesis was carried out (data not shown). Based on these data, we followed a semiautomated synthesis strategy (C) using preloaded Wang resins and manual loading of the second amino acid, as well as of the identified Arg and Asn residues. (1): Fmoc-deprotection: 30% piperidine/DMF, 2 × 20 min; coupling: 5 eq. aa/Oxyma/DIC, o/n. (2)/(4): 40% piperidine/DMF, 3 min; 20% piperidine/DMF, 10 min; 8 eq. aa/Oxyma/DIC, 2 × 20 min. (3): 5 eq. aa/Oxyma/DIC, 2 × o/n. Capping: AC2O/DIPEA/CH2Cl2 (8 : 1 : 1; v/v/v), 15 min. Fmoc-deprotection: 30% piperidine/DMF, 2 × 20 min. (C) Exemplarily LC-MS analysis of CaaX-1; MW calculated: 2463.08 g/mol. Gradient: 10–60% B in A in 15 min, 1.0 mL·min^{-1}. A: 0.1% TFA in H2O; B: 0.1% TFA in CAN.

addition, several more control peptides were included, lacking either the CaaX boxes or the CPP (Table 1).

Cell-permeable CaaX-peptides get intracellularly enriched

We first assessed the cellular uptake of CaaX-peptides in the human cancer cell lines HeLa and MCF-7, as well as in noncancerous mouse fibroblasts (MEF), which all express the wild-type Ras protein. Cells were treated with 10 µM of CF-labeled peptide solutions for 0.5 h at 37 °C (Fig. 3A).

An increase in green fluorescence was recognized when cells were incubated with CaaX-peptides, compared to the control peptides containing the SaaX-motifs and compared to the CPP alone. In fact, we noticed a 20- to 100-fold increased uptake dependent on the CaaX-peptide used (Fig. 3A). For other hybrid CPP-peptide conjugates with improved membrane activity, and thus, increased internalization efficiency, this was a result of a change in secondary structure or amphipathicity [37,38,41–43]. However, the herein obtained results rather suggest that enrichment of the CaaX-peptides is triggered and enhanced after selective intracellular recognition by their CaaX motifs. This hypothesis is in accordance with the observed negligible uptake of the SaaX controls, in which only one amino acid was exchanged (C → S), and which displayed similar secondary structures (Fig. 3C). We further verified this assumption by studying in detail the impact of each motif of the peptides. For this purpose, control peptides lacking the CaaX box, or the CPP,

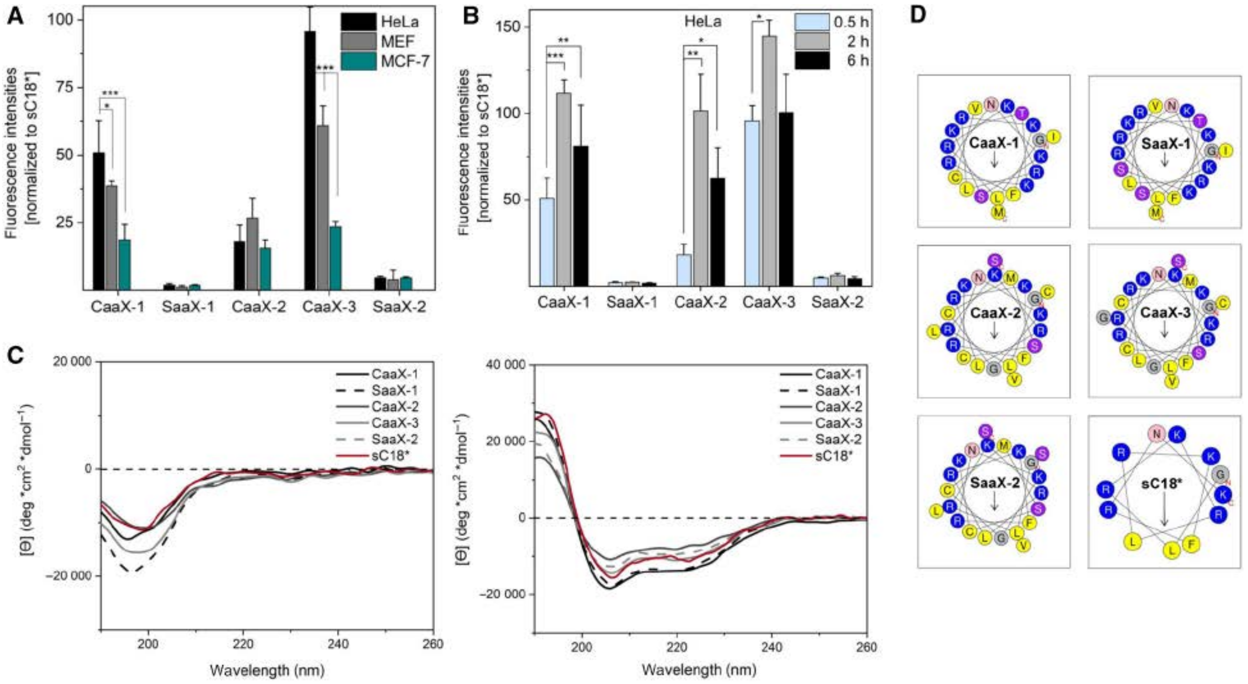

Fig. 3. (A) Cellular uptake of CaaX/SaaX-peptides as quantified by flow cytometry. Cells were incubated with 10 µM of CF-labeled peptide solutions for 0.5 h at 37 °C. Fluorescence intensities of sC18* were set to a value of 1. (B) Time-dependent uptake (0.5–6 h) into HeLa cells. Error bars of (A, B) indicate the standard deviations of $n = 9$ values, and the significances were determined by Student's *t*-test (*$P < 0.05$; **$P < 0.005$; ***$P < 0.0005$). (C) CD spectra of synthesized peptides measured in 10 mM phosphate buffer, pH 7.0, and supplemented with 50 % (v/v) trifluoroethanol (TFE). (D) Helical wheel projections of all synthesized peptides predicted by HeliQuest (https://heliquest.ipmc.cnrs.fr). Hydrophobic residues are marked in yellow, while residues that possess zero hydrophobicity are marked in gray. Hydrophilic uncharged residues are labeled in pink, whereas potentially positively charged residues are labeled in blue.

respectively, were synthesized and their cellular uptake was quantified. Notably, we detected for almost all of these control peptides significantly decreased internalization efficiencies (Fig. 4B,C), underlining again the importance of both moieties for their intracellular function.

Comparing the uptake of the different CaaX-peptides in the studied cell lines, we found that cellular translocation was cell line-dependent; however, the CaaX-3 peptide indicated the highest uptake in all cell lines tested (Fig. 3A). Interestingly, the cellular uptake was lowest for MCF-7 cells, whereby in HeLa and MEF cells relatively similar uptake levels were detected. Moreover, we observed a time-dependent cellular accumulation in HeLa cells, which was highest after 2 h and decreased again after 6 h of incubation pointing to degradation or cellular release of the peptides (Fig. 3B).

To get more insights into the intracellular distribution of the CaaX-peptides, we performed confocal laser scanning microscopy (CLSM) using the same experimental conditions as before. Figure 5 shows the results when cells were incubated for 0.5 and 2 h, which confirm the internalization ability of all CaaX-peptides tested. Again, SaaX-peptides were only hardly detectable (shown for SaaX-1 in Fig. 5F). In addition, CaaX-peptides exhibited a mostly vesicular distribution pattern suggesting an endocytic uptake mechanism (Fig. 3A–C). Interestingly, when inspecting CaaX-3 in HeLa cells after 2 h, the compound displayed also a diffuse cytosolic distribution, corroborating recent results, where it was shown that an EGFP-CVGS mutant was diffusely expressed in HEK293T cells [34,44].

Cell-permeable CaaX-peptides have unexpected impacts on cell viability

To analyze the cytotoxic profile of the novel peptides, we incubated them in several concentrations for 24 h with the aforementioned three cell lines. No significant effects on cellular viability were measured when cells were treated with all of the control peptides, particularly SaaX-1, SaaX-2, and the CPP sC18*, respectively

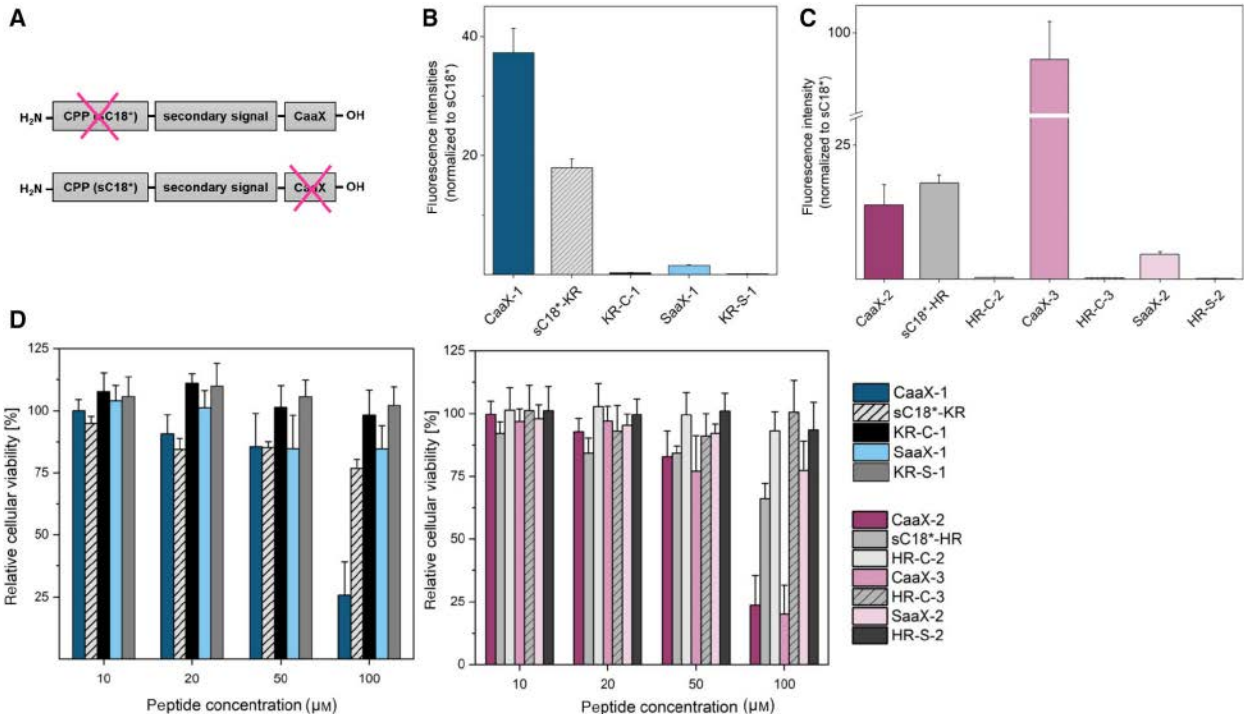

Fig. 4. Synthesis and analysis of control peptides (Table 1). (A) Design of control peptides missing either the CaaX box or the CPP (B). (C) Cellular uptake of synthesized control peptides into HeLa cells quantified by flow cytometry. Cells were incubated with 10 μM of CF-labeled peptide solution for 0.5 h at 37 °C. Fluorescence intensities were normalized to the internalization of sC18*. (D) Cytotoxicity of peptides when incubated with HeLa cells at 37 °C for 24 h with indicated concentrations. Cellular viability was related to untreated cells (100%). Error bars of (B–D) represent the standard deviations of *n* = 9 values.

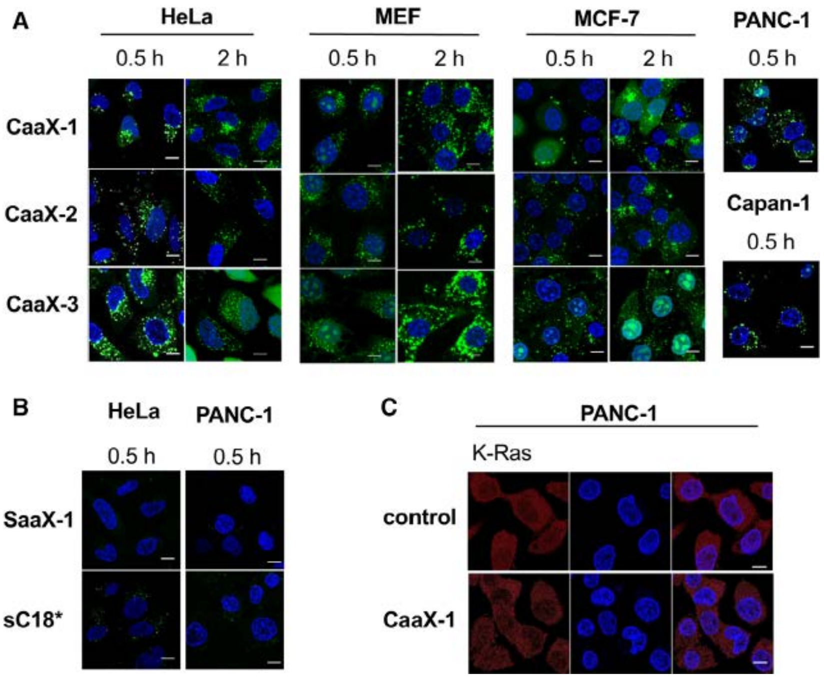

Fig. 5. Microscopic analysis of CaaX-peptides using (A) HeLa, MEF, MCF-7, PANC-1, and Capan-1 cells. (B) Images of control peptides incubated with HeLa and PANC-1 cells. Cells were incubated with 10 μM of CF-labeled peptide solution for 0.5 or 2 h at 37 °C. Green: CF-labeled peptide; blue: nuclear Hoechst 33342 stain; scale bar is 10 μm. (C) K-Ras localization assessed by immunofluorescence staining via the K-Ras antibody and visualized with IgGk light chain binding protein (m-IgGk BP; red) after treating PANC-1 cells for 24 h with 30 μM of unlabeled CaaX-1 peptide. Cells were fixed with 4% paraformaldehyde. Live cell imaging (A, B) was conducted in three replicates, while immunostaining (C) was performed twice.

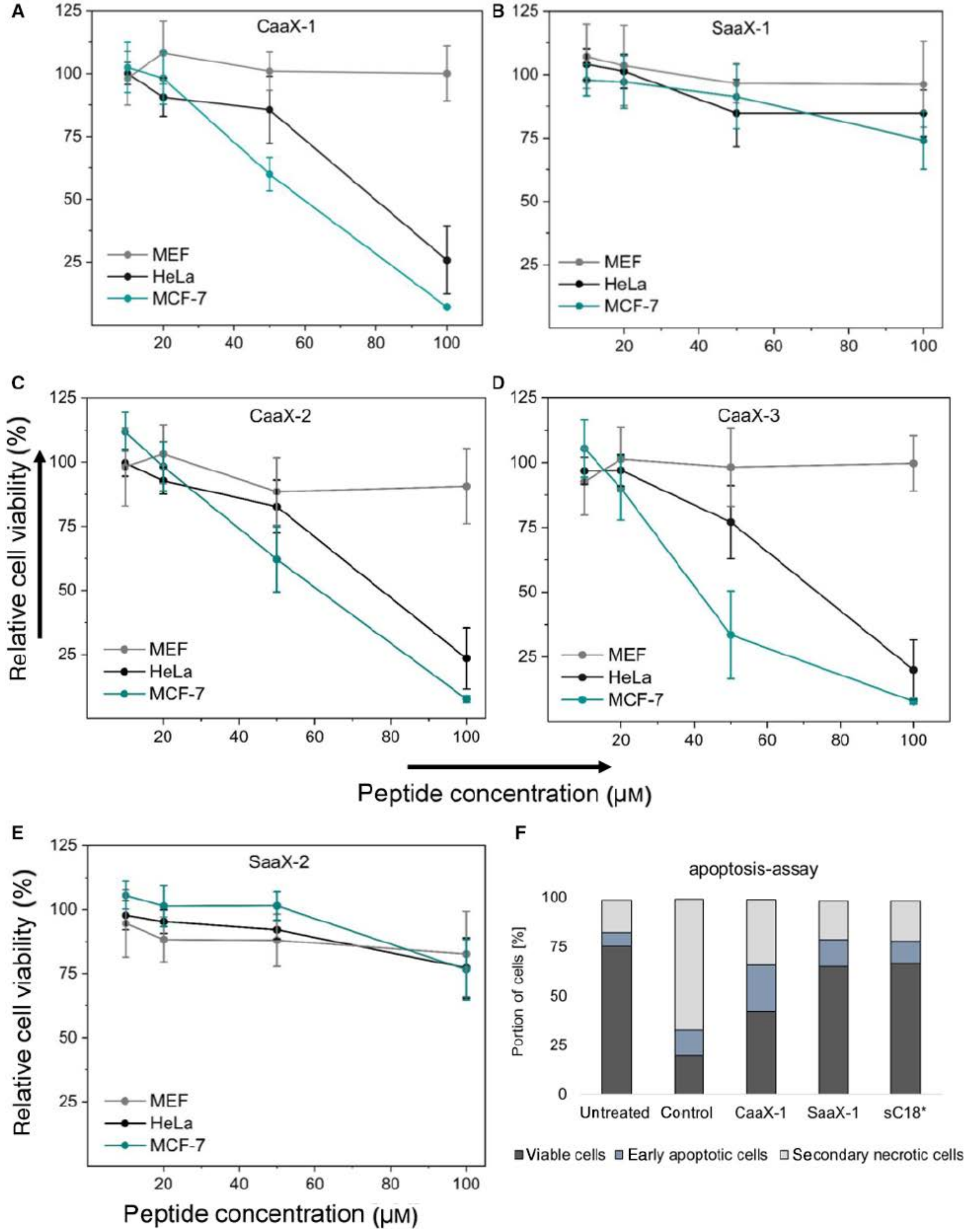

Fig. 6. (A–E) Cytotoxicity profiles of novel peptides. Cells were incubated for 24 h with various concentrations of indicated peptides. Cellular viability was related to untreated cells (100%); assays were performed in triplicates (*n* = 3), and therefore, error bars of (A–E) indicate the standard deviations of *n* = 9 values. (F) Flow cytometric analysis of cell apoptosis/necrosis using the Annexin V-FITC/7-AAD kit (Beckman Coulter). PANC-1 cells were incubated with 30 µM of peptides for 24 h. As a positive control, cells were incubated with 7 µM of staurosporine.

(Figs 4D and 6). The latter is in agreement with previously published data [37,38]. Moreover, no significant decrease in cellular viability was detected when MEF cells were incubated with CaaX-peptides, although high intracellular enrichment near to the range of HeLa cells was observed (Fig. 3A).

Of more interest was that peptides carrying a CaaX motif displayed cytotoxicity when applied in concentrations ≥ 50 µM for HeLa and MCF-7 cells, while in the latter cell line the strongest effects were observed. This was interesting, since MCF-7 cells, like the majority of breast cancer cells, do not carry mutations in Ras proteins. However, it was already shown that cytokines often lead to increased levels of the GTP-bound form of WT-Ras and are able to turn it into tumor-promoting entities regarding breast cancer growth and development [45]. Moreover, antitumor activity of FTase inhibitors (FTIs) in breast cancer was presented recently. This activity was assumedly independent on the mutation status of Ras, but rather dependent on many other factors accompanied by FTase action [46]. Therefore, we speculated that the relatively low cellular uptake in combination with the cytotoxic effects could point to elevated levels of FTase in combination with activated Ras proteins in the MCF-7 cells and, thus, a higher cellular impact of our peptides on intracellular Ras processing and interaction.

Evaluating the influence of CaaX-1 on K-Ras-mutated cells

Inspired by the above-mentioned observation that CaaX-peptides may have an impact on cells in which Ras isoforms are dysregulated, we focused in the following on the K-Ras-derived peptide CaaX-1 and its function in K-Ras-mutated cells. Indeed, K-Ras was shown to be the most frequent mutated isoform in Ras-driven cancers, with high frequencies of around 40% in colorectal cancers, and more than 90% in pancreatic ductal adenocarcinomas (PDAC) [47]. For our following studies, we thus chose two pancreatic cancer cell lines (PANC-1 and Capan-1), and the colorectal cancer cell line LS174T, which all carry a K-Ras

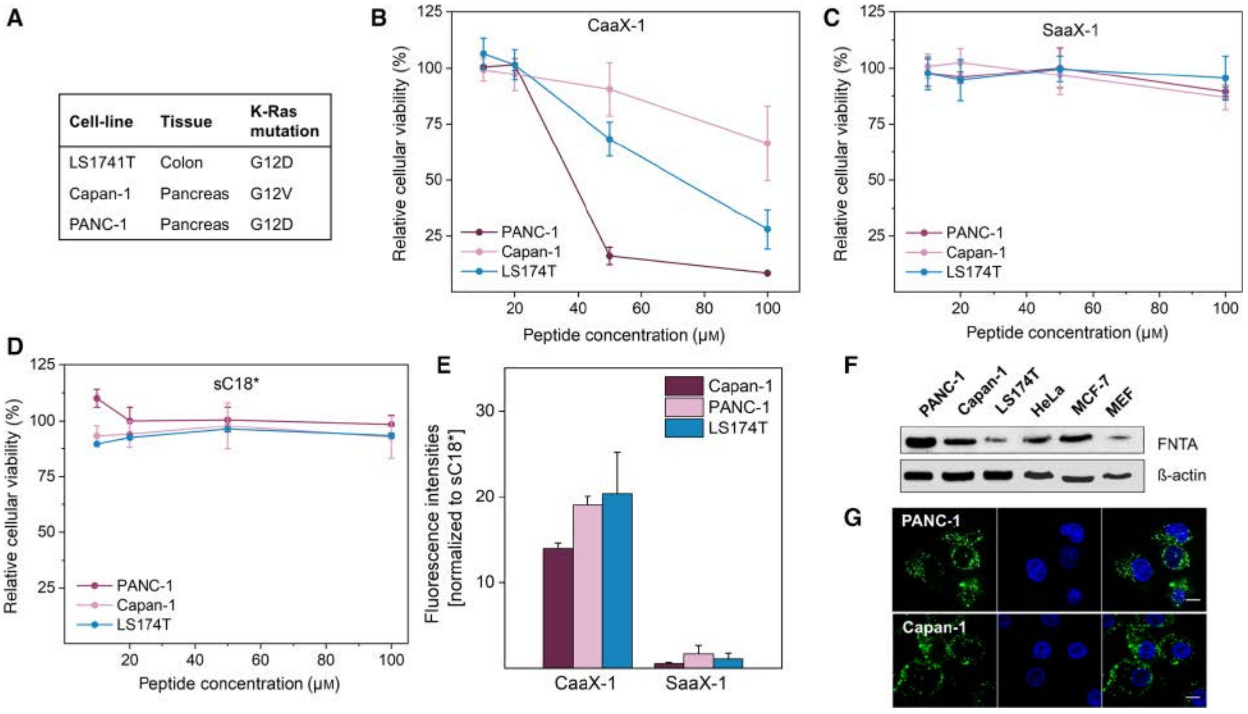

Fig. 7. (A) Pancreatic and colon cell lines used, their origin and K-Ras mutation. (B–D) Cytotoxicity profiles of CaaX-1, SaaX-1, and sC18* in LS174T, PANC-1, and Capan-1 cells. Cells were incubated with indicated concentrations of peptides at 37 °C for 24 h. Cellular viability was related to untreated cells (100%). (E) Cellular uptake of 10 µM peptide solutions into LS174T, PANC-1, and Capan-1 cells after 0.5 h of incubation at 37 °C. Error bars of (b-e) represent the standard deviations of $n = 9$ values. (F) Expression levels of farnesyltransferase as quantified by western blot using 30 µg of cell lysates against the alphasubunit of farnesyltransferase (loading control: β-actin). (G) Intracellular distribution of CaaX-1 in PANC-1 and Capan-1 cells as analyzed by CLSM. Cells were incubated for 2 h with 10 µM of CF-labeled peptide solution. Green: CF-labeled peptide; blue: nuclear Hoechst 33342 stain; scale bar is 10 µm. Experiments of (F, G) were performed in three replicates.

mutation at G12 (Fig. 7A). This oncogenic mutation is present predominantly in human cancers (89%), and impairs intrinsic and GAP-mediated GTP hydrolysis [48]. Interestingly, in terms of toxicity, PANC-1 cells were the most sensitive cell line according to the treatment of the CaaX-1 peptide, followed by LS174T and Capan-1 cells (Fig. 7B). Again, no effects on cellular viability were observed for SaaX-1 or sC18* (Fig. 7C, D). In addition, an apoptosis assay revealed an increased number of PANC-1 cells undergoing apoptosis and necrosis after treatment with CaaX-1 (Fig. 6F).

Regarding the cellular uptake, the results point to comparable internalization efficiencies of CaaX-1 in these three cell lines and MCF-7 cells (Fig. 7E), although the overall uptake was lower in comparison with HeLa and MEF cells (Fig. 3A). To determine whether there was any relationship between the observed toxicity and recognition of prenylation motifs, we validated the expression levels of farnesyltransferase by performing western blot analysis (Fig. 7F). The intensities of FTase expression in the analyzed cell lines correlated well with the degree of toxicity (PANC1>MCF-7>HeLa>LS174T>MEF). In contrast, Capan-1 cells showed no correlation, while displaying high expression levels of FTase, but only low sensitivity to the CaaX-1 peptide. Although the mutation in the K-Ras amino acid sequence of PANC-1 and Capan-1 cells is at the same position (glycine 12), it differs concerning the substituted amino acid (G12V versus G12D), which might also impact gene expression and other factors resulting in this observed effect [48,49].

We then assessed the intracellular distribution after 0.5 and 2 h performing confocal microscopic analysis, which revealed similar phenotypes of PANC-1 and Capan-1 cells after treatment with CaaX-1, demonstrating predominantly punctuate patterns (Figs 5A,B and 7G).

FTase activity is responsible for intracellular enrichment of CaaX-1

Given the high activity of CaaX-1 in PANC-1 cells, we focused in the following on this cell line. First, we further investigated the time-dependent uptake of CaaX-1 (Fig. 8A). We observed a 4.5-fold increase in internalization after 2 h, and in contrast to HeLa cells (Fig. 3B), the signal did not decrease after 6 h, which might be due to the hyperactivated status of K-Ras. In the next step, we explored the cellular uptake of CaaX-1 in a three-dimensional cell model by preparing 3D-PANC-1 spheroids (Fig. 8B,C).

Here, mean fluorescence intensities were lower in comparison with the inspected 2D cell culture models. More interestingly, we recognized a relatively homogenous internalization into all PANC-1 cell layers. Our data were supported by a nearly Gaussian intensity distribution (Fig. 8C). Generally, for a peptide that internalizes only in the periphery of the spheroid the intensity distribution is expected to be broader, than for a peptide that passes through different layers of the spheroid [50]. In comparison, the intensity distribution of the control peptide SaaX-1 displayed more heterogeneity with two populations pointing to a low peripheral uptake only into the outer layers of the spheroids. Also, in this case, uptake efficiencies were negligible supporting again the importance of the presence of the CaaX box for intracellular enrichment.

In order to analyze whether the CaaX-peptides were indeed identified by farnesyltransferase, we studied the impact of different inhibitors on the internalization efficiencies of CaaX-1. Therefore, we used the farnesyl analog AFCME [51], the FTI tipifarnib [52] and we applied Mevastatin [53], which inhibits conversion of hydroxymethylglutaryl (HMG)-CoA into mevalonate, an upstream precursor of FPP and geranylgeranyl pyrophosphate (GGPP) [54]. We preincubated PANC-1 cells with the different inhibitors, respectively, before adding CaaX-1, followed by flow cytometry analysis of the intracellular uptake (Fig. 8D). Interestingly, uptake of CaaX-1 was not altered after incubation with tipifarnib and even increased after incubation with AFCME, which was supposedly the result of cross-prenylation by GGTase [55], a process recently described [56,57]. Therefore, to completely inhibit prenylation of K-Ras, both pathways need to be disrupted. Accordingly, treatment of PANC-1 cells with Mevastatin resulted in significantly decreased cellular uptake of CaaX-1, proving a prenylation-dependent accumulation of CaaX-1.

To further substantiate CaaX-1 interaction with FTase, we synthesized biotinylated CaaX-1 and performed pull-down assays. Indeed, when magnetic streptavidin beads were preloaded with biotinylated CaaX-1, specific interaction with either recombinant rat FTase or prenyltransferases of PANC-1 cell lysate was detected (Fig. 8E,F). Based on our obtained data thus far, we suggest the following model for CaaX cellular uptake and intracellular fate: After internalization of CaaX-peptides, they are recognized and processed by prenyltransferases (e.g., FTase), and assumedly modified with an isoprenoid lipid. This intracellular modification would then induce a removal of the CaaX-peptides from the internalization equilibrium, triggering intracellular enrichment (Fig. 9).

Based on this model, we wondered whether internalization of CaaX-1 would also be responsible for an

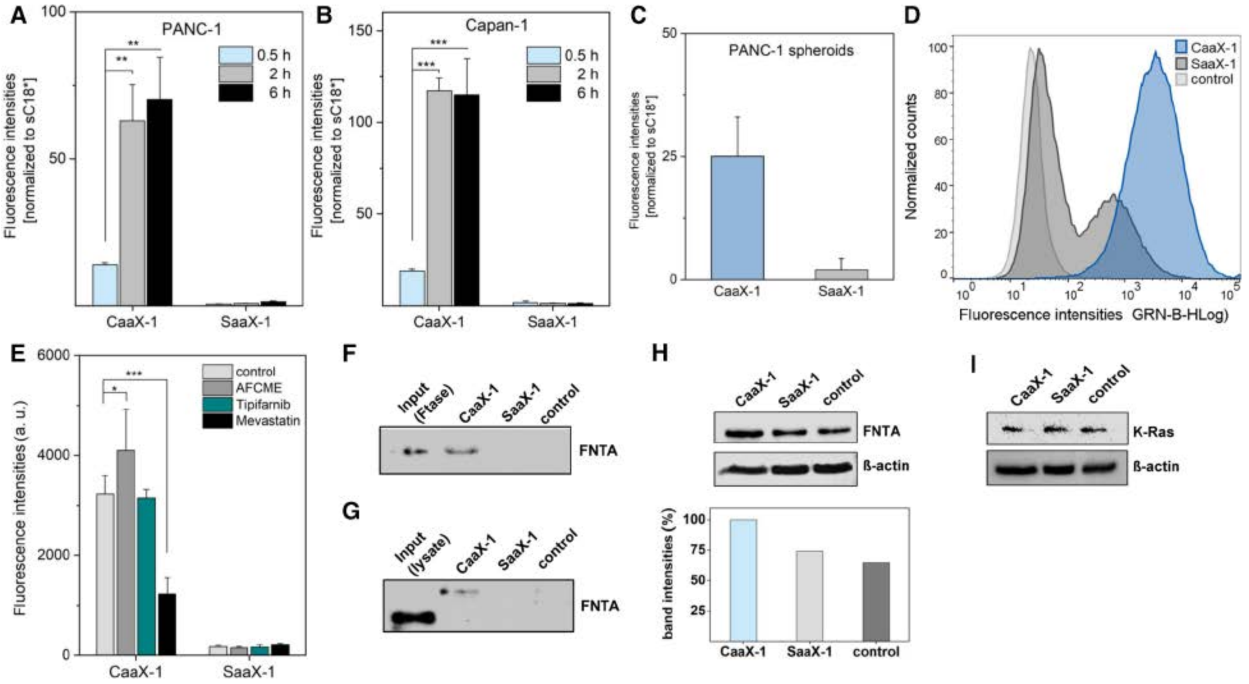

Fig. 8. Time-dependent uptake (0.5–6 h) of CaaX-1 and SaaX-1 into PANC-1 cells (A), and quantitative uptake after 2 h of incubation with PANC-1 spheroids (B, C). Spheroids were incubated for 2 h with 10 µM of CF-labeled CaaX-1 or SaaX-1. Error bars of (A, B, D) indicate the standard deviations of $n = 9$ values. (D) Cellular uptake of CaaX-1 and SaaX-1 after preincubation of PANC-1 cells with either the farnesyl analog *N*-Acetyl-S-farnesyl-l-cysteine-methyl-ester (AFCME) (for 30 min), the FTI tipifarnib, or the isoprenoid metabolism inhibitor Mevastatin (overnight). CF-labeled peptides were incubated for 30 min in a concentration of 10 µM. Significance was determined by Student's *t*-test (*$P < 0.05$; **$P < 0.005$; ***$P < 0.0005$). (E, F) Pull-down assay with either recombinant rat FTase (E) or crude PANC-1 lysate (F). (G, H) Expression level of prenyltransferases (G) or K-Ras (H) of CaaX-1- and SaaX-1-treated PANC-1 cells in comparison with control cells. Peptides were incubated for 24 h in a concentration of 30 µM, and quantification was performed by western blotting (loading control: β-actin). All western blot analysis (E–H) was conducted in three replicates.

upregulated level of FTase, sort of a consequence of its intracellular modification. We measured the expression level of FTase in CaaX-1- and SaaX-1-treated PANC-1 cells, in comparison with untreated cells. As depicted in Fig. 8G, band intensities did indeed reinforce our hypothesis. We also speculated that CaaX-1 peptides did not act as FTI's, but more as competitors to other proteins serving as substrates for prenyltransferases, such as K-Ras. This is supported by the finding that K-Ras expression levels remained unaffected (Fig. 8H) and we did not observe any alteration in K-Ras localization (Fig. 3C). Therefore, we concluded that off-target effects might have led to the observed strong cytotoxicity in PANC-1 cells.

Proteome profiling of CaaX-1-treated PANC-1 cells reveals changes in K-Ras downstream signaling

We further examined the proteomic changes caused by CaaX-1 incubation in comparison with SaaX-1-treated and untreated (control) PANC-1 cells. A label-free quantitative proteome analysis was performed after incubating cells for 24 h with 30 µM peptide solutions. We quantified in total 4361 proteins, of which 186 were significantly altered between the three conditions (based on ANOVA, *P* value < 0.05). Hierarchical clustering revealed four different protein clusters ($n = 146$), from which cluster 1 ($n = 73$) and cluster 4 ($n = 36$) contained proteins that were exclusively upregulated or downregulated after treatment with CaaX-1, respectively (Fig. 10A). Among the upregulated proteins in cluster 1, we found candidates involved in actin binding and actin filament organization including Thymosin beta-4, Thymosin beta-10, and LIM and SH3 domain protein 1. The organization of the actin cytoskeletal is mediated by Ras-regulated signaling pathways, and its dysregulation assumedly is related to a dysfunction of Ras proteins after CaaX-1 treatment [57]. Furthermore, within both clusters (1 and 4), we identified proteins associated with the ER, an important organelle for protein folding, post-translational

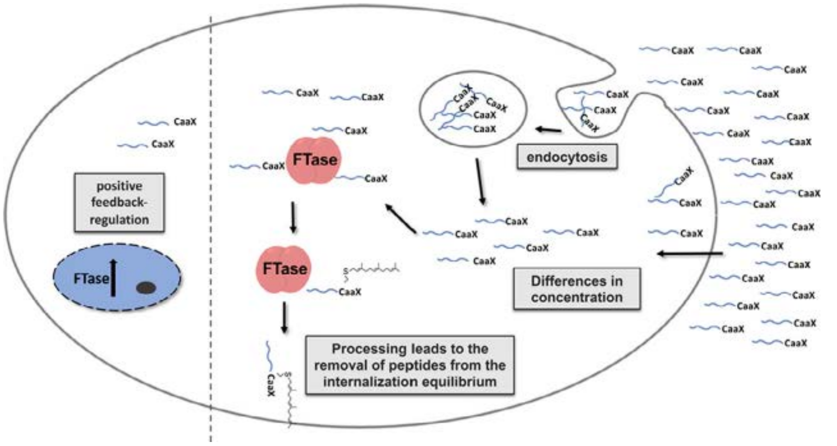

Fig. 9. Model of internalization and processing of the synthesized CaaX-peptides and their possible intracellular effects. Assumedly, CaaX-peptides are taken up mainly by endocytic mechanisms, whereas also direct translocation might be possible. After internalization, they are recognized and processed by prenyltransferases, which potentially modify them with an isoprenoid lipid, possibly leading to localization to membranous structures. This intracellular modification would then induce a removal of the CaaX-peptides from the internalization equilibrium, triggering intracellular enrichment, and possibly also a positive feedback regulation in terms of FTase expression levels.

modifications, and the delivery of proteins to their correct destination [58]. In particular, we detected upregulated proteins implicated in protein folding as well as the unfolded protein response, which is usually triggered by ER stress, for example, heat-shock 70 kDa protein 5, Yip1 interacting factor homolog A, and SEC61 translocon beta subunit. As downregulated proteins, we identified subunit of the eukaryotic translation initiation factor 2, which is known to relieve the ER workload during ER stress by attenuating protein translation [59,60], and the calcium sensor programmed cell death protein 6 playing a key role in ER to Golgi vesicular transport [61].

Of more interest was that we could allocate several proteins in both clusters (1 and 4), which were directly related to Ras signaling cascades. Cluster 1 contained STAM-binding protein, which is involved in the negative regulation of the PI3K-AKT pathway and Ras-related signal transduction. Moreover, we found inositol-3-phosphate synthase 1 in cluster 4, which is a rate-limiting enzyme in the synthesis of all inositol-containing compounds, including PIP3, which is an important mediator in AKT signaling pathways. Also, we found cAMP-dependent protein kinase type I-alpha in cluster 4, which is a regulatory subunit of the protein kinase A, and, in fact, is a negative regulator of the RAF/MEK/ERK (MAPK) pathway [62,63]. Indeed, it was shown that PRKAR1A inactivation is associated with dysregulated PKA resulting in increased expression and activation of the MAPK pathway [64,65]. In line with this, we further identified IRF-2-binding protein 2 in cluster 4, a negative regulator of the NFAT1 transcription factor [66] being one of the many downstream effectors of the RAF/MEK/ERK pathway. We also performed a 1D annotation enrichment analysis to identify global changes in pathways between CaaX-1-treated and untreated control cells (Fig. 10B). We detected again effects in actin polymerization (Arp2/3 complex formation) and ER trafficking (SRP-dependent proteins). However, more of note was that we found changes in pathways related to the PI3K/AKT pathway, affecting PTEN and PIP3, matching our previous observations. Notably, these reside downstream the insulin receptor/insulin-like growth factor receptor cascades, which were also significantly influenced by the CaaX-peptides.

Since it was recently shown that pancreatic cancer initiation, progression, and maintenance depend on K-Ras-PI3K-Pdk1 signaling [67,68], we furthermore assessed the activation state of direct downstream effectors of K-Ras by western blot analysis, including members of the RAF/MEK/ERK and PI3K/AKT pathway (Fig. 10C). While protein levels of MEK1/2, ERK1/2, and AKT were unaffected after treatment, the phosphorylation state of all three proteins was altered compared with untreated samples. Surprisingly, the treatment of PANC-1 cells with CaaX-1 increased phosphorylation of MEK and ERK kinases. In contrast, a decrease in phosphorylation of AKT indicated an inhibition of the PI3K/AKT pathway, which is in accordance with the data obtained in our proteome profiling (Fig. 10A,B). The reason for the relatively low levels of phosphorylated ERK1/2 and MEK1/2 in the control cells may be correlated with the fact that constant activation of the ERK pathway may lead to growth arrest [68].

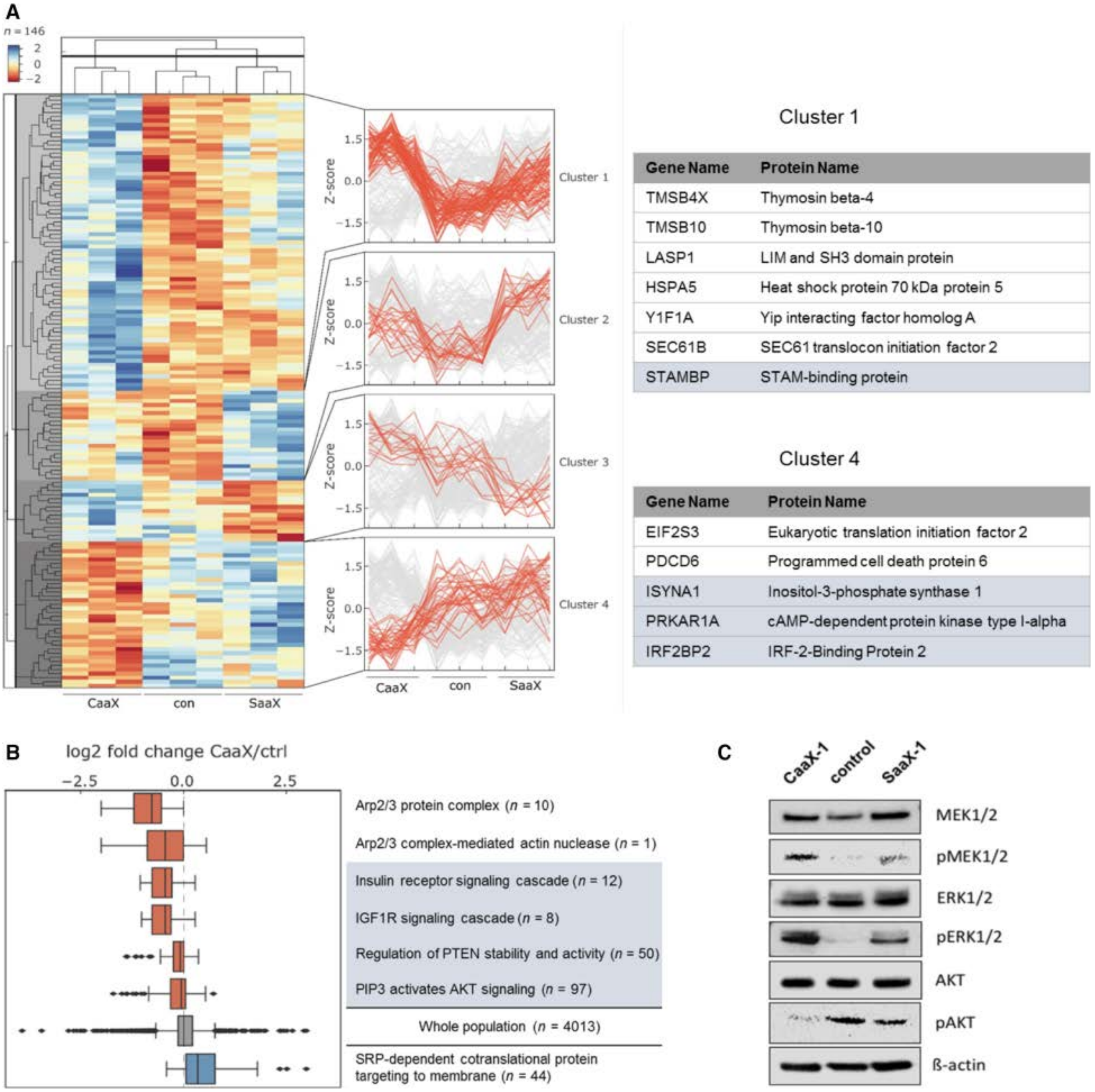

Cluster 1

Gene Name	Protein Name
TMSB4X	Thymosin beta-4
TMSB10	Thymosin beta-10
LASP1	LIM and SH3 domain protein
HSPA5	Heat shock protein 70 kDa protein 5
Y1F1A	Yip interacting factor homolog A
SEC61B	SEC61 translocon initiation factor 2
STAMBP	STAM-binding protein

Cluster 4

Gene Name	Protein Name
EIF2S3	Eukaryotic translation initiation factor 2
PDCD6	Programmed cell death protein 6
ISYNA1	Inositol-3-phosphate synthase 1
PRKAR1A	cAMP-dependent protein kinase type I-alpha
IRF2BP2	IRF-2-Binding Protein 2

Fig. 10. (A) Hierarchical clustering and line-plot of *Z*-score-normalized protein intensities. Clusters were identified by hierarchical clustering of significantly changed proteins (ANOVA, *P* value < 0.05). Representative proteins included in the clusters are listed, those related to Ras signaling pathways are highlighted in light gray. (B) 1D annotation enrichment identified significantly changed terms (FDR < 0.02). Box plots show relative fold change between CaaX-1 and untreated cells for proteins annotated with the indicated terms, whereby significant changes related to Ras signaling pathways are highlighted in light gray. (C) Western blot analysis showing the activation state of the RAF/MEK/ERK and PI3K/AKT pathways in PANC-1 cells after treatment with CaaX-1 ($n = 3$; loading control: ß-actin).

It was already shown that transient activation of ERK was followed by sustained lower levels of ERK activity inducing cell proliferation in many cell systems [69–72]. This finding would also explain the differences of control and SaaX-1-treated samples. In summary, our results indicated once again that CaaX-1 peptides might interfere with FTase and thus, compete with the post-translational modification of farnesylated K-Ras, or with other processes important for the dysregulated K-Ras status in PANC-1 cells. For instance, it was recently demonstrated that Ras dimerization is important to activate effector pathways. Probably, Ras–Ras dimer formation and following protein binding processes were impaired by the intracellular accumulation of CaaX-1 peptides [73]. Moreover, it might be assumed that downstream signaling pathways of K-Ras were directly altered by CaaX-1, leading to a switch from the PI3K/AKT pathway observed in K-Ras-mutated PANC-1 cells to the physiological RAF/MEK/ERK pathway [74].

Conclusion

Within this work, we designed and synthesized so-called CaaX-peptides bearing the cell-penetrating peptide sC18* and *C*-terminal sequences of Ras proteins, which are required for protein prenylation. The purpose of this study was to investigate this novel combination of such PTM motifs with a CPP and to analyze whether these chimeras would potentially be recognized and processed by the protein PTM machinery. Our first finding was that CaaX-peptides are intracellularly highly enriched dependent on their CaaX box. As illustrated in Fig. 3, by using the *C*-terminal CVGS motif, it was even possible to increase cytosolic peptide distribution. Since one bottleneck in the use of cell-penetrating peptides is their often only poor endosomal release, our newly created peptides might offer a really advantage in this direction. Moreover, we showed that a cysteine to serine mutation led to significantly lower internalization efficiencies of such peptides, suggesting an uptake pathway certainly dependent on correct intracellular recognition of CaaX-peptides. This was additionally supported by decreased intracellular accumulation after the treatment of PANC-1 cells with different control peptides and inhibitors, for example, Mevastatin. Furthermore, we highlighted cytotoxic effects of CaaX-peptides in several cancerous cells, which approximately corresponds with the distinct cellular expression levels of prenyltransferases, for example, FTase. Focusing then on PANC-1 cells, we also proofed the direct interaction of CaaX-1 with farnesyltransferase by pull-down assays and verified an upregulation in expression levels of farnesyltransferase.

In future, we will study how these peptides interfere and probably compete with Ras processing, since, within this work, we highlighted significant changes in Ras-related signaling pathways. Particularly, K-Ras would be an intriguing target in terms of PDACs, one of the most severe and K-Ras addicted cancers. Taken all these results into account, our approach might also open up a novel field for the development and study of therapeutics targeting other prenylated proteins, for instance such that are substrates of FTase and occur in the genomes of bacteria and viruses.

Materials and methods

Peptide synthesis and purification

All peptides were synthesized according to the Fmoc/tBu strategy using an automated multiple solid-phase peptide synthesizer Syro I (multiSynTech), as previously described [41]. As solid support, preloaded Wang resins were used and peptides were labeled N-terminally with 5(6)-carboxyfluorescein (CF) to enable their intracellular detection. Labeling of the peptides was performed on resin with fully protected side chains by using 5 equivalents (eq.) of fluorophore, Oxyma, and *N*,*N*′-diisopropylcarbodiimide (DIC) (overnight (o/n), RT). For synthesis of biotinylated conjugates, biotin coupling was performed on resin using 3 eq. of biotin, Oxyma, and DIC and (o/n, RT, *N*-methyl-2-pyrrolidone (NMP)). Peptides were cleaved from the resins using trifluoroacetic acid (TFA)/ thioanisole/ 1, 2-ethanedithiol (90 : 7 : 3, v/v/v) within 3 h at RT, then precipitated in ice-cold diethyl ether and lyophilized. Analytical data were obtained from RP-HPLC (Agilent with Nucleodur column: 100-5; c18ec; 4.6 × 125 mm) using a gradient from 10% to 60% of acetonitrile (ACN) in H_2O with 0.1% formic acid for sample separation, followed by electrospray-ionization mass spectrometry (ESI/MS, Thermo Scientific LTQ-XL, Darmstadt, Germany) measurements. Purification of peptides was achieved by preparative RP-HPLC (Hitachi Elite LaChrom, San Jose, CA, USA) on a 15 × 250 mm Jupiter 4 µm Proteo 90 A column (Phenomenex, Torrance, CA, USA) using linear gradients from 15% to 45% B in A (A = 0.1% TFA in water; B = 0.1% TFA in ACN) over 45 min and a flow rate of 6 $\mathrm{mL \cdot min^{-1}}$.

Peptide sequencing by tandem mass spectrometry

For determining the position of not properly incorporated amino acids, fractions containing side-products in high purity were analyzed by LC-MS/MS. Samples were dissolved in H_2O/MeOH/FA (50 : 50 : 0.1, v/v/v) and diluted to a final concentration of 100 $\mathrm{pmol \cdot \mu L^{-1}}$. Full scans were conducted, and side product ions isolated for fragmentation with a collision energy of 35–40%. Samples were injected by a syringe-pump at a flow rate of 3 $\mathrm{\mu L \cdot min^{-1}}$.

Secondary structure analysis

Circular dichroism (CD) spectroscopy of the CaaX-peptides (20 µm in 10 mm phosphate buffer, pH 7.0, or 10 mm phosphate buffer/ 2,2,2-trifluoroethanol (TFE) (1 : 1 v/v)) was recorded in triplicate using a Jasco Corp J-715 spectropolarimeter in a range from 190 to 260 nm using instrument settings as described in Ref. [75]. The resulting signal was converted from ellipticity (mdeg) to molar ellipticity [Q] in deg * cm^2 * $dmol^{-1}$. *R*-values were calculated by taking the ratio between the molar ellipticity at 222 and 207 nm (*R*-value = [Θ] 222/[Θ] 207) [76]. Helical wheel projections of the synthesized peptides were calculated by using Heliquest [77].

Cell culture

All cell lines used during this work were cultured as subconfluent monolayers in 10-cm petri dishes at 37 °C, in humidified atmosphere containing 5% CO_2. HeLa, MCF-7, LS174T, and PANC-1 cells were maintained in RPMI 1640 medium supplemented with 10% FBS and 2–4 mM glutamine. MEF and Capan-1 cells were cultured in DMEM medium with 10% FBS and 4 mM glutamine for MEF and Capan-1. When reaching a confluency of ~ 80–90%, cells were splitted by using 0.5 mg·mL^{-1} trypsin-EDTA for cell detachment. For cell culture experiments, cells were always grown to a confluency of up to 80%. All experiments were performed minimum twice in triplicates.

Cellular viability

The cellular viability was determined with a resazurin-based cytotoxicity assay (Sigma-Aldrich), as previously reported [41,78]. Therefore, cells were seeded (HeLa: 1.7 × 10^4; MCF: 2 × 10^4; LS174T: 2.4 × 10^4; PANC-1: 1.9 × 10^4; MEF: 1.7 × 10^4; Capan-1: 2.0 × 10^4 cells) in 96-well plates and grown to subconfluency (~ 70–80%) o/n. On the next day, cells were incubated with different peptide concentrations in the appropriate serum-free medium. After 24 h, cells were washed twice with PBS, while the positive controls were treated for 10 min with 70% EtOH. Cells were incubated with a 1 : 10 dilution of the reagent (v/v, in serum-free medium) for 1–2 h at 37 °C. The resazurin product was monitored at 595 nm (λex = 550 nm) on a Tecan infinite M200 plate reader.

Annexin V-FITC/7-ADD assay

PANC-1 cells were seeded (1.2 × 10^5) in 24-well plates and grown to subconfluency o/n. Medium was removed, and cells were incubated with 30 μM of unlabeled peptides for 24 h at 37 °C. Positive controls were treated with 7 μM of staurosporine (Sigma-Aldrich), while untreated cells served as negative controls. After incubation, cells were washed twice with PBS, detached with phenol red-free trypsin, and resuspendend in phenol red-free medium. Cells were centrifugated (7.5 min, 106 ***g***, 4 °C), the supernatant was discarded, and the cell pellet washed with PBS. In the following, the cell pellet was resuspended in ice-cold binding buffer from the kit (Beckmann Coulter, Brea, CA, USA) and incubated for 150 min in the dark with the Annexin V-FITC/7-AAD staining solutions. Cells were analyzed within 30 min with the guava easyCyteTM System (Merck, Darmstadt, Germany) using the GRN-B (525/30) and the RED-B (695/50) channel.

Cellular uptake and intracellular distribution

To study the intracellular fate of the novel peptides, flow cytometry experiments and confocal scanning microscopy were performed, as already described [41]. For the quantification of the cellular uptake, cells were seeded (HeLa: 1.0 × 10^5; MCF: 1.2 × 10^5, LS174T: 1.6 × 10^5; PANC-1: 1.4 × 10^5; MEF: 1.0 × 10^5; Capan-1: 1.5 × 10^5 cells) in 24-well plates and grown to subconfluency (~ 70–80%) o/n. On the next day, fluorophore-labeled peptides were incubated for 30 min in the appropriate serum-free medium. After incubation, cells were washed twice with PBS, detached with phenol red-free trypsin, and resuspended in phenol red-free medium. Cellular uptake was determined with the guava easyCyteTM System (Merck) using the GRN-B (525/30), counting 10 000 cells per well. For the assays with inhibitors, we incubated 10 μM AFCME for 30 min, 5 μM tipifarnib for 24 h, and 10 μM Mevastatin for 24 h with the cells. After preincubation, cells were washed with PBS and peptide incubation was started.

For the microscopic analysis, cells were seeded (HeLa: 4.0 × 10^5; MCF: 4.5 × 10^5, PANC-1: 5.0 × 10^5; MEF: 3.0 × 10^5, Capan-1: 5.0 × 10^5 cells) in a μ-slide eight-well plate (Ibidi) and grown to subconfluency (~ 70–80%). On the next day, cells were incubated with fluorophore-labeled peptides in the appropriate serum-free medium. Cell nuclei were stained for the last 10 min of the incubation time with Hoechst 33342 nuclear dye. Medium was removed, and external fluorescence was quenched with trypan blue (150 μM in 0.1 M acetate buffer, pH 4.1) for 30 s. After washing the cells once and adding fresh medium, microscopic analyses were performed on a Leica TCS SP8 confocal scanning microscope using a 63× immersion oil objective and images were processed with Fiji.

For the immunostaining, PANC-1 cells were seeded as described above. On the next day, cells were incubated for 6 h with 30 μM of CaaX-1 peptide in serum-free medium. Afterward, cells were washed twice with PBS and fixed using 2% paraformaldehyde (PFA) in PBS (30 min, RT). Cells were washed 3 times with 100 mM glycine in PBS (10 min, gentle shaking) and blocked (0.3% Triton X-100, 5% bovine serum albumin (BSA) in PBS) for 2 h at RT under shaking. The anti-K-Ras (Santa Cruz, Dallas, TX, USA; sc-30; 1 : 100) antibody was incubated overnight (RT, gentle shaking). Cells were washed again 3 times with 100 mM glycine in PBS (10 min, gentle shaking), and the secondary antibody was incubated for 2 h (anti mouse igG2a; 1 : 500), and afterward, cell nuclei were stained for 15 min with Hoechst 33342 nuclear dye. Cells were washed twice with PBS, once with ddH2O, mounted with Mowiol, and analyzed on the same microscope as described above.

Preparation of spheroids

3D spheroids of PANC-1 cells were generated with the hanging drop method to analyze the penetration ability of the peptides into more complex tissue. Therefore, a confluent petri dish of PANC-1 cells was washed, trypsinized, and harvested by centrifugation (300 ***g***, 4 °C, 5 min). Cells were seeded in droplets containing each 1.5×10^5 cells onto an inverted lid of a petri dish supplemented with $1.2\ \mathrm{mg{\cdot}mL^{-1}}$ methylcellulose in the appropriate serum-free medium. After 2 days, spheroids were formed and incubation of compounds was performed by addition of CF-labeled peptides directly into the droplets (final concentration: 10 µM). Incubation was carried out for 2 h at 37 °C, and afterward, spheroids were harvested by soaking them carefully with a 1 mL into a tube. For quantification of the uptake, cells were centrifuged (1000 r.p.m., 5 min, 4 °C), the supernatant was discarded, and the pellet was washed twice with PBS. PANC-1 spheroids were treated with phenol red-free trypsin under gentile shaking at 37 °C and after falling apart, resuspended in phenol red-free medium. Cellular uptake was determined as described above.

Cell lysates and western blotting

Cells were grown to confluency in 6-well plates, washed twice with PBS, and trypsinized using 500 µL trypsin. After detachment, cells were resuspended with ~ 6 mL of the appropriate full medium. Cells were centrifuged (5 min, 1000 r.p.m. and 4 °C), the supernatant was discarded, and the cell pellet washed with 1 mL PBS and centrifuged using the same conditions. The pellet was resuspended in ~ 200 µL lysis buffer (25 mM Tris pH 7.4, 150 mM NaCl, 1 mM TCEP, 2 mM EDTA, 1% Triton X-100, 1 : 100 HaltTM protease inhibitor cocktail) and rotated for 40 min at 4 °C. Cell debris was removed by centrifugation (20817 ***g***, 30 min, and 4 °C). Protein concentration was measured with Roti®-Nanoquant (Promega), and the appropriate amount of lysate was denatured in Laemmli buffer (10 min, 95 °C). Samples were electrophoresed on a 10% polyacrylamide gel via Tricine-SDS/PAGE, transferred onto a PVDF membrane (1.5 h, 100 mV), and blocked with 5% milk in PBS T for 1.5 h. Incubation with primary antibodies was carried out overnight followed by an incubation with HRP-conjugated rabbit or mouse antibody for 1.5 h (Cell Signaling Technology (CST), Danvers, MA, USA; 1 : 3000). The following primary antibodies were used as follows: anti-FNTA (Abnova, Taipeh, Taiwan Cat#4326; 1 : 250), anti-ERK1/2 (CST Cat#4695; 1 : 1000), anti-phospho-ERK1/2 (CST Cat#4370; 1 : 1000), anti-MEK1/2 (CST Cat#8727; 1 : 1000), anti-phospho-MEK1/2 (CST Cat#9154; 1 : 1000), anti-AKT (CST Cat#9272; 1 : 1000), anti-phospho-AKT (CST Cat#4060; 1 : 1000), and anti-K-Ras (Santa Cruz; sc-30; 1 : 1000). Samples were visualized by using the SignalFire™ ECL Reagent (CST). To obtain a loading control, the membrane was washed 2 × 10 min with stripping buffer (0.2 M glycine, 0.1% SDS, 1% Tween 20, pH 2.2), blocked again, and incubated with an anti-β-actin antibody (Santa Cruz; sc-47778 HRP; 1 : 1000) for 1.5 h. Samples were again visualized using the ECL Reagent.

Pull-down analysis

The interaction between CaaX-1 and the prenyltransferases was studied with crude lysates (a) and recombinant rat FTase (b) (Jena Bioscience, Jena, Germany) via a pull-down assay. Since high amounts of crude lysates were required, PANC-1 cells were seeded in 100 × 200 mm petri dishes and lysed as described above when reaching a confluency of around 80%. Magnetic streptavidin beads (Dynabeads™ MyOne™ Streptavidin C1 (Thermo Scientific)) were washed three times with (a) lysis buffer or (b) PBS and preloaded for 30 min at RT with 40 µg of biotinylated CaaX-1 or SaaX-1 in (a) lysis buffer or (b) PBS. Beads were washed once with (a) lysis buffer or (b) PBS, and unbound streptavidin was blocked with 1 mM biotin in PBS. After washing once with lysis buffer, beads were rotated for 2 h at 4 °C with (a) 500 µg crude PANC-1 lysate or (b) 400 ng recombinant rat FTase which was again followed by three times washing with lysis buffer. Elution was carried out, by rotating the beads for 15 min at RT in hexafluoroisopropanol (HFIP). HFIP was evaporated for 20 min at 40 °C under continuous N_2 flow (XcelVap, Biotage, Uppsala, Sweden). Western blotting was performed as described above.

Quantitative proteome analysis

8.0×10^5 PANC-1 cells were seeded in 6-well plates and grown to confluency. Cells were incubated for 24 h with 30 µM of the peptide solutions. On the next day, cells were lysed with modified RIPA buffer (50 mM Tris pH 7.5, 150 mM NaCl, 1 mM EDTA, 1 mM EGTA, 0.1% SDS, 1% Triton, 1 : 100 HaltTM Protease Inhibitor Cocktail) as described above. DNA was shared by sonification for 10 min at 4 °C with a Bioruptor. In the following, proteins were precipitated with cold acetone o/n. On the next day, sample was centrifugated (15 000 ***g***, 10 min, 4 °C), the pellet was washed twice with acetone and then air-dried. For the in-solution digest, the pellet was dissolved in 6 M urea/2 M thiourea and incubated for 30 min at RT with 5 mM DTT to reduce disulfide bonds. To alkylate cysteines, 40 mM iodoacetamide was added to the samples and the mixture was incubated for 20 min in the dark (RT). Endoproteinase Lys-C was added (enzyme: substrate ratio of 1 : 100) for further 3 h at RT. Afterward, samples were first diluted with 50 mM ABC to an urea concentration of 2 M and trypsin (enzyme: substrate ratio of 1 : 100) was added o/n. To stop the digestion, formic acid (FA) was supplemented to a final concentration of 1%. Before MS analysis, samples were desalted on Stage tips. Proteomic analysis was performed as already described [79], using an Easy nLC 1000 UHPLC coupled to a QExactive Plus mass spectrometer (Thermo Fisher). Peptides were resuspended in solvent A (0.1% FA), picked up with an autosampler, and loaded onto in-house made 50-cm fused silica columns (internal diameter (I.D.) 75 µm, C18 2.7 µm, Poroshell beads, Agilent) at a flow rate of 0.75 µL·min^{-1}. A 240-min segmented gradient of 5–34% solvent B (80% ACN in 0.1% FA) over 215 min, 34–55% solvent B over 5 min, and 55–90% solvent B over 5 min at a flow rate of 250 nL·min^{-1} was used to elute peptides. Eluted peptides were sprayed into the heated transfer capillary of the mass spectrometer using a nanoelectrospray ion source (Thermo Fisher Scientific). The mass spectrometer was operated in a data-dependent mode, where the Orbitrap acquired full MS scans (300–1750 m/z) at a resolution (R) of 70 000 with an automated gain control (AGC) target of 3×10^6 ions collected within 20 ms. The dynamic exclusion time was set to 20 s. From the full MS scan, the 10 most intense peaks ($z \geq 2$) were fragmented in the high-energy collision-induced dissociation (HCD) cell. The HCD normalized collision energy was set to 25%. MS/MS scans with an ion target of 5×10^5 ions were acquired with R = 17 500, with a maximal injection time of 60 ms and an isolation width of 2.1 m/z. The raw files were processed using MaxQuant software and its implemented Andromeda search engine [80] Parameters were set to default values. ANOVA and 1D annotation enrichment analysis were performed using Perseus [81]. Hierarchical clustering was performed using Instant Clue [82].

Acknowledgements

The authors acknowledge the infrastructure provided by the Imaging Facility at the Cluster of Excellence—Cellular Stress Responses in Aging-Associated Diseases (CECAD) for confocal microscopy measurements. We thank B. Chapple for help in peptide synthesis and D. Lindenblatt for support with Pymol. Open access funding enabled and organized by ProjektDEAL.

Conflict of interest

The authors declare no conflict of interest.

Author contributions

AK, KS, and JLW performed the experiments. AK, KS, JLW, MK, and IN analyzed the data. AK, JLW, MK, and IN wrote the manuscript.

References

1 Jiang H, Zhang X, Chen X, Aramsangtienchai P, Tong Z & Lin H (2018) Protein lipidation: occurrence, mechanisms, biological functions, and enabling technologies. *Chem Rev* **118**, 919–988.

2 Zhang FL & Casey PJ (1996) Protein prenylation: molecular mechanisms and functional consequences. *Annu Rev Biochem* **65**, 241–269.

3 Gao J, Liao J & Yang GY (2009) CAAX-box protein, prenylation process and carcinogenesis. *Am J Transl Res* **1**, 312–325.

4 Ahearn IM, Haigis K, Bar-Sagi D & Philips MR (2011) Regulating the regulator: post-translational modification of RAS. *Nat Rev Mol Cell Biol* **13**, 39–51.

5 Yokoyama K, Goodwin GW, Ghomashchi F, Glomset JA & Gelb MH (1991) A protein geranylgeranyltransferase from bovine brain: implications for protein prenylation specificity. *Proc Natl Acad Sci USA* **88**, 5302–5306.

6 Baron R, Fourcade E, Lajoie-Mazenc I, Allal C, Couderc B, Barbaras R, Favre G, Faye JC & Pradines A (2000) RhoB prenylation is driven by the three carboxyl-terminal amino acids of the protein: evidenced in vivo by an anti-farnesyl cysteine antibody. *Proc Natl Acad Sci USA* **97**, 11626–11631.

7 Moores SL, Schaber MD, Mosser SD, Rands E, O'Hara MB, Garsky VM, Marshall MS, Pompliano DL & Gibbs JB (1991) Sequence dependence of protein isoprenylation. *J Biol Chem* **266**, 14603–14610.

8 Boyartchuk VL, Ashby MN & Rine J (1997) Modulation of Ras and a-factor function by carboxyl-terminal proteolysis. *Science* **275**, 1796–1800.

9 Hampton SE, Dore TM & Schmidt WK (2018) Rce1: mechanism and inhibition. *Crit Rev Biochem Mol Biol* **53**, 157–174.

10 Dai Q, Choy E, Chiu V, Romano J, Slivka SR, Steitz SA, Michaelis S & Philips MR (1998) Mammalian prenylcysteine carboxyl methyltransferase is in the endoplasmic reticulum. *J Biol Chem* **273**, 15030–15034.

11 Yang J, Kulkarni K, Manolaridis I, Zhang Z, Dodd RB, Mas-Droux C & Barford D (2011) Mechanism of isoprenylcysteine carboxyl methylation from the crystal structure of the integral membrane methyltransferase ICMT. *Mol Cell* **44**, 997–1004.

12 Downward J (2003) Targeting RAS signalling pathways in cancer therapy. *Nat Rev Cancer* **3**, 11–22.

13 Wennerberg K, Rossman KL & Der CJ (2005) The Ras superfamily at a glance. *J Cell Sci* **118**, 843–846.

14 Barbacid M (1987) ras genes. *Annu Rev Biochem* **56**, 779–827.

15 O'Bryan JP (2019) Pharmacological targeting of RAS: Recent success with direct inhibitors. *Pharmacol Res* **139**, 503–511.

16 Hobbs GA, Der CJ & Rossman KL (2016) RAS isoforms and mutations in cancer at a glance. *J Cell Sci* **129**, 1287–1292.

17 Bos JL (1989) ras oncogenes in human cancer: a review. *Cancer Res* **49**, 4682–4689.

18 Bateman A (2019) UniProt: a worldwide hub of protein knowledge. *Nucleic Acids Res* **47**, D506–D515.

19 Long SB, Hancock PJ, Kral AM, Hellinga HW & Beese LS (2001) The crystal structure of human protein farnesyltransferase reveals the basis for inhibition by CaaX tetrapeptides and their mimetics. *Proc Natl Acad Sci USA* **98**, 12948–12953.

20 Brunner TB, Cengel KA, Hahn SM, Wu J, Fraker DL, McKenna WG & Bernhard EJ (2005) Pancreatic cancer cell radiation survival and prenyltransferase inhibition: the role of K-Ras. *Cancer Res* **65**, 8433–8441.

21 Almoguera C, Shibata D, Forrester K, Martin J, Arnheim N & Perucho M (1988) Most human carcinomas of the exocrine pancreas contain mutant c-K-ras genes. *Cell* **53**, 549–554.

22 Chuang HC, Huang PH, Kulp SK & Chen CS (2017) Pharmacological strategies to target oncogenic KRAS signaling in pancreatic cancer. *Pharmacol Res* **117**, 370–376.

23 Seabra MC (1998) Membrane association and targeting of prenylated Ras-like GTPases. *Cell Signal* **10**, 167–172.

24 Novotny CJ, Hamilton GL, McCormick F & Shokat KM (2017) Farnesyltransferase-mediated delivery of a covalent inhibitor overcomes alternative prenylation to mislocalize K-Ras. *ACS Chem Biol* **12**, 1956–1962.

25 Wang M & Casey PJ (2016) Protein prenylation: unique fats make their mark on biology. *Nat Rev Mol Cell Biol* **17**, 110–122.

26 Willumsen BM, Christensen A, Hubbert NL, Papageorge AG & Lowy DR (1984) The p21 ras C-terminus is required for transformation and membrane association. *Nature* **310**, 583–586.

27 Gibbs JB, Oliff A & Kohl NE (1994) Farnesyltransferase inhibitors: Ras research yields a potential cancer therapeutic. *Cell* **77**, 175–178.

28 Sousa SF, Fernandes PA & Ramos MJ (2008) Farnesyltransferase inhibitors: a detailed chemical view on an elusive biological problem. *Curr Med Chem* **15**, 1478–1492.

29 Jeong A, Suazo KF, Wood WG, Distefano MD & Li L (2018) Isoprenoids and protein prenylation: implications in the pathogenesis and therapeutic intervention of Alzheimer's disease. *Crit Rev Biochem Mol Biol* **53**, 279–310.

30 Storck EM, Morales-Sanfrutos J, Serwa RA, Panyain N, Lanyon-Hogg T, Tolmachova T, Ventimiglia LN, Martin-Serrano J, Seabra MC, Wojciak-Stothard B *et al.* (2019) Dual chemical probes enable quantitative system-wide analysis of protein prenylation and prenylation dynamics. *Nat Chem* **11**, 552–561.

31 Palsuledesai CC & Distefano MD (2015) Protein prenylation: enzymes, therapeutics, and biotechnology applications. *ACS Chem Biol* **10**, 51–62.

32 Wang YC, Dozier JK, Beese LS & Distefano MD (2014) Rapid analysis of protein farnesyltransferase substrate specificity using peptide libraries and isoprenoid diphosphate analogues. *ACS Chem Biol* **9**, 1726–1735.

33 DeGraw AJ, Hast MA, Xu J, Mullen D, Beese LS, Barany G & Distefano MD (2008) Caged protein prenyltransferase substrates: tools for understanding protein prenylation. *Chem Biol Drug Des* **72**, 171–181.

34 Flynn SC, Lindgren DE & Hougland JL (2014) Quantitative determination of cellular farnesyltransferase activity: towards defining the minimum substrate reactivity for biologically relevant protein farnesylation. *ChemBioChem* **15**, 2205–2210.

35 Wollack JW, Zeliadt NA, Mullen DG, Amundson G, Geier S, Falkum S, Wattenberg EV, Barany G & Distefano MD (2009) Multifunctional prenylated peptides for live cell analysis. *J Am Chem Soc* **131**, 7293–7303.

36 Ochocki JD, Igbavboa U, Gibson Wood W, Wattenberg EV & Distefano MD (2010) Enlarging the scope of cell-penetrating prenylated peptides to include farnesylated "CAAX" box sequences and diverse cell types. *Chem Biol Drug Des* **76**, 107–115.

37 Gronewold A, Horn M & Neundorf I (2018) Design and biological characterization of novel cell-penetrating peptides preferentially targeting cell nuclei and subnuclear regions. *Beilstein J Org Chem* **14**, 1378–1388.

38 Horn M & Neundorf I (2018) Design of a novel cell-permeable chimeric peptide to promote wound healing. *Sci Rep* **8**, 16279–16291.

39 Gelabert-Baldrich M, Soriano-Castell D, Calvo M, Lu A, Vina-Vilaseca A, Rentero C, Pol A, Grinstein S, Enrich C & Tebar F (2014) Dynamics of KRas on endosomes: involvement of acidic phospholipids in its association. *FASEB J* **28**, 3023–3037.

40 Horn M, Reichart F, Natividad-Tietz S, Diaz D & Neundorf I (2016) Tuning the properties of a novel short cell-penetrating peptide by intramolecular cyclization with a triazole bridge. *Chem Commun* **52**, 2261–2264.

41 Klimpel A & Neundorf I (2018) Bifunctional peptide hybrids targeting the matrix of mitochondria. *J Control Release* **291**, 147–156.

42 Lindenblatt D, Horn M, Götz C, Niefind K, Neundorf I & Pietsch M (2019) Design of CK2β-mimicking peptides as tools to study the CK2α/CK2β interaction in cancer cells. *ChemMedChem* **14**, 833–841.

43 Kuhlmann N, Chollet C, Baldus L, Neundorf I & Lammers M (2017) Development of substrate-derived sirtuin inhibitors with potential anticancer activity. *ChemMedChem* **12**, 1703–1714.

44 Hougland JL, Lamphear CL, Scott SA, Gibbs RA & Fierke CA (2009) Context-dependent substrate recognition by protein farnesyltransferase. *Biochemistry* **48**, 1691–1701.

45 Leibovich-Rivkin T, Liubomirski Y, Meshel T, Abashidze A, Brisker D, Solomon H, Rotter V, Weil M & Ben-Baruch A (2014) The inflammatory cytokine TNFα cooperates with Ras in elevating metastasis and turns WT-Ras to a tumor-promoting entity in MCF-7 cells. *BMC Cancer* **14**, 158–177.

46 Rowinsky EK (2006) Lately, it occurs to me what a long, strange trip it's been for the farnesyltransferase inhibitors. *J Clin Oncol* **24**, 2981–2984.

47 Deer EL, Gonzalez-Hernandez J, Coursen JD, Shea JE, Ngatia J, Scaife CL, Firpo MA & Mulvihill SJ (2010) Phenotype and genotype of pancreatic cancer cell lines. *Pancreas* **39**, 425–435.

48 Lu S, Jang H, Nussinov R & Zhang J (2016) The structural basis of oncogenic mutations G12, G13 and Q61 in small GTPase K-Ras4B. *Sci Rep* **6**, 21949.

49 Monticone M, Biollo E, Maffei M, Donadini A, Romeo F, Storlazzi CT, Giaretti W & Castagnola P (2008) Gene expression deregulation by KRAS G12D and G12V in a BRAF V600E context. *Mol Cancer* **7**, 92.

50 van den Brand D, Veelken C, Massuger L & Brock R (2018) Penetration in 3D tumor spheroids and explants: adding a further dimension to the structure-activity relationship of cell-penetrating peptides. *Biochim Biophys Acta Biomembr* **1860**, 1342–1349.

51 Zhao B, Hu W, Kumar S, Gonyo P, Rana U, Liu Z, Wang B, Duong WQ, Yang Z, Williams CL *et al.* (2017) The Nogo-B receptor promotes Ras plasma membrane localization and activation. *Oncogene* **36**, 3406–3416.

52 Xu D, Tong X, Sun L, Li H, Jones RD, Liao J & Yang GY (2019) Inhibition of mutant Kras and p53-driven pancreatic carcinogenesis by atorvastatin: Mainly via targeting of the farnesylated DNAJA1 in chaperoning mutant p53. *Mol Carcinog* **58**, 2052–2064.

53 Ali BR, Nouvel I, Leung KF, Hume AN & Seabra MC (2010) A novel statin-mediated "prenylation block-and-release" assay provides insight into the membrane targeting mechanisms of small GTPases. *Biochem Biophys Res Commun* **397**, 34–41.

54 Li L, Zhang W, Cheng S, Cao D & Parent M (2012) Isoprenoids and related pharmacological interventions: potential application in Alzheimer's disease. *Mol Neurobiol* **46**, 64–77.

55 Lerner EC, Zhang TT, Knowles DB, Qian Y, Hamilton AD & Sebti SM (1997) Inhibition of the prenylation of K-Ras, but not H- or N-Ras, is highly resistant to CAAX peptidomimetics and requires both a farnesyltransferase and a geranylgeranyltransferase I inhibitor in human tumor cell lines. *Oncogene* **15**, 1283–1288.

56 Rowell CA, Kowalczyk JJ, Lewis MD & Garcia AM (1997) Direct demonstration of geranylgeranylation and farnesylation of Ki-Ras in vivo. *J Biol Chem* **272**, 14093–14097.

57 Whyte DB, Kirschmeier P, Hockenberry TN, Nunez-Oliva I, James L, Catino JJ, Bishop WR & Pai JK (1997) K- and N-Ras are geranylgeranylated in cells treated with farnesyl protein transferase inhibitors. *J Biol Chem* **272**, 14459–14464.

58 Schwarz DS & Blower MD (2016) The endoplasmic reticulum: structure, function and response to cellular signaling. *Cell Mol Life Sci* **73**, 79–94.

59 Harding HP, Zhang Y, Bertolotti A, Zeng H & Ron D (2000) Perk is essential for translational regulation and cell survival during the unfolded protein response. *Mol Cell* **5**, 897–904.

60 Oslowski CM & Urano F (2011) Measuring ER stress and the unfolded protein response using mammalian tissue culture system. *Methods Enzymol* **490**, 71–92.

61 Yamasaki A, Tani K, Yamamoto A, Kitamura N & Komada M (2006) The Ca2+-binding protein ALG-2 is recruited to endoplasmic reticulum exit sites by Sec31A and stabilizes the localization of Sec31A. *Mol Biol Cell* **17**, 4876–4887.

62 Burgering BMT & Bos JL (1995) Regulation of Ras-mediated signalling: more than one way to skin a cat. *Trends Biochem Sci* **20**, 18–22.

63 Robinson-White A, Hundley TR, Shiferaw M, Bertherat J, Sandrini F & Stratakis CA (2003) Protein kinase-A activity in PRKAR1A-mutant cells, and regulation of mitogen-activated protein kinases ERK1/2. *Hum Mol Genet* **12**, 1475–1484.

64 Robinson-White A, Meoli E, Stergiopoulos S, Horvath A, Boikos S, Bossis I & Stratakis CA (2006) PRKAR1A mutations and protein kinase A interactions with other signaling pathways in the adrenal cortex. *J Clin Endocrinol Metab* **91**, 2380–2388.

65 Robinson-White AJ, Leitner WW, Aleem E, Kaldis P, Bossis I & Stratakis CA (2006) PRKAR1A inactivation leads to increased proliferation and decreased apoptosis in human B lymphocytes. *Cancer Res* **66**, 10603–10612.

66 Carneiro FRG, Ramalho-Oliveira R, Mognol GP & Viola JPB (2011) Interferon regulatory factor 2 binding protein 2 is a new NFAT1 partner and represses its transcriptional activity. *Mol Cell Biol* **31**, 2889–2901.

67 Pollock CB, Shirasawa S, Sasazuki T, Kolch W & Dhillon AS (2005) Oncogenic K-RAS is required to maintain changes in cytoskeletal organization, adhesion, and motility in colon cancer cells. *Cancer Res* **65**, 1244–1250.

68 Eser S, Reiff N, Messer M, Seidler B, Gottschalk K, Dobler M, Hieber M, Arbeiter A, Klein S, Kong B

et al. (2013) Selective requirement of PI3K/PDK1 signaling for kras oncogene-driven pancreatic cell plasticity and cancer. *Cancer Cell* **23**, 406–420.

69 Eser S, Schnieke A, Schneider G & Saur D (2014) Oncogenic KRAS signalling in pancreatic cancer. *Br J Cancer* **111**, 817–822.

70 Choi C & Helfman DM (2014) The Ras-ERK pathway modulates cytoskeleton organization, cell motility and lung metastasis signature genes in MDA-MB-231 LM2. *Oncogene* **33**, 3668–3676.

71 Nussinov R, Muratcioglu S, Tsai CJ, Jang H, Gursoy A & Keskin O (2015) The key role of calmodulin in KRAS-driven adenocarcinomas. *Mol Cancer Res* **13**, 1265–1273.

72 Pumiglia KM & Decker SJ (1997) Cell cycle arrest mediated by the MEK/mitogen-activated protein kinase pathway. *Proc Natl Acad Sci USA* **94**, 448–452.

73 Ambrogio C, Köhler J, Zhou ZW, Wang H, Paranal R, Li J, Capelletti M, Caffarra C, Li S, Lv Q *et al.* (2018) KRAS dimerization impacts MEK inhibitor sensitivity and oncogenic activity of mutant KRAS. *Cell* **172**, 857–868.e15.

74 Qui MS & Green SH (1992) PC12 cell neuronal differentiation is associated with prolonged p21ras activity and consequent prolonged ERK activity. *Neuron* **9**, 705–717.

75 Gessner I, Klimpel A, Klußmann M, Neundorf I & Mathur S (2020) Interdependence of charge and secondary structure on cellular uptake of cell penetrating peptide functionalized silica nanoparticles. *Nanoscale Adv* **2**, 453–462.

76 Manning MC & Woody RW (1991) Theoretical CD studies of polypeptide helices: examination of important electronic and geometric factors. *Biopolymers* **31**, 569–586.

77 Gautier R, Douguet D, Antonny B & Drin G (2008) HELIQUEST: a web server to screen sequences with specific α-helical properties. *Bioinformatics* **24**, 2101–2102.

78 Gronewold A, Horn M, Ranđelović I, Tóvári J, Muñoz Vázquez S, Schomäcker K & Neundorf I (2017) Characterization of a cell-penetrating peptide with potential anticancer activity. *ChemMedChem* **12**, 42–49.

79 Pla-Martín D, Schatton D, Wiederstein JL, Marx M, Khiati S, Krüger M & Rugarli EI (2020) CLUH granules coordinate translation of mitochondrial proteins with mTORC1 signaling and mitophagy. *EMBO J* **39**, e102731.

80 Cox J, Neuhauser N, Michalski A, Scheltema RA, Olsen JV & Mann M (2011) Andromeda: a peptide search engine integrated into the MaxQuant environment. *J Proteome Res* **10**, 1794–1805.

81 Tyanova S, Temu T, Sinitcyn P, Carlson A, Hein MY, Geiger T, Mann M & Cox J (2016) The Perseus computational platform for comprehensive analysis of (prote)omics data. *Nat Methods* **13**, 731–740.

82 Nolte H, MacVicar TD, Tellkamp F & Krüger M (2018) Instant Clue: a software suite for interactive data visualization and analysis. *Sci Rep* **8**, 12648–12660.

Journal of Pathology
J Pathol 2020; **251:** 310–322
DOI: 10.1002/path.5452

Fundamental control of grade-specific colorectal cancer morphology by Src regulation of ezrin–centrosome engagement

Lisa Rainey[1†], Ravi K Deevi[1†], Jane McClements[1], Hajrah Khawaja[1], Chris J Watson[2], Martine Roudier[3], Sandra Van Schaeybroeck[1] and Frederick C Campbell[1*]

[1] *Centre for Cancer Research and Cell Biology, Queen's University Belfast and Belfast Health and Social Care Trust, Belfast, UK*
[2] *Wellcome Wolfson Institute for Experimental Medicine, Queen's University Belfast, Belfast, UK*
[3] *Molecular Pathology Laboratory, AstraZeneca Oncology Translational Science, Cambridge, UK*

**Correspondence to: FC Campbell, Centre for Cancer Research and Cell Biology, Lisburn Rd, Queen's University of Belfast, Belfast BT9 7AE. UK.
E-mail: f.c.campbell@qub.ac.uk*

†Equal first authors.

Abstract

The phenotypic spectrum of colorectal cancer (CRC) is remarkably diverse, with seemingly endless variations in cell shape, mitotic figures and multicellular configurations. Despite this morphological complexity, histological grading of collective phenotype patterns provides robust prognostic stratification in CRC. Although mechanistic understanding is incomplete, previous studies have shown that the cortical protein ezrin controls diversification of cell shape, mitotic figure geometry and multicellular architecture, in 3D organotypic CRC cultures. Because ezrin is a substrate of Src tyrosine kinase that is frequently overexpressed in CRC, we investigated Src regulation of ezrin and morphogenic growth in 3D CRC cultures. Here we show that Src perturbations disrupt CRC epithelial spatial organisation. Aberrant Src activity suppresses formation of the cortical ezrin cap that anchors interphase centrosomes. In CRC cells with a normal centrosome number, these events lead to mitotic spindle misorientation, perturbation of cell cleavage, abnormal epithelial stratification, apical membrane misalignment, multilumen formation and evolution of cribriform multicellular morphology, a feature of low-grade cancer. In isogenic CRC cells with centrosome amplification, aberrant Src signalling promotes multipolar mitotic spindle formation, pleomorphism and morphological features of high-grade cancer. Translational studies in archival human CRC revealed associations between Src intensity, multipolar mitotic spindle frequency and high-grade cancer morphology. Collectively, our study reveals Src regulation of CRC morphogenic growth via ezrin–centrosome engagement and uncovers combined perturbations underlying transition to high-grade CRC morphology.

Keywords: Src; ezrin; polo-like kinase; centrosome; mitotic spindle; cell division; phenotype; human; colorectal cancer; prognosis

Received 12 August 2019; Revised 27 February 2020; Accepted 7 April 2020

No conflicts of interest were declared.

Introduction

For over a century, histological grading of cellular and multicellular morphology has provided a robust readout of cancer aggressiveness [1]. Although causal molecular mechanisms are still unclear, fundamental and embryological studies provide important clues [2–4]. During development, evolution of tissue-specific architecture is coordinated by molecular interactions within the cell cortex, at the outer shell of the cell [2–4]. The cortex comprises the cell membrane linked to the underlying actin cytoskeleton meshwork by ezrin, radixin or moesin (ERM) proteins [5]. Ezrin recruitment from the cytosol to the cortex is aided by binding between the ezrin NH_2 terminal domain and phosphatidylinositol 4,5-bisphosphate (PIP_2) in the cell membrane [6]. Ezrin and other ERM molecules are then redistributed within the cortex to sustain mechanical stability [7,8] and to form a polarised accumulation called the ezrin cap, which provides a cue for centrosome anchoring [9]. These processes set bipolar symmetry for mitotic fidelity and control of emergent tissue properties [9,10].

Previous studies have uncovered spatiotemporal control of tissue assembly by crosstalk between the cortex and mitotic machinery [11–13]. Src family tyrosine kinases (SFKs) integrate cell cortex remodelling [11], alignment of the cell division axis [11], mitotic spindle dynamics [12] and 3D lumenised multicellular assembly [13]. Src controls these important life processes by key signalling loops. A crucial event is Src phosphorylation of ezrin at tyrosines (Y) 145 [14] and Y477 [15]. In particular, the Src interaction with ezrin Y145 enhances Src activity [14], which in turn, increases Akt signalling [16]. Akt phosphorylates ezrin at threonine (T) 567 [17] to promote wide ezrin conformational opening and binding to NHERF1 (also known as ezrin-binding protein 50; EBP50) [18], resulting in ezrin stabilisation at the cortex [19]. Subsequent cortical flow of ezrin during interphase leads to the formation of the polarised ezrin cap, which provides the cue for centrosome anchoring and establishment of mitotic symmetry [9,10]. Although this homeostatic machinery can be challenged by centrosome amplification induced by oncogenic polo-like kinase 4 (PLK4) [20], the ezrin cap clusters extra centrosomes [9,10], to conserve bipolar symmetry and evolution of regular 3D multicellular morphology [10].

To explore the molecular interplay underlying colorectal cancer (CRC) morphology, we dissected Src signalling crosstalk in CRC model systems. Because Src enhances Akt signalling by suppression of the tumour suppressor phosphatase and tensin homologue (PTEN) [16], we used stable isogenic PTEN-expressing and -deficient CRC cells to explore molecular interactions. We investigated the roles of ezrin phosphotyrosine domains at Y145 [14] and Y477 [15], as well as SFK specificity, in the control of ezrin cap formation. Because Src promotes aggressive cancer evolution from cells with extra centrosomes in a *Drosophila* model system [21], we investigated the interplay between Src, centrosome number and the evolution of multicellular morphology. We used isogenic Caco-2 CRC cells that predominantly have normal centrosome number, or a subclone where formation of extra centrosomes was induced by stable overexpression of PLK4. Using these models, we explored Src regulation of the morphogenic trajectory of a single CRC cell to lumenised multicellular architecture. We assessed sequential morphogenic processes, including ezrin cap integrity, centrosome positioning or clustering, mitotic spindle geometry and junctional protein dynamics. To explore clinical relevance, we conducted translational studies in archival human CRC.

This study addressed the provocative question of how subcellular processes guide evolution of grade-specific CRC morphology. We show that Src perturbation of ezrin cap formation in cells with a normal centrosome number leads to misorientation of the mitotic spindle. In turn, this process is causally implicated in the evolution of cribriform morphology [10,22], a feature of low-grade cancer [23]. Conversely, in cells with centrosome amplification, Src suppression of the ezrin cap drives asymmetric dispersal of extra centrosomes and the formation of multipolar mitotic spindles (MMS). These phenomena promote morphological features consistent with high-grade cancer [10]. Our translational studies support experimental findings and we found correlations between Src intensity, MMS frequency and high-grade morphology in human CRC. Collectively, the study provides a new molecular paradigm for the evolution of grade-specific CRC morphology by Src perturbation of ezrin–centrosome engagement.

Materials and methods

Reagents and antibodies

Most laboratory chemicals were purchased from Sigma-Aldrich (Poole, UK).

Cell lines

Stable PTEN-expressing Caco-2 and HCT116 PTEN$^{+/+}$ (PTEN$^{+/+}$) and

PTEN-deficient Caco-2 ShPTEN (ShPTEN) and HCT116 PTEN$^{-/-}$ (PTEN$^{-/-}$) cells were raised or obtained and cultured as previously described [10]. Stable PLK4 overexpressing Caco-2 (Caco-2 PLK4OE) cells were generated as previously described [10].

Transfections

We carried out mammalian siRNA and plasmid DNA transfections using RNAiMAX and X-tremeGENE transfection reagents (Thermo Fisher, Dublin, Ireland), respectively, as previously described [10].

Confocal imaging

Assays of cell cortex dynamics, centrosome disposition, mitotic spindle orientation and geometry and multicellular patterns were conducted using a Leica SP5 confocal microscope (Leica Biosystems, Milton Keynes, UK) with an HCX PL APO lambda blue 63× 1.40 oil immersion objective at 1× or 2× zoom, as previously described [10].

Human tumour samples

Anonymised formalin-fixed, paraffin-embedded (FFPE) colorectal primary tumours from previously described study cohorts [10] were released from the Northern Ireland Biobank, which has ethical approval to collect, store and distribute anonymised tissue samples to researchers by an approved protocol. Ezrin and Src immunohistochemistry (IHC) and quantification were conducted in the AstraZeneca Molecular Pathology Laboratory (Cambridge, UK). Full details of antibodies, siRNA oligonucleotides, plasmids, transfection reagents, cell culture methods, selection, confocal imaging, human tumour samples, IHC, immunofluorescence, ethical approval, reference numbers and data analysis are provided in supplementary material, Supplementary materials and methods.

Results

Src regulates ezrin via molecular crosstalk

To dissect molecular crosstalk underlying CRC morphology, we explored Src interactions with PTEN, using isogenic stable PTEN-expressing or -deficient Caco-2 and HCT116 CRC cells. We validated the Src kinase inhibitor AZD0530 [24] in dose/time course studies (see supplementary material, Figure S1A,B) and selected the dose of 1 μM for all experiments. We conducted dominant-negative (DN) or constitutively active (CA) Src mutant transfections versus an empty vector only control (see supplementary material, Figure S1C). Here we found greater p-Src$^{(Y416)}$ expression in PTEN-deficient Caco-2 cells (Figure 1A,B). AZD0530 treatment suppressed p-Src$^{(Y416)}$ in Caco-2 and shPTEN cells and inhibited PTEN phosphorylation at S380/T382/T383 (p-PTEN$^{(S380/T382/T383)}$) in Caco-2 cells (Figure 1A–C). EGF treatment activates Src [25] and in this study EGF treatment enhanced p-Src $^{(Y416)}$ in Caco-2 and shPTEN cells and increased p-PTEN$^{(S380/T382/T383)}$ in Caco-2 cells (Figure 1D–F). Results were similar in PTEN-expressing and -deficient HCT116 (PTEN$^{+/+}$ and PTEN$^{-/-}$) in untreated conditions or after AZD0530 or EGF treatment, respectively (data not shown). Ezrin exists in multiple phosphorylation-dependent conformational states and p-ezrin $^{(T567)}$ is regarded as the active form [26]. Expression of p-ezrin $^{(T567)}$ was enhanced or suppressed by CA-Src and DN-Src transfection, respectively (Figure S1C,D). In 3D organotypic cultures of Caco-2 clones, we found maximal p-Src $^{(Y416)}$ subcellular localisation at plasma membranes and found higher intensity in shPTEN than in Caco-2 cultures (Figure 1G,H). AZD0530 treatment suppressed p-Src $^{(Y416)}$ intensity in 3D cultures (Figure 1G,H). Collectively, these studies uncovered functional PTEN/Src feedback signalling that controlled Src activity at cell membranes that in turn regulated ezrin phosphorylation.

Src regulates cell cortex dynamics

The cell cortex is an important regulator of cell fate and perturbations are fundamental to tumour growth and metastasis [27]. We and others have previously uncovered sequential processes of ezrin recruitment to the cell cortex from the cytosol at 3.5 h and subsequent ezrin cortical cap formation at 14 h, after synchronisation of cells in G0 [9,10]. To investigate Src regulation of these processes, we used phosphomimetic (E) and non-phosphorylatable (F) ezrin mutants at Src phosphorylation domains Y145 and Y377. Furthermore, we assessed the Src specificity of the effect by siRNA knockdown of the related SFKs, YES and FYN. We also modulated Src activity by transfection or treatment studies. We found accumulation of GFP-tagged wild type (WT) ezrin at the cortex at 3.5 h and formation of a polarised cap at 14 h after cell synchronisation. No cortical localisation or restriction of the GFP-tagged empty vector control was observed. The phosphomimetic GFP-tagged ezrin Y145E mutant also localised at the cortex and formed a cap more frequently than WT ezrin but the Y145 non-phosphorylatable mutant failed to localise or form a cap. However, neither phosphomimetic nor non-phosphorylatable mutations at ezrin 477 affected cortical recruitment or cap formation (Figure 2A,B). These results show that phosphorylation of ezrin at Y145 is crucial for ezrin redistribution from the cytosol to the cortex. Because ezrin is stabilised in the cortex by binding NHERF1 [19], we investigated the effects of AZD0530 treatment on cortical recruitment of each protein. AZD0530 treatment suppressed ezrin cortical recruitment at 3.5 h but did not affect cortical NHERF1 localisation (see supplementary material, Figure S2A, B; summary data for NHERF1 not shown). Although AZD0530 can suppress both Src family (e.g. c-Src, YES and FYN) and Abl tyrosine kinases [28,29], it has greater selectivity for the former, with more than 10-fold greater potency against Src than Abl [29].To investigate SFK functional specificity, we conducted siRNA knockdown studies (see supplementary material, Figure S2C,D). We found that siRNA knockdown of YES but not FYN suppressed ezrin cortical recruitment and cap formation (see supplementary material, Figure S2E,F). These data show SFK functional overlap in relation to ezrin cortical dynamics. We then investigated the effects of Src overactivity by transfection of CA-Src versus DN-Src and empty vector control. In accordance with AZD0530 suppression of ezrin cortical recruitment (see supplementary material, Figure S2A, B), we found that DN-Src transfection suppressed ezrin cap formation (Figure 2C,D). Although CA-Src did not affect ezrin cap frequency (Figure 2C), it did affect ezrin cap phenotypes inducing multiple discrete ezrin accumulations within the cortex (Figure 2D) or increased intensity of p-ezrin$^{(T567)}$ localisation at the cap (see supplementary material, Figure S2E,F) in approximately 30% and 32% of cells, respectively. Collectively, these studies implicate p-ezrin Y145 in cortical recruitment, show Src and YES functional overlap and uncover ezrin cap phenotypes resulting from Src overactivity.

Src regulates bipolar mitotic spindle orientation and multicellular assembly

Assembly of lumenised colorectal glandular architecture is shaped by sequential processes of ezrin–centrosome engagement and bipolar mitotic spindle orientation [9,10,30]. To investigate Src regulation of spindle dynamics and multicellular assembly we conducted AZD0530 treatment studies in monolayer and 3D organotypic Caco-2 cultures. Here we found that AZD0530 treatment had a modest inhibitory effect on bipolar spindle formation (Figure 3A,B) but promoted spindle misorientation (Figure 3C,D) and aberrant multicellular assembly with the formation of multiple lumens (Figure 3E,F) in 4-day, 3D cultures. Although core processes of tissue assembly can be uncovered in short-term organotypic cultures, the evolution of cancer-relevant morphology often requires longer-term growth. At 12 days of culture, vehicle only treated control Caco-2 cultures formed regular glands comprising a uniform columnar epithelial monolayer arranged around a single central lumen. Conversely, AZD0530 treatment suppressed p-Src$^{(Y416)}$ signal intensity, induced epithelial stratification and multiple aberrant lumens consistent with cribriform multicellular morphology (see supplementary material, Figure S3A). In accordance with previous studies, we found that shPTEN cultures had

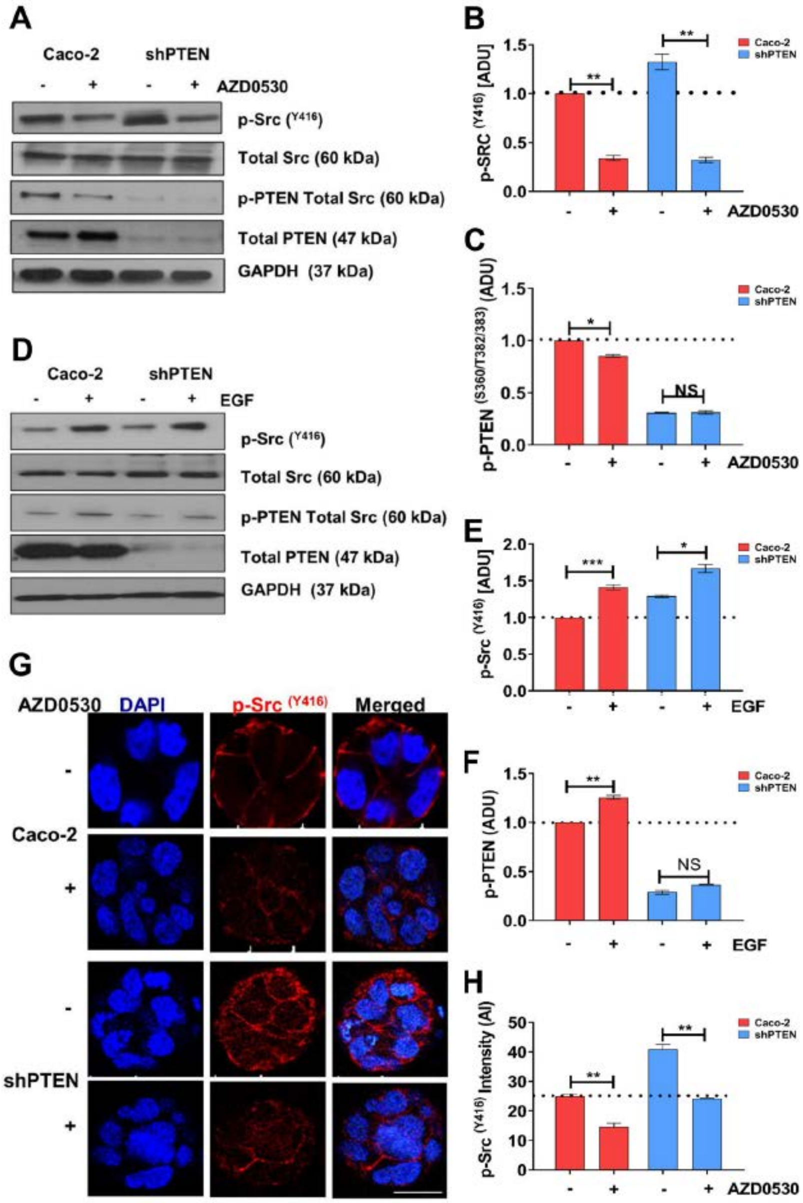

Figure 1. Src molecular interactions. (A) Effects of AZD0530 treatment on p-Src$^{(Y416)}$ and phospho-PTEN [p-PTEN$^{(S380/T382/T383)}$] in Caco-2 and shPTEN cells. (B) p-Src$^{(Y416)}$ densitometry values expressed as fold-change over vehicle only control [AZD0530 (−)] treatment in Caco-2, **$p < 0.01$ and shPTEN cells **$p < 0.01$. (C) p-PTEN$^{(S380/T382/T383)}$ densitometry values expressed as fold-change over vehicle only control in Caco-2 cells; $p < 0.05$; shPTEN; p = NS. (D) EGF treatment effects on total Src and p-Src$^{(Y416)}$ levels as well as total PTEN and p-PTEN$^{(S380/T382/T383)}$ in Caco-2 and shPTEN cells. (E) Densitometry values for EGF effects on p-Src$^{(Y416)}$, expressed as fold-change over vehicle only treated Caco-2 control; ***$p < 0.001$; EGF shPTEN versus vehicle only shPTEN; *$p < 0.05$. (F) Densitometry values for EGF treatment effects on p-PTEN$^{(S380/T382/T383)}$ expressed as fold-change over vehicle only treated Caco-2 control, **$p < 0.01$; EGF shPTEN versus shPTEN; p = NS. (G) Expression of p-Src$^{(Y416)}$ in control or AZD0530 treated Caco-2 and shPTEN organotypic cultures at 4 days. At least 10 glandular structures were assayed in triplicate for each experimental condition. (H) Summary AZD0530 treatment effects on p-Src$^{(Y416)}$ membrane intensity versus control in Caco-2; **$p < 0.01$ and shPTEN; **$p < 0.01$. GAPDH used as loading controls. Minor differences in magnification have been used to accommodate scale bars. Analysis by one-way ANOVA with Tukey's *post hoc* test or paired Student's *t*-test. Staining: DAPI for nuclear DNA (blue); anti-p-Src$^{(Y416)}$ (red). Scale bar = 20 μm.

constitutively misorientated mitotic spindles relative to gland centres [10] (see supplementary material, Figure S3B,C). AZD0530 treatment did not significantly affect spindle orientation (see supplementary material, Figure S3B,C) or single central lumen formation in 3D shPTEN cultures (see supplementary material, Figure S3D). Taken together, these studies showed Src regulation of mitotic spindle orientation and

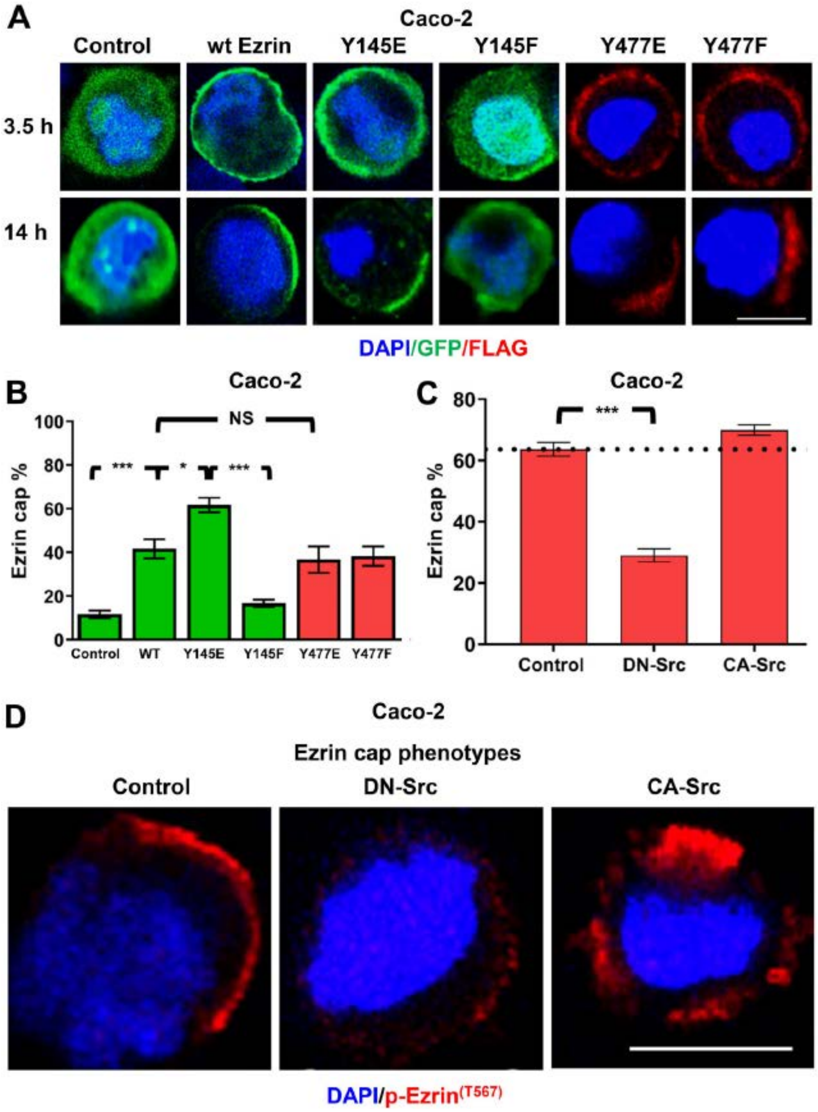

Figure 2. Src regulation of cell cortex dynamics. (A) Cortical recruitment (top row) and cap formation (bottom row) from WT ezrin or phosphomimetic (E) or non-phosphorylatable(F) ezrin mutants at Y145 (GFP-labelled; green) or Y477 (FLAG-tagged; red) versus GFP-labelled empty vector control. Assays for ezrin cortical recruitment and cap formation were conducted at 3.5 and 14 h after synchronisation of cells in G0. At least 30 cells were counted in triplicate at each interval. (B) Summary cap formation by WT ezrin or Y145 or Y477 mutants versus control. WT versus control; ***$p < 0.001$; WT versus Y145E; $p < 0.05$; Y477 E or F versus WT; $p =$ NS. (C) Summary effects of Src mutant transfections on percentage of cells with an Erin cap in Caco-2 cells at 14 h after synchronisation (DN-Src versus empty vector control; $p < 0.001$). (D) Ezrin cortical phenotypes after transfection by empty vector control, DN-Src or CA-Src at 14 h after synchronisation. Minor differences in magnification accommodate scale bars. Staining DAPI (blue), NHERF1 (green), p-ezrin$^{(T567)}$ (red). At least 30 cells were counted in triplicate in each experimental condition. Analysis by one-way ANOVA with Tukey's *post hoc* test. Scale bar = 20 µm.

multicellular assembly in PTEN-expressing cells. Conversely, spindle defects arising from PTEN deficiency were unaffected by Src inhibitory treatment.

Src regulates bipolar spindle orientation via the focal adhesion complex

During tissue assembly, bipolar spindle orientation is controlled by focal adhesion molecules focal adhesion kinase (FAK) and paxillin [31]. Although these proteins are important Src substrates, their role in Src regulation of bipolar spindle orientation and tissue morphogenesis remains unclear. FAK ^{Y861} and paxillin ^{Y118} are major Src phosphorylation sites [32,33], whereas FAK ^{Y397} is an autophosphorylation site, activated by extracellular signalling [34]. Here we found that p-FAK$^{(Y861)}$ (Figure 4A,B) and p-paxillin$^{(Y118)}$(Figure 4A) levels were suppressed by AZD0530 treatment. Conversely,

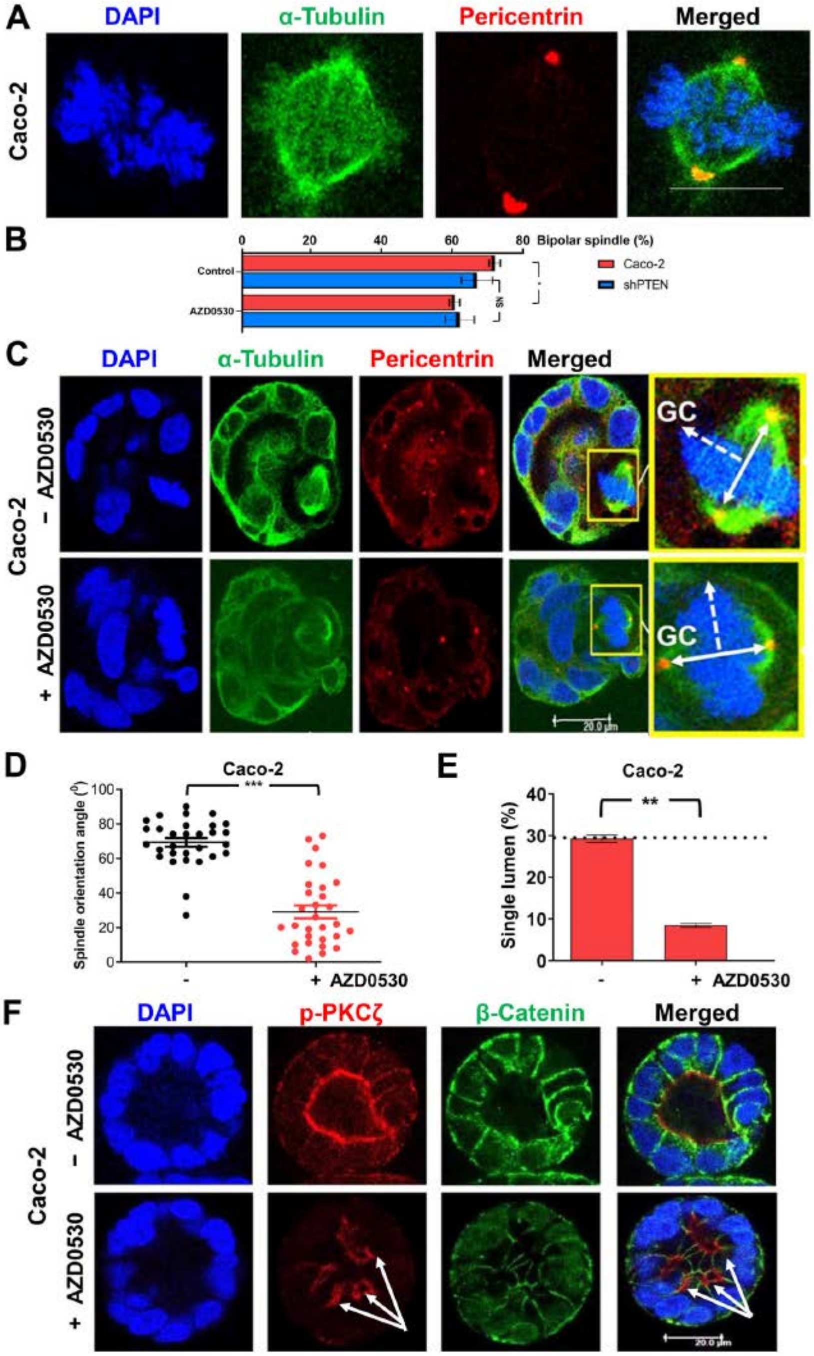

Figure 3. Src regulation of bipolar mitotic spindle dynamics and multicellular assembly. (A) Confocal images of spindle architecture in Caco-2 cells. (B) Summary treatment effects on bipolar spindle formation in Caco-2 and shPTEN cells (Caco-2 AZD0530 versus control; $*p < 0.05$; shPTEN AZD0530 versus control; $p =$ NS). Values represent percentage of mitotic cells with bipolar spindles. At least 30 metaphase cells were assessed in triplicate for each experiment. (C) Treatment effects on mitotic spindle orientation and lumen formation in 4-day 3D Caco-2 glands. Insets (yellow box) show high-power views of spindle planes (solid white arrows) and their orientation relative to gland centres (GC, dashed white arrows). (D) Summary treatment effects on spindle orientation angles relative to gland centres in 3D Caco-2 cultures [AZD0530 (−) versus AZD0530 (+), $***p < 0.001$]. (E) Summary treatment effects on single lumen formation in 4 day 3D Caco-2 cultures [AZD0530 (−) versus AZD0530 (+); $**p < 0.01$]. (F) Confocal images of treatment effects on lumen formation in 4-day 3D Caco-2 cultures. Minor differences in magnification accommodate marker of gland centres. At least 10 glandular structures were assayed in triplicate for each experimental condition. Staining: DAPI for nuclear DNA (blue); p-PKCζ for apical membrane marker (red); β-catenin for basolateral membrane. White arrows denote multiple lumens in AZD0530 treated cultures. Scale bar = 20 µm.

p-FAK ^{Y397} levels were unaffected (see supplementary material, Figure S4A,B). Depletion of FAK by siRNA knockdown (see supplementary material, Figure S4C, D) led to mitotic spindle misorientation in 4-day Caco-2 organotypic cultures (Figure 4C,D). Taken together, these studies implicate focal adhesion complex molecules FAK and paxillin in Src control of spindle orientation and multicellular assembly.

Src regulation of supernumerary centrosome clustering and mitotic spindle architecture

Although bipolar spindle misorientation perturbs the plane of cell cleavage [35] and lumen formation [30], MMS formation devastates the spatial directives for multicellular assembly [10]. MMS frequently arises from centrosome amplification but clustering of extra centrosomes at the ezrin cap during interphase rescues bipolar spindle architecture [10]. To investigate relationships between Src signalling, centrosome amplification and spindle architecture, we used Caco-2 clones transfected with doxycycline-inducible PLK4 [10] and/or FLAG-tagged CA-Src (Figure 5A,B). Centrosome amplification was observed in 7.2 ± 1.18% (sem) parental Caco-2 cells and doxycycline induction of PLK4 in transfectants enhanced the frequency of extra centrosomes (Figure 5C). We observed clustering of extra centrosomes at spindle poles and rescue of bipolar spindle

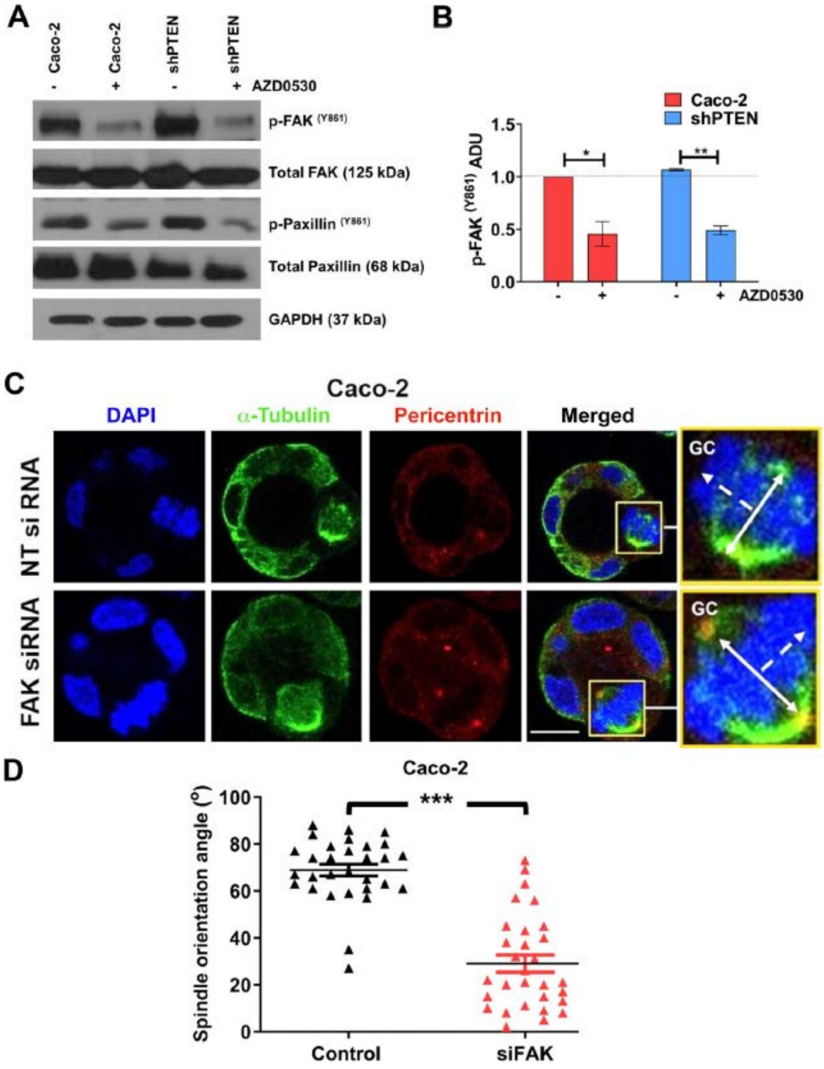

Figure 4. Src regulation of bipolar spindle orientation via the focal adhesion complex. (A) Effects of AZD0530 treatment on FAK and paxillin phosphorylation in Caco-2 and shPTEN cells. (B) Summary treatment effects on p-FAK$^{(Y861)}$. Densitometry values AZD0530 (−) versus AZD0530 (+) in Caco-2; *$p < 0.05$; AZD0530 (−) versus AZD0530 (+) in shPTEN; **$p < 0.01$. (C) Effects of FAK siRNA knockdown (KD) on mitotic spindle orientation in 3D organotypic Caco-2 cultures at 4 days. Insets (yellow boxes) show high-power views of spindle planes (solid white arrows) and their orientation relative to gland centres (GC, dashed white arrows). (D) Summary effects of FAK siRNA transfection on spindle orientation angles in 4-day Caco-2 glands. Control versus FAK siRNA; ***$p < 0.001$. Student's *t*-test. At least 10 glandular structures were assayed in triplicate for each experimental condition. Staining: DAPI (blue), α-tubulin (green), pericentrin (red). Scale bar = 20 μm.

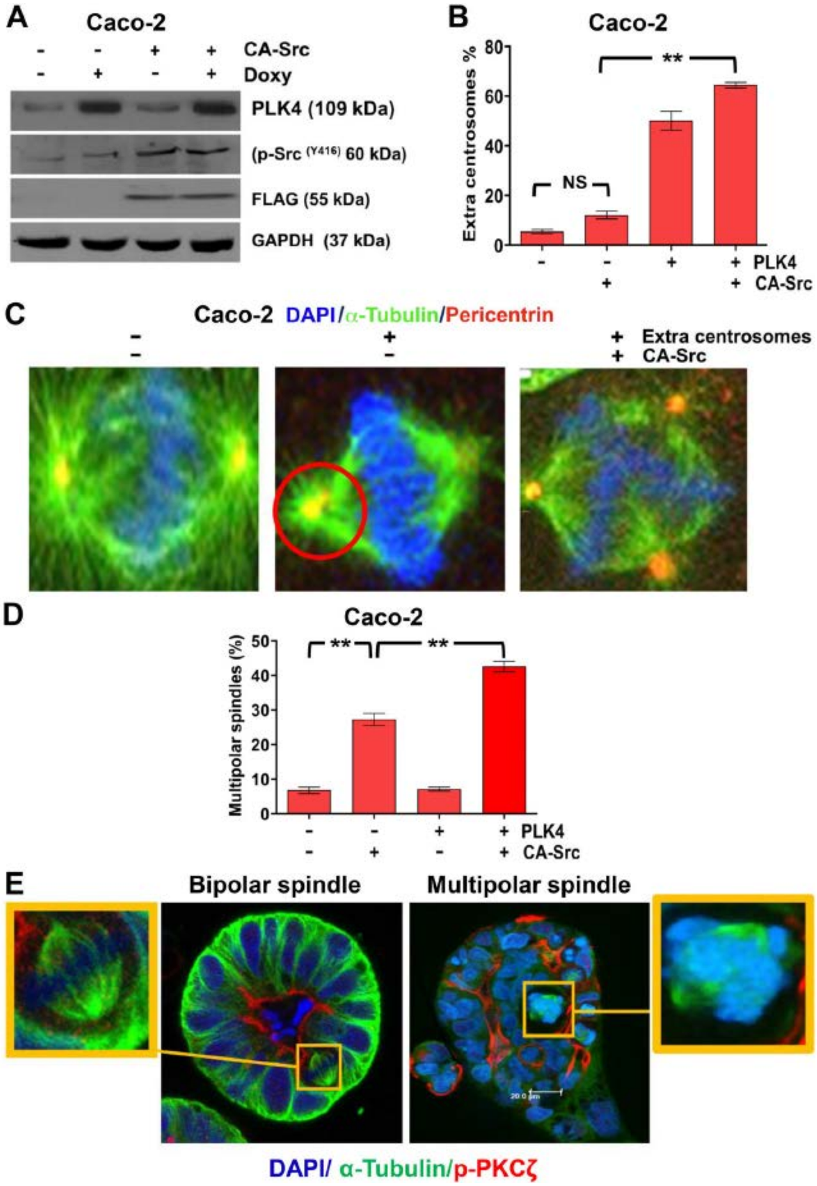

Figure 5. Src regulation of supernumerary centrosome clustering and mitotic spindle architecture. (A) PLK4 and p-Src^{Y416} expression in Caco-2 cells transfected with a lentiviral doxycycline-inducible PLK4 expression vector and FLAG-tagged CA-Src, then treated with or without doxycycline. (B) Summary effects of PLK4OE alone or in combination with CA-Src on centrosome amplification; CA-Src versus untreated control = NS. PLK4 + CA-Src versus CA-Src; $^{**}p < 0.01$. At least 30 cells were assessed in triplicate for each experiment. (C) Confocal images of MMS architecture in Caco-2 cells with or without extra centrosomes, with or without CA-Src transfection. Red circle highlights clustering of extra centrosomes at a spindle pole and bipolar spindle architecture. (D) Summary effects of PLK4OE alone or in combination with CA-Src on MMS formation; CA-Src versus control; $^{**}p < 0.01$; CA-Src + PLK4OE versus CA-Src $^{**}p < 0.01$. At least 30 metaphase cells were assessed in triplicate for each experiment. (E) Multicellular morphology in parental 3D Caco-2 cultures and in subclones with high MMS frequency induced by PLK4OE and suppression of ezrin cap formation. Minor differences in magnification accommodate the size differences between regular and irregular glandular structures. At least 10 glandular structures were assessed in triplicate for each experimental condition. Insets show bipolar and multipolar spindles. Staining: DAPI (blue), α-tubulin (green), p-PKC ζ (red). Scale bar = 20 μm.

architecture both in WT Caco-2 cells and in PLK4 transfectants. CA-Src transfection suppressed centrosome clustering and enhanced MMS formation both in parental Caco-2 cells and in PLK4 transfectants (Figure 5C,D and see supplementary material, Figure S5A). In PLK4 transfectants, clustering of higher numbers of centrosomes was observed but dispersal induced by CA-Src led to more complex MMS formation, than in parental Caco-2 cells (see supplementary material, Figure S5A). To assess morphological consequences of MMS formation, we compared multicellular morphology of parental Caco-2 3D cultures that predominantly have bipolar spindles with a subclone with high MMS frequency. The MMS-high Caco-2 subclone was induced by stable PLK4 transfection and suppression of ezrin cap formation, in combination. We found that bipolar spindle architecture in parental 3D Caco-2 cultures associated with the formation of regular multicellular colorectal glandular structures with a single central lumen surrounded by a polarised columnar epithelial monolayer. Conversely, high MMS frequency associated with gross cytological and morphological disturbances including cellular and nuclear pleomorphism, misalignment of the apical membrane and loss of lumen formation (Figure 5E). Collectively, these results show that Src overactivity can suppress centrosome clustering and induce MMS formation that in turn promotes multicellular morphological perturbations, evocative of high-grade CRC.

Src association with spindle architecture in human CRC

To explore the clinical relevance of our *in vitro* studies, we investigated Src and ezrin expression using IHC on 35 human CRC and five normal colon tissue samples that had previously been characterised for apical NHERF1 expression, mitotic spindle architecture and histopathological prognostic features [10]. Src and ezrin IHC assays were optimised using normal human colon, then IHC intensities were assessed at three levels of intensity. Semiquantitative scoring of Src and ezrin expression was conducted using the H-score method (Figure 6A and see supplementary material, Supplementary materials and methods). Src intensity differed between distinct histological tumour grades (Figure 6B). Src and ezrin IHC intensities correlated (Figure 6C). Although Src intensity directly associated with the number of lymph node metastases in CRC (Figure 6D), ezrin intensity was unrelated to nodal metastases (see supplementary material, Figure S6A). Ezrin expression was greater in grade 3 versus grade 1 or 2 CRC but no difference was observed between grade 1 and 2 CRC (see supplementary material, Figure S6B). Furthermore, Src but not ezrin intensity directly associated with multipolar spindle formation (Figure 6E and see supplementary material, Figure S6C). Src and ezrin IHC intensities were unrelated to apical NHERF1 IHC intensity (data not shown). Collectively, these studies show the relationships between Src IHC intensity, MMS formation and high-grade multicellular morphology in human CRC.

Discussion

The elucidation of molecular circuits that control cancer cell growth to form distinct tumour type- or grade-specific morphological phenotypes has fundamental importance in pathology. Assembly of multicellular tissues is coordinated by the tumour suppressor PTEN and Src tyrosine kinase [13,36] through feedback signalling [16,37,38] and interactions with other key genes [14–17]. As the blueprint for lumenised glandular architecture is set by ezrin cortical dynamics [9,10], a key question is how PTEN/Src crosstalk engages these processes. In the present study, we found inverse associations between PTEN and p-Src$^{(Y416)}$ expression in accordance with previous studies in breast cancer cell lines [38]. AZD0530 or EGF treatment or transfection by DN- or CA-Src, respectively, suppressed or enhanced Src kinase activity that in turn suppressed PTEN function [16]. Although not directly targeted by Src, we found that PTEN phosphorylation at S380/T382/T383 increased in proportion to Src activity. Phosphorylation at S380/T382/T383 promotes a more compact PTEN conformation that suppresses PTEN membrane binding and reduces its catalytic activity [39]. In 3D cultures, we found p-Src$^{(Y416)}$ localisation at cell membranes in accordance with previous cell monolayer studies [40] and found higher membrane p-Src$^{(Y416)}$ intensity in PTEN-deficient cells. Src is a member of a family of membrane-bound tyrosine kinases and membrane recruitment is enhanced by myristoylation [41]. AZD0530 treatment suppressed cell membrane p-Src$^{(Y416)}$ intensity in both PTEN-expressing and -deficient 3D cultures. These studies show functional PTEN/Src feedback and we investigated the role of this molecular crosstalk in ezrin dynamics.

Upon binding to cell membrane PIP$_2$ [6], ezrin undergoes complex reconfigurations, including partial conformational opening [26]. Ezrin then becomes phosphorylated at specific tyrosines [14] and at T567 [42]. Akt [17] and other kinases [10,43–45] promote ezrin T567 phosphorylation that is required for binding NHERF1 [46]. p-ezrin$^{(T567)}$ is widely used as a marker of the active ezrin state [26,42]. In this study, we have shown that p-ezrin$^{(T567)}$ is respectively enhanced or suppressed by CA-Src or DN-Src transfection. Although this effect could be linked to Src-enhanced Akt signalling [16] that promotes p-ezrin$^{(T567)}$ [17], Src is a promiscuous molecule and involvement of other kinases that phosphorylate ezrin at T567 [10,43,44] cannot be excluded.

To investigate the role of Src-driven ezrin phosphorylation in cortical dynamics, we transfected cells with phosphomimetic (E) and non-phosphorylatable (F) ezrin mutants at Src phosphorylation domains Y145 and Y477. We followed their intracellular distribution by confocal microscopy, focussing on ezrin cortical recruitment and cap formation at intervals of 3.5 h and 14 h after synchronisation in G0 [10]. We found that ezrin mutations at Y145 but not Y477 affected ezrin cap formation. Although the phosphomimetic ezrin Y145E enhanced cap formation, non-phosphorylatable ezrin Y145F abrogated ezrin cortical recruitment and generation of the cap. Here our results are in accordance with previous localisation studies of ezrin tyrosine mutants to the cell membrane [47]. How ezrin phosphorylation at Y145 regulates cellular localisation is not known. However, ezrin phosphorylation at this residue enhances binding to Src via SH2 domain interactions [14]. As Src is predominantly membrane-bound [41], this interaction could enrich ezrin at the cell membrane/actin

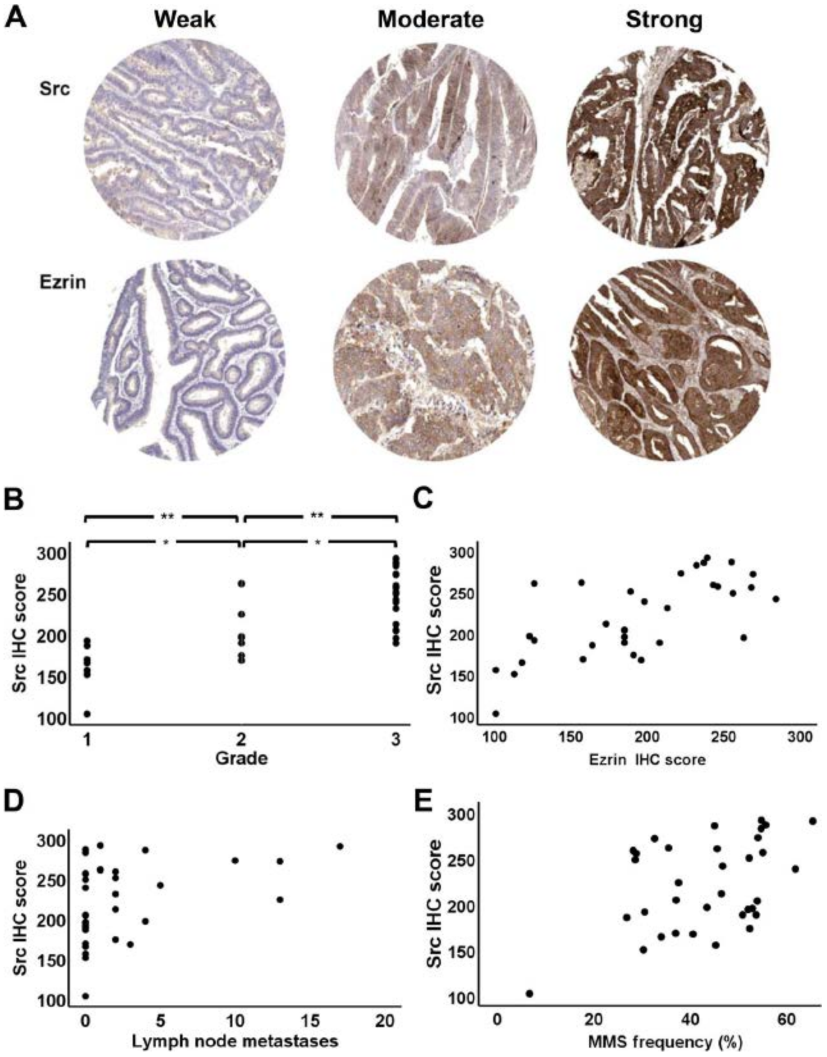

Figure 6. Src association with spindle architecture in human CRC. (A) Weak, moderate and strong immunostaining of Src and ezrin in archival CRC. (B) Src IHC intensity scores versus CRC grades 1–3 CRC; $^{**}p < 0.01$ Wilcoxon signed rank test; grade 3 versus grade 1 or 2 $^{**}p < 0.01$; grade 2 versus grade 1 or 3; $^{*}p < 0.01$; ANOVA with Tukey's *post hoc* test. (C) Src and ezrin IHC scores in archival CRC; Pearson's $r = 0.63$; $^{**}p < 0.01$. (D) Src IHC intensity scores versus number of lymph node metastasis. Pearson correlation = 0.379; $p = 0.025$. (E) Src IHC scores and MMS frequency in archival CRC; Pearson's $r = 0.442$; $^{**}p < 0.01$.

cytoskeleton interface. Following ezrin's cortical recruitment, it colocalises with and binds NHERF1, resulting in ezrin stabilisation [19]. Src affinity for ezrin [14] is important for ezrin subcellular distribution [47] but cortical localisation of NHERF1 was unaffected by Src activity. In siRNA knockdown and functional inhibition studies we found that Src and YES but not FYN regulated ezrin cortical recruitment and cap formation. The extensive sequence homology of these SFKs does not predict their peptide recognition preferences [48]. Src binds via its SH2 domain to a 13 residue (DNAMLEYLKIAQD) peptide in the ezrin FERM domain [14,48] to phosphorylate ezrin at the critical Y145 residue implicated in growth control [14]. In large-scale screens of SH2 domain binding, Src was shown to share its peptide binding preference with YES but not with FYN [48] and may account for the SFK differences in ezrin regulation, shown in this study.

To further investigate the role of Src in ezrin cap formation, we conducted transfection studies. In accordance with our findings of AZD0530 suppression of ezrin cortical recruitment, we found that DN-Src suppressed ezrin cap formation. Although transfection of CA-Src did not affect the frequency of ezrin cap formation, it had substantive effects on ezrin cap phenotypes, causing multiple ectopic ezrin accumulations ('fragmented phenotype') or formation of a 'thickened' cap with greater ezrin intensity, each in approximately 30% of cells. Although the functional significance of the thickened cap is unknown, each ezrin cortical accumulation within the fragmented phenotype can misposition centrosomes [9].

In physiological conditions, the interphase centrosome becomes anchored via astral microtubules to the cortical ezrin cap and then replicates [9]. Actin- and myosin II-mediated forces separate mother and daughter centrosomes to enable bipolar mitotic spindle formation [49]. Thus formed, the spindle is then orientated by mutually antagonistic apical and basolateral polarity forces [50]. Impaired cortical recruitment of ERM proteins [51] or defective cortical capture of astral microtubules [52] induce mitotic spindle misorientation [51,52] that has important consequences for cell cleavage [35], apical membrane alignment [30] and lumenised morphogenesis [30]. In this study, suppression of Src resulted in a modest reduction in bipolar spindle frequency but substantive bipolar spindle misorientation. Spindle misorientation associated with multilumen formation, epithelial stratification and evolution of a multicellular phenotype consistent with cribriform morphology, in 3D organotypic cultures. Cribriform morphology, characterised by multiple abnormal 'back to back' lumens surrounded by atypical stratified epithelium [53], is a feature of low-grade cancer and has a relatively favourable clinical outlook [23]. Bipolar spindle orientation is also regulated by PTEN [54] and in the present study PTEN-deficient cells showed frequent spindle misalignment. By phosphorylation of PTEN, Src drives a conformational change that impedes PTEN membrane binding but Src inhibitory treatment did not rescue morphogenesis of PTEN-deficient cells in this study. Collectively, our findings show that Src regulation of cortical dynamics in cells affects spindle assembly, bipolar spindle orientation and the formation of lumenised glandular architecture in 3D cultures of CRC cells with normal centrosome number.

Because mitotic spindle dynamics can be modulated by focal adhesion complexes [31], maintained by Src phosphorylation of FAK [32] and paxillin [33], we investigated Src regulation of those proteins in our model system. AZD0530 treatment suppressed phosphorylation of Src targets FAK Y861 and paxillin Y118 [32,33], but had no effects at FAK Y397, which is a FAK autophosphorylation domain [34]. Furthermore, siRNA knockdown of FAK promoted abnormal bipolar spindle orientation. Hence, our findings show that Src coordinates precise multimodal tissue assembly by regulation of bipolar spindle orientation, mediated in part by FAK phosphorylation.

Although Src has a central role in tissue homeostasis [11–13], stochastic increases in Src activity [55] or Src engagement of other oncogenes can perturb cell control mechanisms in cancerous tissues [56]. Highly conserved Src crosstalk with centrosomal kinases promote cancer hallmarks of invasion and metastasis [21]. To explore oncogenic co-dependency between Src and a centrosomal kinase, we conducted transfection of CA-Src and doxycycline-inducible PLK4 in Caco-2 cells. Most parental Caco-2 cells have a normal centrosome complement and as anticipated [20], PLK4OE induced substantial centrosome amplification. Parental Caco-2 cells with normal centrosome number formed bipolar spindles and the minority with extra centrosomes predominantly clustered them to rescue bipolar spindle formation. Transfection of Caco-2 cells with CA-Src did not affect centrosome number but suppressed centrosome clustering and enhanced MMS formation. Although PLK4OE induced substantive numbers of extra centrosomes, effective centrosome clustering and rescue of bipolar spindle formation was observed. However, the combination of PLK4OE and CA-Src induced dispersal of greater numbers of centrosomes and increased the frequency of MMS with complex configurations. Although bipolar spindle architecture directs the assembly of regular multicellular glandular structures, forced MMS formation promoted morphological features typical of high-grade cancer in organotypic cultures. Clinically, high MMS frequency in histological tumour sections associates with high grade in CRC [10] and poor outlook in CRC [10] and pancreatic cancer [57]. Although Src hyperactivity in combination with centrosome amplification promotes mitotic error, defective abscission and aberrant cytokinesis in 2D cultures [58], MMS-associated molecular signals that perturb 3D multicellular morphology and drive tumour progression have yet to be determined.

To investigate the clinical relevance of experimental findings, we investigated spindle architecture in archival human CRC. We found direct associations between high Src IHC intensity, multipolar spindle frequency and high-grade morphology. Furthermore, Src IHC intensity in CRC associates with regional lymph node metastasis. Hence, Src perturbation of basic processes of cortical remodelling and mitotic spindle assembly may have major prognostic significance in CRC. Collectively, the present study uncovers Src regulation of an interconnected repertoire of morphogenic processes, including cell cortex rearrangements, mitotic spindle organisation, cell division and multicellular patterning. As well as acting as a transforming agent on its own, Src can also facilitate other oncogenic processes [59]. In this study, we have identified centrosome amplification as a cooperating partner of aberrant Src in the promotion of multipolar spindle formation and phenotypic attributes of high-grade CRC morphology.

Acknowledgements

We thank Dr Todd Waldman (Lombardi Cancer Center, Georgetown University, Washington DC, USA) for supplying PTEN $^{+/+}$ and $^{-/-}$ HCT116 cells. We gratefully acknowledge support by the Medical Research Council (grant number MR/L015110/1) and AstraZeneca for financial support, consumables, access to an automated immunostainer, consumables and expertise. We thank Dr Caroline Hirst and Dr Vidalba Rocher (Molecular Pathology Laboratory, AstraZeneca, Cambridge, UK) for help with antibody validations and staining of the FFPE tumour sections. We thank Professor Daniela

Rotin, Hospital for Sick Children, University of Toronto for access to ezrin Y477 E and F mutants.

Author contributions statement

LR conducted signalling, transfection, treatment centrosome, spindle and multicellular morphogenesis assays, data analysis and figure preparation. RKD conducted signalling assays, some transfections, siRNA knockdowns, ezrin mutant transfections and supervised some morphogenesis assays. HK generated the ezrin 145 mutants and sequenced them and the ezrin 477 mutants. JMcC conducted assays of spindle polarity in archival CRC specimens by Aurora A immunofluorescence. MR supervised IHC assays of Src and ezrin in archival cancer specimens. SVS and CJW helped to design some experiments and critically reviewed the manuscript. FCC conceived the study, designed some experiments, analysed data and wrote the manuscript with additional input from all co-authors. All authors approved the final version of the manuscript.

References

1. Jass JR, Atkin WS, Cuzick J, *et al*. The grading of rectal cancer: historical perspectives and a multivariate analysis of 447 cases. *Histopathology* 1986; **10:** 437–459.
2. Karsenti E. Self-organization in cell biology: a brief history. *Nat Rev Mol Cell Biol* 2008; **9:** 255–262.
3. Kunda P, Baum B. The actin cytoskeleton in spindle assembly and positioning. *Trends Cell Biol* 2009; **19:** 174–179.
4. Munjal A, Lecuit T. Actomyosin networks and tissue morphogenesis. *Development* 2014; **141:** 1789–1793.
5. Roubinet C, Tran PT, Piel M. Common mechanisms regulating cell cortex properties during cell division and cell migration. *Cytoskeleton (Hoboken)* 2012; **69:** 957–972.
6. Barret C, Roy C, Montcourrier P, *et al*. Mutagenesis of the phosphatidylinositol 4,5-bisphosphate (PIP(2)) binding site in the NH(2)-terminal domain of ezrin correlates with its altered cellular distribution. *J Cell Biol* 2000; **151:** 1067–1080.
7. Carreno S, Kouranti I, Glusman ES, *et al*. Moesin and its activating kinase Slik are required for cortical stability and microtubule organization in mitotic cells. *J Cell Biol* 2008; **180:** 739–746.
8. Roubinet C, Decelle B, Chicanne G, *et al*. Molecular networks linked by moesin drive remodeling of the cell cortex during mitosis. *J Cell Biol* 2011; **195:** 99–112.
9. Hebert AM, DuBoff B, Casaletto JB, *et al*. Merlin/ERM proteins establish cortical asymmetry and centrosome position. *Genes Dev* 2012; **26:** 2709–2723.
10. Deevi RK, Javadi A, McClements J, *et al*. Protein kinase C zeta suppresses low- or high-grade colorectal cancer (CRC) phenotypes by interphase centrosome anchoring. *J Pathol* 2018; **244:** 445–459.
11. Bei Y, Hogan J, Berkowitz LA, *et al*. SRC-1 and Wnt signaling act together to specify endoderm and to control cleavage orientation in early *C. elegans* embryos. *Dev Cell* 2002; **3:** 113–125.
12. Nakayama Y, Matsui Y, Takeda Y, *et al*. c-Src but not Fyn promotes proper spindle orientation in early prometaphase. *J Biol Chem* 2012; **287:** 24905–24915.
13. Warren SL, Handel LM, Nelson WJ. Elevated expression of pp60c-src alters a selective morphogenetic property of epithelial cells in vitro without a mitogenic effect. *Mol Cell Biol* 1988; **8:** 632–646.
14. Srivastava J, Elliott BE, Louvard D, *et al*. Src-dependent ezrin phosphorylation in adhesion-mediated signaling. *Mol Biol Cell* 2005; **16:** 1481–1490.
15. Heiska L, Carpen O. Src phosphorylates ezrin at tyrosine 477 and induces a phosphospecific association between ezrin and a kelch-repeat protein family member. *J Biol Chem* 2005; **280:** 10244–10252.
16. Lu Y. Src family protein-tyrosine kinases alter the function of PTEN to regulate phosphatidylinositol 3-kinase/AKT cascades. *J Biol Chem* 2003; **278:** 40057–40066.
17. Shiue H, Musch MW, Wang Y, *et al*. Akt2 phosphorylates ezrin to trigger NHE3 translocation and activation. *J Biol Chem* 2005; **280:** 1688–1695.
18. Reczek D, Bretscher A. The carboxyl-terminal region of EBP50 binds to a site in the amino-terminal domain of ezrin that is masked in the dormant molecule. *J Biol Chem* 1998; **273:** 18452–18458.
19. Georgescu MM, Cote G, Agarwal NK, *et al*. NHERF1/EBP50 controls morphogenesis of 3D colonic glands by stabilizing PTEN and ezrin-radixin-moesin proteins at the apical membrane. *Neoplasia* 2014; **16:** 365–374e361–362.
20. Kleylein-Sohn J, Westendorf J, Le Clech M, *et al*. Plk4-induced centriole biogenesis in human cells. *Dev Cell* 2007; **13:** 190–202.
21. Das TK, Dana D, Paroly SS, *et al*. Centrosomal kinase Nek2 cooperates with oncogenic pathways to promote metastasis. *Oncogenesis* 2013; **2:** e69.
22. Deevi RK, McClements J, McCloskey KD, *et al*. Vitamin D3 suppresses morphological evolution of the cribriform cancerous phenotype. *Oncotarget* 2016; **7:** 49042–49064.
23. Pereira H, Pinder SE, Sibbering DM, *et al*. Pathological prognostic factors in breast cancer. IV: should you be a typer or a grader? A comparative study of two histological prognostic features in operable breast carcinoma. *Histopathology* 1995; **27:** 219–226.
24. Chang YM, Bai L, Liu S, *et al*. Src family kinase oncogenic potential and pathways in prostate cancer as revealed by AZD0530. *Oncogene* 2008; **27:** 6365–6375.
25. Osherov N, Levitzki A. Epidermal-growth-factor-dependent activation of the src-family kinases. *Eur J Biochem* 1994; **225:** 1047–1053.
26. Viswanatha R, Wayt J, Ohouo PY, *et al*. Interactome analysis reveals ezrin can adopt multiple conformational states. *J Biol Chem* 2013; **288:** 35437–35451.
27. Madsen CD, Hooper S, Tozluoglu M, *et al*. STRIPAK components determine mode of cancer cell migration and metastasis. *Nat Cell Biol* 2015; **17:** 68–80.
28. Gwanmesia PM, Romanski A, Schwarz K, *et al*. The effect of the dual Src/Abl kinase inhibitor AZD0530 on Philadelphia positive leukaemia cell lines. *BMC Cancer* 2009; **9:** 53.
29. Green TP, Fennell M, Whittaker R, *et al*. Preclinical anticancer activity of the potent, oral Src inhibitor AZD0530. *Mol Oncol* 2009; **3:** 248–261.
30. Jaffe AB, Kaji N, Durgan J, *et al*. Cdc42 controls spindle orientation to position the apical surface during epithelial morphogenesis. *J Cell Biol* 2008; **183:** 625–633.
31. Petridou NI, Skourides PA. FAK transduces extracellular forces that orient the mitotic spindle and control tissue morphogenesis. *Nat Commun* 2014; **5:** 5240.
32. Calalb MB, Zhang X, Polte TR, *et al*. Focal adhesion kinase tyrosine-861 is a major site of phosphorylation by Src. *Biochem Biophys Res Commun* 1996; **228:** 662–668.
33. Sachdev S, Bu Y, Gelman IH. Paxillin-Y118 phosphorylation contributes to the control of Src-inducedanchorage-independent growth by FAK and adhesion. *BMC Cancer* 2009; **9:** 12.
34. Mitra SK, Schlaepfer DD. Integrin-regulated FAK-Src signaling in normal and cancer cells. *Curr Opin Cell Biol* 2006; **18:** 516–523.

35. Lechler T, Fuchs E. Asymmetric cell divisions promote stratification and differentiation of mammalian skin. *Nature* 2005; **437:** 275–280.
36. Martin-Belmonte F, Gassama A, Datta A, *et al*. PTEN-mediated apical segregation of phosphoinositides controls epithelial morphogenesis through Cdc42. *Cell* 2007; **128:** 383–397.
37. Dey N, Crosswell HE, De P, *et al*. The protein phosphatase activity of PTEN regulates SRC family kinases and controls glioma migration. *Cancer Res* 2008; **68:** 1862–1871.
38. Zhang S, Huang WC, Li P, *et al*. Combating trastuzumab resistance by targeting SRC, a common node downstream of multiple resistance pathways. *Nat Med* 2011; **17:** 461–469.
39. Bolduc D, Rahdar M, Tu-Sekine B, *et al*. Phosphorylation-mediated PTEN conformational closure and deactivation revealed with protein semisynthesis. *Elife* 2013; **2:** e00691.
40. Patwardhan P, Resh MD. Myristoylation and membrane binding regulate c-Src stability and kinase activity. *Mol Cell Biol* 2010; **30:** 4094–4107.
41. Murray D, Hermida-Matsumoto L, Buser CA, *et al*. Electrostatics and the membrane association of Src: theory and experiment. *Biochemistry* 1998; **37:** 2145–2159.
42. Fievet BT, Gautreau A, Roy C, *et al*. Phosphoinositide binding and phosphorylation act sequentially in the activation mechanism of ezrin. *J Cell Biol* 2004; **164:** 653–659.
43. Matsui T, Maeda M, Doi Y, *et al*. Rho-kinase phosphorylates COOH-terminal threonines of ezrin/radixin/moesin (ERM) proteins and regulates their head-to-tail association. *J Cell Biol* 1998; **140:** 647–657.
44. Ng T, Parsons M, Hughes WE, *et al*. Ezrin is a downstream effector of trafficking PKC-integrin complexes involved in the control of cell motility. *EMBO J* 2001; **20:** 2723–2741.
45. Viswanatha R, Ohouo PY, Smolka MB, *et al*. Local phosphocycling mediated by LOK/SLK restricts ezrin function to the apical aspect of epithelial cells. *J Cell Biol* 2012; **199:** 969–984.
46. Chambers DN, Bretscher A. Ezrin mutants affecting dimerization and activation. *Biochemistry* 2005; **44:** 3926–3932.
47. Murchie R, Guo CH, Persaud A, *et al*. Protein tyrosine phosphatase sigma targets apical junction complex proteins in the intestine and regulates epithelial permeability. *Proc Natl Acad Sci U S A* 2014; **111:** 693–698.
48. Tinti M, Kiemer L, Costa S, *et al*. The SH2 domain interaction landscape. *Cell Rep* 2013; **3:** 1293–1305.
49. Karsenti E, Vernos I. The mitotic spindle: a self-made machine. *Science* 2001; **294:** 543–547.
50. Ahringer J. Control of cell polarity and mitotic spindle positioning in animal cells. *Curr Opin Cell Biol* 2003; **15:** 73–81.
51. Luxenburg C, Pasolli HA, Williams SE, *et al*. Developmental roles for Srf, cortical cytoskeleton and cell shape in epidermal spindle orientation. *Nat Cell Biol* 2011; **13:** 203–214.
52. Giansanti MG, Gatti M, Bonaccorsi S. The role of centrosomes and astral microtubules during asymmetric division of Drosophila neuroblasts. *Development* 2001; **128:** 1137–1145.
53. Fletcher C. Chapter 9: Tumors of the small and large intestines, including anal canal. In *Diagnostic Histopathology of Tumors* (4th edn). Elsevier: Boston, 2013; 379–416.
54. Toyoshima F, Matsumura S, Morimoto H, *et al*. PtdIns(3,4,5)P3 regulates spindle orientation in adherent cells. *Dev Cell* 2007; **13:** 796–811.
55. Aleshin A, Finn RS. SRC: a century of science brought to the clinic. *Neoplasia* 2010; **12:** 599–607.
56. Heigwer F, Scheeder C, Miersch T, *et al*. Time-resolved mapping of genetic interactions to model rewiring of signaling pathways. *Elife* 2018; **7**: e40174.
57. Matsuda Y, Yoshimura H, Ishiwata T, *et al*. Mitotic index and multipolar mitosis in routine histologic sections as prognostic markers of pancreatic cancers: a clinicopathological study. *Pancreatology* 2016; **16:** 127–132.
58. Liu X, Zheng H, Li X, *et al*. Gain-of-function mutations of Ptpn11 (Shp2) cause aberrant mitosis and increase susceptibility to DNA damage-induced malignancies. *Proc Natl Acad Sci U S A* 2016; **113:** 984–989.
59. Ishizawar R, Parsons SJ. C-Src and cooperating partners in human cancer. *Cancer Cell* 2004; **6:** 209–214.
60. Jagan I, Fatehullah A, Deevi RK, *et al*. Rescue of glandular dysmorphogenesis in PTEN-deficient colorectal cancer epithelium by PPARgamma-targeted therapy. *Oncogene* 2013; **32:** 1305–1315.
61. Capes-Davis A, Reid YA, Kline MC, *et al*. Match criteria for human cell line authentication: where do we draw the line? *Int J Cancer* 2013; **132:** 2510–2519.
62. John T, Liu G, Tsao MS. Overview of molecular testing in non-small-cell lung cancer: mutational analysis, gene copy number, protein expression and other biomarkers of EGFR for the prediction of response to tyrosine kinase inhibitors. *Oncogene* 2009; **28**(Suppl. 1): S14–S23.
63. Bankhead P, Loughrey MB, Fernandez JA, *et al*. QuPath: open source software for digital pathology image analysis. *Sci Rep* 2017; **7:** 16878.

References 60 – 63 are cited only in the supplementary material.

SUPPLEMENTARY MATERIAL ONLINE

Supplementary materials and methods

Supplementary figure legends

Figure S1. Modulation of Src activity

Figure S2. Src regulation of cell cortex dynamics

Figure S3. Src regulation of bipolar mitotic spindle dynamics, multicellular assembly and gland lumen formation

Figure S4. Src regulation of focal adhesion proteins

Figure S5. Src/PLK4 co-dependent regulation of centrosome and mitotic spindle dynamics

Figure S6. Ezrin IHC scores and prognostic variables in human CRC

Impact of the Nuclear Envelope on Malignant Transformation, Motility, and Survival of Lung Cancer Cells

Sílvio Terra Stefanello, Isabelle Luchtefeld, Ivan Liashkovich, Zoltan Pethö, Ihab Azzam, Etmar Bulk, Gonzalo Rosso, Lilly Döhlinger, Bettina Hesse, Andrea Oeckinghaus, and Victor Shahin**

Nuclear pore complexes (NPCs) selectively mediate all nucleocytoplasmic transport and engage in fundamental cell-physiological processes. It is hypothesized that NPCs are critical for malignant transformation and survival of lung cancer cells, and test the hypothesis in lowly and highly metastatic non-small human lung cancer cells (NSCLCs). It is shown that malignant transformation is paralleled by an increased NPCs density, and a balanced pathological weakening of the physiological stringency of the NPC barrier. Pharmacological interference using barrier-breaking compounds collapses the stringency. Concomitantly, it induces drastic overall structural changes of NSCLCs, terminating their migration. Moreover, the degree of malignancy is found to be paralleled by substantially decreased lamin A/C levels. The latter provides crucial structural and mechanical stability to the nucleus, and interacts with NPCs, cytoskeleton, and nucleoskeleton for cell maintenance, survival, and motility. The recent study reveals the physiological importance of the NPC barrier stringency for mechanical and structural resilience of normal cell nuclei. Hence, reduced lamin A/C levels in conjunction with controlled pathological weakening of the NPC barrier stringency may facilitate deformability of NSCLCs during the metastasis steps. Modulation of the NPC barrier presents a potential strategy for suppressing the malignant phenotype or enhancing the effectiveness of currently existing chemotherapeutics.

1. Introduction

Nuclear pore complexes (NPCs) span the double-membraned nuclear envelope of eukaryotic cells at regular distances. Their total numbers vary from several hundreds to tens of millions in different cell types and can change dynamically depending on the life cycle, physiological and pathophysiological states amongst others.[1–3] The NPC is a sophisticated supramolecular cylindrical structure with a rotational octagonal symmetry,[4] built from multiple copies of ≈30 different proteins, termed nucleoporins (Nups).[5] Two thirds of the Nups build the NPC core scaffold and anchor it within the nuclear envelope while the remaining third generates the selective NPC transport barrier amongst others.[6,7] Transport through the NPC proceeds through its central channel that is occupied by Nups exhibiting peculiar biochemical and biophysical properties. They are unstructured, flexible, and highly dynamic and are rich in hydrophobic motifs consisting of varied phenylalanine (F) and glycine (G) repeats that are in turn connected with spacers rich in polar amino acids.[8] FG-Nups provide the NPC with transport selectivity by specific interaction with import and export receptors bearing cargos with identifiable import/export signals. Receptor-mediated transport can accommodate cargos up to megadalton sizes or ≈39 nm, consistent with the diameter of the NPC channel at its narrowest part.[9] At the same time FG-Nups form a physical barrier inside the NPC channel which restricts unselective transport to a sharp threshold of ≈5 nm or ≈40 kDa.[5] In addition to mediating the canonical nucleocytoplasmic transport function of NPCs, several FG-Nups are potent gene transcription regulators which commute dynamically between the NPC and the nucleus[10] to play key roles in development, differentiation, maintenance, and survival of cells.[11,12] Alteration of their physiological expression levels is linked to cancer onset and progression,[13–18] but the underlying mechanisms remain to be explored. There is overwhelming evidence for the crucial roles of alteration of the properties of the cell nucleus and nuclear envelope environment in promoting malignant transformation of cancer cells.[13,19–21] However, the specific involvement of the NPC barrier function remains barely explored.

S. T. Stefanello, I. Luchtefeld, I. Liashkovich, Z. Pethö, E. Bulk, G. Rosso,
L. Döhlinger, B. Hesse, V. Shahin
Institute of Physiology II
University of Münster
Robert-Koch-Str. 27b, Münster 48149, Germany
E-mail: liashkov@uni-muenster.de; shahin@uni-muenster.de

I. Azzam
Institute of Immunology
University of Münster
Röntgen-Str. 21, Münster 48149, Germany

A. Oeckinghaus
Institute of Molecular Tumor Biology
University of Münster
Robert-Koch-Str. 43, Münster 48149, Germany

The ORCID identification number(s) for the author(s) of this article can be found under https://doi.org/10.1002/advs.202102757

DOI: 10.1002/advs.202102757

The vast majority of publications involving NPCs in malignant transformation of cancer cells deal with the roles of certain NPC proteins as transcriptional regulators, while barely any studies specifically address the possible alteration of the selective NPC barrier despite its fundamental relevance for cancer cells survival and therapy.[22] Structure and organization of the nucleus, as well as physical cues, interactions, and mechanical forces promoting malignant transformation and metastasis are addressed in comprehensive reviews and citations therein.[19,20,23,24] Chow et al., review alterations in the nuclear envelope environment associated with cancer.[13] Vargas et al., show transient nuclear envelope rupturing during interphase in human cancer cells.[25] Hatch et al., demonstrate catastrophic nuclear envelope collapse in cancer cell micronuclei.[26] Denais et al., show nuclear envelope rupture and repair during cancer cell migration.[21] Nuclear deformation causes localized loss of nuclear envelope integrity, which leads to uncontrolled exchange of nucleocytoplasmic content, herniation of chromatin across the nuclear envelope, and DNA damage.[21] Mohamed et al., reveal loss of mechanical resilience of NPCs in colorectal cancer cells.[27] Recent study by McCloskey et al., reports that experimental depletion of the NPC basket protein Tpr dramatically increases the total NPC number in various cell types.[1] They suggest the extension of their findings to cancer cells and contemplate that tweaking NPC numbers in cancer cells may usher in the design of novel cancer therapies. Emerging evidence suggests that besides hematological cancers, Nups act as tumor drivers of major non-hematological malignancies such as carcinomas of skin, breast, lung, pancreas, prostate, and colon. Hence, nucleoporins are emerging as novel therapeutic targets in human tumors.[28] As obvious from the aforementioned publications, the specific and direct involvement of the physiological NPC barrier function remains barely explored if at all. Our recent study introduces novel and crucial role of the selective nucleocytoplasmic NPC barrier function in maintaining nuclear mechanics and eventually structure too in normal cells.[29] With respect to the critical physiological roles of nuclear structure and mechanics in maintenance and survival of normal cells, pathophysiological alteration in the newly revealed NPC barrier function is most likely to be associated with transformation of normal cells to cancer cells. In the present work, we demonstrate that malignant transformation of lung cancer cells is closely associated with transformation of the NPC barrier. In addition, pharmacological interference with the barrier has direct implications for the survival of cancer cells.

2. Results and Discussion

The remarkable plasticity of NPCs enables them to undergo changes in their number, structure, function, and composition in response to physiological cues.[2,11] The redistribution of oncogene products and tumor suppressors between the cytosol and the nucleus of cancer cells[30] hints at a possible alteration of the primary transport and/or barrier function of the NPCs. We set out to study potential changes of NPCs in lowly metastatic (A549_0R) and highly metastatic (A549_3R) non-small cell lung cancer (NSCLC) cell lines,[31] in comparison to non-cancer cells. Lung cancer is worldwide by far the most common cause of cancer deaths, accounting for almost 25% of all cases, resulting in well over 1.6 million deaths each year,[32,33] and the histological subtypes NSCLC are the most common accounting for ≈85%.[32] In spite of significant clinical advances made in cancer research over the past years, the 5-year relative survival rate of patients with metastatic NSCLC remains extremely low at 5%.[33] Continued research of the pathophysiological mechanisms underlying the molecularly heterogeneous NSCLC is crucial to increasing the effectiveness of therapies and advancing the devastating prognosis.[32] The cell lines we used are proper in vitro models for NSCLC. The lowly metastatic and commercially available A549 ((ATCC CCL-185)), is human epithelial carcinoma cell line derived from explanted cultures of human lung cancer tissue of a 58 year old Caucasian patient,[34] and is widely used for basic cancer research and drug discovery. They retain cancerous characteristics associated with their original tumor.[34] In the present work, we refer to A549 as A549_0R. A549_3R are highly aggressive NSCLCS generated from the parental A549_0R cell line in an in vivo selection approach in mice, following three rounds (R) of selection upon injection of A549_0R into the tail vein of mice, as described in the original publication.[31] The high metastatic potential of A549_3R was demonstrated in vivo in NOD/SCID mice following intravenous injection.[31] Further in vitro investigations showed that A549_3R exhibited additional features linked to their high metastatic potential, including enhanced clonogenic growth and increased mutation rate.[31] Consistently, our previous publication demonstrates that migration and proliferation rate of A549_3R cells in vitro are enhanced.[35] As control for non-cancer cells, we utilized the human cell line EA.hy926. This cell line was obtained by fusing the stable human cell line A549 with primary human umbilical vein endothelial cells.[36] The resulting immortalized EA.hy926 cell line preserves the specific cellular physiological properties of the primary cell line, for instance the release of Weibel–Palade bodies and factor VIII-related antigen. It also exhibits tissue-specific organelles, characteristics of differentiated endothelial cell functions such as angiogenesis, homeostasis/thrombosis, blood pressure, and inflammation, which is why it widely serves as valuable in vitro biomedical model for vascular endothelial cell research.[36,37] We started our investigations by examining passive NPC permeability, which is a measure of the NPC barrier stringency, in control versus A540_0R and A549_3R cells, using fluorescein isothiocyanate (FITC) dextrans of different sizes. The utilized experimental approach is based on the well-established digitonin-permeabilized cell assay;[38] each experimental condition is repeated five times or more and the total number of analyzed cells is at least 200 in each individual condition. The choice of the molecular sizes 10, 20, and 150 kDa is based on the stringency and functional integrity of the NPC permeability barrier, which was experimentally determined to have an upper cut-off < 40 kDa for FITC-dextran;[39] NPCs should permit passive diffusion of 10 and 20 kDa dextrans at decreasing size-dependent rates, whereas 150 kDa serves as an integrity marker for both the NPC and nuclear envelope.[38,39] The results of the NPC barrier stringency measurements are summarized in **Figure 1**.

All tested cells exhibit high passive NPC permeability for 10 kDa FITC-dextran. However, the relative permeability levels of A549_0 and A549_3R for 10 kDa FITC-dextran at the start of the measurement are 14.8 ± 1.8% and 20 ± 1.5% higher than control, respectively. The differences in the levels are largely maintained well after an equilibrium is reached. The permeability levels also

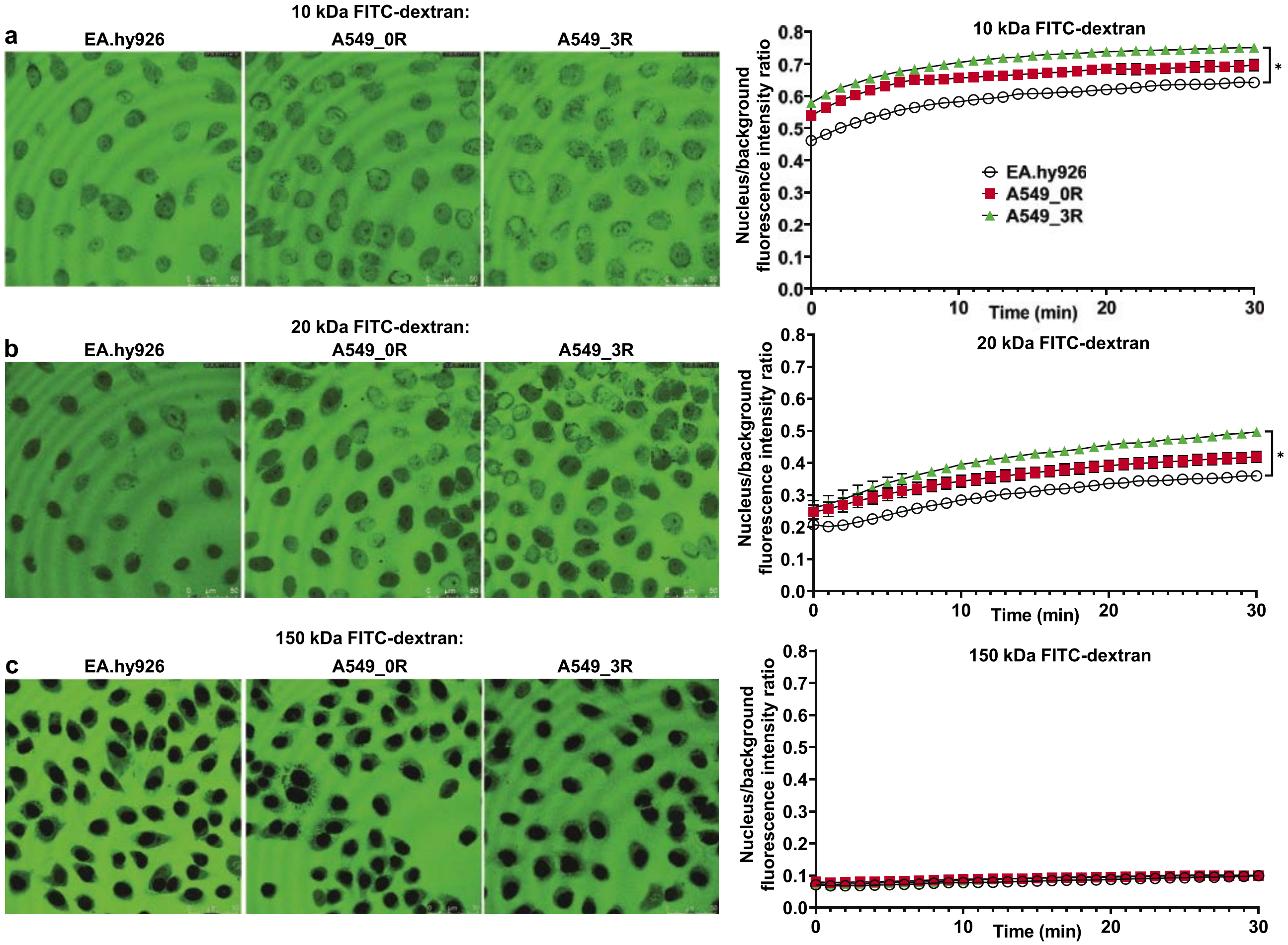

Figure 1. Functional state of the NPC permeability barrier in non-cancer (EA.hy926) versus cancer cells (A549_0R and A549_3R). a–c left) Confocal microscopy imaging of the three cell lines EA.hy926 (non-cancerous), A549_0R (cancerous, low malignancy), and A549_3R (high malignancy) show that the nuclei of the cells with the highly aggressive phenotype are characterized by a reduced stringency of the nucleocytoplasmic permeability barrier, tested with fluorescent tracer of different sizes (FITC-dextran 10, 20 and 150 kDa; 150 kDa serves as functional integrity marker of the nuclear envelope). a,b,c right) The corresponding graphs of (a,b,c left) respectively, show the kinetics of influx of the FITC-dextrans into the nuclei of the three cell lines, and demonstrate that influx rates correlate with malignancy. Data are shown as the mean ± SEM. Asterisks indicate statistically significant differences ($P < 0,05$, Two Way ANOVA followed by Tukey's Multiple Comparison test). $N = 10$ and ≥400 cells analyzed in each experimental condition. Images are 250 µm × 250 µm each.

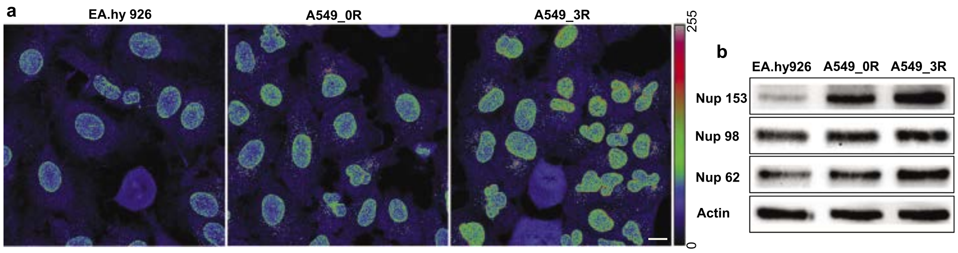

Figure 2. NPCs density in non-cancer (EA.hy926) versus cancer cells (A549_0R and A549_3R). a) Immunofluorescence staining with mAb414 antibody, which recognizes at least four different FG-nups.[41,42] b) Western blots of the expression levels of Nups 62, Nup98, and Nup153. Malignant transformation of cancer cells is associated with increased NPC density. Scale bar is 10 µm, and $N = 3$ in both experiments.

increase significantly from control to A549_0 to A549_3R cells for 20 kDa FITC-dextran. However, unlike 10 kDa FITC-dextran, the relative permeabilities of the tested cells for 20 kDa FITC-dextran start out at almost the same levels, which then increase from control to A549_0R to A549_3R. At the end of the measurement, the relative permeability levels of A549_0R and A549_3R are 13 ± 2.7% and 26 ± 2.4% higher than control, respectively. All analyzed cells fully exclude 150 kDa FITC-dextran from nuclear entry. This demonstrates the integrity of the nuclear envelope permeability barrier[38] in all analyzed non-cancer and cancer cells and rules out a possible presence of membrane ruptures or NPC barrier leakiness which would arise from cell cycle-dependent changes in the overall structure of the nuclear envelope.[40]

The aforementioned measurements show that the NPC barrier stringency in lung cancer cells is weakened compared to control non-cancer cells, and that the transformation from lowly metastatic to highly metastatic stage is associated with gradual weakening of the NPC barrier stringency. The observations indicate that in addition to weakened barrier stringency, an increase in total number of NPCs in the nuclear envelope gives rise to increased nuclear envelope permeability, as cancer cells progress from lowly metastatic to highly metastatic stage. This suggestion is supported by immunostaining and western blots experiments shown in **Figure 2**.

A monoclonal anti-Nups antibody (mAb414), which recognizes at least four different FG-Nups,[41,42] is utilized for the detection of NPCs in nuclear envelopes of non-cancer and cancer cells. Confocal microscopy images in Figure 2a reveal that the brightness of the nuclear envelopes, as a function of NPC density, rises gradually from non-cancer (control), through A549_0R to A549_3R cells ($N = 3$). Consistently, western blotting experiments ($N = 3$) show progressive increase of NPC proteins (tested for major FG-Nups 62, 98, and 153) from control, through A549_0R to A549_3R cells (Figure 2b). We therefore conclude that the increase of passive nuclear envelope permeability in cancer cells results partly from increased NPC density in nuclear envelopes, and reason that this might be a consequence of increasing metabolic demands on transformation from non-cancerous to cancerous types. Figure 2a also shows that nuclei of cancer cells are substantially deformed compared to the homogenous nuclei of non-cancer cells, which hints at increased compliance of malignant cell nuclei. With respect to the central roles of the nuclear lamina proteins lamins A/C in the overall biomechanical and structural behavior of nuclei,[43,44] we wondered whether alteration of their physiological levels is associated with malignant transformation of cells.

Figure 3 compares the levels of lamin A/C in non-cancer to cancer cells, using immunofluorescence staining and western blotting, and shows that the expression levels of lamins A/C are substantially lowered in cancer cells.

Analogous to our observations with human lung cancer cells, previous publications demonstrate that the expression levels of lamins A/C are markedly reduced in diverse cancer types, which makes lamins A/C a valuable diagnostic and risk biomarker for breast and colorectal cancers.[45–47] Reduced levels of lamins A/C result in softening of the cell nucleus.[43] For metastasis, cancer cells have to detach from the primary tumor to reach distant organs and spread, generally via narrow gaps between the endothelial linings of the vasculature.[20] For this purpose, cancer cells must be able to undergo transient dramatic changes in their overall morphology, as seen in Figure 2. The nucleus is the largest intracellular structure and is up to ten times stiffer than the cytoplasm.[20] Pathologically induced softening of the nuclei in malignantly transformed cancer cells, resulting from reduction of lamin A/C levels, serves their deformability and enhances their invasion and extravasation potential.[20] Our recent study reveals that the physiological stringency of the NPC barrier in non-cancer cells has a profound impact on the crucial maintenance of nuclear mechanics, which is discussed later. We therefore assume that the parallel pathological reduction of both the NPC barrier stringency and lamin A/C expression levels in malignantly transformed lung cancer cells act synergistically to drive nuclear mechanopathology and enhance cancer metastasis. Indeed, nuclear mechanopathology and resulting dramatic changes in cancer cell morphology and pathophysiology serve as powerful diagnostic tool for the grade of malignancy.[24]

Another observation made in Figure 3 regards the apparently increased importin ß activity in cancer compared to non-cancer cells, as supported by findings from immunofluorescence staining and Western blot investigations. This observation lends further support to increased NPC density in cancer cells and may indicate elevated nucleocytoplasmic exchange rates of material. Receptor-mediated transport of diverse regulatory proteins and newly synthesized ribonucleoproteins between the cytosol and the nucleus is critical for cancer cells homeostasis and survival. Having observed a correlation between the NPC barrier and malignant transformation of non-small human lung cancer cells, we set out to study the potential impact of pharmacological modulation of the NPC barrier function on cancer cells migration

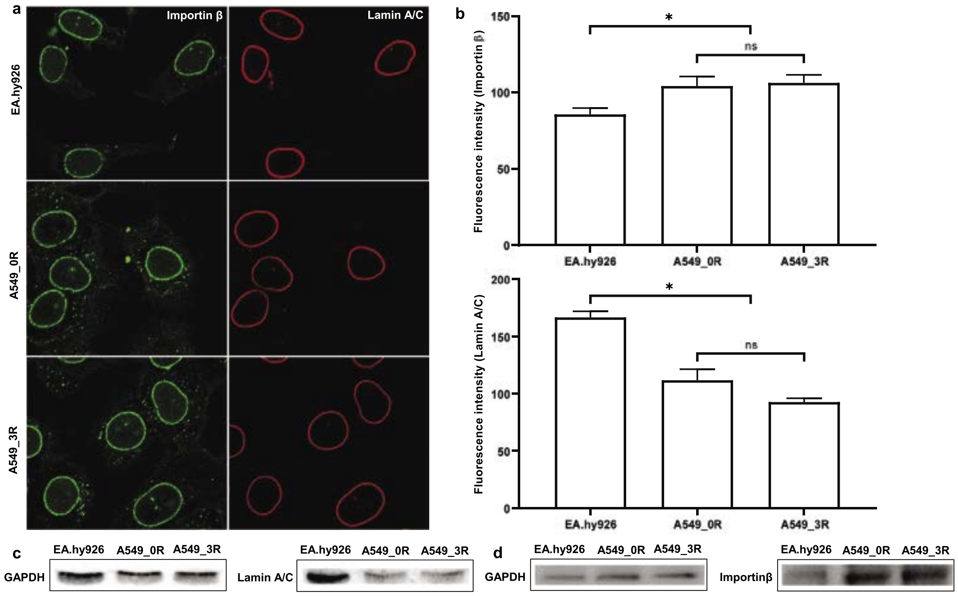

Figure 3. Lamin A/C levels in non-cancer (EA.hy926) versus cancer cells (A549_0R and A549_3R). a) Immunofluorescence staining of NPCs (importin β) and lamin A/C (anti-lamin C antibody). $N = 3$, and $n \geq 100$ cells each. b) Importin β and lamin A/C fluorescence intensity quantification after analysis of cells ($n = 20$) from each experiment ($N = 3$) where the averaged intensity was determined from 3 different sections of each cell. c) Western blotting of the expression levels of lamin A/C in EA.hy926, A549_0R, and A549_3R cells. d) Western blotting of the levels of importin β in EA.hy926, A549_0R, and A549_3R cells. Data are shown as the mean ± SEM. Significant statistical differences ($P < 0.05$, one-way analysis of variance followed by Bonferroni's multiple comparison test) exist between A549_0R-A549_3R and EA.hy926 but none between A549_0R and A549_3R ($N \geq 3$). The housekeeping protein GAPDH is used as a loading control. Scale bars are 10 µm each.

and motility, using NPC barrier breakers. Cancer cells master the controlled manipulation of cell physiology. We hypothesized that lung cancer cells may induce a weakening of the NPC barrier stringency to a well-balanced level that is just low as absolutely required to promote their pathological transformation and ensure their maintenance. Pharmacological exacerbation of the weakening beyond a "soft spot" may tip the balance and negatively impact lung cancer cells.

At concentrations applied in the present work, the utilized compounds do not dissociate FG-Nups from the NPC barrier but interfere with their mutual bonds and consequently relax the barrier, as reported in our recent publications.[48,49] We used time-lapse video microscopy to observe highly metastatic A549_3R cells over a time interval of 10 h whereby they were exposed to 2% (m/v) of either NPC barrier breakers 1,2-trans-Cyclohexanediol (1,2-TCHD), 1,6-Hexanediol (1,6-HD), in combination (1% each), or their negative controls 1,4-Cyclohexanediol (1,4-CHD) and 1,2,3-Hexanetriol (1,2,3-HT), respectively.

As seen in **Figure 4**, the NPC barrier breakers 1,6-HD and 1,2-TCHD immediately stop the migratory activity of A549_3R cells, in opposite to their negative controls 1,4-CHD and 1,2,3-HT, respectively (Videos S1–S6, Supporting Information). 2D cell migration experiments show that the inhibitory effects of the barrier breakers on cell migration correlate with the degree to which they compromise the stringency of the NPC barrier. A combination of 1,6-HD and 1,2-TCHD enables 50% reduction of their individual concentrations, while achieving the highest pharmacological effects on both the weakening of the NPC barrier stringency and the inhibition of the migratory behavior of cells. This clearly demonstrates their synergistic behavior.

The NPC barrier breakers and their negative controls show similar behavior in non-cancer cells (Figure S1, Supporting Information).

The disruption of the NPC barrier stringency is associated with immediate drastic overall structural changes of the cells, which round up and appear to lose traction as shown in **Figure 5** (Videos S1–S6, Supporting Information).

Analysis of the resulting structural index of A549_3R cells, following 10 h of exposure to NPC barrier breakers and their negative controls is summarized in **Table 1**.

Table 1 Summary of the structural index analysis of highly metastatic lung cancer cells (A549_3R) after 10 h of exposure to the NPC barrier breakers 1,2-trans-Cyclohexanediol (1,2-TCHD), 1,6-Hexanediol (1,6-HD), or their negative controls 1,4-Cyclohexanediol (1,4-CHD) and 1,2,3-Hexanetriol (1,2,3-HT), respectively. $N = 3$, at least 100 analyzed cells in each condition. Significant statistical differences exist between all NPC barrier breakers and their negative controls, but none between the barrier breakers separately or in combination ($P < 0.05$, Student's *t*-test).

The two compounds 1,2-TCHD and 1,6-HD seem to possess necessary chemical and pharmacological properties to act so strongly on the NPC barrier. Their negative controls, 1,4-CHD and 1,2,3-HT, respectively, possess similar chemical structures, and yet fail to alter the NPC barrier, migration, motility, or structure of cancer cells.

Figure S2, Supporting Information summarizes LD50 (median lethal dose) measurements following 1 h exposure of non-cancer (EA.hy926) and cancer cells (A549_0R and A549_3R) to progressively increasing concentrations of the

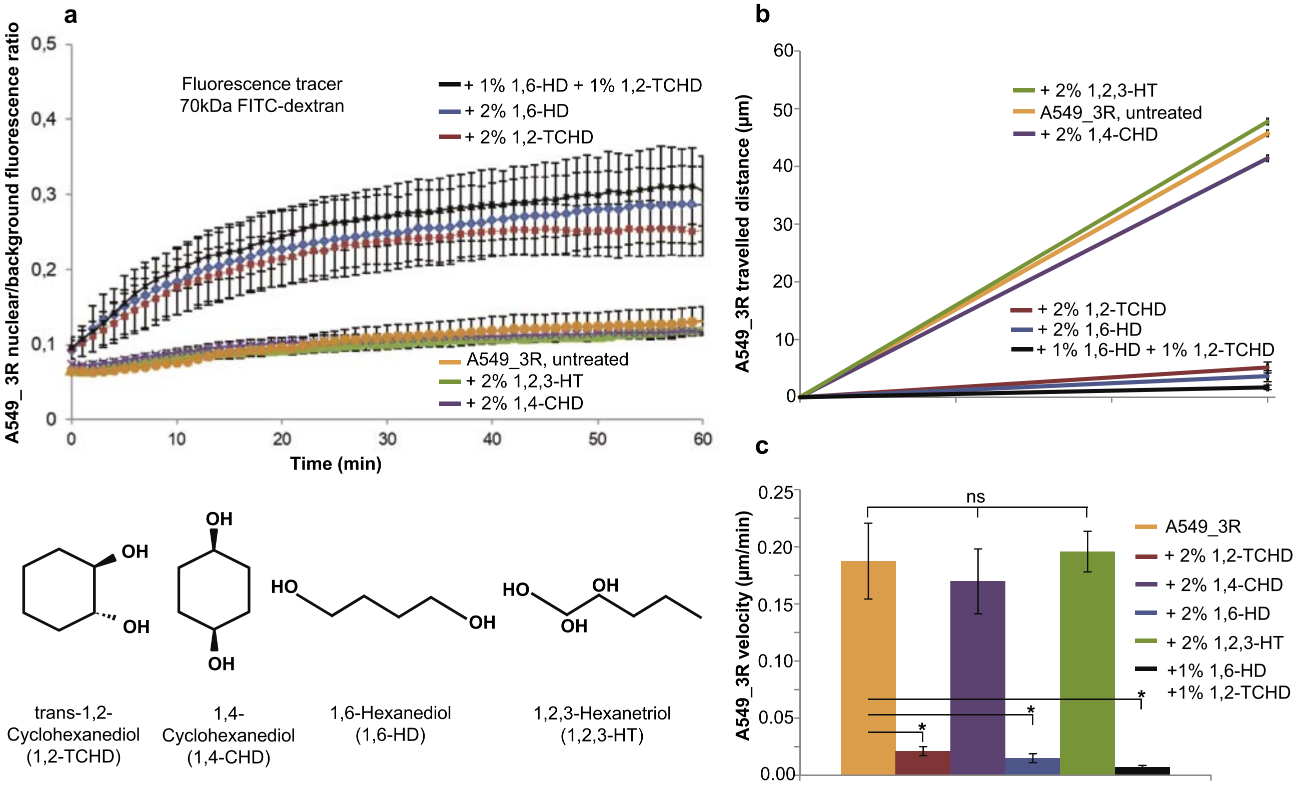

Figure 4. NPC barrier breakers compromise the migratory behavior of highly metastatic lung cancer cells (A549_3R). a) Kinetic profiles of a 70 kDa fluorescent tracer influx into the nuclei of A549_3R cells following cell exposure to NPC barrier breakers 1,6-Hexanediol (1,6-HD), 1,2-trans-Cyclohexanediol (1,2-TCHD), or their negative controls 1,4-Cyclohexanediol (1,4-CHD) and 1,2,3-Hexanetriol (1,2,3-HT), respectively ($N = 5$, and more than 100 cells analyzed in each condition. Data are shown as the mean ± SEM. Statistically significant differences exist between NPC barrier breakers and their negative controls, $P < 0.05$, Student's *t*-test). b,c) 2D cell migration experiments show that the inhibitory effects of the barrier breakers on cell migration correlate with their ability to disrupt the nucleocytoplasmic permeability barrier ($N \geq 3$, asterisks indicate significant statistical differences, $P < 0.05$, Student's *t*-test).

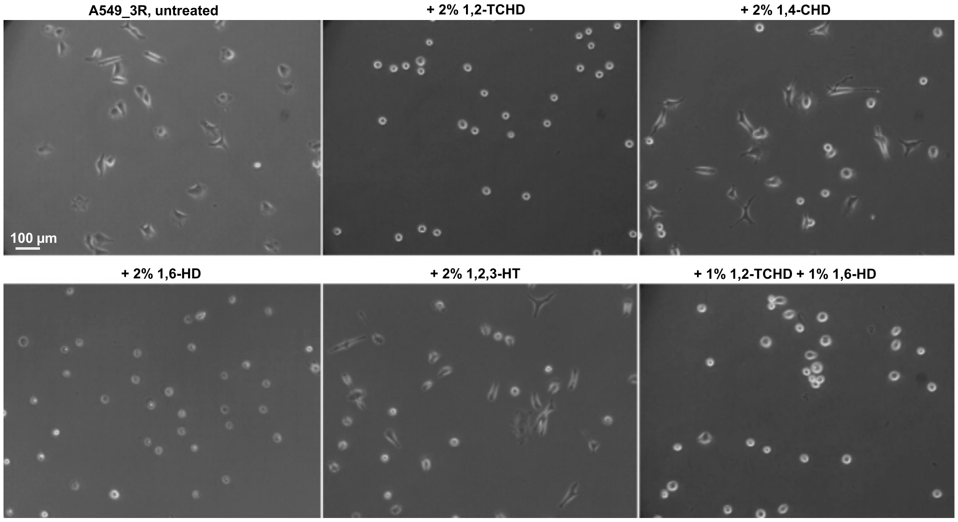

Figure 5. NPC barrier breakers cause drastic overall structural changes of highly metastatic lung cancer cells (A549_3R). Differential interference contrast images collected 10 h after exposure of cells to the NPC barrier breakers 1,2-trans-Cyclohexanediol (1,2-TCHD), 1,6-Hexanediol (1,6-HD), or their negative controls 1,4-Cyclohexanediol (1,4-CHD) and 1,2,3-Hexanetriol (1,2,3-HT), respectively.

Table 1. Structural index analysis of A549_3R cells 10 h after exposure to NPC barrier breakers and their negative controls.

Structural index at 10 h	Untreated A549_3R	+ 2% 1,2-TCHD	+ 2% 1,4-CHD	+ 2% 1,6-HD	+ 2% 1,2,3-HT	+ 1% 1,2-TCHD + 1% 1,6-HD
Mean± SEM	0.41 ± 0.08	0.95 ± 0.04	0.43 ± 0.07	0.96 ± 0.03	0.45 ± 0.06	0.95 ± 0.08

aforementioned NPC barrier breakers and their negative controls.

Summary of the observed effects of NPC barrier breakers leads us to conclude that the extent of migration inhibition as well as the overall structural changes of cells correlate with the degree of the individual compounds to which they compromise the stringency of the NPC permeability. We know from our previous publications that the NPC barrier breakers utilized in the present work at specified concentrations, do not dissociate FG-Nups from the NPC barrier but rather disrupt their crucial interaction with each other and consequently prevent their selective barrier function.[48,49] How can interference with the NPC barrier have such profound impact on the overall structural and dynamical properties of cells? The NPCs are turnstiles of nucleocytoplasmic crosstalk. They are physically and functionally coupled to diverse nucleocytoplasmic structures that span the entire cell.[50,51] This intricate nucleocytoplasmic coupling is not only pivotal for maintenance and survival of cells, but also for their overall morphology, mechanics, and migratory activity amongst others.[51,52] Hence, the following conceivable consequences may arise from indirect interference with nucleocytoplasmic coupling as a result of direct pharmacological manipulation of the NPC barrier: Structural, mechanical, and functional weakening of the nuclear envelope as a nucleocytoplasmic bridge, alteration in cytoskeletal tension, detachment of sensitive bonds between cells and extracellular matrix (ECM), and disruption of mechanosensing and mechanotransduction.[51,52] Given the complexity of such interplay, which remains a subject of intense investigation,[51] we prefer to refrain from suggesting possible mechanisms of action as we believe that it would not be possible without relying heavily on speculations. Rather, the findings obtained in the present work, together with closely related findings from our previous works, set the stage for follow-up studies that will specifically aim at providing mechanistic insights.

We have previously demonstrated that apoptotic cells utilize caspases to dissociate substantial amounts of critical FG-Nups from the NPC barrier and target the nuclear lamina, which softens the nucleus and renders it particularly vulnerable to mechanical stress.[53,54] We therefore postulated the hypothesis that doomed apoptotic cells apply a highly strategic and efficient approach to decisively destabilize nuclear mechanics and ultimately execute the programmed cell death.[55] As highlighted in a recent review by Kirby and Lammerding,[51] the evidence is emerging that the nucleus including the nuclear envelope plays a key role as a cellular mechanosensor, which is pivotal for cell maintenance and survival. Moreover, pathologically caused nuclear softening gives rise to severe diseases.[52] Our recent work reveals that the NPC barrier breaker 1,2-TCHD, whose potency is similar to that of the other barrier breaker 1,6-HD as demonstrated in the present work, leads to substantial softening of the cell nucleus.[29] We show that slight pharmacological relaxation of the barrier stringency causes remarkable reduction of nuclear resilience to mechanical loads. We also prove that the effects of NPC barrier breakers result primarily from specific interference with the barrier configuration.[29] Pharmacologically induced exacerbation of the pathological weakening of the NPC barrier stringency in malignantly transformed cancer cells may compromise their survival ability. Destabilization of nuclear mechanics resulting from NPC barrier breakers may render cancer cells highly sensitive to severe damage during metastatic steps, which pose substantial mechanical stress and require extraordinary high degree of resilience.[20] Besides, destabilization of nuclei may impede their critical roles as central hubs for processing mechanical ques from the environment.[51,21]

To verify that our utilized compounds are not only effective in 2D cell culture models of cancer but also in tumor-relevant environment, we established 3D cancer models based on our recent publication.[56] We tested the compounds for their ability to impact the survival and invasion of cancer cells in cancer spheroids embedded in 3D desmoplastic-like extracellular matrix (ECM). ATP is crucial for survival of cells and ATP luminescence assays are used as highly sensitive parameter for the prediction and evaluation of tumor sensitivity and resistance to chemotherapeutic drugs.[57] Accordingly, we performed ATP luminescence assays to examine the ATP production rates in cancer spheroids embedded in desmoplastic-like ECM, before and after treatment with the compounds. In addition to A549_3R spheroids and in order to confirm the effectiveness of the compounds in primary cancer cells, we generated spheroids from primary pancreatic ductal adenocarcinoma (PDAC)-derived cells, isolated from our murine animal model.[56] The compounds were added to the mediums of the individual experimental models and compared to compound-free control cancer spheroids (solvent-treated), summarized in **Figure 6**.

As seen in Figure 6 pharmacological treatment is effective in both cancer spheroid models and the effectiveness of the NPC barrier breakers is significantly higher compared to their negative controls. In PDAC spheroids, 2% 1,2,3-HT (0.61 ± 0.07, $P < 0.0001$) and 2% 1,4-CHD (0.64 ± 0.05, $P < 0.0001$) decrease total ATP content by around one-third compared to control (1 ± 0.07). In A549_3R spheroids, 2% 1,4-CHD is similarly effective at decreasing ATP content (0.64 ± 0.06, $P < 0.0001$), in contrast to 2% 1,2,3-HT, which does not significantly alter the ATP production (0.84 ± 0.06, $P = 0.14$). In presence of the potent NPC barrier breakers 1,2-TCHD (2%) and 1,6-HD (2%) and their combination (1% each), the ATP production in both PDAC (0.12 ± 0.03, $P < 0.05$; 0.2 ± 0.05, $P < 0.05$; 0.13 ± 0.05, respectively) and A549_3R spheroids (0.47 ± 0.04, $P < 0.05$; 0.52 ± 0.08, $P < 0.05$, 0.46 ± 0.04, $P < 0.05$, respectively) is dramatically decreased compared to control treatment.

The aforementioned findings demonstrate that tumor-cell derived spheroids embedded into a desmoplastic-like ECM react

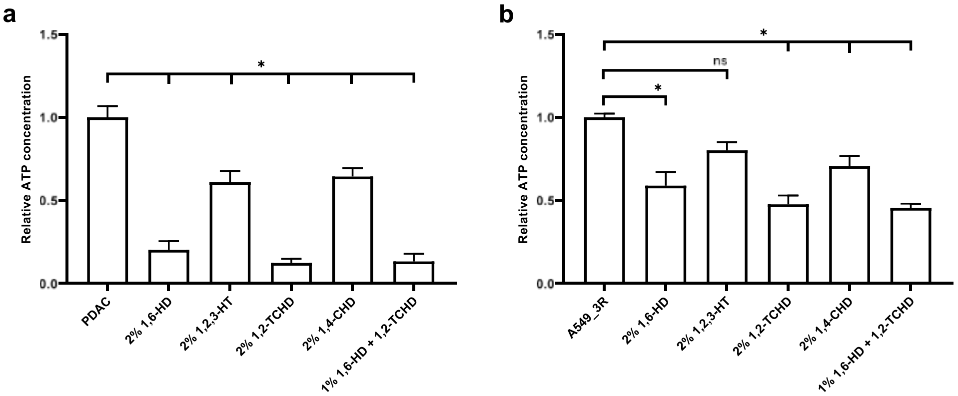

Figure 6. ATP levels in cancer spheroids generated from a) primary pancreatic ductal adenocarcinoma (PDAC)-derived cells and b) A549_3R cells after 20 h of exposure to the NPC barrier breakers 1,2-trans-Cyclohexanediol (1,2-TCHD), 1,6-Hexanediol (1,6-HD), or their negative controls 1,4-Cyclohexanediol (1,4-CHD) and 1,2,3-Hexanetriol (1,2,3-HT), respectively. Data are shown as the mean ± SEM of 4 individual experiments. Asterisks represent a significant difference compared with the untreated control group, determined using one-way analysis of variance followed by Bonferroni's multiple comparison test, $P < 0.05$.

to treatment with the compounds by markedly decreasing ATP production. The treatment-induced strong reduction of the ATP content in cancer spheroids results in their inability to establish sufficient mechanical interaction with the ECM as observed in time-lapse video microscopy tracing over 20 h (Videos S7–S9, Supporting Information). This observation has direct implications for the survival of tumors and escaping cancer cells. Mechanical interactions between the tumor and its microenvironment are well known to be of fundamental importance for tumor survival. Besides, escape of cancer cells from the tumor and invasion depends crucially on their ability to generate traction forces and contract the ECM in the initial steps preceding the invasion.[58] The highly energetic mechanical interactions rely heavily on ATP content in cancer cells. Consequently, the substantial reduction of ATP levels in treated cancer spheroids prevents them from generating sufficient traction forces, which is why they fail to pull on the ECM, in contrast to untreated control PDAC spheroids. The pharmacologically induced reduction of ATP levels may thus be of significant clinical relevance as it may result in decreased tumor spreading in vivo. Interestingly, the applied compounds are differentially effective at decreasing ATP production in A549_3R (≈50% maximal inhibition) and PDAC (≈90% maximal inhibition) spheroids. Here, a likely explanation can be that the basic metabolic profile of these cancers is substantially different. The extreme inhibition of ATP production in primary pancreatic cancer-derived spheroids is very promising and can further be explained by the fact that these cells did not undergo cell culture-dependent phenotypic selection.[59] The differences in the efficacies of the compounds in the 2D culture as compared to the 3D spheroid systems may arise from the fact that 2D cultures are deficient of the complex tissue architecture and cell-matrix and cell-cell interactions which are present in the body.[60]

It is evident that in particular the NPC barrier breakers have a profound impact on cells, which is further supported by the fact that they give rise to substantial increase of reactive oxygen species (ROS) in cancer cells (Figure S3, Supporting Information). Furthermore, they promote apoptosis as detected in flow cytometric measurements (Figure S4, Supporting Information). Viability, apoptosis, and necrosis values in EA.hy926 cells after treatment with 2% NPC barrier breakers either separately or in combination, remain in the same range as untreated controls. In contrast, in A549_3R the combination of 1,2-TCHD and 1,6-HD promotes apoptosis and causes significant decrease in viability while maintaining low levels of necrosis. This makes the combination an interesting approach for apoptosis-based treatment of cancer cells, which are known for their apoptosis evasion.[61]

Currently, there is a limited number of FDA-approved drugs for cancer therapy that target the apoptotic pathway, many of which target BCL-2 family members specifically.[62] Further research is still needed to understand how NPC barrier breakers affect proteins such as BCL-2 or NF-kB. NF-kB has been shown to mediate the nuclear import of plasmids, for example in lung cancer cells,[63] and is a limiting factor in TNF-oriented apoptosis-based cancer therapies, due to the systemic inflammation response it triggers.[62] Understanding these interactions could help in the development of more efficient approaches for plasmid delivery in gene therapy.

Finally, in the light of the profound impact of the introduced compounds on highly aggressive lung and pancreatic cancers they should be considered for intratumoral application in solid tumor cancers that are fairly common. Their demonstrated instant and substantial effectiveness in 3D scaffold-based cancer spheroids, which mimic solid tumors, holds promise that they may be able to overcome the harsh tumor barriers, probably owing to their small size and amphiphilic character. The direct delivery of the anticancer drug into the desired place of action has decisive advantages – it achieves instant high local drug concentrations, is more likely to accumulate inside the tumor owing to the prevailing conditions therein, improves drug bioavailability and efficacy, reduces systemic drug concentration, and lowers serious side effects.[64,65] The fact that the introduced compounds maintain their effect over at least 10 h of exposure is another significant advantage of particular clinical relevance. For example, the anticancer drug paclitaxel is eliminated to almost 50% within the first 24 h of intravenous administration, and eventually barely 0.5% of the drug is bioavailable at its destined place of action, the tumor site in the lung.[65]

3. Conclusions

The urgently needed improvement of the devastating prognosis of metastatic lung cancer, the major cause of cancer deaths worldwide, requires the refinement of our understanding of the cellular pathophysiological processes that are associated with malignant transformation of lung cancer cells. Despite the overwhelming amount of evidence pointing toward the critical importance of signaling across the nuclear envelope for promoting malignant transformation, the actual involvement of the NPCs is far from being adequately characterized. Our observations demonstrate that the critical ability of the NPCs to exclude substances from the nuclear interior is compromised in lung cancer cells. Apparently, the severity of the defect correlates to some degree with the aggressiveness of the malignant phenotype displayed by the tested cell lines. We also demonstrate the critical importance of an intact selective NPC barrier function for the migration of lung cancer cells. Pharmacological interference instantly disrupts the selective barrier function, which immediately results in prevention of cancer cell migration. The exact cellular physiological mechanisms underlying this inextricable relationship remain to be investigated.

We have recently revealed a profound role of the physiological NPC barrier stringency in maintenance of nuclear mechanics and thus structure.[29] When extended to the aforementioned alterations of the factors affecting nucleocytoplasmic transport and the barrier function in cancer, our postulated "ultrafiltration model"[29] of nuclear mechanics has several implications for the progression of the process of malignant transformation. An increased expression of the nuclear export factors could shift the balance of macromolecular distribution toward the cytoplasm making the nucleus less resistant toward mechanical deformation. Coupled with the reduced levels of a critical load-bearing component of the nuclear envelope lamin A/C, this could result in a greatly increased sensitivity of the cancer cell nuclei to physical stresses. These stresses may further exacerbate genomic instability of premalignant cells,[66] thus accelerating the rate of malignant transformation. In addition, altered mechanics of the nuclear envelope may interfere with physiological mechanotransduction cascades leading to biochemical signaling which causes active remodeling of the ECM.[67]

Understanding the ways lung cancer cells exploit this particular element of cellular communication infrastructure may usher in the design of novel anti-cancer drugs. NPCs are highly conserved among species and so we can imagine that the observations made with aggressive lung and pancreatic cancer models in the present work may be relevant to other types of cancer cells, which should be investigated in future works.

Finally, we would like to propound the idea that NPC barrier breakers may qualify for intratumoral application in solid tumors, pending thorough examination of their drug safety. We can also imagine that a combination of our compounds with well-established anticancer drugs may have strong synergistic effects. The synergy would not only enable a marked drug dosage reduction, and thus reduction of severe side effects of anticancer drugs, but it may also decisively impact the pharmacological effectiveness and the outcome of the treatment.

4. Experimental Section

Cell Culture: A549 lung adenocarcinoma cells were cultured at 37 °C under 5% CO_2 in modified Eagle's medium (Invitrogen, Carlsbad, CA), which was supplemented with 10% fetal calf serum. The approach for the generation of highly aggressive non-small lung cancer cells (A549_3R; R = Selection round) from parental lowly metastatic cancer cells A549_0R was described earlier.[68] EA.hy926 endothelial cells were cultured at 37 °C, 5% CO_2 minimal essential medium (MEM) supplemented with 1% non-essential amino-acids, 1% MEM vitamins (Invitrogen), penicillin (100 ug mL^{-1}), streptomycin (100 ug mL^{-1}), and 10% fetal calf serum (FCS, PAA, Germany). For experimental use, cells were grown to confluence on glass bottom petri dishes (WillCo Wells B. V., Amsterdam, Netherlands).

Passive Nuclear Pore Permeability Experiments: The diffusion of FITC-dextran through nuclear pores was tested to evaluate their passive permeability with confocal laser-scanning microscopy. Cells were cultured on glass bottom petri dishes (WillCo Wells B. V., Amsterdam, Netherlands). Nuclear envelopes were specifically permeabilized following treatment of cells for 5 min with 20 µg mL^{-1} digitonin in transport buffer (TB, 20 mM HEPES, 110 mM K-Acetate, 5 mM Na-Acetate, 2 mM Mg-Acetate, 1 mM EGTA (pH 7.3), 2 mM DTT) containing 200 µg mL^{-1} 10, 20 or 150 kDa FITC-dextran (Sigma Aldrich, Steinheim, Germany); 150 kDa FITC-dextran served as an integrity marker of nuclear pores and nuclear envelope. Directly after permeabilization the tested compounds 1,4-Cyclohexanediol, 1,2-trans-Cyclohexanediol, 1,6-Hexanediol, and 1,2,3-Hexanetriol (Sigma Aldrich, Steinheim, Germany) were added either separately or in specified combinations at 1 or 2% each. For control experiments, the compounds were replaced with their solvent (water). Confocal microscopy images (objective 63× oil) were taken in the mid-plane of the nuclei using Leica SP8 confocal laser scanning microscope equipped with hybrid detection system for photon counting (Leica, Wetzlar, Germany) at a rate of one image per minute for 30 min. Subsequently, FITC-dextran influx dynamics was evaluated by determining the ratio between the intranuclear fluorescence intensity and the extracellular background intensity.

Western Blot: The lysates of EA.hy96, the A549_0, and A540_3R cells were obtained by adding triton-lysis buffer (1% Triton X-100, 150 mM NaCl, 5 mM EDTA, 50 mM Tris-HCL) and protease inhibitor (cOmplete Mini, Roche Diagnostics GmbH, Mannheim, Germany) to the cells. The protein concentration was detected by the BCA Pierce Protein Assay Kit (Thermo Fisher Scientific Inc., Waltham, MA), and all samples were added with the same amount of protein when tested by Western Blot. Lysate was size-fractionated with 10% SDS-Page and blotted onto nitrocellulose membrane (Hybond C-Extra, Amersham Bioscience, Amersham, UK). The membrane was blocked in 5% skim milk powder solved in TBS (10 mM Tris/HCL, 1,5 M NaCl) with 0.05% Tween 20. The proteins were labeled by using primary and secondary antibodies. First, nitrocellulose membranes were incubated in primary antibodies (Mab414, Covance, 1:1000; Anti-Nup 98 antibody, Abcam, 1:1000; Anti-KPNB1 (for importin ß), Abcam 1:5000; Lamin A/C, Cell Signaling Technology, 1:2000; Anti-β-Actin, Sigma, 1:10 000; Anti-GAPDH antibody, Abcam, 1:5000) added in blocking buffer overnight. Afterward, the membranes were incubated with the secondary antibodies (Goat anti mouse, DIANOVA, 1:10 000; Anti-rabbit IgG, Sigma, 1:3000) rarefied in milk for 1 h. By using enzyme substrates (Super Signal West pico/femto, Thermo Scientific), protein bands were visualized by the gel documentation system (ChemiDoc XRS, Bio-Rad). For quantification, the program ImageJ was used.

Cell Motility Analysis: EA.hy926 and A549_3R cells were separately seeded on collagen coated culture flasks (containing 1× RPMI, 10 mmol L^{-1} HEPES, 0.02 mg mL^{-1} laminin, 0.04 mg mL^{-1} fibronectin, 0.01 mg mL^{-1} collagen IV, 0.01 mg mL^{-1} collagen III, 0.8 mg mL^{-1} collagen I at pH 7.4) and were left to attach for at least 3 h. Prior to the start of image recording with time-lapse video microscopy, cells were kept for 10 min in epidermal growth factor (EGF) (1%)-medium containing the same compounds, combination, and concentration as used in confocal microscopy. In control experiments, the compounds were replaced with their solvent (water). The flasks were transferred to heating chambers (37 °C) on the microscopes (Zeiss Axiovert 40C). The cells were imaged in 600 s intervals for 10 h controlled by HiPic 32 or WASABI software (Hamamatsu). For analysis the Amira Imaging Software and the image processing program ImageJ were used by labeling the cell contours each frame. The cell velocity was calculated from the movement of the cell center per time, the traveled distance was computed by the distance from beginning to the end location and the structure index defines cell morphology (1 = spherical cell, 0 = complex cell).

Cell Proliferation Assay and LD50 (Median Lethal Dose) Measurements: The CCK-8 (cell counting kit-8) assay was used to determine the LD50 values in non-cancer and cancer cells. The cells were cultured in a 96-well plate for 24 h at 37 °C, 5% CO_2. Next, the cells (containing CCK-8 kit) were exposed for 1 h to progressively increasing concentrations (0.5, 1, 2, 3, 4, 5, 6, 7 and 8%) of the NPC barrier breakers 1,2-trans-Cyclohexanediol (1,2-TCHD), 1,6-Hexanediol (1,6-HD), or 1,2-TCHD and 1,6-HD in combination, or their negative controls 1,4-Cyclohexanediol (1,4-CHD) and 1,2,3-Hexanetriol (1,2,3-HT), respectively. The absorbance measurement was performed at 450 nm using the plate reader, Molecular Devices.

Viability and Apoptosis Measurements with Flow Cytometry: Cells were exposed for 1 h to either 1,2-TCHD (2%), or 1,6-HD (2%), or combination of 1,2-TCHD and 1,6-HD (1% each), or their negative controls 1,4-CHD (2%) and 1,2,3-HT (2%), respectively. After removal of the compounds by several washing steps, a double-staining was performed with Annexin-V APCs and propidium iodide (PI) to check for apoptosis and cell viability, respectively. PI was an intercalating dye and stains cells with a compromised plasma membrane as an indicator of necrotic death, measured at 488 nm. Annexin-V APC was an indicator of apoptosis because it binds the membrane phospholipid phosphatidylserine which was translocated from the inner to the outer leaflet of the plasma membrane during apoptosis, measured at 650–660 nm. 2.5 µL of Annexin-V APC (Immunotools, Friesoythe, Germany) stock was added to the cells and they were incubated for 15 min in the dark. 300 µL of cell culture medium were added and the cells were placed on ice. Propidium iodide (Merck, Darmstadt, Germany) was added (20 ng mL^{-1}) to the cells and the measurements were done immediately using a BD FACS Calibur (BD Biosciences, Erembodegem, Belgium). Data analysis was performed using FlowJo v10 10.5.3 (FlowJo, LLC, Ashland OR) and Microsoft Excel (Microsoft Office 2016).

Measurement of Intracellular ROS: After treatment of cells for 1 h with NPC barrier breakers and their negative controls at the same concentrations as in the aforementioned experiments, the compounds were washed out and subsequently the intracellular ROS levels were evaluated by using the cellular ROS detection assay kit (ab113851, Abcam), utilizing 2′,7′-dichlorofluorescin diacetate according to the manufacturer's protocol. The fluorescence measurements were performed using a Fluoroskan II Fluorescent with excitation/emission wavelengths filter: Ex/Em = 485/535 nm.

Animal Model for Pancreatic Cancer: The animal experiments were conducted with the approval of the local ethics committee for animal care (Landesamt für Natur, Umwelt und Verbraucherschutz Nordrhein-Westfalen, permit number 81-02.04.2019.A281). KPfC mice conditionally express mutant K-Ras (K-RasG12D) and mutant p53 (p53R172H) in the pancreas under physiological control from the endogenous locus (KRaswt/LSL-G12D p53wt/LSL-R172H Pdx1-Cre+). This was achieved by Lox-SOP-Lox (LSL) cassettes that prevent expression of the mutant proteins prior to Cre recombinase-mediated recombination and consequent excision of the stop cassette.[69–71]

Primary murine pancreatic cancer-derived cells were isolated as follows. KPfC mice were sacrificed at 24 weeks of age and subsequently, the pancreas was removed. Afterward, pancreata were digested with 1 mg mL^{-1} collagenase P (Sigma Aldrich, Merck KGaA, Darmstadt, Germany) in PBS for 30 min at 37 °C. Then, tissue fragments were centrifuged at 200 g for 5 min RT and cultured in DMEM/HAM F-12 medium containing 10% FCS and 1% Pen-Strep in a tissue-culture dish for 24 h at 37 °C. After 24 h, non-adherent tissue was washed away 3× with medium and a heterogeneous population of cancer cells, stromal fibroblasts, and immune cells remained in the dish. For the experiments involving spheroids, cells were used from passages 0 to 1.

Cancer Spheroids Assembly, Matrix Embedding, and Time-Lapse Video Microscopy: Spheroids of A549 and primary PDAC-derived cells were created as described previously.[56] Briefly, a hanging drop-based method was used for inducing spheroid formation from 10 000 cells/spheroid, in medium containing 0.25% methylcellulose.

After 48 and 72 h for A549 and PDAC-derived cells, respectively, spheroids were harvested and embedded in a desmoplastic ECM-like in vitro polymerized matrix, as described previously.[72] The final composition of matrix components were 40 µg mL^{-1} laminin (Sigma Aldrich, Merck KGaA, Darmstadt, Germany), 40 µg mL^{-1} fibronectin (Sigma Aldrich, Merck KGaA, Darmstadt, Germany), 800 µg mL^{-1} collagen I (Corning, New York, NY, USA), 12 µg mL^{-1} collagen III (Corning, New York, NY, USA) and 5.4 µg mL^{-1} collagen IV (BD Biosciences, Heidelberg, Germany). After embedding, spheroids in matrix were further investigated by video microscopy or luminometry.

Time-lapse video microscopy of spheroids in matrix was performed as described previously.[56] First, spheroids in ECM were seeded in 12.5 cm^2 flasks. After matrix polymerization for 2 h at 37 °C, control medium or medium with target compounds was added to the flasks. After an equilibration period of another 2 h at 37 °C in a 5% CO_2/air atmosphere, matrix traction of spheroids in the matrix was monitored using time-lapse video microscopy. Time-lapse acquisition was recorded in temperature-controlled chambers (37 °C) with CMOS cameras for 20 h at 5 min intervals using the MicroCamLab 3.1 software (Bresser, Rhede, Germany).

Measurement of ATP Content in Cancer Spheroids: For measurement of ATP Production, black-walled 96-well plates (Corning, New York, NY, USA) were first coated with 1% agarose gel to prevent cell adhesion and spreading at the bottom of the well. Afterward, 50 µL ECM containing one spheroid was applied to each well and left to polymerize for 2 h at 37 °C. Subsequently, control medium or medium with target compounds was added to the wells and spheroids were incubated for 20 h at 37 °C. ATP production of spheroids was measured using the CellTiter-Glo 3D kit (Promega, Madison, WI, USA) according to manufacturer's protocol. Briefly, 100 µL reagent was added to each well, followed by mechanical disruption of the extracellular matrices containing a spheroid. After 15 min shaking with 200 RPM at RT, total ATP content of the wells was determined using a luminometer (Berthold Technologies, Tristar LB941). The luminescence of each well was background subtracted by luminescence of wells containing ECM without a spheroid.

Statistical Analysis: Each experimental condition was repeated at least three times. Data are presented as mean values ± standard error of the mean (SEM). Results were considered as statistically significant at the probability level $P < 0.05$. The details regarding the number of experiments and analyzed cells, applied statistical tests and P values were specified in the corresponding parts. Statistical tests and graph production were performed using software Origin Pro 9 and GraphPad Prism 9.0.0.

Supporting Information

Supporting Information is available from the Wiley Online Library or from the author.

Acknowledgements

S.T.S. and I.L. contributed equally to this work. S.T.S is supported by a Capes-Humboldt Research Fellowship for Postdoctoral Researchers (Program CAPES-HUMBOLDT N. 88881.197729/2018-01).

The authors acknowledge the financial support of the Deutsche Forschungsgemeinschaft (SH 167/6-1, SH 167/9-1, SH 167/6-2, LI 2157/3-1, OE 531/2-2 and GRK 2515/1, Chembion) , Marie Skłodowska-Curie Innovative Training Network (H2020-MSCA-ITN-2018, Grant Agreement number: 813834 (pHioniC)). This study was financed in part by the Coordenação de Aperfeiçoamento de Pessoal de Nível Superior - Brasil (CAPES) - Finance Code 001.

Open Access funding enabled and organized by Projekt DEAL.

Correction added on April 6, 2022, after first online publication: Projekt Deal funding statement has been added.

Conflict of Interest

The authors declare no conflict of interest.

Data Availability Statement

Research data are not shared.

Keywords

cancer, cellular physiology and biophysics, nanomedicine, nuclear envelope, nuclear pores

Received: June 28, 2021
Revised: August 11, 2021
Published online: October 17, 2021

---

[1] A. McCloskey, A. Ibarra, M. W. Hetzer, *Genes Dev.* **2018**, *32*, 1321.
[2] G. Maul, L. Deaven, *J. Cell Biol.* **1977**, *73*, 748.
[3] V. Shahin, *Nuclear Pore Complexes in Genome Organization, Function and Maintenance*, Springer, Cham **2018**, pp. 63–86.
[4] A. Hoelz, E. W. Debler, G. Blobel, *Annu. Rev. Biochem.* **2011**, *80*, 613.
[5] K. E. Knockenhauer, T. U. Schwartz, *Cell* **2016**, *164*, 1162.
[6] F. Alber, S. Dokudovskaya, L. M. Veenhoff, W. Zhang, J. Kipper, D. Devos, A. Suprapto, O. Karni-Schmidt, R. Williams, B. T. Chait, A. Sali, M. P. Rout, *Nature* **2007**, *450*, 695.
[7] A. von Appen, J. Kosinski, L. Sparks, A. Ori, A. L. DiGuilio, B. Vollmer, M.-T. Mackmull, N. Banterle, L. Parca, P. Kastritis, K. Buczak, S. Mosalaganti, W. Hagen, A. Andres-Pons, E. A. Lemke, P. Bork, W. Antonin, J. S. Glavy, K. H. Bui, M. Beck, *Nature* **2015**, *526*, 140.
[8] L. J. Terry, S. R. Wente, *Eukaryotic Cell* **2009**, *8*, 1814.
[9] N. Panté, M. Kann, *Mol. Biol. Cell* **2002**, *13*, 425.
[10] G. Rabut, V. Doye, J. Ellenberg, *Nat. Cell Biol.* **2004**, *6*, 1114.
[11] M. Raices, M. A. D'Angelo, *Nat. Rev. Mol. Cell Biol.* **2012**, *13*, 687.
[12] M. Beck, E. Hurt, *Nat. Rev. Mol. Cell Biol.* **2017**, *18*, 73.
[13] K. H. Chow, R. E. Factor, K. S. Ullman, *The Nuclear Envelope Environment and Its Cancer Connections*, Vol. *12*, Nature Publishing Group, London **2012**, pp. 196–209.
[14] V. Rodriguez-Bravo, R. Pippa, W.-M. Song, M. Carceles-Cordon, A. Dominguez-Andres, N. Fujiwara, J. Woo, A. P. Koh, A. Ertel, R. K. Lokareddy, A. Cuesta-Dominguez, R. S. Kim, I. Rodriguez-Fernandez, P. Li, R. Gordon, H. Hirschfield, J. M. Prats, E. P. Reddy, A. Fatatis, D. P. Petrylak, L. Gomella, W. K. Kelly, S. W. Lowe, K. E. Knudsen, M. D. Galsky, G. Cingolani, A. Lujambio, Y. Hoshida, J. Domingo-Domenech, *Cell* **2018**, *174*, 1200.
[15] K. Holzer, A. Ori, A. Cooke, D. Dauch, E. Drucker, P. Riemenschneider, A. Andres-Pons, A. L. DiGuilio, M. T. Mackmull, J. Baßler, S. Roessler, K. Breuhahn, L. Zender, J. S. Glavy, F. Dombrowski, E. Hurt, P. Schirmacher, M. Beck, S. Singer, *Nat. Commun.* **2019**, *10*, 2147.
[16] S. Sakuma, M. Raices, J. Borlido, V. Guglielmi, E. Y. S. Zhu, M. A. D'Angelo, *Cancer Discovery* **2021**, *11*, 176.
[17] S. Sakuma, M. A. D'Angelo, *Semin. Cell Dev. Biol.* **2017**, *68*, 72.
[18] V. Nofrini, D. Di Giacomo, C. Mecucci, *Eur. J. Hum. Genet.* **2016**, *24*, 1388.
[19] D. Zink, A. H. Fischer, J. A. Nickerson, *Nat. Rev. Cancer* **2004**, *4*, 677.
[20] D. Wirtz, K. Konstantopoulos, P. C. Searson, *Nat. Rev. Cancer* **2011**, *11*, 512.
[21] C. M. Denais, R. M. Gilbert, P. Isermann, A. L. McGregor, M. Te Lindert, B. Weigelin, P. M. Davidson, P. Friedl, K. Wolf, J. Lammerding, *Science* **2016**, *352*, 353.
[22] T. R. Kau, J. C. Way, P. A. Silver, *Nuclear Transport and Cancer: From Mechanism to Intervention*, Vol. *4*, Nature Publishing Group, London **2004**, pp. 106–117.
[23] H. Mohammadi, E. Sahai, *Mechanisms and Impact of Altered Tumour Mechanics*, Vol. *20*, Nature Publishing Group, London **2018**, pp. 766–774.
[24] C. Uhler, G. V. Shivashankar, *Trends Cancer* **2018**, *4*, 320.
[25] J. D. Vargas, E. M. Hatch, D. J. Anderson, M. W. Hetzer, *Nucleus* **2012**, *3*, 88.
[26] E. M. Hatch, A. H. Fischer, T. J. Deerinck, M. W. Hetzer, *Cell* **2013**, *154*, 47.
[27] M. S. Mohamed, A. Kobayashi, A. Taoka, T. Watanabe-Nakayama, Y. Kikuchi, M. Hazawa, T. Minamoto, Y. Fukumori, N. Kodera, T. Uchihashi, T. Ando, R. W. Wong, *ACS Nano* **2017**, *11*, 5567.
[28] A. Roy, G. Narayan, *Oncogenic Potential of Nucleoporins in Non-hematological Cancers: Recent Update Beyond Chromosome Translocation and Gene Fusion*, Vol. *145*, Springer-Verlag, Berlin **2019**, pp. 2901–2910.
[29] V. Shahin, I. U. Kouzel, G. Rosso, I. Liashkovich, *Adv. Sci.* **2019**, *6*, 1900709.
[30] R. Hill, B. Cautain, N. de Pedro, W. Link, *Oncotarget* **2014**, *5*, 11.
[31] A. Hascher, A.-K. Haase, K. Hebestreit, C. Rohde, H.-U. Klein, M. Rius, D. Jungen, A. Witten, M. Stoll, I. Schulze, S. Ogawa, R. Wiewrodt, L. Tickenbrock, W. E. Berdel, M. Dugas, N. H. Thoennissen, C. Muller-Tidow, *Clin. Cancer Res.* **2014**, *20*, 814.
[32] R. S. Herbst, D. Morgensztern, C. Boshoff, *Nature* **2018**, *553*, 446.
[33] R. L. Siegel, K. D. Miller, A. Jemal, *Ca-Cancer J. Clin.* **2020**, *70*, 7.
[34] D. J. Giard, S. A. Aaronson, G. J. Todaro, P. Arnstein, J. H. Kersey, H. Dosik, W. P. Parks, *J. Natl. Cancer Inst.* **1973**, *51*, 1417.
[35] E. Bulk, A. S. Ay, M. Hammadi, H. Ouadid-Ahidouch, S. Schelhaas, A. Hascher, C. Rohde, N. H. Thoennissen, R. Wiewrodt, E. Schmidt, A. Marra, L. Hillejan, A. H. Jacobs, H. U. Klein, M. Dugas, W. E. Berdel, C. Müller-Tidow, A. Schwab, *Int. J. Cancer* **2015**, *137*, 1306.
[36] C. J. Edgell, C. C. McDonald, J. B. Graham, *Proc. Natl. Acad. Sci. U. S. A.* **1983**, *80*, 3734.
[37] C. J. S. Edgell, J. E. Haizlip, C. R. Bagnell, J. P. Packenham, P. Harrison, B. Wilbourn, V. J. Madden, *In Vitro Cell. Dev. Biol.* **1990**, *26*, 1167.
[38] I. Liashkovich, D. Pasrednik, V. Prystopiuk, G. Rosso, H. Oberleithner, V. Shahin, *Sci. Rep.* **2015**, *5*, 9994.
[39] O. Keminer, R. Peters, *Biophys. J.* **1999**, *77*, 217.
[40] E. Dultz, S. Huet, J. Ellenberg, *Biophys. J.* **2009**, *97*, 1891.
[41] L. I. Davis, G. Blobel, *Cell* **1986**, *45*, 699.
[42] J. Sukegawa, G. Blobel, *Cell* **1993**, *72*, 29.
[43] J. Swift, I. L. Ivanovska, A. Buxboim, T. Harada, P. C. D. P. Dingal, J. Pinter, J. D. Pajerowski, K. R. Spinler, J.-W. Shin, M. Tewari, F. Rehfeldt, D. W. Speicher, D. E. Discher, *Science* **2013**, *341*, 1240104.
[44] K. N. Dahl, A. J. S. Ribeiro, J. Lammerding, *Circ. Res.* **2008**, *102*, 1307.
[45] A. Aljada, J. Doria, A. M. Saleh, S. H. Al-Matar, S. AlGabbani, H. B. Shamsa, A. Al-Bawab, A. A. Ahmed, *Cell. Oncol.* **2016**, *39*, 161.
[46] N. D. Willis, T. R. Cox, S. F. Rahman-Casañs, K. Smits, S. A. Przyborski, P. van den Brandt, M. van Engeland, M. Weijenberg, R. G. Wilson, A. de Bruïne, C. J. Hutchison, *PLoS One* **2008**, *3*, e2988.
[47] I. M. Alhudiri, C. C. Nolan, I. O. Ellis, A. Elzagheid, E. A. Rakha, A. R. Green, C. J. Chapman, *Breast Cancer Res. Treat.* **2019**, *174*, 661.
[48] I. Azzam, I. Liashkovich, I. Luchtefeld, I. U. Kouzel, V. Shahin, *Bioeng. Transl. Med.* **2019**, *4*, e10136.
[49] I. Liashkovich, A. Meyring, H. Oberleithner, V. Shahin, *J. Controlled Release* **2012**, *160*, 601.
[50] N. Wang, J. D. Tytell, D. E. Ingber, *Mechanotransduction at a Distance: Mechanically Coupling the Extracellular Matrix with the Nucleus*, Vol. *10*, Nature Publishing Group, London **2009**, pp. 75–82.
[51] T. J. Kirby, J. Lammerding, *Emerging Views of the Nucleus as a Cellular Mechanosensor*, Vol. *20*, Nature Publishing Group, London **2018**, pp. 373–381.

[52] M. Maurer, J. Lammerding, *Annu. Rev. Biomed. Eng.* **2019**, *21*, 443.
[53] A. Kramer, I. Liashkovich, H. Oberleithner, S. Ludwig, I. Mazur, V. Shahin, *Proc. Natl. Acad. Sci. U. S. A.* **2008**, *105*, 11236.
[54] A. Kramer, I. Liashkovich, H. Oberleithner, V. Shahin, *Nanomedicine* **2010**, *6*, 605.
[55] V. Shahin, *Semin. Cell Dev. Biol.* **2017**, *68*, 85.
[56] A. Kuntze, O. Goetsch, B. Fels, K. Najder, A. Unger, M. Wilhelmi, S. Sargin, S. Schimmelpfennig, I. Neumann, A. Schwab, Z. Pethő, *Front. Physiol.* **2020**, *11*.
[57] P. E. Andreotti, D. M. Hartmann, D. Linder, G. Harel, I. Gleiberman, P. A. Caruso, S. H. Ricks, I. A. Cree, C. M. Kurbacher, M. Untch, C. Sartori, H. W. Bruckner, *Cancer Res.* **1995**, *55*, 5276.
[58] K. S. Kopanska, Y. Alcheikh, R. Staneva, D. Vignjevic, T. Betz, *PLoS One* **2016**, *11*, e0156442.
[59] J. Hoarau-Véchot, A. Rafii, C. Touboul, J. Pasquier, *Int. J. Mol. Sci.* **2018**, *19*, 181.
[60] D. Lv, Z. Hu, L. Lu, H. Lu, X. Xu, *Three-Dimensional Cell Culture: A Powerful Tool in Tumor Research and Drug Discovery*, Vol. *14*, Spandidos Publications, London **2017**, pp. 6999–7010.
[61] C. M. Pfeffer, A. T. K. Singh, *Int. J. Mol. Sci.* **2018**, *19*, 448.
[62] B. A. Carneiro, W. S. El-Deiry, *Targeting Apoptosis in Cancer Therapy*, Vol. *17*, Nature Research, London **2020**, pp. 395–417.
[63] A. Mesika, I. Grigoreva, M. Zohar, Z. Reich, *Mol. Ther.* **2001**, *3*, 653.
[64] A. P. Castano, P. Mroz, M. R. Hamblin, *Nat. Rev. Cancer* **2006**, *6*, 535.
[65] A. Fakhari, J. Anand Subramony, *J. Controlled Release* **2015**, *220*, 465.
[66] P. Shah, K. Wolf, J. Lammerding, *Trends Cell Biol.* **2017**, *27*, 546.
[67] R. Malik, P. I. Lelkes, E. Cukierman, *Trends Biotechnol.* **2015**, *33*, 230.
[68] E. Bulk, A. Hascher, R. Liersch, R. M. Mesters, S. Diederichs, B. Sargin, V. Gerke, M. Hotfilder, J. Vormoor, W. E. Berdel, H. Serve, C. Muller-Tidow, *Cancer Res.* **2008**, *68*, 1896.
[69] E. L. Jackson, N. Willis, K. Mercer, R. T. Bronson, D. Crowley, R. Montoya, T. Jacks, D. A. Tuveson, *Genes Dev.* **2001**, *15*, 3243.
[70] S. R. Hingorani, E. F. Petricoin, A. Maitra, V. Rajapakse, C. King, M. A. Jacobetz, S. Ross, T. P. Conrads, T. D. Veenstra, B. A. Hitt, Y. Kawaguchi, D. Johann, L. A. Liotta, H. C. Crawford, M. E. Putt, T. Jacks, C. V. E. Wright, R. H. Hruban, A. M. Lowy, D. A. Tuveson, *Cancer Cell* **2003**, *4*, 437.
[71] S. R. Hingorani, L. Wang, A. S. Multani, C. Combs, T. B. Deramaudt, R. H. Hruban, A. K. Rustgi, S. Chang, D. A. Tuveson, *Cancer Cell* **2005**, *7*, 469.
[72] B. Fels, N. Nielsen, A. Schwab, *Role of TRPC1 Channels in Pressure-Mediated Activation of Murine Pancreatic Stellate Cells*, Vol. 45, Springer-Verlag, Berlin **2016**, pp. 657–670.

3D-Engineered Scaffolds to Study Microtubes and Localization of Epidermal Growth Factor Receptor in Patient-Derived Glioma Cells

Nastaran Barin, Hayri E. Balcioglu, Iris de Heer, Maurice de Wit, Martine L. M. Lamfers, Martin E. van Royen, Pim J. French, and Angelo Accardo**

A major obstacle in glioma research is the lack of in vitro models that can retain cellular features of glioma cells in vivo. To overcome this limitation, a 3D-engineered scaffold, fabricated by two-photon polymerization, is developed as a cell culture model system to study patient-derived glioma cells. Scanning electron microscopy, (live cell) confocal microscopy, and immunohistochemistry are employed to assess the 3D model with respect to scaffold colonization, cellular morphology, and epidermal growth factor receptor localization. Both glioma patient-derived cells and established cell lines successfully colonize the scaffolds. Compared to conventional 2D cell cultures, the 3D-engineered scaffolds more closely resemble in vivo glioma cellular features and allow better monitoring of individual cells, cellular protrusions, and intracellular trafficking. Furthermore, less random cell motility and increased stability of cellular networks is observed for cells cultured on the scaffolds. The 3D-engineered glioma scaffolds therefore represent a promising tool for studying brain cancer mechanobiology as well as for drug screening studies.

1. Introduction

Gliomas are the most common primary malignant tumors of the central nervous system with poor patient survival rates.[1] One contributor to the absence of novel effective therapies is the lack of cell culture models that can faithfully capture the native glioma phenotype[2,3] even despite increasing use of patient-derived cell cultures (that more accurately capture the cancer cell genotypes compared to standard cell lines).[4,5] Current in vitro models for example, rapidly lose high copy epidermal growth factor receptor (EGFR) amplification and have limited ability to monitor cells and (microtube-based) networks.[6,7] High copy EGFR amplification and microtube-based networks are two important features that are known to promote glioma progression.[8–11] To further study the role of microtubes in glioma progression and also the potential of EGFR-targeting treatments in glioma, in-vitro cell culture models that can retain these features are needed.[10] Currently, in vitro cell culture research predominantly involves the use of 2D planar surfaces. Although these 2D surfaces are cheap, easy-to-use, and reproducible, they often do not mimic the 3D spatial configuration of cells in real tissues. Indeed, cells behave differently in 3D environments[12,13] and can have differences in terms of cellular morphology, formation of cell–cell junctions, cell proliferation, gene and protein expression levels, and even in responses to treatments.[14–17] 3D tumor spheroids, which are generally employed for glioma research, can overcome these limitations by better mimicking tissue-like features. However, they are difficult to monitor especially when analyzing subcellular structures like microtubes.[6,14,16]

N. Barin, A. Accardo
Department of Precision and Microsystems Engineering
Delft University of Technology
Mekelweg 2, Delft 2628 CD, The Netherlands
E-mail: a.accardo@tudelft.nl

N. Barin, I. de Heer, M. de Wit, P. J. French
Department of Neurology
Erasmus MC Cancer Institute
University Medical Center
Doctor Molewaterplein 40, Rotterdam 3015 GD, The Netherlands
E-mail: p.french@erasmusmc.nl

The ORCID identification number(s) for the author(s) of this article can be found under https://doi.org/10.1002/smll.202204485.

DOI: 10.1002/smll.202204485

H. E. Balcioglu
Department of Medical Oncology
Erasmus MC Cancer Institute
University Medical Center
Doctor Molewaterplein 40, Rotterdam 3015 GD, The Netherlands

M. L. M. Lamfers
Department of Neurosurgery
Erasmus MC Cancer Institute
University Medical Center
Doctor Molewaterplein 40, Rotterdam 3015 GD, The Netherlands

M. E. van Royen
Department of Pathology
Erasmus MC Cancer Institute
University Medical Center
Doctor Molewaterplein 40, Rotterdam 3015 GD, The Netherlands

With technological advances, 3D cell culturing (growing cells in three dimensions) on structures created by micro- and nanofabrication has become an appealing alternative.[18–20] The most accurate additive manufacturing processes for the creation of cell scaffolds are two-photon polymerization (2PP) and stereolithography.[18,21,22] 2PP is a relatively recent light-assisted direct-writing fabrication technique based on the nonlinear two-photon absorption of near-infrared photons from a femtosecond pulsed laser source. Using this technique, infrared femtosecond laser pulses are focused onto an organic prepolymer material that is absorptive in the UV radiation range but nonabsorptive in the infrared one.[20,23] This mechanism is tuned to photopolymerize the exposed material in extremely confined volumes called voxels.[23] The advantages of the 2PP technique include: high resolution (up to 100 nm), high reproducibility, precise control of intricate structural features, and freedom in architecture design.[20,24,25] Importantly, the recent development of a biocompatible and low-autofluorescent methacrylate photosensitive polymer (IP-Visio) for 2PP has facilitated the use of this approach for life science applications.[23,26,27]

Here, we have studied patient-derived glioma cells cultured on biomimetic 3D-engineered IP-Visio microscaffolds, fabricated by the 2PP technique, and compared them to standard 2D control models. Our results show that a standard glioma cell line (U-87) as well as four patient-derived glioma cultures can efficiently adhere and colonize the structures. Compared to 2D models, our 3D-engineered glioma microenvironment more closely resembled in vivo glioma cellular features including nucleus size, and protrusion width. A major advantage of our model system is that it enables more accurate detection of individual cells, their protrusions, and intracellular trafficking. Furthermore, real-time microscopy also enabled the assessment of cell mobility and demonstrated reduced speed of cells and increased stability of cellular networks in 3D versus 2D. The developed 3D-engineered scaffold therefore provides a new suitable model to study glioma cells with advantages over the traditional 2D models.

2. Results and Discussion

2.1. Design and Fabrication of the 3D-Engineered Scaffolds Inspired by Microvessel Geometries

The design of the 3D scaffolds (**Figure 1**a) was inspired by the features of blood vessels present in the in vivo glioma environment as it is known how glioma cells migrate, proliferate, and cluster especially at the vascular branch points.[6,28] A porous design was selected to allow cell migration within the structures and to facilitate the diffusion of nutrients. The pore size was chosen to be larger than the cell nuclei to allow for cell invasion but small enough to allow for cellular network formation.[29] To avoid shadowing which would hamper imaging of the bottom and middle layers of the scaffolds during confocal microscopy, highly dense structures were not considered.

The base element of the scaffolds consisted of rods connected as cubic unit cells with one additional interconnecting diagonal rod (Figure 1b). Cylindrical rods were chosen as the building blocks of the unit cells to resemble the circular cross-section of the blood vessels. Diagonal rods were added to provide angles in the structure that resemble those observed in blood vessels.[6,28] Each scaffold consisted of multiple unit cells arranged to form a pyramid. The scaffolds featured a rod size of 10 µm and a pore size of 50 µm × 50 µm. The overall dimension of each scaffold was 370 µm × 370 µm × 190 µm. For some experiments, an alternative scaffold was used with the same unit cells but with an inverted unit cell arrangement that resulted in the presence of a cavity inside the scaffold to study the span of cellular protrusions (Figure S1a,b, Supporting Information). The scaffolds were fabricated by 2PP following the routine procedure of the 2PP fabrication methodology, which is described step by step in the Experimental Section. To obtain accurate scaffold geometries and overcome technical issues, we optimized several manufacturing process steps, which are described hereafter.

DeScribe software (Nanoscribe proprietary software to define printing parameters such as laser power, writing speed, hatching/slicing and to simulate the 2PP fabrication steps) considers surfaces with gaps or sharp edges as defective and attempts to repair them,[30] which led to undesirable filled pores (Figure S2a, Supporting Information). We found that pore filling could be prevented via rounding the corners in our design. In addition, as the voxel size is larger along the *Z* direction than the *X* and *Y* directions (where *Z* is the direction of the laser beam), pores along the *Z*-axis were clogged in the fabricated scaffolds (Figure S2b, Supporting Information). To prevent this, we changed the cross-section of the top rods of the unit cells from circular to oval, making the circular structures narrower along the *Z* direction (Figure S2c, Supporting Information). An additional complication was the occasional delamination of the scaffolds after exposure to cell culture media (Figure S3a, Supporting Information). To address this issue and to increase the stability of the 3D structures (Figure S3b, Supporting Information), the cross-sections of the rods connected to the substrate were changed to a flattened bottom (semicircle on a pedestal, Figure S3c, Supporting Information). For 2D structures, pedestals of 500 µm × 500 µm × 10 µm were chosen. Four pedestals were connected to each other by their corners (Figure S1c, Supporting Information) to prevent delamination.

The most important printing parameters that needed tuning were the scan speed, laser power, hatching, and slicing. Hatching is the spacing distance between voxels in the *X*–*Y* plane, while slicing is the spacing distance between voxels along the *Z* direction.[31] Decreasing slicing and hatching values increased the shape accuracy and steadiness of the structures but noticeably increased the printing time. For the final 3D scaffolds, 10 000 µm s^{-1} scan speed and 60% laser power (100% laser power is 50 mW) were chosen to provide a suitable combination of precision and stability. A 50 000 µm s^{-1} scan speed and 80% laser power provided a suitable 2D pedestal quality. The slicing and hatching values for the scaffolds were both 0.5 µm. The corresponding values for the pedestals were 1 and 0.5 µm, respectively.

Both 3D scaffolds and 2D pedestals exceeded the addressable printing range of the galvanometric mirrors of the 2PP-printer setup (the galvanometric mirrors scan the laser beam laterally while vertical movements are carried out with piezoactuators). Therefore, the structures needed to be split into smaller unit

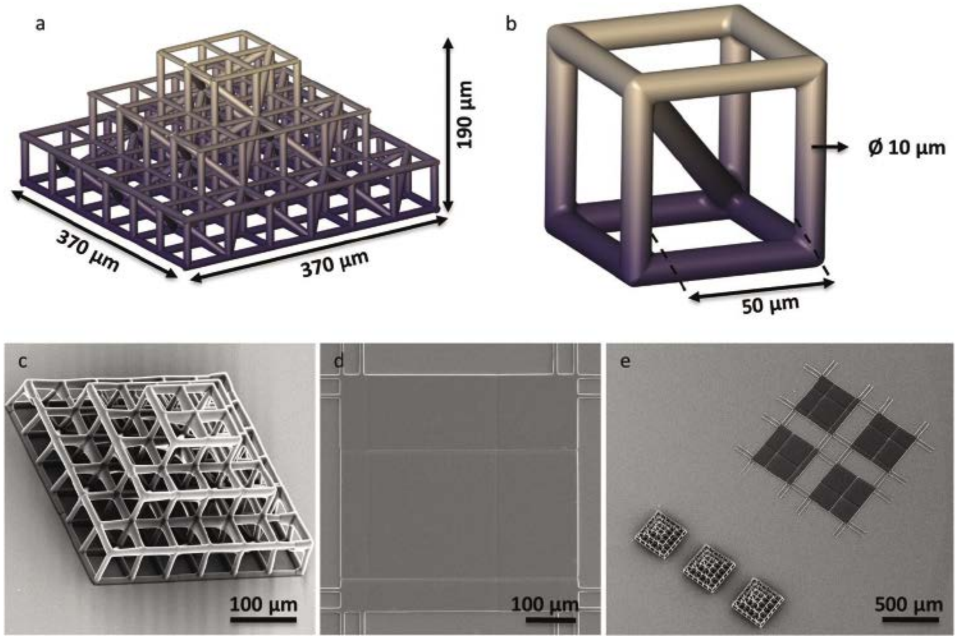

Figure 1. Design of the 3D and 2D microenvironments. a) Design of the 3D-engineered scaffolds. b) Scaffold unit. c) SEM micrograph of the fabricated 3D-engineered scaffold. d) SEM micrograph of the fabricated 2D pedestal. e) Three scaffolds and four pedestals constituting one "sample set".

blocks (block splitting) and these blocks needed to be bonded together during the printing process (stitching). Block splitting was avoided at locations where it led to the creation of overhanging rods (Movies S1 and S2, Supporting Information). In order to increase the adhesion between blocks, an angled interface between blocks was selected instead of an orthogonal interface (Figure S4, Supporting Information). The acceptable angle value was found by printing scaffolds and pedestals with varying angles. The suitable stitching angles for 2D pedestals and 3D scaffolds were found to be 45° and 15°, respectively. The stitched blocks featured some overlap in order to avoid disjoined blocks caused by unpolymerized resin. The suitable overlap between stitched blocks in the *X*, *Y*, and *Z* directions were found to be 3, 3, and 2 µm for the 2D pedestals, and 1, 1, and 2 µm for the 3D scaffolds, respectively. Representative scanning electron microscopy (SEM) images of the final structures are shown in Figure 1c,d. Three replicas of the scaffold as well as four replicas of 2D flat pedestals were printed on each substrate creating one sample set (Figure 1e). The fabrication time for each sample set was 95 min. The structures were then coated with a Cultrex extracellular matrix coating (see Experimental Section).

Our approach aims at resembling the geometrical features of the brain microvessels, however one of its limitations is the relatively high stiffness of the scaffolds' material (≈1 GPa) compared to that of the brain (ranging from 0.1 to 1 kPa).[32] Developing materials for 2PP with lower Young's modulus can be further investigated to overcome current challenges. The challenges of fabricating complex geometries with soft materials (such as hydrogels) include higher tendency to collapse, difficulties handling the load of cells, and lower feature resolution.[33] An alternative option worth exploring is using structures in which cells perceive a low effective shear modulus[34] or encapsulating cells (bioprinting) whithin 2PP-manufactured scaffolds. Overcoming the cytotoxic effects of photo initiators has been one of the major challenges of 2PP bioprinting. Although reports of such cultures have been published, these materials are not yet commercially available.[35,36] In addition to mechanical cues, cells respond also to topographical cues,[13,37] therefore, the effects of different geometrical features (e.g. pore size, surface nanotopography, rod size, curvature) on the behavior and morphology of glioma cell can be investigated.[38]

2.2. Colonization of the 3D Scaffolds by Patient-Derived Glioma Cells

To test the suitability of the fabricated structures for glioma cell culture experiments, we first cultured a standard cell line (U-87) on the 3D scaffolds and the 2D pedestals. As these cultures readily colonized the scaffolds (Figure S5, Supporting Information), we subsequently cultured four patient-derived glioma cell cultures (GS-580, GS-827, GS-830, and GS-921) on the structures. All four patient-derived cultures were able to successfully colonize the scaffolds and the 2D pedestals as shown by confocal imaging (**Figure 2**a–c; Movie S3, Supporting Information). SEM micrographs showed that cells formed long protrusions and clearly invaded the inner regions of the scaffolds (Figure 2d–f). These protrusions were frequently present between the building blocks of the scaffolds (Figure 2e). Interestingly, some of these interconnecting protrusions were suspended within the 3D structure (Figure 2e,f). Such suspended protrusions were not observed in the alternative 3D design (Figure S1a, Supporting Information) with gaps exceeding 100 µm (Figure S6, Supporting Information).

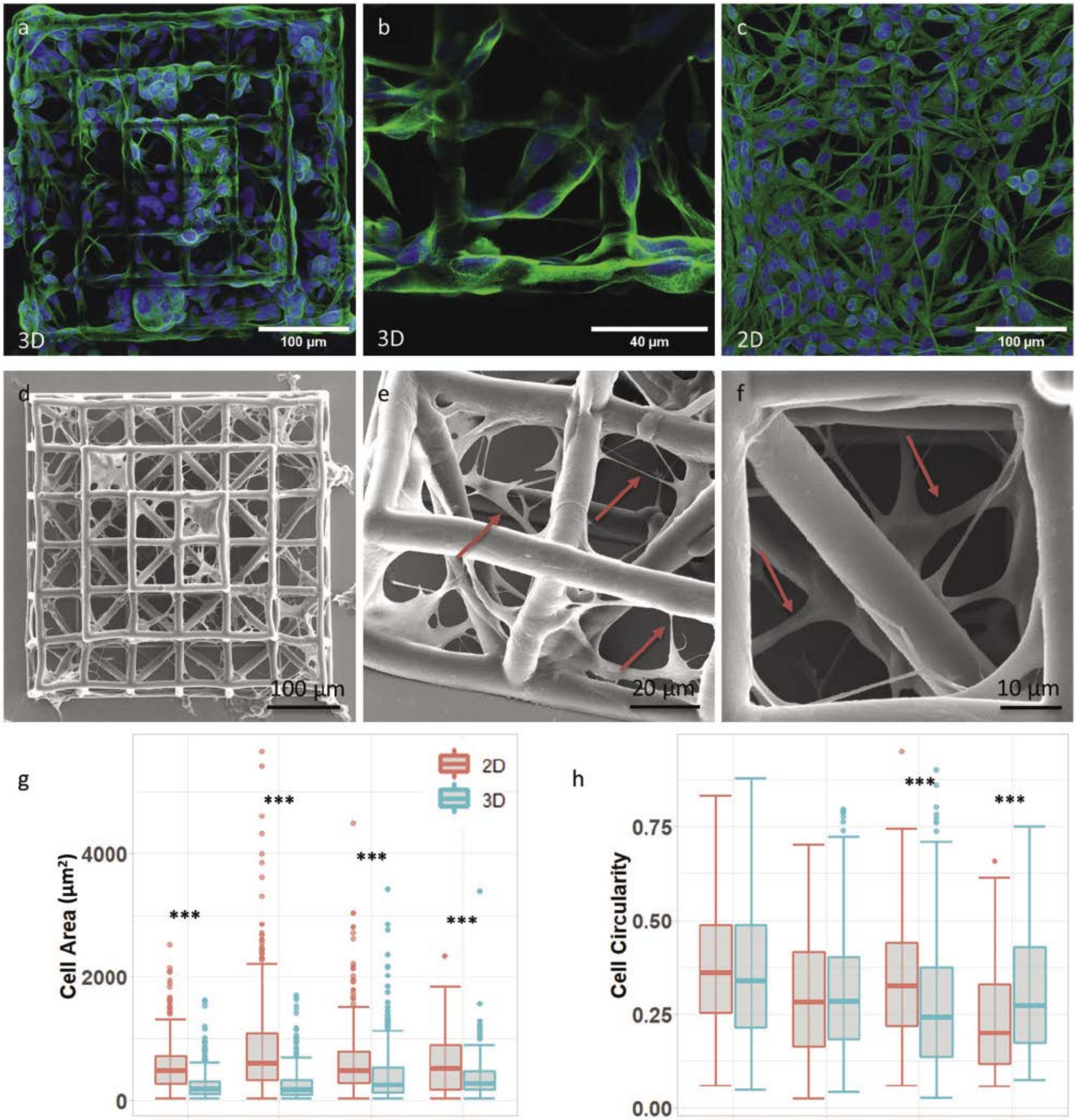

Figure 2. Characterization of patient-derived glioma cells cultured on 2D pedestals and 3D scaffolds. Confocal images of GS-830 patient-derived glioma cells on a,b) 3D scaffolds and c) 2D pedestals (Blue: nuclei; Green: tubulin). d) SEM image of GS-830 cells cultured on the 3D scaffolds. e,f) Zoomed in SEM image of the GS-830 cells on the 3D scaffolds showing that the cells have reached the inner units. Red arrows denote examples of glioma cell protrusions. g,h) Boxplots comparing morphological differences between cells cultured in 2D and 3D. g) Cell area and h) cell circularity. Boxplots display the median, interquartile range (IQR) with the whiskers drawn at 1.5IQR. Statistical significance is indicated by $p < 0.001$(***). Sample size (n) for GS580, GS287, GS830, and U87 are 683, 937, 890, and 294 respectively. Two independent experimental replicates (one replicate for U-87 experiments) were included.

2.3. Cytoskeletal and Nuclear Morphological Differences between Glioma Cells Cultured on 3D Scaffolds and 2D Pedestals

To determine whether the scaffolds provided a suitable model system for glioma research, we then compared morphological features of GS-830, GS-827, GS-580, and U-87 cells cultured on 3D versus 2D structures. Cellular morphology was studied in two independent experimental replicates (one replicate for U-87 experiments) using confocal fluorescent images of the cells stained for nuclei and tubulin.

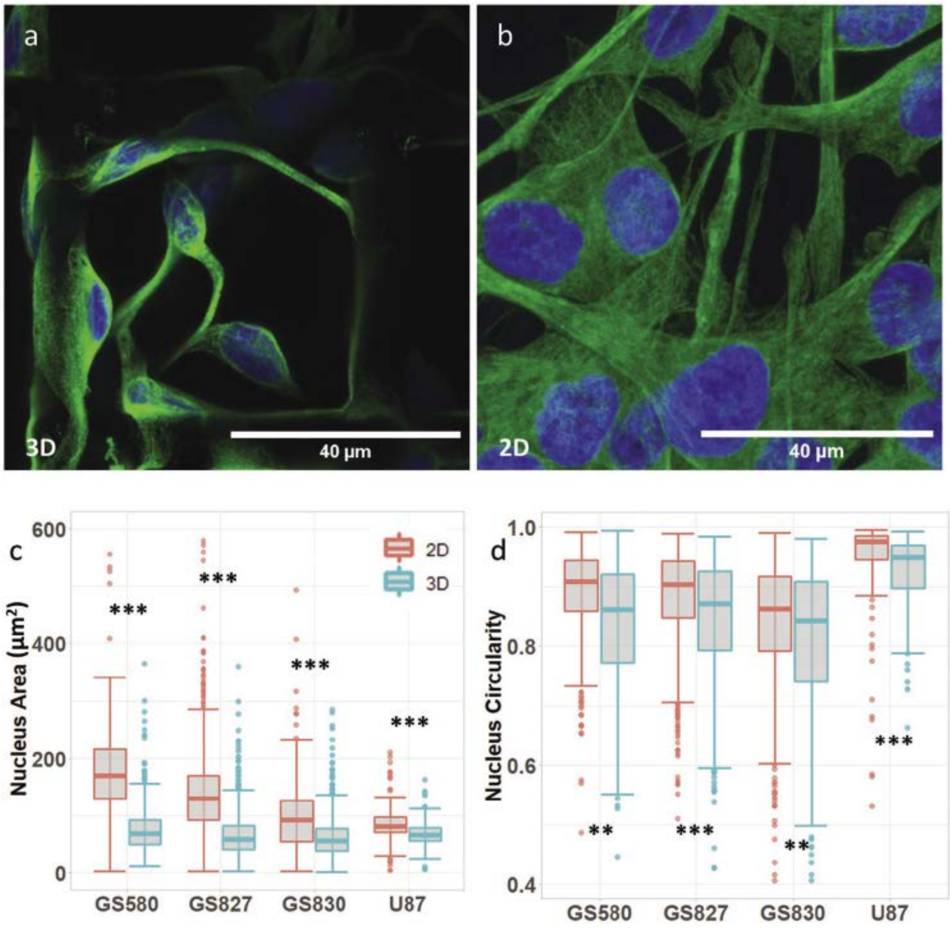

Figure 3. Characterization of patient-derived glioma cell nuclei cultured on 2D pedestals and 3D scaffolds. Confocal images of GS-830 patient-derived glioma cells cultured on a) 3D scaffolds and b) 2D pedestals (Blue: nuclei; Green: tubulin). c,d) Boxplots comparing morphology differences between cells cultured in 2D and 3D structures. c) Nuclear area and d) nuclear circularity. Boxplots display the median, IQR with the whiskers drawn at 1.5IQR. Statistical significance is indicated by $p < 0.01$ (**) and $p < 0.001$(***). Sample size (*n*) for GS580, GS287, GS830, and U87 are 970, 2059, 1395, and 286, respectively. Two independent experimental replicates (one replicate for U-87 experiments) were included.

Interestingly, we found that cells grown on 2D pedestals had larger areas compared to those on the 3D scaffolds (Figure 2g). We did not observe consistent differences between 2D pedestals and 3D substrates in terms of cellular circularity (Figure 2h). In addition to cellular morphology, we also studied nuclear morphology. For all cell cultures, nucleus area of cells cultured on 2D pedestals were larger compared to those on the 3D scaffolds and were on average more circular (**Figure 3**a–d). Although the larger cell and nuclear areas on 2D pedestals most likely pointed to the flatter morphology of cells on 2D surfaces, such morphological differences, especially those related to the nuclei, can be important for replicating the behavior of glioma cells in vivo.[39,40]

The nucleus, through cytoskeleton and cell–matrix adhesions, is physically coupled to the extracellular matrix. In this way, forces can be transmitted from the cytoskeleton to the nucleus, and the external mechanical cues on the cell can affect the shape of the nuclear envelope.[41] This can affect the nuclear function by altering: chromatin condensation and organization (thereby directing cells toward differential gene expression), translocation of transcriptional regulators, accessibility of histone modifying enzymes to the chromatin and their distribution in the nucleoplasm, and nuclous membrane permeability and rupture.[41–47] Furthermore, nuclei morphology is frequently altered in cancer cells and many cancers can even be graded based on the nucleus size.[48] Particularly, for high-grade glioma tumor cells, previous studies reported how nuclear size and shape are significantly related to the survival time of patients.[39,49]

To compare our results to in vivo values, we studied the morphology of nuclei in six glioma tumor samples. Three grade 3 and three grade 4 formalin-fixed paraffin-embedded (FFPE) glioma tumor tissue sections were analyzed for nuclei area and circularity. The measured average nuclear area on tissue sections (55.72 ± 27.79 µm^2) was nearly identical to previously reported (i.e., 55.22 ± 13.48 µm^2)[49] and was close to the value observed for tumor cells cultured on 3D scaffolds (67.51 ± 38.19 µm^2, *p*-value < 0.0001). Nucleus areas on 3D scaffolds and on tissue sections were both smaller than the nucleus area on 2D pedestals (130.21 ± 75.72 µm^2, both *p*-values < 0.0001). However, nuclei on our 3D scaffolds on average were less circular (0.84 ± 0.11) compared to those on 2D pedestals (0.88 ± 0.09, *p*-value < 0.0001) and tissue sections

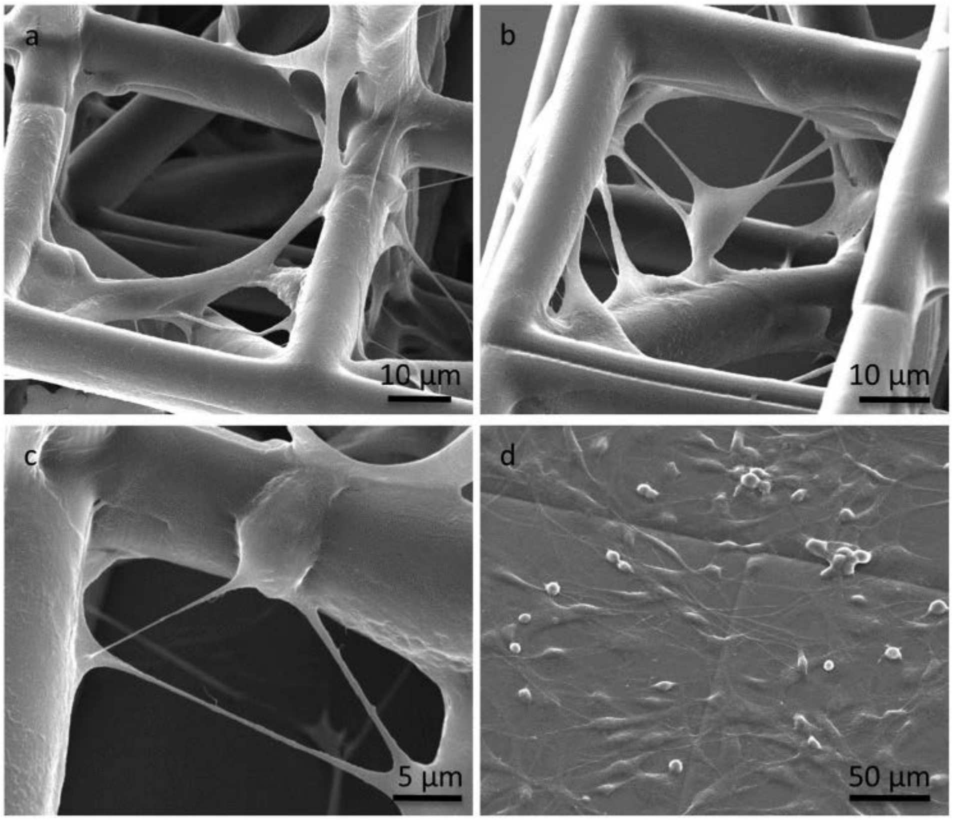

Figure 4. SEM images of patient derived glioma cells cultured on 2D pedestals and 3D scaffolds showing microtube-like protrusions. a) Cells cultured on the 3D scaffold showing several tube-like protrusions with widths in the b) microscale and c) in the nanoscale. d) Cell protrusions on the 2D pedestals are harder to detect.

(0.89 ± 0.07, p-value < 0.0001). Yet, it should be noted that tissue sectioning likely leads to an underestimation of nucleus area and overestimation of nucleus roundness compared to Z projection of stacks of images as used for our scaffold and pedestal analysis. Moreover, the increased cell circularity for tumor cells on tissue may be related to their more compact microenvironment.

2.4. Microtube Morphological Discrepancies between 3D Scaffolds and 2D Pedestals

To further examine the relevance of our culture model, we characterized the presence of microtube like protrusions. Microtubes are long and thin cellular protrusions that allow formation of functional cellular networks.[8] These protrusions enable aggressive tumor invasion and make gliomas more therapy resistant.[6,8] SEM micrographs showed intercellular tube-like protrusions on both 3D scaffolds and 2D pedestals (**Figure** 4a–d). Protrusions longer than 50 µm were observed on the 3D scaffolds (Figure 4a), with multiple protrusions departing from a single cell (Figure 4b). These protrusions were easier to observe on 3D scaffolds due to their suspended nature. In particular, nanotubes, tube-like protrusions at the nanoscale (<1 µm wide), were observed only on 3D scaffolds (Figure 4c) and not on 2D pedestals (Figure 4d).

We then further studied these protrusions with immunostaining (**Figure** 5a–d). Confocal fluorescent images with tubulin and nucleus staining confirmed the presence of tube-like protrusions (Figure 5a,b). These protrusions were observed on both 2D pedestals and 3D scaffolds for all patient-derived cultures and U-87 standard cell line (additional images in Figure S7, Supporting Information). In order to characterize the nature of microtubes, we stained GS-830 cells for GAP-43, which is a protein reported as a molecular driver for microtubes and previously employed to identify these protrusions.[50,51] Cells cultured on 3D scaffolds and 2D pedestals expressed GAP-43 in membranes and protrusions (Figure 5c,d). GAP-43 did not seem to exclusively stain the tube-like protrusions in our experiments.[6,50] Instead, it was detected throughout the cell membranes and was more prominent at the end-cone of protrusions, consistent with its function in neurons.[9,50,52]

We then employed the confocal images to quantify the size of these protrusions (Figure 5e,f). Overall the geometrical characteristics of the observed protrusions matched that of microtubes or nanotubes.[51] In two of the cell cultures, the recorded average length of the microtube-like protrusions was higher in 2D pedestals versus the 3D scaffolds (Figure 5e). All cultures had average protrusion lengths in the range of 38 to 60 µm. GS-827 showed longer protrusion lengths up to 241 µm in 2D pedestals and 179 µm in 3D scaffolds. However, it should

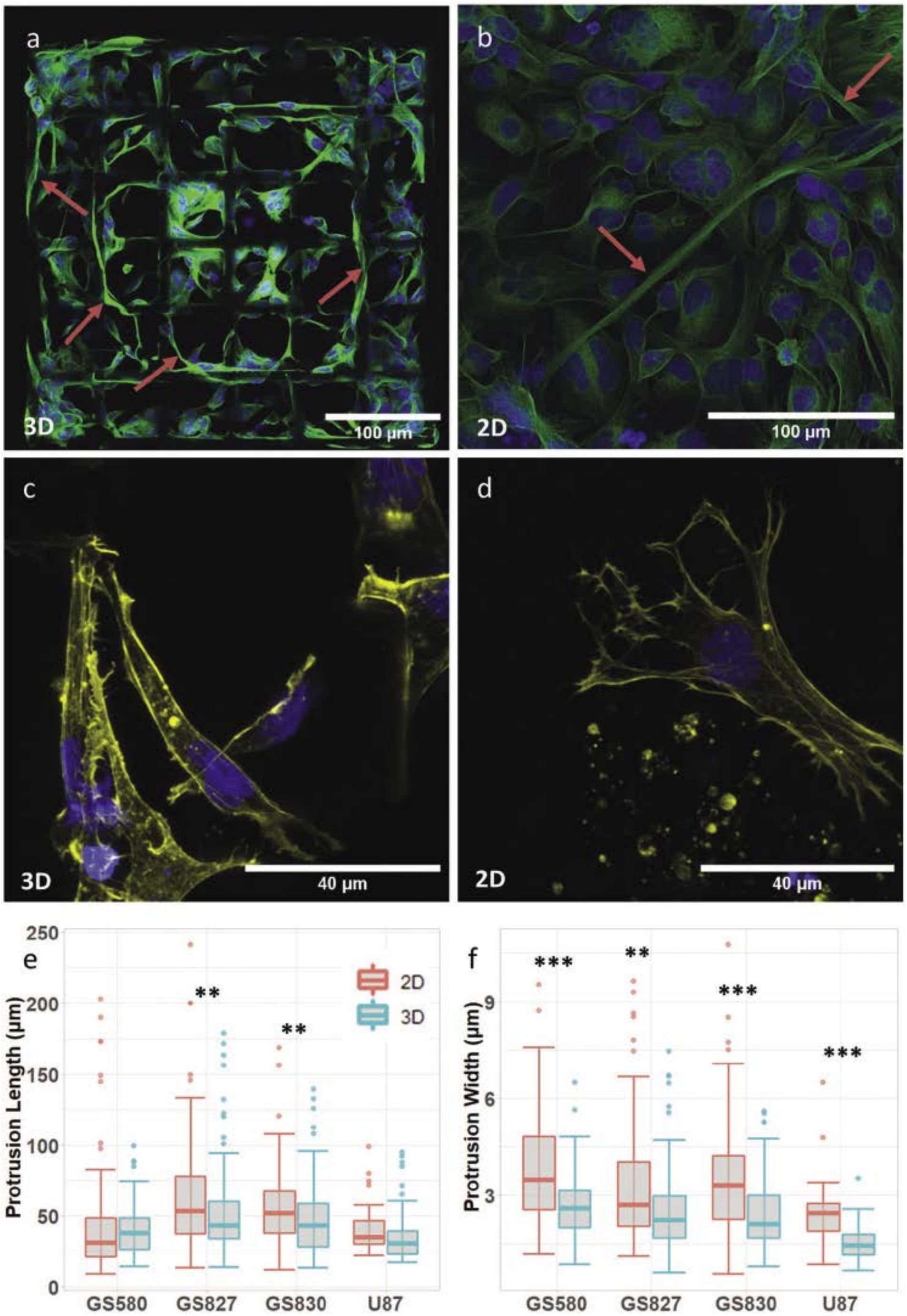

Figure 5. Characterization of microtube-like protrusions in patient derived glioma cells cultured on 2D pedestals and 3D scaffolds. a–d) Confocal images of patient-derived glioma cells on 2D pedestals and 3D scaffolds (Blue: nuclei; Green: tubulin; Yellow: Gap-43). Microtube-like protrusions were observed on GS-827 cells cultured on (a) the 3D scaffolds and (b) the 2D pedestals. Gap-43 staining was observed on cell membrane for GS-830 cells cultured on (c) the 3D scaffolds and (d) the 2D pedestals. e,f) Boxplots comparing microtube morphology. e) Protrusion length, and (f) protrusion width. Boxplots display the median, IQR with the whiskers drawn at 1.5IQR. Statistical significance is indicated by $p < 0.01$ (**) and $p < 0.001$(***). Sample size (n) for protrusion length in GS580, GS287, GS830, and U87 are 191, 257, 247, and 106, respectively. Sample size for protrusion width in GS580, GS287, GS830, and U87 are 184, 214, 336, and 68 respectively. Two independent experimental replicates (one replicate for U-87 experiments) were included.

be noted that the lengths of protrusions in 3D scaffolds were likely underestimated because the measurements were based on Z projections.

The width of protrusions showed differences between cells cultured on 2D pedestals versus 3D scaffolds for all cultures with significantly thinner protrusions observed for 3D scaffolds

(Figure 5f). The larger width of these protrusions in 2D pedestals may point to the flatter morphology of cells in 2D settings (similar to the observations on the cells and nuclei). Interestingly, the average measured protrusion width of 2.4 ± 1.1 µm in the 3D scaffolds was closer to the reported *in-vivo* value of 1.7 µm[51] and smaller than the 2D average value of 3.4 ± 1.7 µm. The morphology of the tube-like protrusions observed in 3D scaffolds therefore seems to better mimic what is described as microtubes in vivo[6,50] compared to those formed in 2D pedestals or even in other 3D culture models such as tumor organoids.[53] Moreover, these protrusions seem to be more abundant in our 3D scaffolds compared to the glioma spheroids[6] and glioma organoids.[53] It is also possible that these protrusions are simply easier to visualize in our model.

To evaluate the persistence of the cellular network and the possibility of tracking cells on the scaffolds, we employed live confocal imaging over a period of 16.5 h (**Figure 6**a,b). Migration of GS-830 cells in the *X*–*Y* plane was tracked (Figure 6c) and compared between cells growing on 2D surfaces and 3D scaffolds (Figure 6d). On average, the speed of cells on 2D surfaces (4.2 ± 2.7 µm h^{-1}) was double the speed of cells on 3D scaffolds (2.1 ± 1.8 µm h^{-1}) (*p*-value < 0.0001). The speed of cells in the *Z* direction is not considered in these measurements, but manual tracking of 31 cells in 3D shows a Z speed of 1.1 ± 0.6 µm h^{-1}, which does not compensate for the difference between 2D and 3D. Even theoretically, with *Z* speeds similar to those observed in *X* and *Y* (1.5 µm h^{-1}), cells grown in 3D (2.6 µm h^{-1}) would still migrate slower than cells in 2D.

Cancer progression is affected by the cellular microenvironment.[2,13,54] For instance, glioma cells interact with the vascular niche and tend to move along the blood tracks and the white matter tracks.[28,55–57] Multiple studies have reported on the differences of cell migration between 2D and 3D environments.[58–60] GS-830 cells in our 3D model moved along the scaffold rods (Movie S4, Supporting Information) and occasionally established protrusions between the rods (Figure S8, Movie S5, Supporting Information). This cell migration on the scaffolds was reminiscent of cells on the brain tissue,[57] whereas

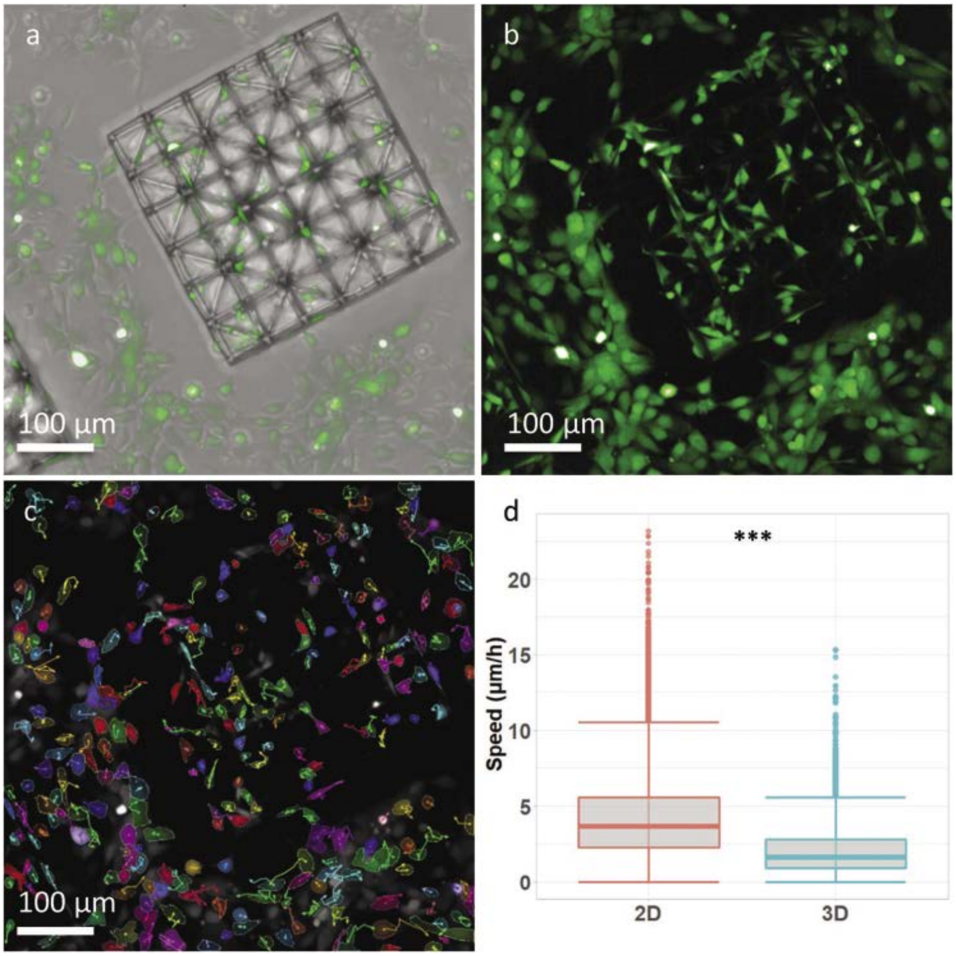

Figure 6. Tracking the movement of patient-derived glioma cells on 3D scaffolds and 2D surfaces. a,b) Representative frame of the live experiment showing GS-830 glioma cells on 3D scaffolds and on the surrounding 2D surface (Green: glioma cells stained with CellTracker Green). a) Brightfield and fluorescent maximum intensity projection image showing glioma cells on 3D scaffolds. (b) Fluorescent maximum intensity projection image of the cells. c) Movements of individual cells tracked on the 3D scaffolds and the surrounding 2D surface. d) Boxplot comparing *X*–*Y* speed of cells cultured on 2D and 3D structures. Boxplots display the median, IQR with the whiskers drawn at 1.5IQR. Statistical significance is indicated by $p < 0.001$(***). Sample size (*n*) is 47 447.

the movement of the cells on 2D surfaces appeared to be more random (Movie S6, Supporting Information) and this difference was consistent with previous reports.[59]

Strikingly however, individual cellular protrusions were more stable in 3D, where those in 2D had a shorter half-life (12.8 ± 3.9 vs 7.9 ± 4.6 hours, *p*-value = 0.006) (Figure S9, Supporting Information), suggesting a more stable network of cells grown on 3D scaffolds. Furthermore, compared to 2D surfaces, within the 3D scaffolds we observed slower cell migration and protrusions that last longer, therefore the presence of a more stable cellular network in the 3D scaffolds.

2.5. Differential Distribution of EGFR on 3D Scaffolds and 2D Pedestals

EGFR is one of the most commonly altered receptors in gliomas.[11,61,62] Therefore, we next assessed the potential of the model in capturing the subcellular localization of EGFR. In the presence of the EGFR ligand, epidermal growth factor (EGF), EGFR was present in spots that were distributed throughout the cells but concentrated close to the nuclei on both scaffolds and pedestals (**Figure 7**a; Figure S10, Supporting Information). These spots were also detectable on long cellular protrusions in cells cultured on the 3D scaffolds (Figure 7b) but were hardly detectable on long protrusions in cells cultured on the 2D pedestals (Figure S10, Supporting Information). Two independent EGFR antibodies (ab76153 Abcam and M3563 DAKO), stained on the same sample, showed a near identical staining pattern (Figure 7c,d). When EGF was absent from the culture media (for duration of three days), only a few EGFR spots remained and general plasma membrane staining was observed, in line with the ligand-induced internalization of the receptor (Figure 7e,f).

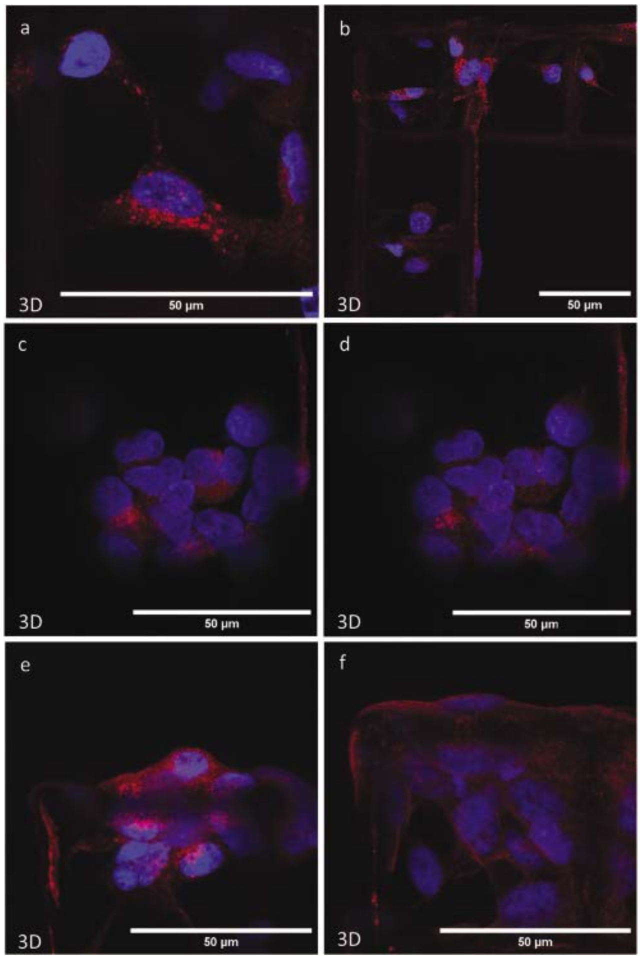

Figure 7. Characterization of EGFR expression on GS-830 cells cultured on 3D scaffolds. a) Zoomed in confocal image showing EGFR spots close to the nuclei on a 3D scaffold. b) EGFR spots observed in cellular protrusions. c,d) GS-830 cells stained using two different EGFR antibodies, which both give similar signals. c) Anti-EGFR Abcam ab76153, d) anti-EGFR DAKO M3563. e,f) Fewer EGFR spots are observed in the absence of EGF. (e) Cells cultured in the presence of EGF. (f) Cells cultured in the absence of EGF (Blue: nuclei; Red: EGFR).

To evaluate our model's ability in drug screening, we then tested two known EGFR tyrosine kinase inhibitors (TKIs), Erlotinib, and Dacomitinib. In this experiment, GS-830 cells were seeded on the 2D pedestals and the 3D scaffolds under four conditions: i) with EGF in the culture media (+EGF, control experiment), ii) without EGF in the culture media (−EGF), iii) with Erlotinib added to the +EGF culture media for 2 h (+Erlotinib), and iv) with Dacomitinib added to the +EGF culture media for 2 h (+Dacomitinib) (**Figure 8**). Interestingly, even in the presence of Erlotinib or Dacomitinib, some (perinuclear) spots were present in cells. Although there were fewer internalized EGFR spots, they did not completely disappear (**Figure 9**a). The perinuclear EGFR spots remained even when the exposure time to Dacomitinib was increased from 2 to 24 h (Figure S11, Supporting Information). For all conditions except for −EGF, the Kolmogorov–Smirnov test showed that the distance of EGFR spots to the cell nuclei for 2D versus 3D cultures came from separate distributions (+EGF: *p*-value < 0.0001, −EGF: *p*-value < 0.0001, +Erlotinib: *p*-value < 0.0001, +Dacomitinib: *p*-value < 0.0001). The Kruskal–Wallis test showed that the difference of medians of this distance between 2D and 3D structures were statistically significant in all conditions except for +EGF condition (Figure 9b). Although EGFR spot localizations on 2D and 3D structures were similar, in most conditions, spots were larger and had lower signal intensity in 2D experiments (Figure 9c,d). Additionally, spot detection in 3D was superior due to higher signal-to-noise ratio, possibly because of the autofluorescence signal of the material in 2D. Interestingly, in the +EGF condition, a negative correlation (ρ = −0.13, *p*-value < 0.0001) was observed between the distances of EGFR spots to the nuclei and the brightness of the spots (Figure 9e). Generally, brighter spots were not detected far from the nuclei (Figure 9e). Same negative correlation was observed, but with lower correlation coefficient, in the presence of Erlotinib (ρ = −0.10, *p*-value < 0.0001) or Dacomitinib (ρ = −0.05, *p*-value = 0.01), but was not significant for the −EGF condition (ρ = −0.04, *p*-value = 0.25) (Figure S12, Supporting Information).

The EGFR spots observed in our experiments (+EGF conditions) are consistent with endocytosed EGFR proteins.[63–68] Endocytosed EGFR can either be recycled back to the membrane (either fast or slow recycling) or can be directed toward degradation.[69] Our data suggests that at least part of the

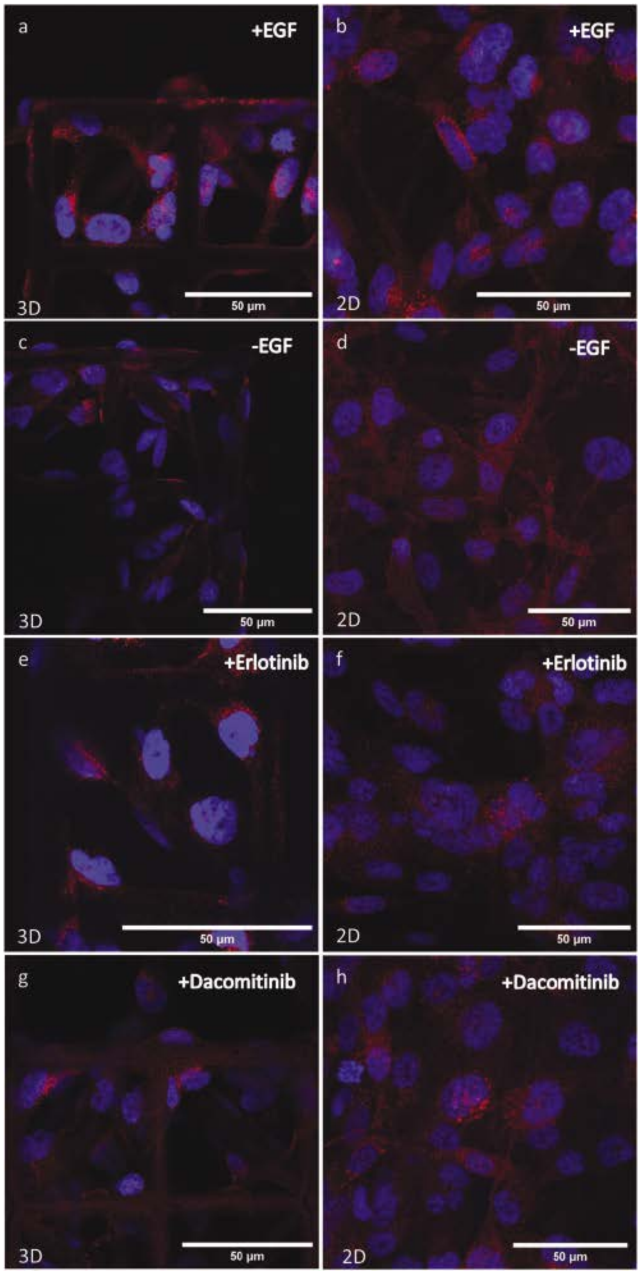

Figure 8. Representative confocal images of GS-830 cells with and without EGF/EGFR inhibitors. Exposure time to inhibitors was 2 h. a) Image of the cells on the 3D scaffold and in presence of EGF. b) Image of the cells on the 2D pedestal and in presence of EGF. c) Image of the cells on the 3D scaffold without EGF. d) Image of the cells on the 2D pedestal without EGF. e) Image of the cells on the 3D scaffold with EGF and Erlotinib. f) Image of the cells on the 2D pedestal with EGF and Erlotinib. g) Image of the cells on the 3D scaffold with EGF and Dacomitinib. h) Image of the cells on the 2D pedestal with EGF and Dacomitinib (Blue: nuclei; Red: EGFR).

EGFR is directed to the perinuclear endosomal sorting compartment[70] and this localization is not entirely inhibited by TKIs. Although the function of the subcellular localization is unknown, several reports have suggested the importance of EGFR localization near the nuclei in patient outcome and tumor progression.[63,64,71,72] The 3D-engineered scaffolds offer a platform in which the EGFR localization can be tracked and analyzed in vitro, in 3D and with high resolution. The use of these scaffolds for live imaging of the EGFR spots and tracking their transfer to the nuclear area may add to our understanding of their functions and of the resistance to EGFR inhibition in patients.[10,73–76]

3. Conclusions

In conclusion, we designed and engineered 3D-microscaffolds, fabricated by the 2PP method, and showed that they can be used to successfully culture and analyze patient-derived glioma cells. The design of the biomimetic scaffolds is inspired by the geometry of microvessel architecture in the brain. These structures are reproducible and biocompatible, and the low-autofluorescence nature of the employed biomaterial enables an accurate detection of fluorescent markers. The scaffolds offer the opportunity to study patient-derived glioma cells with morphological features more similar to those observed in glioma tumor cells in vivo. A major advantage of our scaffold approach is that it enabled the study of (EGFR in) individual cells within a connected cellular network, whereas in conventional 2D cultures this is more error prone due to overlapping cells. These scaffolds could also be used to study nano- and microtube dynamics, cell networks, and cell migration strategies as they better represented the dimensionality of 3D tumor microenvironments, enable tracking of individual cells and provide more stable cell networks. Such features are much more difficult to study in conventional 2D "petri-dish" and 3D spheroid model systems. Therefore, the developed scaffolds offer new insights on glioma cell-to-cell and cell-to-environment interactions in three dimensions. In the future, our 3D-engineered culture model will be further improved by coculturing glioma cells with other nontumor cells, such as endothelial cells and immune cells, which are predicted to have roles in glioma prognosis.

4. Experimental Section

Scaffold Design and Fabrication: The 3D-engineered scaffolds and the 2D pedestals were fabricated with the 2PP method. The scaffolds and the pedestals were designed using a computer aided design (CAD) software, SolidWorks (Dassault Systèmes, France). A Standard Triangle Language file from the CAD software was then imported to the DeScribe software (Nanoscribe, Germany). The resulting General Writing Language file was imported to Nanowrite (printing software, Nanoscribe, Germany) directly from DeScribe.

For the fabrication, the Photonic Professional GT+ printer (Nanoscribe, Germany) was used in Dip-in Laser Lithography configuration with a 25× objective featuring 0.8 numerical aperture. IP-Visio (Nanoscribe, Germany), a methacrylate photosensitive polymer, was casted on indium-tin oxide (ITO)-coated glass substrates (dimensions of 25 mm × 25 mm × 0.7 mm, Nanoscribe, Germany).

Before printing, the ITO-coated substrates (resistance of 100 to 400 Ω) went through a few preparatory steps. First, the substrates were cleaned by acetone and ISO-Propanol (IPA). Then, the ITO-coated side was blow-dried with a nitrogen gun. Next, for further substrate activation, the ITO-coated side of the substrates was exposed to oxygen plasma for the duration of 10 min at 80 W power with 5 sccm oxygen flow rate and pressure of 0.12 bar. Then, the substrates were silanized

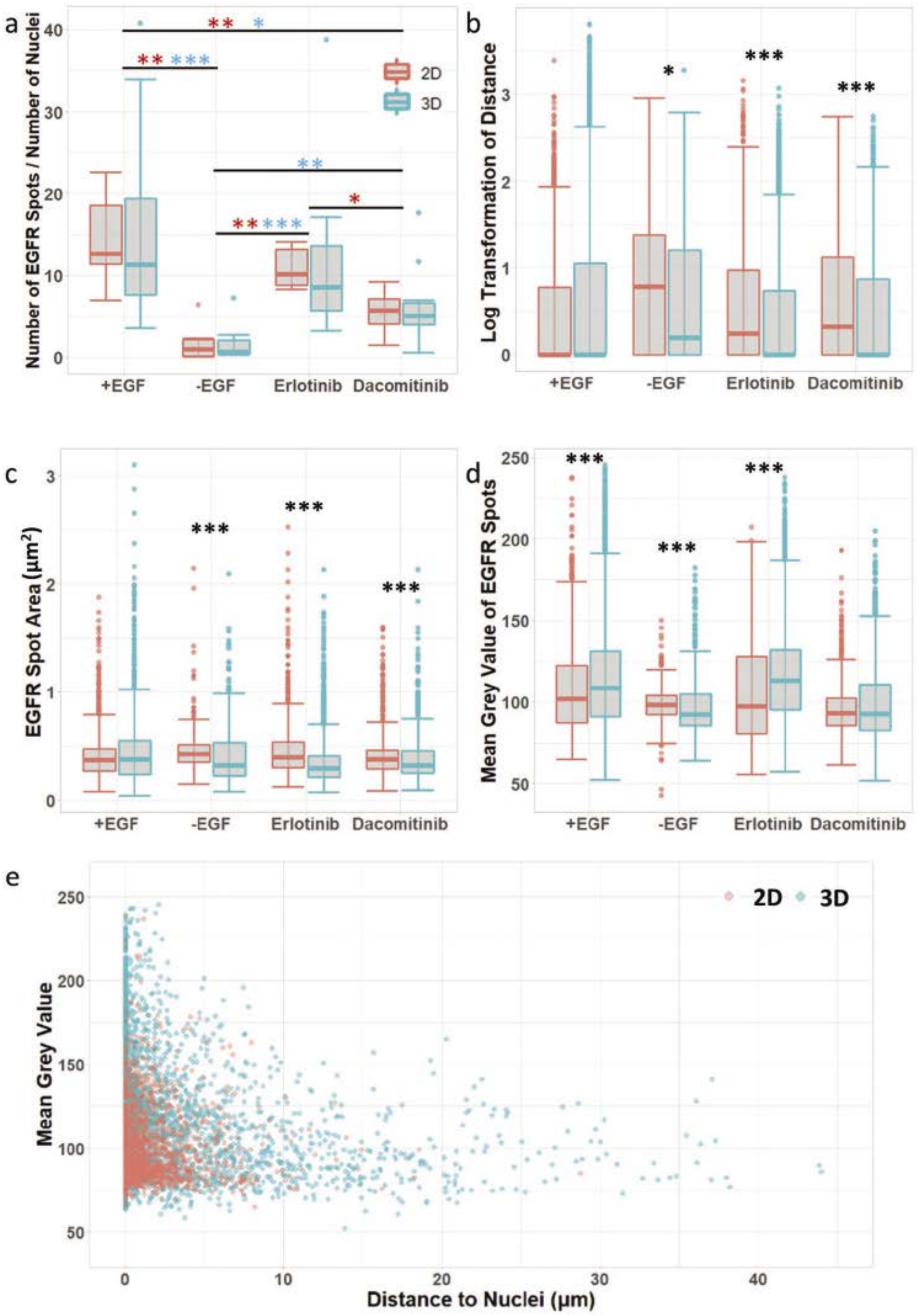

Figure 9. Characterization of EGFR spot localization on GS-830 cells cultured on 2D pedestals and 3D scaffolds. a) Boxplots of number of EGFR spots per number of nuclei in each image. Red asterisks show significance between conditions in 2D pedestals and blue asterisks show significance between conditions on 3D scaffolds. b) Boxplots of distances of EGFR spots to the nuclei in 2D and 3D conditions. Value of 0 for the distance means that in the *Z* projection of images, the spot was situated in the nucleus region. c) Boxplots of areas of EGFR spots. d) Boxplots of mean gray values of EGFR spots. The value shows the average signal intensity of a selected region. e) Dot plot of EGFR spot mean gray value versus EGFR spot distance to the nucleus in +EGF condition. Boxplots display the median, IQR with the whiskers drawn at 1.5IQR. Statistical significance is indicated by $p < 0.05$ (*), $p < 0.01$ (**), and $p < 0.001$(***). Sample size (n) for (a) for +EGF, −EGF, +Erlotinib, +Dacomitinib are 22, 15, 19, and 16, respectively. Sample size for (b–d) for +EGF, −EGF, +Erlotinib, and +Dacomitinib are 6979, 811, 5324, and 2639, respectively. Sample size for (e) is 6979. Two independent experimental replicates were included.

to make the substrate surface hydrophobic and enable a chemical bond between the polymerized 2PP resin and the substrate itself. The silanization solution consisted of ethanol and 3-(trimethoxysilyl) propyl methacrylate (#440159, Sigma-Aldrich, USA). The dipping time and the concentration of the solution were 1 h and 2% v/v 3-(trimethoxysilyl) propyl methacrylate in ethanol, respectively.[77] After silanization, the samples were rinsed first with acetone, then with water, and finally air-dried for ≈5 min. Immediately after drying, the resin was placed on the substrates and the samples were placed in the Nanoscribe printer for fabrication. Several printing and geometrical parameters were tested to obtain a suitable print quality (Figure S13, Supporting Information). The details of these parameters are presented in Section 2.1.

After fabrication, to remove the unpolymerized resin, samples were immersed in propylene glycol methyl ether acetate for 30 min. They were then immediately rinsed in IPA for 5 min. Later, samples were left in a fume hood to air-dry. To fit the samples in 6-well cell culture plates (used for culturing and immunofluorescence staining steps), the corners of the ITO-coated glass were scraped by creating diagonal lines with a diamond pen cutter. The corners were then broken off with tweezers. To fit the samples in 24-well cell culture plates (used for live cell confocal imaging), the ITO-coated glass was cut into 4 mm × 13 mm rectangles with an in-house femtosecond laser cutter.

The samples were visually inspected to be free from defects such as breakage, deformity, delamination, and geometrical flaws. Optical microscopy with 10× or 20× magnification was employed for quick inspections and the fabrication quality was checked more extensively by SEM.

Glioblastoma Cell Culture: Four patient-derived glioma cell cultures, GS-830, GS-580, GS-827, and GS-921, alongside U87 standard cell line were tested. GS-830 and GS-921 are isocitrate dehydrogenase (IDH)-wild-type glioblastoma cells, and GS-580 and GS-827 are IDH-mutant astrocytomas.[5,78] EGFR is expressed in both (IDH)-wild-type and (IDH)-mutant cell cultures used in the experiments, but EGFR amplification is lost in culture.[78] The use of patient tissue was approved by the Medical Ethical Review Committee Erasmus MC, code MEC-2013-090, and all patients signed informed consent forms according to the guidelines of the Institutional review board.

The cell culture steps were adopted from a published protocol.[5,78] Unless otherwise specified, 20 ng mL^{-1} basic fibroblast growth factor, 20 ng mL^{-1} EGF, and 5 µg mL^{-1} heparin was used in Dulbecco's modified Eagle medium/Nutrient Mixture F-12 (DMEM/F-12, 11320-033, Gibco, USA) as the cell culture media. Each sample set, containing three scaffolds and four pedestals fabricated on one ITO substrate, was placed in one well of a 6-well plate and washed with ethanol 70% followed by two washes with phosphate buffered saline (PBS). Structures were coated with Cultrex Basement Membrane Extract Reduced Growth Factor (3500-096-01, Trevigen, USA). This coating is cell line derived and consists of a mixture of extracellular matrix proteins such as laminin and collagen IV. For this experiment, 100 µL coating solution (1:100 Cultrex coating diluted in culture media) was used to cover the surface of each substrate. In the meantime, cells were kept in flasks until they reached 80% confluency. At that time, 1 mL of cell suspension (1 000 000 cells mL^{-1}) was seeded on each coated sample set. 2 mL cell culture medium was then added to each well. For experiments with Dacomitinib (S2727, Selleckchem, USA) and Erlotinib (S1023, Selleckchem, USA), 10 µM of the inhibitors was added to the culture medium 2 h before cell fixation. For -EGF conditions, cell culture media was used without the addition of EGF.

Scanning Electron Microscopy: For SEM imaging of cells seeded on the fabricated structures, the cells were fixed and dehydrated. Concerning cell fixation, cell culture medium was removed and samples were washed two times with PBS. Then, 2% paraformaldehyde was added for 30 min followed by 4% glutaraldehyde for 2 h. Scaffolds and cells within them were then washed two times with PBS and dehydrated sequentially in 50% ethanol (15′), 70% ethanol (20′), and ethanol (20′) and dried at room temperature.

SEM was employed to assess the fabrication quality of the structures and the cell–microstructure interaction. To avoid charge build-up, the samples were sputter-coated with a gold nanolayer. A Sputter Coater JEOL JFC-1300 (Tokyo, Japan) was used for this purpose. All samples were coated once horizontally and two times in opposing 45° tilted configurations in order to ensure a homogeneous metal coating also along sidewalls. In the horizontal configuration, the samples were sputter-coated using a 20 mA current for 20 s adding ≈13 nm thick gold layer. The duration was reduced to 10 s for each tilted configuration adding ≈6.5 nm thick gold layer.

For SEM imaging, secondary electron generated images were recorded using a JEOL JSM-6010LA scanning electron microscope (Tokyo, Japan). Concerning the recorded images, the accelerating voltage ranged from 10 to 20 kV and the spot size (diameter of the electron beam) ranged from 50 down to 30 nm.

Immunofluorescence Staining and Confocal Imaging Configuration: Primary antibodies were anti-Beta-Tubulin (ab6046, Abcam, UK, 1:200 dilution), anti-GAP-43 (8945, Cell Signaling Company, USA, 1:200 dilution), and anti-EGFR (M3563, DAKO, Germany, 1:500 dilution, or ab76153, Abcam, UK, 1:200 dilution). Secondary antibodies were Alexa Flour 488 anti-rabbit (A11008, Life Technologies, USA, 1:500 dilution) and Alexa Fluor 647 anti-mouse (A21240, Life Technologies, USA, 1:500 dilution). The anti-EGFR made by Abcam provided stronger signals and therefore was preferred. All antibodies were diluted in PBS with 1% W/V bovine serum albumin. Samples were incubated with primary or secondary antibodies each for 1 h at room temperature in humidity chambers. Scaffolds were mounted with Vectrashield fluorescent mounting with DAPI (Vector Laboratories, USA) for the visualization of nuclei. A coverglass was placed on top of the scaffolds. In order to prevent damaging the scaffolds during imaging, two spacers (Imaging Spacers, GBL654002, Grace Bio-Labs, USA) with the thickness of 120 µm were used (Figure S14, Supporting Information). An oil immersion upright microscope Stellaris 5 (Leica Microsystems, Germany) with 40× objective and numerical aperture 1.30 was used for confocal immunofluorescent imaging. To avoid cross-talk between channels, the imaging for individual markers was carried out sequentially.

Staining of FFPE tissue slices was performed for tumor cell marker IDH (DIA-H09, Dianova, USA, for IDH-mutant, low grade tissue slices) or Glial Fibrillary Acidic Protein (GFAP, M0761, DAKO, Germany, for IDH-wildtype, high grade tumors) and nuclear counterstaining with DAPI. Staining was performed on 4 µm FFPE sections as previously described.[79] Staining for tumor marker was performed by antigen retrieval with microwave treatment in AR6 buffer (AR600250ML, Akoya Biosciences, USA), blocking (ARD1001EA, Akoya Biosciences, USA), primary antibody incubation (1:20 for IDH and 1:50 for GFAP, diluted in blocking solution), secondary antibody incubation (ARH1001EA, Akoya Biosciences, USA), and subsequent incubation with tyramide signal amplification plus fluorophore (OP-001006, Akoya Biosciences, 1:100, diluted in amplification diluent FP1498, Akoya Biosciences), with washing steps in between. Finally, sections were counterstained with spectral DAPI (Spectral DAPI, FP1490, AKOYA Biosciences, USA) and mounted with mounting medium (P36970, Invitrogen, USA). Following staining, whole sections were scanned (10× magnification) and representative sections per patient (three low grade and three high grade patients) were imaged in higher magnification (20×; area: 690 × 516 µm; resolution: 2 pixels µm^{-1}, pixel size: 0.5 × 0.5 µm^2) with the use of Vectra 3.0 (Akoya Biosciences, Menlo Park, CA, USA) as previously described.[79] Images were manually thresholded for identification of tumor marker positive regions, and nuclei in these regions were identified using the Stardist plugin.[80] These images were then exported to be used for downstream image analysis.

Live Confocal Imaging: Prior to cell seeding, cells were stained with a fluorescent dye, CellTracker Green CMFDA Dye (C2925, Invitrogen, USA), diluted in DMEM/F-12 medium (5 µM) and were incubated for 30 min at 37 °C. Next, this mixture was replaced with normal medium and the cells were seeded on the scaffolds according to the stated cell culture protocol. Cells were left to grow and attach to the scaffolds in an upright configuration for ≈16 h. Then the samples were flipped upside down for imaging (Figure S15, Supporting Information). To keep samples in the inverted configuration, Grace Bio-Labs imaging spacers were used. Three scaffolds and the 2D surfaces were imaged every 1.5 h for a total of 16.5 h using Opera Phenix High-Content Screening System (Perkin Elmer, USA) with an inverted 20× objective and 0.4 numerical aperture.

Image Analysis: Concerning fluorescent images, the analysis was performed on maximum intensity *Z* projections of stacks of image slices. Images were analyzed using ImageJ software (National Institutes of Health, USA). Macrocodes were developed to extract and quantify the features of interest from each image (nucleus size, circularity, EGFR "spot" size, fluorescence intensity, and location). All codes are explained in the Supporting Information. The Stardist plug-in was used for nuclei segmentation.[80] The cell area was defined as the combination of nuclei and tubulin areas. Circularity, used to quantify nuclei and cell circularity, is defined in ImageJ software as $4\pi(A\,P^{-2})$, where A is area and P is perimeter. To quantify the EGFR localization, a combination of Stardist for nuclei detection,[80] ComDet for EGFR spot detection,[81] and NearestNeighbour to find distances was used.[82] All tube-like protrusions were marked in ImageJ based on the tubulin staining and were quantified in terms of length and width. For this, fluorescent images (with 380 µm × 380 µm field of view) of the stained cells on 2D pedestals and 3D scaffolds were recorded and then analyzed. All experiments were independently replicated at different points in time using subsequent passage numbers to colonize the scaffolds. All conditions within one experiment (i.e., cultured ± EGF, +Erlotinib, +Dacomitinib) were simultaneously performed, processed, and imaged using identical imaging parameters.

Harmony high-content imaging and analysis software (Perkin Elmer, USA) was used to analyze the live experiment images. Position and speed of the cells on 2D and 3D structures were tracked and recorded based on the maximum intensity Z projections of stacks of image slices. Analysis is explained in more detail in the Supporting Information.

Statistical Analysis: The data were analyzed with R programming using RStudio. The Shapiro–Wilk test was used to verify normal distribution of data ($p < 0.05$). A one-way analysis of variance test for normal data and a Kruskal–Wallis test for non-normal data were used. The Kolmogorov–Smirnov test was used to compare the distribution of data sets. Spearman's rank-order correlation test was used to find correlation between variables with non-normal distributions. Statistical significance was set at $p < 0.05$ (*), $p < 0.01$ (**), and $p < 0.001$(***). Sample size (n) for each test is displayed in the related figure legends. Boxplots display the median, interquartile range (IQR) with the whiskers drawn at 1.5IQR.

Supporting Information

Supporting Information is available from the Wiley Online Library or from the author.

Acknowledgements

P.J.F. and A.A. contributed equally to this work. Part of this work was supported by a grant from the Brain Tumour Charity (Grant No. ET_2019__2_10470) and the ErasmusMC Academic Centre of Excellence "Tumor Immunology and Immune Therapy" and the TU Delft Bioengineering Institute MSc Grant. The authors would like to acknowledge P. A. E. Sillevis Smitt (Neurology Department, Erasmus Medical Center (Erasmus MC)) and U. Staufer (Department of Precision and Microsystems Engineering (PME), Delft University of Technology (TU Delft)) for their insightful comments. The authors' sincerely thank G. van Cappellen (Erasmus Optical Imaging Center, Erasmus MC) for his assistance in immunofluorescence imaging and image analysis. Special thanks to A. Sharaf (PME, TU Delft) for his help with 2PP fabrication and S. Aghajani (PME, TU Delft) for his help with SEM. The authors would also like to acknowledge the assistance of TU Delft PME laboratory staff specially G. Emmaneel for his help with laser cutting. The authors are grateful to the TU Delft Micro and Nano Engineering and the Erasmus MC Neuro-Oncology research groups for their kind support.

Conflict of Interest

The authors declare no conflict of interest.

Data Availability Statement

The data that support the findings of this study are available from the corresponding author upon reasonable request.

Keywords

2-photon polymerization, 3D cell culture, brain cancer, epidermal growth factor receptor, microtubes

Received: July 20, 2022
Revised: September 9, 2022

[1] Q. T. Ostrom, L. Bauchet, F. G. Davis, I. Deltour, J. L. Fisher, C. E. Langer, M. Pekmezci, J. A. Schwartzbaum, M. C. Turner, K. M. Walsh, M. R. Wrensch, J. S. Barnholtz-Sloan, *Neuro. Oncol.* **2014**, *16*, 896.
[2] S. Caragher, A. J. Chalmers, N. Gomez-Roman, *Cancers* **2019**, *11*, 44.
[3] M. L. Goodenberger, R. B. Jenkins, *Cancer Genet.* **2012**, *205*, 613.
[4] B. W. Stringer, B. W. Day, R. C. J. D'Souza, P. R. Jamieson, K. S. Ensbey, Z. C. Bruce, Y. C. Lim, K. Goasdoué, C. Offenhäuser, S. Akgül, S. Allan, T. Robertson, P. Lucas, G. Tollesson, S. Campbell, C. Winter, H. Do, A. Dobrovic, P. L. Inglis, R. L. Jeffree, T. G. Johns, A. W. Boyd, *Sci. Rep.* **2019**, *9*, 4902.
[5] C. Verheul, I. Ntafoulis, T. V. Kers, Y. Hoogstrate, P. G. Mastroberardino, S. Barnhoorn, C. Payán-Gómez, R. T. C. Yen, E. A. Struys, S. L. W. Koolen, C. M. F. Dirven, S. Leenstra, P. J. French, M. L. M. Lamfers, *Neurooncol Adv.* **2021**, *3*, 103.
[6] S. Weil, M. Osswald, G. Solecki, J. Grosch, E. Jung, D. Lemke, M. Ratliff, D. Hänggi, W. Wick, F. Winkler, *Neuro Oncol.* **2017**, *19*, 1316.
[7] A. Pandita, K. D. Aldape, G. Zadeh, A. Guha, C. D. James, *Genes Chromosomes Cancer.* **2004**, *39*, 29.
[8] M. Osswald, G. Solecki, W. Wick, F. Winkler, *Neuro Oncol.* **2016**, *18*, 479.
[9] M. Schneider, F. A. Giordano, T. Kuner, W. Wick, U. Herrlinger, F. Winkler, *Nat. Rev. Cancer* **2022**, *22*, 481.
[10] E. Eskilsson, G. V. Røsland, G. Solecki, Q. Wang, P. N. Harter, G. Graziani, R. G. W. Verhaak, F. Winkler, R. Bjerkvig, H. Miletic, *Neuro Oncol.* **2018**, *20*, 743.
[11] W. Szopa, T. A. Burley, G. Kramer-Marek, W. Kaspera, *Biomed. Res. Int.* **2017**, *2017*, 8013575.
[12] J. M. Heffernan, D. J. Verstreet, L. D. Le, B. L. Vernon, R. W. Sirianni, *Ann. Biomed. Eng.* **2015**, *43*, 1965.
[13] K. A. Jansen, D. M. Donato, H. E. Balcioglu, T. Schmidt, E. H. J. Danen, G. H. Koenderink, *Biochim. Biophys. Acta, Mol. Cell Res.* **2015**, *1853*, 3043.
[14] R. Edmondson, J. J. Broglie, A. F. Adcock, L. Yang, *Assay Drug Dev. Technol.* **2014**, *12*, 207.
[15] N. Gomez-Roman, K. Stevenson, L. Gilmour, G. Hamilton, A. J. Chalmers, *Neuro Oncol.* **2017**, *19*, iii26.
[16] C. Jensen, Y. Teng, *Front. Mol. Biosci.* **2020**, *7*, 33.
[17] L. Ma, B. Zhang, C. Zhou, Y. Li, B. Li, M. Yu, Y. Luo, L. Gao, D. Zhang, Q. Xue, Q. Qiu, B. Lin, J. Zou, H. Yang, *Colloids Surf., B* **2018**, *172*, 665.
[18] E. D. Lemma, B. Spagnolo, M. De Vittorio, F. Pisanello, *Trends Biotechnol.* **2019**, *37*, 358.
[19] D. Fan, U. Staufer, A. Accardo, *Bioengineering* **2019**, *6*, 133.
[20] W. S. Harley, C. C. Li, J. Toombs, C. D. O'Connell, H. K. Taylor, D. E. Heath, D. J. Collins, *Int. J. Bioprint.* **2021**, *23*, 00147.
[21] A. Accardo, M. C. Blatché, R. Courson, I. Loubinoux, C. Vieu, L. Malaquin, *Mater. Today* **2018**, *21*, 315.
[22] A. Accardo, R. Courson, R. Riesco, V. Raimbault, L. Malaquin, *Addit. Manuf.* **2018**, *22*, 440.
[23] Q. Akolawala, M. Rovituso, H. H. Versteeg, A. M. R. Rondon, A. Accardo, *ACS Appl. Mater. Interfaces* **2022**, *14*, 20778.
[24] A. K. Nguyen, R. J. Narayan, *Mater. Today* **2017**, *20*, 314.

[25] A. Accardo, M. Blatché, R. Courson, I. Loubinoux, C. Vieu, L. Malaquin, *Biomed. Phys. Eng. Express* **2018**, *4*, 027009.
[26] C. Liao, A. Wuethrich, M. Trau, *Appl. Mater. Today* **2020**, *19*, 100635.
[27] Nanoscribe, "Resins for Printing, IP-Visio," https://support.nanoscribe.com/hc/en-gb/articles/360011709499-IP-Visio#Ch:IPVisio_general (accessed: February 2021).
[28] A. Farin, S. O. Suzuki, M. Weiker, J. E. Goldman, J. N. Bruce, P. Canoll, *Glia* **2006**, *53*, 799.
[29] Y. Yang, S. Motte, L. J. Kaufman, *Biomaterials* **2010**, *31*, 5678.
[30] Nanoscribe, "NanoGuide CAD Model Creation," https://support.nanoscribe.com/hc/en-gb/articles/360000810253-CAD-Model-Creation (accessed: April 2021).
[31] J. Song, C. Michas, C. S. Chen, A. E. White, M. W. Grinstaff, *Adv. Healthcare Mater.* **2020**, *9*, 2192.
[32] A. J. Engler, S. Sen, H. L. Sweeney, D. E. Discher, *Cell* **2006**, *126*, 677.
[33] A. I. Ciuciu, P. J. Cywiński, *RSC Adv.* **2014**, *4*, 45504.
[34] A. Sharaf, B. Roos, R. Timmerman, G.-J. Kremers, J. Bajramovic, A. Accardo, *Front. Bioeng. Biotechnol.* **2022**, *10*, 926642.
[35] M. Tromayer, A. Dobos, P. Gruber, A. Ajami, R. Dedic, A. Ovsianikov, R. Liska, *Polym. Chem.* **2018**, *9*, 3108.
[36] A. Ovsianikov, S. Mühleder, J. Torgersen, Z. Li, X. H. Qin, S. Van Vlierberghe, P. Dubruel, W. Holnthoner, H. Redl, R. Liska, J. Stampfl, *Langmuir* **2014**, *30*, 3787.
[37] O. Tolde, D. Rösel, R. Janoštiak, P. Veselý, J. Brábek, *Folia Biol.* **2012**, *58*, 177.
[38] M. Babi, R. Riesco, L. Boyer, A. Fatona, A. Accardo, L. Malaquin, J. Moran-Mirabal, *ACS Appl. Bio Mater.* **2021**, *4*, 8443.
[39] R. Nafe, K. Franz, W. Schlote, B. Schneider, *Clin. Cancer Res.* **2005**, *11*, 2141.
[40] L. Liu, Q. Luo, J. Sun, G. Song, *Exp. Cell Res.* **2016**, *348*, 56.
[41] T. P. Driscoll, B. D. Cosgrove, S. J. Heo, Z. E. Shurden, R. L. Mauck, *Biophys. J.* **2015**, *108*, 2783.
[42] M. Webster, K. L. Wikin, O. Cohen-Fix, *J. Cell Sci.* **2009**, *122*, 1477.
[43] S. Cho, J. Irianto, D. E. Discher, *J. Cell Biol.* **2017**, *216*, 305.
[44] D. H. Kim, D. Wirtz, *Biomaterials* **2015**, *48*, 161.
[45] D. B. Lovett, N. Shekhar, J. A. Nickerson, K. J. Roux, T. Lele, *Cell. Mol. Bioeng.* **2013**, *6*, 230.
[46] D. M. Graham, K. Burridge, *Curr. Opin. Cell Biol.* **2016**, *40*, 98.
[47] K. Miranda, D. A. Pace, R. Cintron, J. C. F. Rodrigues, J. Fang, A. Smith, P. Rohloff, E. Coelho, F. De Haas, D. Souza, I. Coppens, L. D. Sibley, S. N. J. Moreno, *Science* **2013**, *341*, 1240104.
[48] P. Jevtić, L. J. Edens, L. D. Vuković, D. L. Levy, *Curr. Opin. Cell Biol.* **2014**, *28*, 16.
[49] D. Boruah, P. Deb, *ISRN Oncol.* **2013**, *2013*, 760653.
[50] M. Osswald, E. Jung, F. Sahm, G. Solecki, V. Venkataramani, J. Blaes, S. Weil, H. Horstmann, B. Wiestler, M. Syed, L. Huang, M. Ratliff, K. Karimian Jazi, F. T. Kurz, T. Schmenger, D. Lemke, M. Gömmel, M. Pauli, Y. Liao, P. Häring, S. Pusch, V. Herl, C. Steinhäuser, D. Krunic, M. Jarahian, H. Miletic, A. S. Berghoff, O. Griesbeck, G. Kalamakis, O. Garaschuk, et al., *Nature* **2015**, *528*, 93.
[51] M. Osswald, E. Jung, W. Wick, F. Winkler, *Cancer Rep.* **2019**, *2*, 1181.
[52] L. I. Benowitz, A. Routtenberg, *Trends Neurosci.* **1997**, *20*, 84.
[53] G. Pinto, I. Saenz-De-Santa-Maria, P. Chastagner, E. Perthame, C. Delmas, C. Toulas, E. Moyal-Jonathan-Cohen, C. Brou, C. Zurzolo, *Biochem. J.* **2021**, *478*, 21.
[54] A. Vollmann-Zwerenz, V. Leidgens, G. Feliciello, C. A. Klein, P. Hau, *Int. J. Mol. Sci.* **2020**, *21*, 1932.
[55] C. Calabrese, H. Poppleton, M. Kocak, T. L. Hogg, C. Fuller, B. Hamner, E. Y. Oh, M. W. Gaber, D. Finklestein, M. Allen, A. Frank, I. T. Bayazitov, S. S. Zakharenko, A. Gajjar, A. Davidoff, R. J. Gilbertson, *Cancer Cell* **2007**, *11*, 69.
[56] Y. Yi, I. Y. Hsieh, X. Huang, J. Li, W. Zhao, *Front. Pharmacol.* **2016**, *7*, 477.
[57] C. J. Liu, G. A. Shamsan, T. Akkin, D. J. Odde, *Biophys. J.* **2019**, *117*, 1179.
[58] P. Friedl, E. Sahai, S. Weiss, K. M. Yamada, *Nat. Rev. Mol. Cell Biol.* **2012**, *13*, 743.
[59] P.-H. Wu, A. Giri, S. X. Sun, D. Wirtz, *Proc. Natl. Acad. Sci. USA* **2014**, *111*, 3949.
[60] S. I. Fraley, Y. Feng, R. Krishnamurthy, D. H. Kim, A. Celedon, G. D. Longmore, D. Wirtz, *Nat. Cell Biol.* **2010**, *12*, 598.
[61] S. Sigismund, D. Avanzato, L. Lanzetti, *Mol. Oncol.* **2018**, *12*, 3.
[62] P. C. Pan, R. S. Magge, *Int. J. Mol. Sci.* **2020**, *21*, 8471.
[63] W. Xia, Y. Wei, Y. Du, J. Liu, B. Chang, N. L. Yu, L. F. Huo, S. Miller, M. C. Hung, *Mol. Carcinog.* **2009**, *48*, 610.
[64] I. Hadžisejdi, E. Mustać, N. Jonjić, M. Petković, B. Grahovac, *Mod. Pathol.* **2010**, *23*, 392.
[65] S. Scharaw, M. Iskar, A. Ori, G. Boncompain, V. Laketa, I. Poser, E. Lundberg, F. Perez, M. Beck, P. Bork, R. Pepperkok, *J. Cell Biol.* **2016**, *215*, 543.
[66] I. Pinilla-Macua, A. Grassart, U. Duvvuri, S. C. Watkins, A. Sorkin, *eLife* **2017**, *6*, 31993.
[67] B. M. Chung, S. M. Raja, R. J. Clubb, C. Tu, M. George, V. Band, H. Band, *BMC Cell Biol.* **2009**, *10*, 84.
[68] T. Tanaka, Y. Zhou, T. Ozawa, R. Okizono, A. Banba, T. Yamamura, E. Oga, A. Muraguchi, H. Sakurai, *J. Biol. Chem.* **2018**, *293*, 2288.
[69] J. Bakker, M. Spits, J. Neefjes, I. Berlin, *J. Cell Sci.* **2017**, *130*, 4087.
[70] A. Baldys, J. R. Raymond, *Biochemistry* **2009**, *48*, 9321.
[71] T. Brand, M. Iida, N. Luthar, M. Starr, E. Huppert, D. Wheeler, *Radiother. Oncol.* **2013**, *108*, 370.
[72] A. Tomas, C. E. Futter, E. R. Eden, *Trends Cell Biol.* **2014**, *24*, 26.
[73] S. Mazzoleni, L. S. Politi, M. Pala, M. Cominelli, A. Franzin, L. S. Sergi, A. Falini, M. De Palma, A. Bulfone, P. L. Poliani, R. Galli, *Cancer Res.* **2010**, *70*, 7500.
[74] Y. Gao, W. R. Vallentgoed, P. J. French, *Cancers* **2018**, *10*, 489.
[75] A. H. Thorne, C. Zanca, F. Furnari, *Neuro Oncol.* **2016**, *18*, 914.
[76] A. A. Brandes, E. Franceschi, A. Tosoni, M. E. Hegi, R. Stupp, *Clin. Cancer Res.* **2008**, *14*, 957.
[77] X. Liu, H. Gu, M. Wang, X. Du, B. Gao, A. Elbaz, L. Sun, J. Liao, P. Xiao, Z. Gu, *Adv. Mater.* **2018**, *30*, 1800103.
[78] R. K. Balvers, A. Kleijn, J. J. Kloezeman, P. J. French, A. Kremer, M. J. Van Den Bent, C. M. F. Dirven, S. Leenstra, M. L. M. Lamfers, *Neuro Oncol.* **2013**, *15*, 1684.
[79] C. Phanthunane, R. Wijers, M. de Herdt, T. P. M. Langeveld, S. Koljenovic, S. Dasgupta, S. Sleijfer, R. J. Baatenburg de Jong, J. Hardillo, H. E. Balcioglu, R. Debets, *Oncoimmunology* **2021**, *10*, 1882743.
[80] U. Schmidt, M. Weigert, C. Broaddus, G. Myers, presented at the Int. Conf. on Medical Image Computing and Computer-Assisted Intervention (MICCAI), Granada, Spain, September 2018.
[81] E. Katrukha, ComDet plugin for ImageJ, v0.5.3 2020, https://github.com/ekatrukha/ComDet (accessed: February 2022).
[82] ErasmusOIC, Simple nearest neighbour plugIn for ImageJ, https://github.com/ErasmusOIC/NearestNeighbour (accessed: December 2021).

Dynamically Crosslinked Poly(ethylene-glycol) Hydrogels Reveal a Critical Role of Viscoelasticity in Modulating Glioblastoma Fates and Drug Responses in 3D

*Sauradeep Sinha, Manish Ayushman, Xinming Tong, and Fan Yang**

Glioblastoma multiforme (GBM) is the most prevalent and aggressive brain tumor in adults. Hydrogels have been employed as 3D in vitro culture models to elucidate how matrix cues such as stiffness and degradation drive GBM progression and drug responses. Recently, viscoelasticity has been identified as an important niche cue in regulating stem cell differentiation and morphogenesis in 3D. Brain is a viscoelastic tissue, yet how viscoelasticity modulates GBM fate and drug response remains largely unknown. Using dynamic hydrazone crosslinking chemistry, a poly(ethylene-glycol)-based hydrogel system with brain-mimicking stiffness and tunable stress relaxation is reported to interrogate the role of viscoelasticity on GBM fates in 3D. The hydrogel design allows tuning stress relaxation without changing stiffness, biochemical ligand density, or diffusion. The results reveal that increasing stress relaxation promotes invasive GBM behavior, such as cell spreading, migration, and GBM stem-like cell marker expression. Furthermore, increasing stress relaxation enhances GBM proliferation and drug sensitivity. Stress-relaxation induced changes on GBM fates and drug response are found to be mediated through the cytoskeleton and transient receptor potential vanilloid-type 4. These results highlight the importance of incorporating viscoelasticity into 3D in vitro GBM models and provide novel insights into how viscoelasticity modulates GBM cell fates.

1. Introduction

Glioblastoma multiforme (GBM) is the most prevalent and aggressive primary brain cancer in adults.[1] The standard-of-care for GBM consists of surgical resection followed by concurrent radiotherapy and chemotherapy. Despite such aggressive treatment interventions, GBM patients face a bleak 5-year survival rate of 7% and a median survival of less than 2 years.[2,3] Such dismal outcomes are largely attributed to GBM's highly diffusive invasion into surrounding brain tissue. GBM's diffuse nature makes complete resection impossible without interfering with normal brain function, and residual migrating cells outside of the tumor core are generally unaffected by local therapies and invariably lead to recurrence.[4,5] GBM tumors contain stem-like cells (GSCs), expressing putative markers such as Nestin, CD133, and Sox2, and have been found to be essential in driving invasion and disease propagation into healthy brain parenchyma, ultimately resulting to poor patient outcomes.[6] To improve treatment strategies for GBM, it is critical to understand key factors driving aggressive GBM invasion and phenotype.

Toward this goal, engineered biomaterials-based hydrogels have been utilized to create 3D in vitro brain tumor models to elucidate how brain extracellular matrix (ECM) properties modulate GBM progression and drug responses.[7] Using synthetic and naturally derived materials like poly(ethylene-glycol) (PEG) or collagen-I, respectively, previous studies have demonstrated that matrix stiffness, degradability, and biochemical cues are critical in driving GBM malignant phenotype and progression in 3D.[8–11] Recently, viscoelasticity has been discovered as a matrix niche cue that modulates multiple biological processes including stem cell differentiation, morphogenesis, and maintenance of neural progenitor stemness.[12–15] Importantly, the brain tissue is viscoelastic and exhibits stress relaxation, or a time-dependent decrease in storage or elastic modulus when under constant strain.[13,16] Furthermore, magnetic resonance elastography measurements demonstrate that GBM tumors are viscoelastic as well.[17,18] However, how viscoelasticity modulates GBM fate and drug response in 3D remains largely unknown. Previously established PEG hydrogels were covalently crosslinked, rendering the resulting hydrogel network to be elastic in their response to mechanical forces, and thereby lack stress relaxation.[8,9] While collagen-I matrices are viscoelastic, varying the polymer concentration to tune the stress relaxation profile simultaneously induces changes in the stiffness and biochemical ligand density.[11,19] As a result, there remains a critical need

---

S. Sinha, M. Ayushman, F. Yang
Department of Bioengineering
Stanford University
Stanford, CA 94305, USA
E-mail: fanyang@stanford.edu

X. Tong, F. Yang
Department of Orthopaedic Surgery
Stanford University School of Medicine
Stanford, CA 94305, USA

The ORCID identification number(s) for the author(s) of this article can be found under https://doi.org/10.1002/adhm.202202147

DOI: 10.1002/adhm.202202147

to develop hydrogels with tunable stress relaxation without confounding factors to elucidate the unknown role of viscoelasticity on driving GBM cell fates in 3D.

To introduce viscoelasticity in 3D hydrogels, dynamic covalent chemistries have been recently reported for crosslinking, which allows the hydrogel network to adapt and reorganize to dissipate stresses at the molecular level in response to deformation.[20] Specifically, hydrazone crosslinking exhibits reversibility under physiological conditions and has shown biocompatibility in supporting 3D culture of myoblasts, chondrocytes, and neurons.[21–23] Hydrazone bonds (R–HC=NH–NH–R) are formed when a carbonyl electrophile, such as an aldehyde, attacks a nucleophilic hydrazine in a condensation reaction.[24] The resulting hydrazone bond is reversible, and the chemical equilibria of the bonds, which governs the rate of network reorganization, can be modulated via the choice of the aldehyde end group, either using an alkyl-aldehyde or a benzaldehyde. Consequently, the stress relaxation properties of the resulting hydrogel network can be easily tuned by varying the molar ratios of the resulting alkyl-hydrazone (AH) and benzyl-hydrazone (BH) bonds.[21,22] However, this chemistry has not been used to culture and study GBM in 3D.

Here, we report a PEG-based hydrogel system with tunable stress relaxation to investigate the role of matrix viscoelasticity on GBM tumor fate in 3D using the hydrazone crosslinking chemistry. In this work, we functionalize PEG macromers with reactive components to form hydrazone hydrogels with AH and/or BH crosslinks. To allow for cell adhesion, collagen-I is incorporated at a constant concentration to form an interpenetrating network (IPN) with the PEG hydrazone-crosslinked network. We demonstrate that increasing stress relaxation in 3D promotes invasive behavior of GBM including cell spreading, migration, and GSC marker expression. Furthermore, increasing stress relaxation leads to enhanced proliferation and drug sensitivity. We further elucidate that stress relaxation-induced changes in GBM cell responses are modulated through the cytoskeleton and transient receptor potential vanilloid-type 4 (TRPV4). Pharmacological inhibition studies were also performed to validate cytoskeletal tension and TRPV4 are required to induce invasive GBM behavior and drug sensitivity in stress relaxing hydrogels.

2. Results and Discussion

2.1. Developing Dynamically Crosslinked Poly(ethylene-glycol) Hydrogels with Tunable Stress Relaxation and Brain-Mimicking Stiffness

To interrogate the role of viscoelasticity on GBM tumor fate, we first established and characterized dynamically crosslinked PEG hydrogels with tunable stress relaxation and brain-mimicking stiffness. To form the hydrazone-crosslinked PEG network, 3 8-arm PEG macromers (MW ≈ 10 kDa) were synthesized with hydrazine, alkyl-aldehyde (AA), or benzaldehyde (BA) end groups (**Figure 1**a). PEG hydrazine can react with AA or BA to form either dynamic (alkyl-hydrazone, AH) or stable (benzyl-hydrazone, BH) crosslinks (Figure 1b). Three hydrogel groups with tunable stress relaxation profiles were achieved by varying the molar ratio of AH:BH crosslinks (100:0, 70:30, 0:100) used within the PEG network (Figure 1c). Collagen-I was incorporated at a constant concentration to provide cell adhesive cues (Figure 1c). In GBM tumors, collagen-I has been found to be elevated and plays an important role in tumor progression through providing adhesion sites and a fibrillar architecture.[25–27]

Rheological testing confirmed that varying the molar ratio of AH:BH crosslinks led to hydrogels with tunable stress relaxation (Figure 1d). The $\tau_{1/2}$ (the time for modulus to be relaxed to half its original value in shear) were ≈187 s, ≈1600 s, and ≈21,000 s for the hydrogels, which were termed fast-, medium-, and slow-relaxing hydrogels, respectively (Figure 1e). In particular, the fast-relaxing hydrogels exhibited comparable stress relaxation and $\tau_{1/2}$ to that of mouse brain ($\tau_{1/2} \approx 133$ s), demonstrating that fast-relaxing hydrogels recapitulate brain-mimicking stress relaxation (Figure 1d,e). Consistent with the stress relaxation results, further rheological characterization demonstrated that the loss tangent (another viscoelastic property and a measurement of energy dissipation) in fast-relaxing hydrogels was also comparable to that of mouse brain and diminished with decreasing stress relaxation (Figure 1f). To ensure that stiffness was not a confounding factor, the concentration of PEG and collagen-I used was held constant across all hydrogel groups. The results show that all 3 hydrogel formulations exhibited a Young's Modulus around 400 Pa, similar to that of mouse brain (Figure 1g). Furthermore, all hydrogel formulations demonstrated minimal degradation, as verified by relative stable swelling ratio, over the course of 6 days — the duration of the longest cell culture experiment in the present study (Figure S2a, Supporting Information). By day 6, the fast-relaxing hydrogel group demonstrated a slight decrease in polymer retention, which is likely attributed to the dynamic nature of AH crosslinks (Figure S2b, Supporting Information). This was accompanied by a slight increase in swelling ratio in the fast-relaxing hydrogels (Figure S2c, Supporting Information). Using confocal reflectance imaging, we further confirmed that tuning stress relaxation does not change the collagen distribution or fibrillar architecture across the different hydrogel formulations (Figure S2d, Supporting Information). Moreover, collagen-I was stably retained within the IPN over 6 days (Figure S2d, Supporting Information). Finally, all hydrogel formulations supported high cell viability of GBM cells after encapsulation and throughout culture (Figure S2e, Supporting Information). Together, these data confirm that dynamically crosslinked PEG hydrogels can serve as a 3D niche for GBM with tunable stress relaxation and brain-mimicking stiffness, without confounding factors of biochemical cues.

2.2. Increasing Stress Relaxation Promotes Glioblastoma Multiforme Cell Spreading, Motility, and Proliferation

We first investigated how tuning stress relaxation impacts GBM invasion, a hallmark feature of GBM disease progression.[28] Since cell spreading is a prerequisite for migration,[29,30] GBM cell morphology was first assessed. A patient-derived tumor xenograft (PDTX) GBM cell line (D-270 MG) was used given its ability to retain critical features of the parental tumor and inherent intratumoral heterogeneity.[31] After 3 days of culture in hydrogels, D-270 MG cells displayed distinct morphological differences in response to tuning stress relaxation. Increasing stress relaxation promoted robust cell spreading, whereas cells exhibited rounded

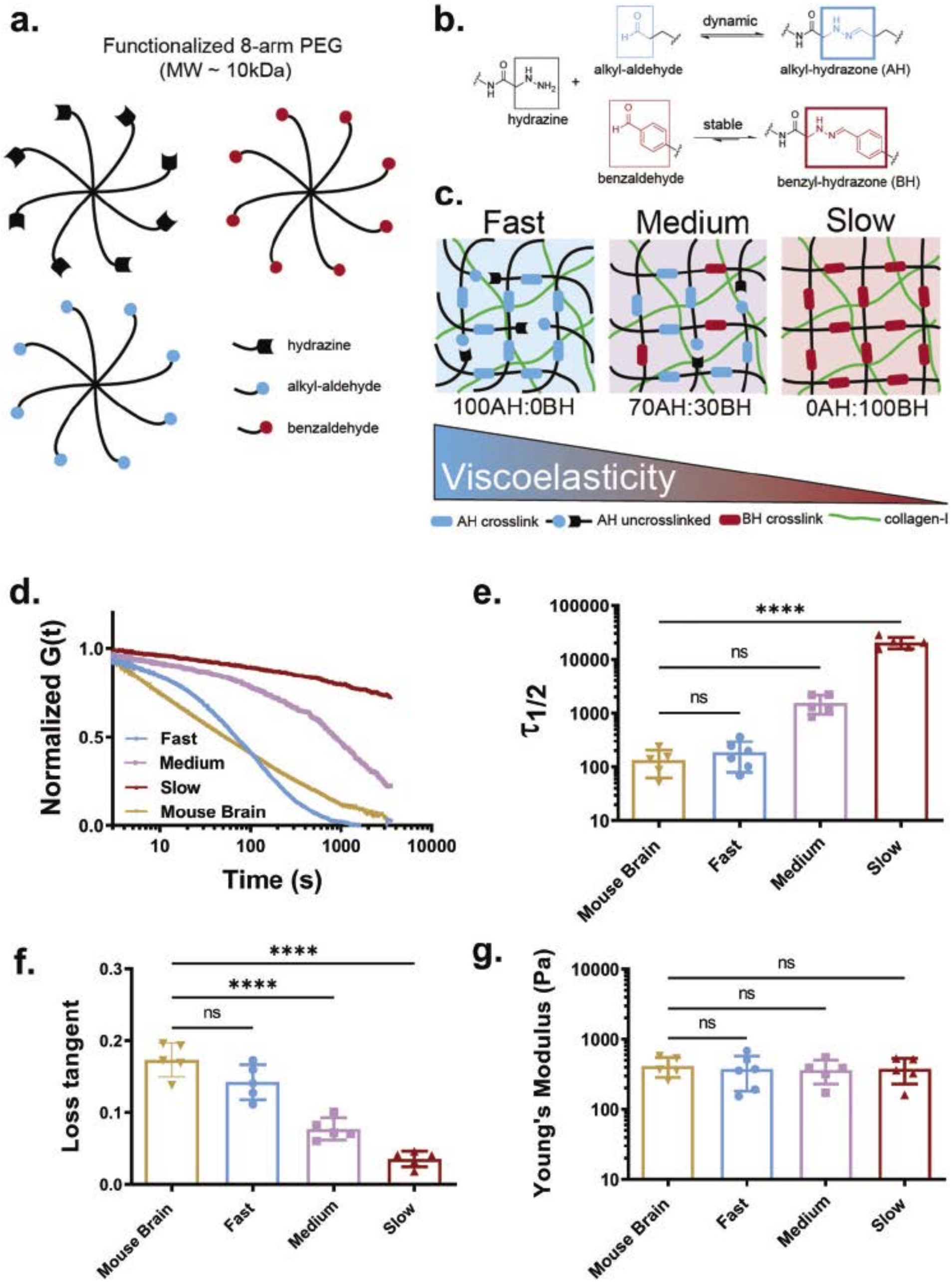

Figure 1. Dynamically crosslinked PEG hydrogels demonstrate tunable stress relaxation with brain-mimicking stiffness. a) Schematic representing 8-arm PEG macromers functionalized with reactive groups that enable hydrazone crosslinking. b) Chemical structures of dynamic alkyl-hydrazone (blue) and stable benzyl-hydrazone (red) crosslinks. c) Schematic depicting how varying the molar ratio of alkyl-hydrazone:benzyl-hydrazone (AH:BH) crosslinks allows formation of 3 hydrogel groups with tunable stress relaxation. Collagen-I (green) is incorporated at a constant concentration to provide cell adhesion. Characterizing the mechanical property of the 3 hydrogel formulations using shear rheology. Mouse brain was included as a positive control. d) Representative stress relaxation profiles of fast-, medium-, and slow-relaxing hydrogels and mouse brain. e) Time for the normalized modulus to reduce to half its original value, $\tau_{1/2}$, from stress relaxation tests. f) Loss tangent measurements. g) Young's modulus. One-way ANOVA with Dunnett's multiple comparisons test was used for analysis of the data in (e–g), comparing with mouse brain: ns, not significant; $****p < 0.0001$; $n = 6, 5, 5,$ and 5 independent samples (fast, medium, slow, and mouse brain). Data reported in (e–g) represent mean value ± s.d.

morphologies in slow-relaxing hydrogels (**Figure 2**a). Quantification of cell roundness corroborated these observations, as decreasing stress relaxation resulted in increasing the distribution of rounded cells (Figure 2b). A similar trend in GBM morphology in response to tuning stress relaxation was confirmed using U-87 MG, a well-established GBM cell line (Figure S3a,b, Supporting Information).

We next studied the impact of matrix stress relaxation on cell motility at the single cell and population levels using live-cell time-lapse imaging. Single cell motility was monitored over the

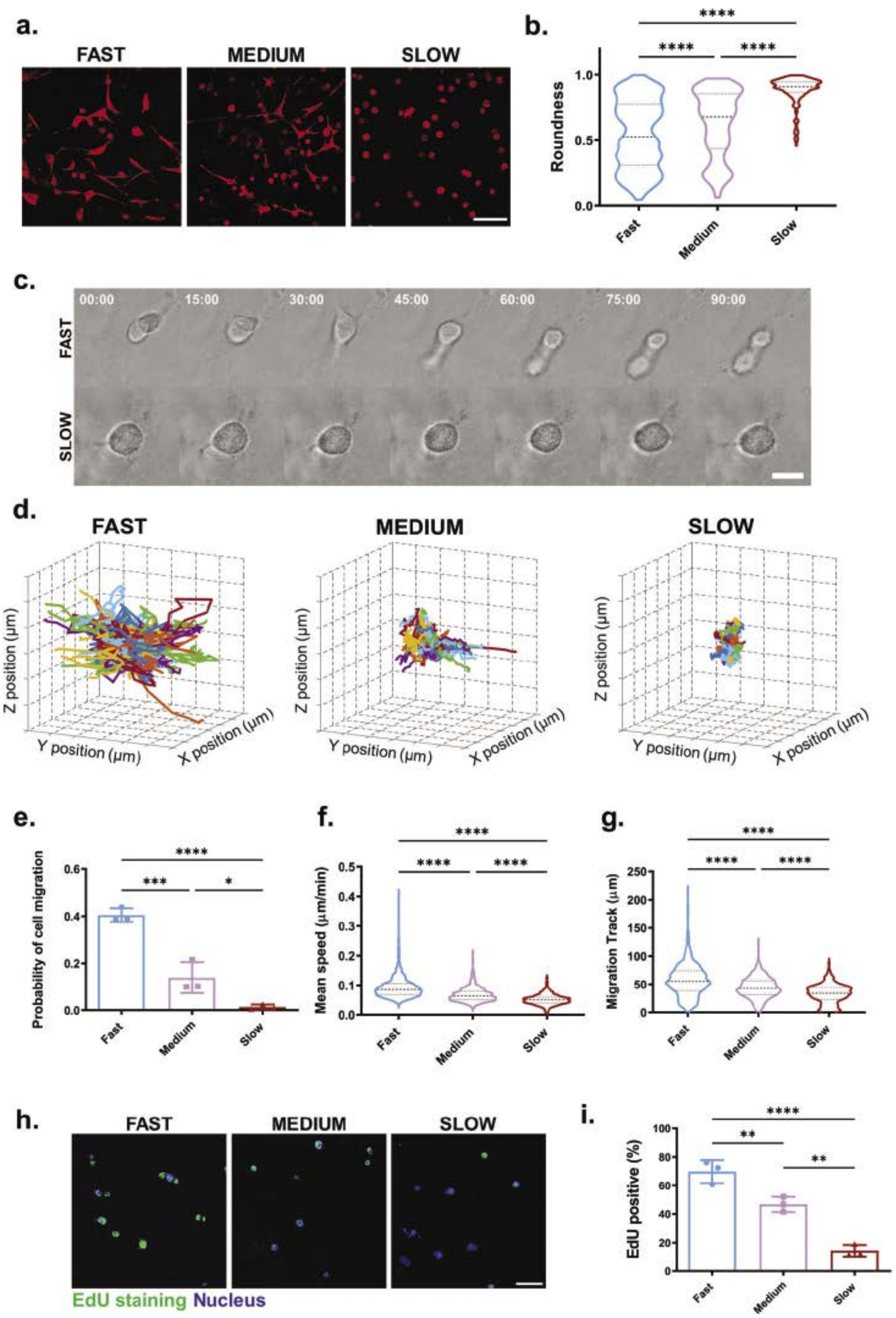

Figure 2. Stress relaxation promotes GBM cell spreading, migration, and proliferation in 3D. a) Representative maximum intensity projection images of membrane stained (R18) D-270 MG cells cultured within fast-, medium-, and slow-relaxing hydrogels on day 3. Scale bar, 100 µm. b) Roundness quantification of D-270 MG cells in the 3 hydrogel groups on day 3. One-way ANOVA with Tukey's multiple comparisons test was used for analysis of the data: ****$p < 0.0001$; $n = 498$, 343, and 216 (fast, medium, and slow) cells across 3 independent biological replicates. The dashed lines in the violin plots represent median values. c) Brightfield time-lapse imaging of a single cell within fast- and slow-relaxing hydrogels over 90 min. Times are indicated in min:s. Scale bar, 20 µm. d) Representative 3D track reconstructions for cell migration in the 3 hydrogel groups from time-lapse imaging. 80 randomly selected cell migration track trajectories are shown for each condition. Grid size, 10 µm. Analysis of cell migration track data from time-lapse imaging: e) Probability of cell migration, f) mean speed, and g) migration track length of cells tracked within the 3 hydrogel groups. One-way ANOVA with Tukey's multiple comparisons test was used for analysis of the data: *$p < 0.05$, ***$p < 0.001$, ****$p < 0.0001$; $n = 855$, 500, and 556 (fast, medium, and slow) cells tracked across 3 independent biological replicates. Bars indicate mean value ± s.d. The dashed lines in the violin plots represent median values. h) Representative immunostaining images of D-270 MG cells for EdU staining (green) and nucleus (blue) on day 3. Scale bar, 50 µm. i) Fraction of EdU-positive D-270 MG cells on day 3. One-way ANOVA with Tukey's multiple comparisons test was used for analysis of the data: **$p < 0.01$, ****$p < 0.0001$; $n = 212$, 191, and 153 (fast, medium, and slow) cells across 3 independent biological replicates. Data reported represent mean value ± s.d.

course of 90 min within fast and slow-relaxing hydrogels. D-270 MG cells quickly spread and migrate in a protrusive manner, whereas cells remain rounded and stationary in slow-relaxing hydrogels (Figure 2c). To confirm the observed motility on a population level, image analysis software was used to track the migration of labeled D-270 MG cells in the different hydrogel groups over 14 h (Movies S1–S3, Supporting Information). The projected cell migration tracks indicate that cells in fast-relaxing hydrogels were more migratory compared to those in medium and slow-relaxing hydrogels (Figure 2d). Using analysis from the cell track data, the probability that a cell would migrate within a particular hydrogel was further calculated. Cells within fast-relaxing hydrogels demonstrated ≈40% likelihood of migrating, significantly higher when compared to ≈13% and 1% in medium- and slow-relaxing hydrogels, respectively (Figure 2e). Cells in fast-relaxing hydrogels also demonstrate significantly higher migration speeds and track lengths, compared to cells in both medium- and slow-relaxing hydrogels (Figure 2f,g). These observations confirm that fast stress relaxation promotes robust GBM cell invasive phenotype including spreading and migratory ability. In contrast, within slow-relaxing hydrogels, GBM cells were uniformly confined and remained stationary.

Furthermore, we assessed the impact of stress relaxation on cell proliferation, another hallmark feature of GBM. The proliferation of D-270 MG cells, as indicated by EdU (5-ethynyl-2′-deoxyuridine), was enhanced in fast-relaxing hydrogels but reduced as stress relaxation was decreased (Figure 2h,i). This finding demonstrates that stress relaxation directly mediates GBM proliferation. Our finding is consistent with a previous report that stress relaxation promotes breast cancer cell proliferation, which was shown using a 3D alginate hydrogel model with tunable viscoelasticity.[32] Together, these results demonstrate that brain-mimicking fast stress relaxation facilitates more aggressive GBM phenotypes, such as increased cell spreading, migratory ability, and proliferation. These hallmark features are fundamental for GBM tumor invasion, recurrence, and growth — highlighting the important role of stress relaxation on aggressive GBM behavior.[2,33] One motivation for using a PDTX GBM cell line is their ability to better retain intratumoral heterogeneity, a key feature of GBM in vivo.[31,34] An ideal biomimetic hydrogel niche should support retention of such heterogeneity. Our results indicate that fast-relaxing hydrogels best support retention of GBM heterogeneity, in which cells exhibit varying degrees of spreading, migration and proliferation (Figure 2). In contrast, such heterogeneity in cell behavior is largely lost in slow-relaxing hydrogels, with minimal spreading, migration, or proliferation observed across all cells. These results suggest that stress relaxation may play an important role in supporting retention of GBM heterogeneity, which is important for drug screening and predicting in vivo response.

2.3. Stress Relaxation Promotes Stemness of Glioblastoma Multiforme Cells

GBM tumors contain GSCs, which have been shown to drive aggressive GBM phenotype and contribute to drug resistance and tumor recurrence.[6,34,35] Given that regulation of GSCs is dependent not only on intrinsic factors but also on microenvironmental niche cues,[6,36,37] we sought to investigate the role of matrix stress relaxation on GSC phenotype within GBM tumors, which has never been studied before. PDTX GBM cells were encapsulated in the 3 hydrogel formulations with varying stress relaxation for 3 days, and immunostaining was used to characterize the expression of 3 putative GSC markers — Nestin, CD133, and Sox2. Strikingly, all GSC markers demonstrated the highest expression in fast-relaxing hydrogels, and expression diminished with decreasing stress relaxation (**Figure 3**a). GSC marker expression was minimal at day 0 in all hydrogel formulations (Figure S4, Supporting Information), indicating that fast stress relaxation promotes GSC phenotype over the 3-day culture period. These trends were further validated on a population level using western blot, with significantly higher levels of GSC marker expression in hydrogels with faster stress relaxation (Figure 3b,c). These results suggest that matrix viscoelasticity promotes GBM cells to be in a more stem-like state, and it is important to incorporate viscoelasticity in 3D in vitro models for interrogating GSC biology and drug responses.

Enhanced GSC marker expression has also been shown to strongly correlate with enhanced GBM invasive phenotype in vivo.[35] Together, the observed trend from this 3D model recapitulates the in vivo GBM phenotype, in which fast-relaxing hydrogels support both higher GSC marker expressions (Figure 3) and enhanced migratory ability of GBM cells (Figure 2d–g). Similar to the trend with GSC markers, expression of GFAP, an astrocyte marker commonly used to identify GBM cells,[38,39] was also the highest in fast-relaxing gels (Figure S5a–c, Supporting Information). Given GFAP expression was reduced in slow-relaxing gels over 3 days of culture (Figure S5a,d, Supporting Information), we found that viscoelasticity is also important in preserving GFAP expression in GBM cells. Cumulatively, these results reveal a critical role of viscoelasticity in supporting in vivo-mimicking GBM cell phenotype and promoting GBM stemness, which correlates with an increased invasive GBM phenotype.

2.4. Stress Relaxation Induces Enhanced Glioblastoma Multiforme Drug Sensitivity to Chemotherapeutics

An important criterion for assessing the physiological relevance of a 3D cancer model is its potential for drug screening and ability to recapitulate drug responses in vivo. Having established that viscoelasticity plays a critical role in regulating invasive GBM phenotype, we next studied how stress relaxation impacts GBM drug response to clinically used chemotherapeutics. Two model drugs were tested including Temozolomide (TMZ) and Carmustine (BCNU). For each drug, 2 GBM cell lines (D-270 MG and U-87 MG) were tested. GBM cells were cultured in the different stress relaxing hydrogel groups for 3 days followed by an additional 3 days of drug treatment. The range of drug concentrations were selected based on previous reports.[9,40] At low TMZ concentration (3–100 µM), both GBM cell lines showed minimal response. At 300 and 600 µM, cells within fast-relaxing hydrogels displayed enhanced drug sensitivity compared to slow-relaxing hydrogels. At the very high drug concentration (1000 µM), cytotoxicity was saturated, and no significant difference was seen across the hydrogel groups (**Figure 4**a). A similar trend was observed in U-87 MG cells (Figure 4b). It is important to note

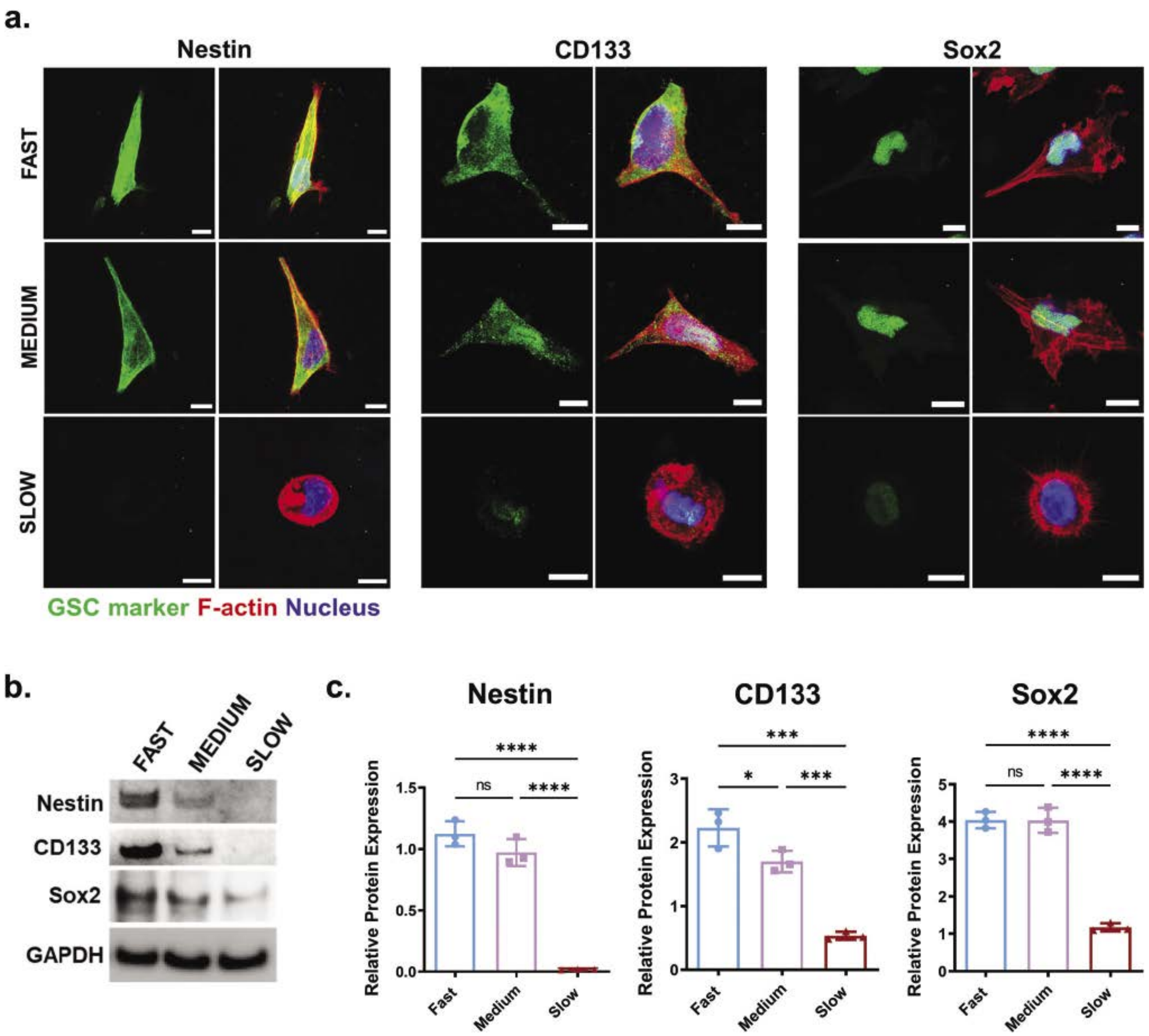

Figure 3. Stress relaxation promotes glioblastoma stem-like cell (GSC) marker expression in 3D. a) Representative immunostaining images of D-270 MG cells for GSC marker expression (Nestin, CD133, or Sox2; green), F-actin (red), and nucleus (blue) in fast-, medium-, and slow-relaxing hydrogels on day 3. Scale bar, 10 µm. b) Western blot analysis of GSC marker expression by GBM cells in fast-, medium-, and slow-relaxing hydrogels. c) Quantification of western blot images by normalizing each marker to GAPDH. One-way ANOVA with Tukey's multiple comparisons test was used for statistical analysis: ns, not significant; $^*p < 0.05$, $^{***}p < 0.001$, $^{****}p < 0.0001$; $n = 3$ independent biological replicates per group. Data reported represent mean value ± s.d.

that comparable TMZ diffusion was observed across all hydrogel groups (Figure S6a, Supporting Information), eliminating drug diffusion as a potential contributor to the observed differences in drug response. The effect of viscoelasticity on GBM drug response was further verified with BCNU, another drug used for treating GBM patients. Similar to the trend observed with TMZ, D-270 MG, and U-87 MG displayed enhanced drug sensitivity in fast-relaxing hydrogels compared to slow-relaxing hydrogels (Figure 4c,d). Together, these results reveal that stress relaxation increases GBM drug sensitivity.

Like many chemotherapeutics, TMZ and BCNU's mechanism of action depends on cell proliferation.[41–43] Given GBM cells displayed enhanced proliferation in fast-relaxing hydrogels (Figure 2h,i), we speculated that the enhanced drug sensitivity in fast-relaxing hydrogels was driven by the increased proliferation. To test this, D-270 MG cells were treated with mitomycin C to inhibit cell proliferation. Indeed, viscoelasticity-induced GBM drug sensitivity was abolished with mitomycin C treatment, with all groups exhibiting comparable drug response as the slow-relaxing hydrogels (Figure S6b, Supporting Information).

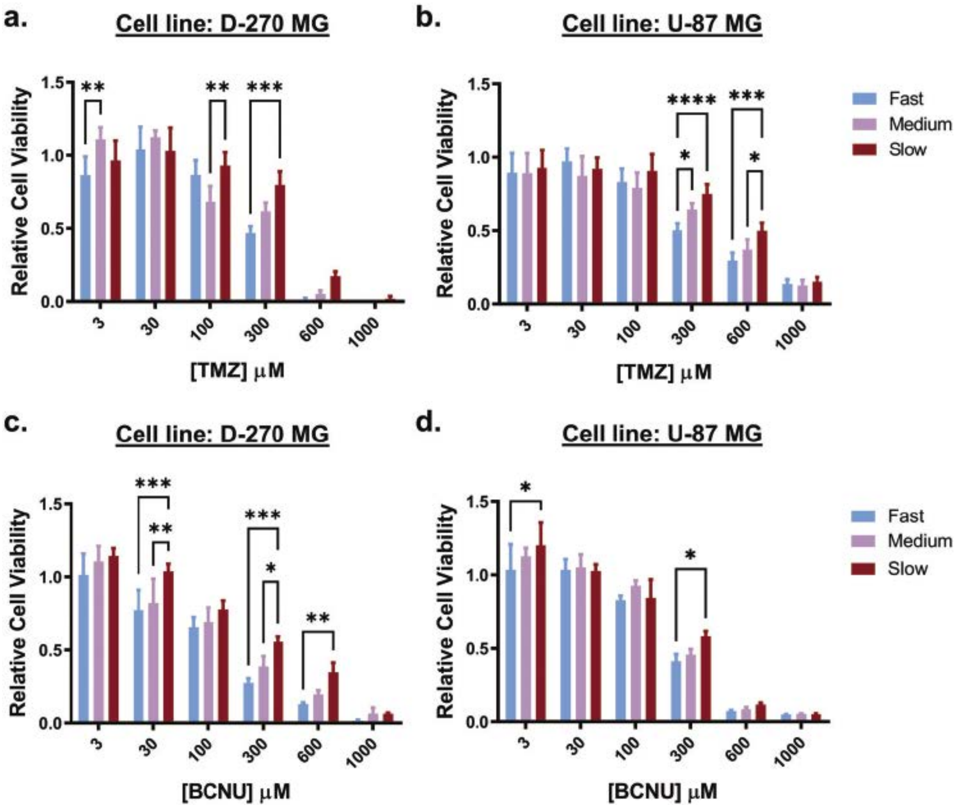

Figure 4. Stress relaxation increases drug sensitivity of GBM cells in 3D. Two model chemotherapeutic drugs were used, including a,b) Temozolomide (TMZ) and c,d) Carmustine (BCNU), to treat 2 GBM cell lines (D-270 MG and U87-MG). Relative cell viability was reported by normalizing treated to untreated GBM cells in fast (blue), medium (purple), and slow (red) stress relaxing hydrogels. Both GBM cell lines demonstrate enhanced chemosensitivity to both TMZ and BCNU as stress relaxation increases. Two-way ANOVA with Tukey's multiple comparisons test was used for statistical analysis: $^{*}p < 0.05$, $^{**}p < 0.01$, $^{***}p < 0.001$, $^{****}p < 0.0001$; $n = 3$ independent biological replicates per condition. Data reported represent mean value ± s.d.

Furthermore, GSCs have been postulated to be important mediators in GBM chemotherapy response.[6] Our data demonstrated that increasing stress relaxation enhanced both GSC marker expression and chemotherapy sensitivity (Figures 3 and 4). This correlation mimics previous in vivo findings, in which tumors with enriched GSCs showed enhanced drug sensitivity to TMZ.[44,45] However, there exists conflicting reports suggesting GSCs can evade drug treatment, contributing to overall GBM drug resistance and tumor growth.[46,47] While normal neural stem cells are quiescent, GSCs may present varying degrees of stemness with distinct proliferative capacities, which may explain conflicting findings on GSC susceptibility to chemotherapy.[48] In addition, it has also been suggested that TMZ treatment can induce a phenotypic shift in which GSCs adaptively transition from a sensitive to a more drug resistant state.[49] Future studies can harness this 3D model to characterize the drug resistant cell subpopulation after initial chemotherapeutic treatment to better understand the relationship between GSCs and chemotherapy. It should be noted that TMZ response has also been found to be patient cell-line specific and may depend on other factors such as methylated O^6-DNA methylguanine-methyltransferase status in the patient's tumor.[50] Future studies can therefore utilize this 3D viscoelastic GBM model to investigate other potential mechanisms GBM cells use to evade chemotherapeutic treatment.

2.5. Cytoskeletal Tension is Required for Stress Relaxation-Induced Glioblastoma Multiforme Spreading, Motility, and Chemosensitivity

Given that the cytoskeleton plays a major role in governing how cells sense and transduce mechanical cues from their environment,[51–53] we next probed how tuning stress relaxation impacts D-270 MG cytoskeletal organization. Immunostaining was performed for 2 key cytoskeletal markers, F-actin and myosin-IIa. Increasing stress relaxation enhanced cell spreading and promoted the formation of robust actomyosin stress fiber bundles (**Figure** 5a), characteristic of a high-tensional state.[54] Furthermore, distinct F-actin organization was observed across the hydrogel groups. D-270 MG cells in slow-relaxing hydrogels displayed cortical F-actin with narrow protrusions penetrating the matrix; however, as stress relaxation was increased, F-actin stress fibers were visibly discrete and elongated (Figure 5a).

We next assessed whether the actomyosin cytoskeleton is required for GBM cells to assume invasive phenotype in response to stress relaxation. Two common cytoskeletal inhibitors were used — blebbistatin (a myosin II inhibitor) and cytochalasin-D (an actin polymerization inhibitor) — to disrupt the actomyosin cytoskeleton. Both inhibitor treatments significantly diminished D-270 MG cell spreading and reduced myosin-IIa staining signal

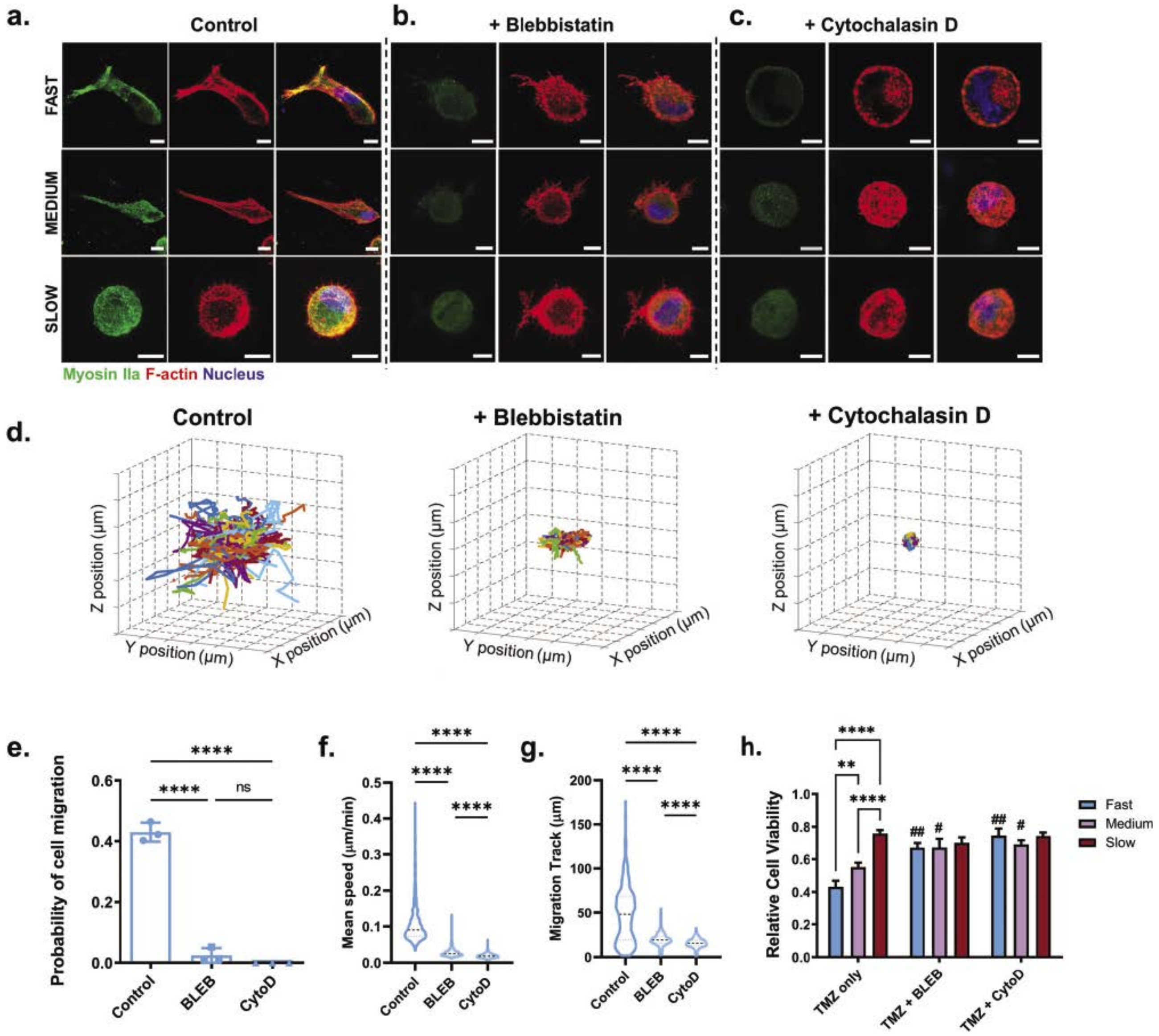

Figure 5. Stress relaxation enhances cytoskeletal formation in GBM cells in 3D, and pharmacologically disrupting the cytoskeleton abrogates stress relaxation-induced GBM spreading, migration and drug sensitivity. a–c) Representative immunostaining images of D-270 MG cells for myosin IIa (green), F-actin (red), and nucleus (blue) within fast-, medium-, and slow-relaxing hydrogels on day 3: a) Vehicle-alone (control), b) a myosin inhibitor (+ Blebbistatin), or c) an inhibitor of actin polymerization (+Cytochalasin D). Scale bar, 10 μm. d) Representative 3D track reconstructions for cell migration in fast-relaxing hydrogels with vehicle alone, Blebbistatin, or Cytochalasin D treatment from time-lapse imaging. 80 randomly selected cell migration track trajectories are shown for each condition. Grid size, 10 μm. e–g) Analysis of cell migration track data from time-lapse imaging: e) Probability of cell migration, f) mean speed, and g) migration track length of cells tracked within fast-relaxing hydrogels. One-way ANOVA with Tukey's multiple comparisons test was used for data analyses: ns, not significant; ****$p < 0.0001$; $n = 670$, 845, and 710 (control, BLEB, and CytoD) cells tracked across 3 independent biological replicates. Bars indicate mean value ± s.d. The dashed lines in the violin plots represent median values. h) Relative cell viability of D-270 MG cells treated with Temozolomide (TMZ only), TMZ with Blebbistatin (TMZ + BLEB), or TMZ with Cytochalasin D (TMZ + CytoD). Two-way ANOVA with Tukey's multiple comparisons test was used for analysis of the data: **$p < 0.01$, ****$p < 0.0001$; comparison with TMZ only: #$p < 0.01$, ##$p < 0.0001$; $n = 3$ independent biological replicates per condition. Data reported represent mean value ± s.d.

across all hydrogel groups relative to the control. Interestingly, subtle differences in F-actin formation and organization were observed when treated with either blebbistatin or cytochalasin-D. Although the F-actin stress fibers were completely disorganized due to blebbistatin treatment, cells extended disjointed protrusions into the matrix of all hydrogel groups. However, upon cytochalasin-D treatment, cells were completely rounded with F-actin displaying large puncta-like formations regardless of the degree of stress relaxation (Figure 5a–c). These results suggest that enhanced cell spreading within fast stress-relaxing hydrogels is mediated through the actomyosin cytoskeleton. Since GBM cell migration has been demonstrated to depend on actomyosin-generated contractile forces,[55] we also examined how disrupting the actomyosin cytoskeleton would impact GBM migratory potential within fast-relaxing hydrogels, which best recapitulated the stress relaxation properties of brain tissues. Live-cell tracking analysis from time-lapse imaging confirmed both blebbistatin and cytochalasin-D treatments drastically reduced GBM cell motility (Figure 5d–g, Movies S4–S6, Supporting Information). Together, these results indicate that the actomyosin cytoskeleton is required for GBM cells to sense and respond to the viscoelastic matrix cues.

Having established the importance of the cytoskeleton in mediating stress relaxation-induced GBM spreading and migration, we further tested if the cytoskeleton is required for cells to respond to TMZ within viscoelastic matrices. Remarkably, blebbistatin or cytochalasin-D treatment largely abolished stress relaxation-induced changes in TMZ response (Figure 5h). A similar trend was observed in U-87 MG cells within fast-relaxing hydrogels (Figure S7, Supporting Information). These data validate that stress relaxation sensitizes GBM cells to chemotherapy through the enhanced cytoskeletal organization. Cytoskeletal organization and tension have been shown to impact cell proliferation, and interfering actomyosin contractility can inhibit cell proliferation.[56,57] Therefore, disrupting stress relaxation induced actomyosin tension could potentially reduce TMZ response by inhibiting cell proliferation.

2.6. Stress Relaxation Promotes Transient Receptor Potential Vanilloid-Type 4 Expression, and Modulating Transient Receptor Potential Vanilloid-Type 4 Activity Impacts Glioblastoma Multiforme Cytoskeleton, Motility, and Drug Response

Recent studies have demonstrated that the TRPV4 calcium ion channel is an important molecular sensor of matrix viscoelasticity.[32,58] Interestingly, TRPV4 is upregulated in GBM, negatively correlates with patient prognosis, and plays a significant role in glioma motility and invasion.[59,60] Moreover, in GBM and other cancers, TRPV4 has been found to be involved in cytoskeletal regulation, specifically impacting F-actin organization.[59,61,62] However, previous studies on TRPV4 in GBM were limited to 2D studies. Therefore, it remains unknown how TRPV4 regulates GBM behavior such as spreading, migration and drug response within a 3D brain-mimicking viscoelastic matrix.

To fill in this gap of knowledge, we first characterized TRPV4 expression in GBM cells in 3D hydrogels with tunable stress relaxation. Both immunostaining and western blot showed increasing stress relaxation led to significantly higher TRPV4 expression by GBM cells (**Figure 6**a–c). Minimal TRPV4 expression was detected by immunostaining at day 0 (Figure S8a, Supporting Information), suggesting that stress relaxation promotes TRPV4 expression over time. To further interrogate how modulating TRPV4 level regulates GBM cell behavior in fast-relaxing hydrogels, TRPV4 activity was modulated using an agonist (GSK101) and an antagonist (GSK205). For GBM cell spreading, antagonist treatment severely disrupted the F-actin cytoskeletal organization, resulting in a rounded cell morphology, whereas agonist treatment showed no significant change in F-actin organization or cell spreading compared to control (Figure 6d). Within medium- and slow-relaxing hydrogels, modulating TRPV4 activity with GSK101 and GSK205 resulted in minimal to modest changes in F-actin organization compared to control groups (Figure S8b, Supporting Information). This was expected since TRPV4 expression diminished as stress relaxation decreased (Figure 6a–c).

We next assessed how TRPV4 modulation impacts stress relaxation induced GBM migration in fast stress-relaxing hydrogels. Given TRPV4 antagonist treatment drastically disrupts F-actin organization, we hypothesized that blocking TRPV4 activity would also reduce GBM migratory ability within fast-relaxing hydrogels, similar to the trend observed when the GBM actomyosin cytoskeleton was disrupted (Figure 5b–e). As expected, inhibiting TRPV4 with GSK205 significantly reduced GBM cell motility based on cell tracking analysis, while activating TRPV4 with GSK101 showed no difference to control group (Figure 6e–h, Movies S4, S7, S8, Supporting Information).

Since disrupting the cytoskeleton reduced stress relaxation-induced drug sensitivity (Figure 5f), we further hypothesized that TRPV4 inhibition would reduce drug sensitivity due to its effect on F-actin organization. Indeed, TRPV4 inhibition with GSK205 decreased drug sensitivity (Figure 6i). Interestingly, TRPV4 agonist GSK101 significantly increased TMZ sensitivity (Figure 6i), which correlated with significantly higher intracellular calcium levels in D-270 MG cells treated with GSK101 (Figure 6j). This suggests that GBM drug sensitivity to TMZ in viscoelastic hydrogels is mediated through TPRV4 signaling and correlates with intracellular calcium level. Due to lower TRPV4 expression within medium- and slow-relaxing hydrogels (Figure 6a–c), GSK101 and GSK205 treatment showed modest to no effect on intracellular calcium levels (Figure S8c,d, Supporting Information) and minimal effect on GBM TMZ drug response (Figure S8e, Supporting Information). Together, we demonstrate that TRPV4 plays a crucial role in stress relaxation-induced GBM spreading, migration, and drug response. In other words, our findings highlight that TRPV4 expression and activity in GBM is dependent on cells sensing a brain-mimicking viscoelastic environment. Moreover, these results suggest pharmacological modulation of TRPV4 activity may offer a promising strategy to reduce GBM invasion and improve chemosensitivity but done in a spatiotemporally controlled manner to minimize undesirable side effects given TRPV4's role in various physiological processes.[63]

Consistent with our observation that TRPV4 activation enhances TMZ sensitivity (Figure 6i,j), previous work has demonstrated that calcium influx triggered by activation of another mechanosensitive ion channel, TRPV2, resulted in increased GBM chemosensitivity. Specifically, TRPV2 triggered calcium influx enhanced drug uptake and synergistically induced GBM apoptosis.[64] Other mechanosensitive ion channels such as TRPM7 and PIEZO1 can be further investigated as they have been shown to be associated with brain cancer progression,[63,65] and may also be involved in regulating GBM response to stress relaxation.

2.7. Increasing Stress Relaxation Reduces Nascent Protein Deposition, which Correlates with Higher Drug Sensitivity

Finally, the tumor ECM can act as barrier shielding cancer cells from cytotoxic agents.[66] A recent study showed that local nascent protein deposition and remodeling can directly impact

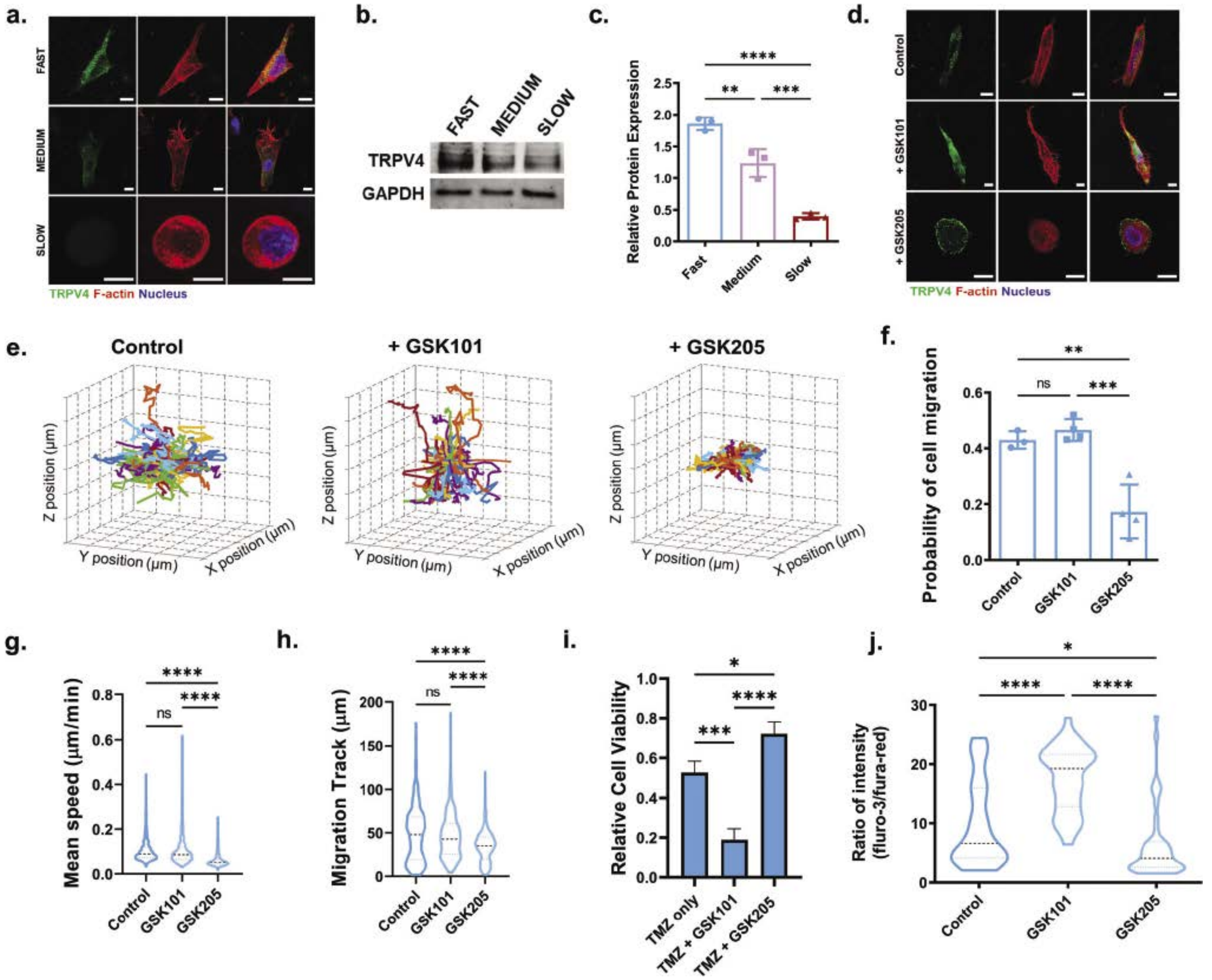

Figure 6. Stress relaxation promotes TRPV4 expression in 3D, and modulating TRPV4 activity impacts GBM cytoskeleton, migration, and drug response. a) Representative immunostaining images of D-270 MG cells for TRPV4 (green), F-actin (red), and nucleus (blue) within fast-, medium-, and slow-relaxing hydrogels on day 3. Scale bar, 10 µm. b) Western blot analysis of TRPV4 for cells in fast-, medium-, and slow-relaxing hydrogels. c) Quantification of TRPV4 expression normalized to GAPDH from western blot. One-way ANOVA with Tukey's multiple comparisons test was used for analysis of the data: ns, not significant; $**p < 0.01$, $***p < 0.001$, $****p < 0.0001$; $n = 3$ independent biological replicates per group. Data reported represent mean value ± s.d. d) Representative immunostaining images of D-270 MG cells for TRPV4 (green), F-actin (red), and nucleus (blue) within fast-relaxing hydrogels treated with vehicle-alone (control), a TRPV4 agonist (GSK101), or a TRPV4 antagonist (GSK205). Scale bar, 10 µm. e) Representative 3D track reconstructions for cell migration in fast-relaxing hydrogels with vehicle-alone (control), GSK101, or GSK205 treatment from time-lapse imaging. 80 randomly selected cell migration track trajectories are shown for each condition. Grid size, 10 µm. f–h) Analysis of cell migration track data from time-lapse imaging: e) Probability of cell migration, f) mean speed, and g) migration track length of cells. One-way ANOVA with Tukey's multiple comparisons test was used for analysis of the data: ns, not significant; $****p < 0.0001$; $n = 670$, 913, and 777 (control, GSK101, and GSK205) cells tracked across 3 independent biological samples. Bars indicate mean value ± s.d. The dashed lines in the violin plots represent median values. i) Relative cell viability of D-270 MG cells treated with TMZ only, TMZ + GSK101, or TMZ + GSK205. One-way ANOVA with Tukey's multiple comparisons test was used for analysis of the data: $*p < 0.05$, $***p < 0.001$, $****p < 0.0001$; $n = 3$ independent biological replicates per condition. Data reported represent mean value ± s.d. j) Intracellular calcium level in D-270 MG cells in fast-relaxing hydrogels treated with vehicle-alone (control), GSK101, or GSK205 treatment. One-way ANOVA with Tukey's multiple comparisons test was used for analysis of the data: $*p < 0.05$, $****p < 0.0001$; $n = 43$, 37, and 46 (control, GSK101, and GSK205) cells across 3 independent biological samples. The dashed lines in the violin plots represent median values.

mesenchymal stem cell mechanosensing and signaling in 3D hydrogels.[67] However, it remains unknown how stress relaxation impacts GBM nascent protein deposition. We next investigated if stress relaxation-induced changes in GBM drug response is mediated through changes in nascent protein deposition. Using immunostaining, we first determined the effects of tuning stress relaxation on nascent protein deposition by GBM cells in our 3D hydrogel model. Common ECM components in the brain tumor microenvironment were assessed including laminin, fibronectin, and collagen-IV. GBM cells in the slow-relaxing

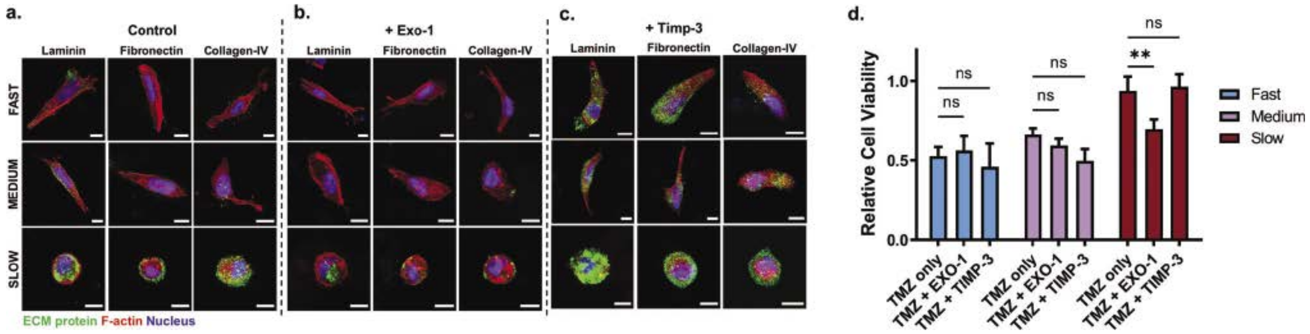

Figure 7. Stress relaxation reduces nascent protein deposition by GBM cells in 3D, which correlates with higher drug sensitivity. Pharmacological inhibition of nascent protein deposition increases GBM drug sensitivity in slow-relaxing hydrogels. a–c) Representative immunostaining images of D-270 MG cells for ECM proteins (Laminin, Fibronectin, or Collagen-IV; green), F-actin (red), and nucleus (blue) on day 3 within fast-, medium-, and slow-relaxing hydrogels. Samples were treated with a) vehicle-alone (control), b) an inhibitor of nascent protein deposition (+Exo-1), or c) an inhibitor for matrix remodeling (+TIMP-3). Scale bar, 10 µm. d) Relative cell viability of D-270 MG cells treated with Temozolomide (TMZ only), TMZ with Exo-1 (TMZ + Exo-1), or TMZ with TIMP-3 (TMZ + TIMP-3). Two-way ANOVA with Tukey's multiple comparisons test was used for analysis of the data, comparing with TMZ only condition: ns, not significant; $^{**}p < 0.01$; $n = 3$ independent biological replicates per condition. Data reported represent mean value ± s.d.

hydrogels demonstrated the highest amount of nascent protein deposition for all tested ECMs, and increasing stress relaxation significantly reduced the amount of nascent protein deposition (**Figure 7**a).

To further probe the effect of modulating nascent protein deposition on TMZ drug response, D-270 MG cells were treated with either Exo-1 or TIMP-3, 2 inhibitors that either disrupt nascent protein deposition or remodeling, respectively. Immunostaining confirmed Exo-1 treatment significantly reduced nascent protein deposition in slow-relaxing hydrogels. Minimal change was observed in cells within fast- and medium-relaxing hydrogels given that the baseline nascent protein deposition was low (Figure 7a,b). Conversely, TIMP-3 treatment enhanced nascent protein accumulation around cells in all groups due to reduced remodeling, especially laminin in slow-relaxing hydrogels (Figure 7c). It is important to note that use of Exo-I or TIMP-3 displayed minimal disruption to the cytoskeleton (Figure 7a–c). In slow-relaxing hydrogels, where nascent protein deposition was the highest, Exo-1 treatment significantly increased drug sensitivity (Figure 7d), indicating that decreasing nascent protein deposition may reduce the cytoprotective barrier to treatment. TIMP-3 treatment within slow-relaxing hydrogels did not significantly impact drug response, suggesting that the baseline ECM deposited was sufficient in providing a cytoprotective barrier. For fast- and medium-relaxing hydrogels, where the baseline ECM was low (Figure 7a), Exo-1 or TIMP-3 treatment had no significant effect in drug response (Figure 7d).

Overall, we find that increasing stress relaxation reduces nascent protein deposition by GBM cells in 3D. Given that the tumor ECM can act as barrier shielding cancer cells from cytotoxic agents,[66] our results suggest fast stress relaxation-induced drug sensitivity in GBM cells is in part mediated through reduced nascent protein deposition around the GBM cells. Previous work in small cell lung cancer has demonstrated that adhesion to ECM proteins confers resistance to chemotherapeutic agents via β1-integrin dependent survival signals.[68] Given that modulating nascent protein deposition and remodeling minimally effected the cytoskeleton or drug responses of GBM cells in fast-relaxing hydrogels, these findings suggest both cytoskeletal organization and nascent protein deposition contribute to stress relaxation-induced changes in GBM drug response in a brain-mimicking niche.

3. Conclusion

In summary, this study established a dynamically crosslinked PEG hydrogel system with tunable stress relaxation and brain-mimicking stiffness as a tool to elucidate the role of viscoelasticity on GBM cell behavior and drug response in 3D. Our findings reveal the critical role of stress relaxation in modulating key GBM features and drug responses (**Figure 8**). Specifically, brain-mimicking, fast-relaxing hydrogels promoted invasive GBM behavior such as cell spreading, migration, proliferation, and GSC marker expression. Strikingly, these hallmark GBM features were largely lost in slow-relaxing hydrogels, indicating that viscoelasticity is a critical niche cue regulating GBM disease progression in vivo. Importantly, we demonstrate that GBM drug sensitivity is directly impacted by stress relaxation, highlighting the importance of incorporating viscoelasticity in 3D in vitro GBM models used for drug screening and prediction of in vivo drug efficacy. Leveraging this hydrogel as a tool for mechanistic study, we identified that the actomyosin cytoskeleton is an essential mediator of stress relaxation in GBM cells. Linked to the cytoskeleton and an important mechanosensitive ion channel, TRPV4 was also found to be regulated by stress relaxation, and modulation of TRPV4 activity impacts GBM behavior. We further elucidated that stress relaxation impacts GBM drug response through enhanced cytoskeletal organization, upregulated TRPV4 activity, and reduced nascent protein deposition. We envision that this dynamically crosslinked PEG-hydrogel GBM model could provide a powerful tool for discovering novel therapeutics for GBM that would be otherwise missed using in vitro GBM models lacking viscoelasticity.

4. Experimental Section

Synthesis of Eight-Arm Poly(ethylene-glycol) Hydrazine: Eight-arm PEG amine (10 kDa, 2 g, Jenkem Technology) and tri-Boc-hydrazinoacetic acid

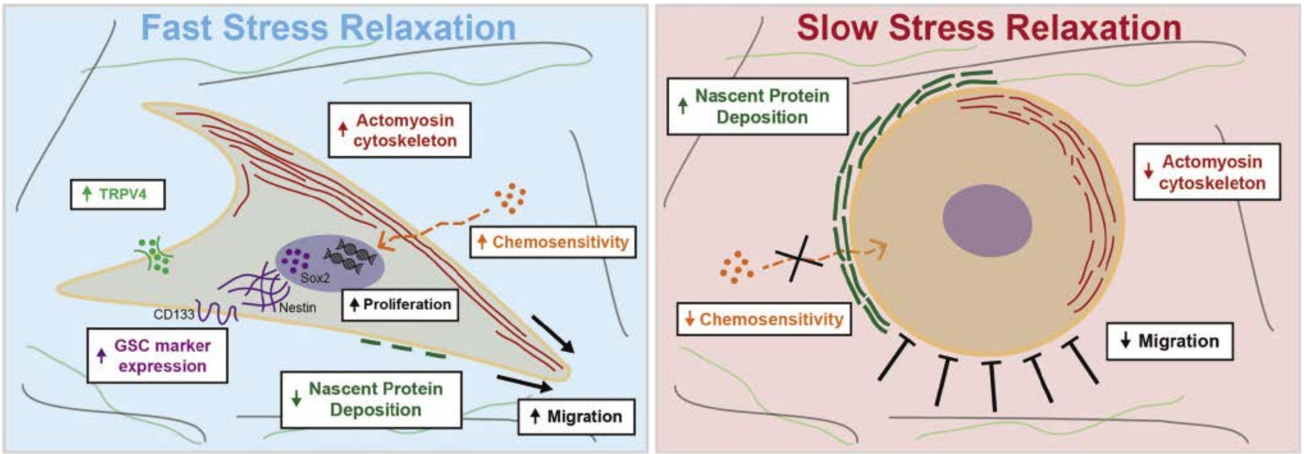

Figure 8. A summary schematic of the key findings on the effect of stress relaxation on GBM cell fates and drug responses in 3D. Brain-mimicking, fast-relaxing hydrogels (left panel) promote GBM drug sensitivity and enhances GBM invasive phenotype including cell spreading, migration, and proliferation. Stress relaxation induced drug sensitivity is associated with enhanced actomyosin cytoskeletal formations, GSC marker expression, TRPV4 activity, and reduced nascent protein deposition. Conversely, slow-relaxing hydrogels (right panel) reduce GBM drug sensitivity and induces opposite trends in corresponding cell fates.

(0.93 g, 1.5 eq per amine, Sigma-Aldrich) were dissolved dichloromethane (DCM, 50 mL), followed by the addition of EDC. HCl (0.61 g, 2.0 eq per amine, Sigma-Aldrich). The reaction was stirred overnight at room temperature (RT). The product was precipitated in cold ether and vacuum dried. The obtained product was then added in 50:50 DCM:TFA for 2 h. The resulting solution was then precipitated in ether, vacuum dried, and then dialyzed (MWCO 1 kDa) against DI water for 2 days. The solution was then lyophilized to get the final product.

Synthesis of Eight-Arm Poly(ethylene-glycol) Alkyl-Aldehyde: Eight-arm PEG-OH (10 kDa, 2 g, Jenkem Technology), TEMPO (12.5 mg, 0.1 eq hydroxyl, Sigma-Aldrich), and diacetoxyiodo benzene (DAIB, 0.77 g, 3 eq hydroxyl, Sigma-Aldrich) were dissolved in DCM (50 mL) and stirred overnight. The solution was then precipitated in cold ether and dialyzed (MWCO 1 kDa) against DI water for 2 days and lyophilized.

Synthesis of Eight-Arm Poly(ethylene-glycol) Benzyl-Aldehyde: Eight-arm PEG-OH (10 kDa, 2 g) and 4-formyl benzoic acid (0.56 g, 1.5 eq hydroxyl, Sigma-Aldrich) were dissolved in DCM, followed by the addition of *N*,*N*'-diisopropylcarbodiimide (0.2 g, 2.0 eq hydroxyl). The reaction was stirred overnight at room temperature and then precipitated in ether to get the product. The obtained product was dialyzed (MWCO 1 kDa) against DI water for 2 days and lyophilized. As previously reported,[21,22] ^{1}H NMR spectroscopy was used to estimate the degree of modification on the PEG macromers (Figure S1, Supporting Information).

Rheological Characterization: Rheological measurements were carried out using a Discovery HR-2 hybrid rheometer (TA Instruments) equipped with 25-mm-diameter top and bottom plates. IPN hydrogels, used for mechanical testing, were directly deposited onto the bottom plate of the rheometer immediately after mixing all IPN hydrogel precursor components together (100 µL final volume). The top plate was immediately lowered and gently spun to spread the hydrogel solution across the plates, forming a 25-mm disk hydrogel. Mineral oil (Sigma) was applied at the edges to prevent sample dehydration. During the gelation period, a time sweep was performed in which the rheometer geometry was oscillated at an amplitude of 1% shear strain and 1 Hz frequency for 1 h at 37 °C. As the gelation completed and the storage and loss moduli had equilibrated, Young's modulus (E) was calculated from the equation:

$$E = 2\,(1 + \nu)\,G^* \tag{1}$$

where Poisson's ratio (ν) is assumed to be 0.5 and G^* is the complex modulus found using the equilibrium values of storage and loss moduli measured. G^* was calculated using:

$$G^* = \left(G'^2 + G''^2\right)^{1/2} \tag{2}$$

Equilibrium values of storage and loss moduli were also used to calculate the loss tangent, which is defined as:

$$\text{Loss tangent }(\tan\delta) = \frac{\text{Loss modulus }(G'')}{\text{Storage modulus }(G')} \tag{3}$$

Next, frequency sweep was performed from 0.1 to 100 rad s^{-1} at 1% constant strain and held at 37 °C. The resulting storage and loss moduli values were measured as function of oscillation frequency (ω). Finally, after the frequency sweep, stress relaxation measurements were conducted at which a constant strain of 10% was applied to the hydrogel at 37 °C. The resulting storage modulus and stress were recorded over the course of 1 h for fast and medium IPNs and 7 h for slow IPNs.

To demonstrate physiological relevance of the IPN hydrogel system, rheological characterization was conducted on mouse brain. Briefly, FVB domestic mice (female, 11 weeks of age, Charles River Lab) were euthanized in compliance with NIH and institutional guidelines. Brain was collected immediately after euthanization, and the same rheological testing procedure, as previously described above, was conducted except for the following. The rheometer was equipped with 20-mm x-Hatch top and bottom plates to minimize sample slippage.

Hydrogel Preparation: Functionalized PEG macromers were dissolved in phosphate buffered saline (PBS) and neutralized to pH 7.0 (15% w/v). IPN hydrogels were prepared by mixing stock solutions of PEG-H, reconstituted collagen-I (TeloCol-10, Advanced Biomatrix), and PEG-aldehyde (PEG alkyl-aldehyde (PEG-AA) and/or PEG benzyl-aldehyde (PEG-BA)) in this successive order. The hydrazine to aldehyde ratio was 1:1 with a final PEG polymer concentration of 2.5% (w/v). To tune the stress relaxation by varying the AH:BH crosslink ratio, the PEG-AA to PEG-BA ratio within the PEG-aldehyde component was adjusted to the following: 100:0, 70:30, or 0:100. A final collagen-I concentration of 2.5 mg mL^{-1} was used and neutralized to pH 7.0 after addition into precursor solution. Finally, after addition of PEG-aldehyde, the hydrogel precursor solution was gently mixed for 1 min before either depositing directly for rheological testing or pipetting into a mold for cell-based studies (described further below).

Cell Culture: A patient-derived human glioblastoma xenograft (PDTX GBM) cell line (D-270 MG) was provided by the laboratory of Dr. Gerald

Grant at Stanford University Medical Center and derived as previously reported.[69,70] D-270 GBM cells were cultured in improved minimal essential zinc option medium (Life Technologies) with 10% fetal bovine serum (FBS, Gibco, Life Technologies) and 0.1% gentamicin (Life Technologies). An immortalized GBM cell line (U-87 MG) was purchased from ATCC and were expanded in cell culture medium consisting of Dulbecco's minimal essential medium (Life Technologies), supplemented with 10% (v/v) FBS (Gibco, Life Technologies), 100 U mL^{-1} penicillin, and 100 µg mL^{-1} streptomycin. Cells were cultured in standard humidified incubator at 37 °C in a 5% (v/v) CO_2 atmosphere.

3D Cell Encapsulation in Hydrogels: For cell encapsulation, GBM cells were trypsinized using trypsin/EDTA, washed, centrifuged, and resuspended in media. Prior to the addition of PEG-aldehyde, trypsinized GBM cells were homogenously mixed into the hydrogel precursor solution at a final concentration of 1.25 ᴍ mL^{-1}. The cell-containing hydrogel precursor solution (55 µL) was dispensed into a cylindrical shaped mold (3 mm in height, 5 mm in diameter). Cell-laden hydrogels were incubated at 37 °C for 40 min and then pushed out into pre-warmed media. All experiments were carried for 3 days in 24 well plates unless otherwise specified. To assess cell viability of GBM cells within hydrogels shortly after encapsulation and at days 3 and 6, D-270 MG cells were stained with LIVE/DEAD Viability/Cytotoxicity Kit (Invitrogen) per manufacturer's instructions for 20 min in PBS. Images were taken using Leica STELLARIS 5 confocal microscope with HC PL APO 10x/0.40 air objective.

Swelling Ratio and Polymer Retention Measurements: Acellular hydrogels (55 µL) were prepared as described above, transferred to a 24-well plate with 1 mL D-270 MG media per well, and incubated at 37 °C. The swelling ratio (Q) was calculated based on the following formula:

$$Q = \frac{W\mathrm{wet}}{W\mathrm{dry}} \tag{4}$$

where W_{wet} is the wet weight of the hydrogel at a specified time and W_{dry} is the initial dry weight of the hydrogel at the beginning of the experiment. To measure the initial W_{dry} for each group, separate hydrogels were collected several hours after hydrogel formation and freeze-dried. After 6 days, hydrogels were freeze-dried to calculate the polymer retention

$$\%\ \mathrm{Polymer\ retention} = \frac{W\mathrm{dry,\ day0}}{W\mathrm{dry,\ day6}} \times 100\% \tag{5}$$

and equilbirum mass swelling ratio

$$\left(Q = \frac{W\mathrm{wet,\ day6}}{W\mathrm{dry,\ day6}} \right) \tag{6}$$

Cell Morphology Quantification: To assess the cell morphology and quantify cell roundness, the cell membrane of D-270 MG and U87 cells were stained with octadecyl rhodamine B chloride (R18, 1:1000 dilution, stock 10 mg mL^{-1}; Thermo Fisher Scientific) on day 3. Briefly, R18 dye was added to cell culture medium and allowed to incubate with cell-laden hydrogels for 1 h. Hydrogels were then washed 3 times with PBS. Cells within the hydrogels were then immediately imaged using a Leica STELLARIS 5 confocal micrscope with a HC FLUOTAR L 25x/.95 numerical aperture (NA) water immersion objective. ImageJ analyze particles function was used on maximum projections from obtained z-stacks from confocal imaging to quantify cell roundness.

Tracking Cell Motility in 3D Using Time-Lapse Confocal Imaging: For cell motility studies, D-270 MG cells were starved overnight in serum-free medium and then trypsinized and encapsulated in hydrogels. For high magnification live-cell time-lapse imaging to capture single cell motility, cell-laden hydrogels were cast directly into wells of a chambered coverglass (LabTek). The hydrogels were allowed to incubate at 37 °C for 40 min, and then were incubated with normal D-270 MG growth media. After one day, brightfield confocal microscopy was used to acquire live-cell images at 15 min intervals for a total of 3 h using a Leica STELLARIS 5 confocal microscope with HC PL APO 63x/1.40 NA oil immersion objective.

To track and analyze cell motility on the population level, D-270 cells were also starved overnight in serum free medium. Prior to encapsulation, D-270 MG cell membranes were labeled with R18 (1:1000 dilution, stock 10 mg mL^{-1}; Thermo Fisher Scientific). Cell-laden hydrogel precursor solutions were then cast into custom made PDMS molds within a 35 mm petri dish to provide sufficient medium volume and ensure high cell viability during the imaging time course. Once cast, hydrogels were allowed to incubate at 37 °C for 40 min. After hydrogel gelation, serum-free starvation medium was added. For inhibitor studies against the cytoskeleton or TRPV4, serum-free starvation medium was supplemented with vehicle-alone or inhibitor. One day later, serum-free starvation medium was removed and replaced with D-270 MG growth media 3 h prior to the start of imaging. For inhibitor studies, serum-free starvation medium with vehicle-alone or inhibitor was replaced by D-270 MG growth media supplemented with vehicle-alone or inhibitor 3 h prior to the start of imaging. Live-cell imaging was conducted at 25 min intervals for at least 14 h using a Leica STELLARIS 5 confocal microscope with HC PL APO 10x/0.40 air objective. 62.5 µm z-stack images were acquired for each position at each time point. The mark-and-find feature of the Leica software was used to capture multiple fields of views across multiple samples at every time point. For all time-lapse experiments, hydrogels were placed in an incubated chamber (37 °C and 5% CO_2). We note that control conditions were added along with the experimental conditions in each time-lapse experiment.

Imaging Analysis: For cell migration studies, Imaris software (Bitplane) was used to track R18 stained D-270 MG cells from live-cell time-lapse confocal imaging. Briefly, a surface rendering analysis in Imaris was performed to track cell migration along the recorded time frames and z-stacks. The parameters that were used were adapted from previously established methods.[71] Cells that were at the edge of the field of view were excluded from analysis. Built in drift correction in Imaris was used as necessary. A custom MATLAB script was used to reconstruct 3D cell migration trajectories from cell track position output analysis. To calculate the probability of cell migration, cells were binned into nonmotile and motile populations, in which the threshold for a motile cell was a track displacement length of at least 15 µm over the 14 h time-lapse. Finally, mean track speed and track length were used to further assess differences among cells cultured in different stress relaxing hydrogels.

Inhibitor Treatments Used in Live-Cell Imaging and Drug Response Studies: The following inhibitors and their respective concentrations were used: blebbistatin (250 µM; Abcam, ab120425), cytochalasin-D (500 nM; Sigma-Aldrich, C8273), GSK1016790A (GSK101, 50 nM; Abcam, ab146191), GSK205 (10 µM; Aobious, AOB1612), Exo-1 (120 nM, EMD Millipore, 341220), TIMP-3 (5 nM; R&D Systems, 973-TM-010). DMSO was the vehicle-alone control for blebbistatin, cytochalasin-D, GSK101, GSK205, and Exo-1. Deionized water was used as the vehicle control for TIMP-3 treatment.

Drug Response: As previously described, GBM cells were encapsulated and cultured within hydrogels for 3 days. At day 3, fresh medium was added with either temozolomide (TMZ, Sigma-Aldrich, T2577) or Carmustine (BCNU, Sigma-Aldrich, C0400). Concentrations used for both TMZ and BCNU were the following: 3, 30, 100, 300, 600, and 1000 µM. Hydrogels were cultured in medium supplemented with drug for an additional 3 days. Based on manufacturer's instructions, Presto Blue cell viability reagent (Thermo Fisher Scientific) was used to measure the cell viability at the end of the drug treatment period (day 6). For both TMZ and BCNU, DMSO was used as the vehicle control. Relative cell viability was calculated by normalizing treatment groups to untreated vehicle alone control.

For drug response studies using inhibitors in combination with TMZ, a similar procedure was used as described above with the following exceptions. Inhibitors targeting the actomyosin cytoskeleton (blebbistatin and cytochalasin-D) or modulating TRPV4 activity (GSK101 and GSK205) were added 24 h prior to TMZ administration. Inhibitors for nascent protein deposition and remodeling (Exo-1 and TIMP3) were added shortly after encapsulation and replenished halfway through the initial 3-day culture period. All inhibitors were replenished in fresh medium along with TMZ (300 µM) at day 3, the start of drug treatment.

To halt cellular proliferation, D-270 MG cells were treated with mitomycin C (10 µg mL^{-1}; Abcam, ab120797) for 2 h prior to trypsinization and encapsulation. Similar to the procedure above, mitomycin C treated cells were then encapsulated within hydrogels, cultured for 3 days, and then treated with vehicle-alone control or TMZ (300 µM) for an additional 3 days. Relative cell viability was calculated by normalizing treatment groups to their respective untreated vehicle alone control.

Inhibitor Treated Hydrogels for Immunofluorescence: For immunofluorescence of hydrogels treated with inhibitors, a similar timeline of administration was followed to that of the drug response studies. This was done to assess the cytoskeleton or baseline expression of interested markers at the start of drug treatment. Briefly, actomyosin cytoskeletal inhibitors (blebbistatin and cytochalasin-D) and TRPV4 agonist (GSK101) and antagonist (GSK205) were added 24 h prior to sample fixation (or on day 2). Nascent protein deposition and remodeling inhibitors (Exo-1 and TIMP3) were added shortly after encapsulations and replenished halfway through the 3-day culture period before fixation on day 3. Hydrogels treated with blebbistatin and cytochalasin-D were saved for whole-gel staining. All other inhibitor treated hydrogels were sectioned for staining.

Immunofluorescence Imaging of Sectioned and Whole-Gel Samples: To prepare samples for immunofluorescence imaging, samples were harvested at day 0 or 3, fixed with 4% paraformaldehyde overnight at 4 °C, and then washed twice for 15 min at RT while gently shaking. Fixed samples were prepared for either sectioned or whole-gel staining. For sectioned samples, fixed samples were dehydrated in optimal cutting temperature (OCT, Tissue-Tek) overnight at room temperature (RT). Samples were embedded into molds surrounded by OCT solution and frozen at −80 °C for at least 20 min. Sections of 30 µm were cut using a Leica CM3050 S Research Cryostat. For whole-gel staining, fixed hydrogels were immediately used for staining.

For expression of Nestin, CD133, TRPV4, laminin, fibronectin, and collagen-IV, sectioned samples were stained using standard immunohistochemistry protocols. Sectioned samples were washed with DI water for 5 min, permeabilized with 0.25% Triton X-100 (Sigma-Aldrich) in DPBS for 5 min, and blocked with 3% bovine serum albumin, 0.1% Triton-X-100 in PBS for 1 h at RT. The samples were then incubated overnight at 4 °C with primary antibody. The following primary antibodies were used: Nestin (EMD Millipore, ABD69), CD133 (Abcam, ab19898), TRPV4 (Abcam, ab39260), Laminin (Abcam, ab11575), Fibronectin (Abcam, ab2413), Collagen-IV (Abcam, ab6586). All primary antibodies were used at 1:100 dilution. After washing 3 times with PBS, samples were incubated with secondary antibody goat anti-Rabbit IgG Alexa Fluor 488 (Invitrogen, A32731, 1:100 dilution) along with Hoechst 33 342 (Thermo Fisher Scientific, H3570, 1:1500 dilution) and ActinRed 555 (Thermo Fisher Scientific, R37112) overnight at 4 °C to stain for the nucleus and F-actin, respectively. Samples were washed 3 times with PBS and mounted in vectashield (Vector Laboratories). Confocal microscopy was used to acquire images using a HC PL APO 40x/1.30 oil immersion objective.

For expression of Myosin-IIa and Sox2, whole-gel staining was used. Fixed whole-gel samples were washed 3 times with PBS, permeabilized with 0.25% Triton X-100 (Sigma) in DPBS for 1 h, and blocked with 3% bovine serum albumin, 0.1% Triton-X-100 in PBS for 3 h at RT. The hydrogels were then incubated overnight at 4 °C with primary antibody while gently shaking. The following antibodies were used: Myosin-IIa (Cell Signaling Technology, 8824S, 1:100 dilution) and Sox2 (Cell Signaling Technology, 23064S, 1:400 dilution). After hydrogels were washed 3 times with PBS for 30 min at RT while gently shaking, samples were incubated with same secondary staining solution used for the sectioned samples overnight at 4 °C while gently shaking. Samples were washed 3 times with PBS for 30 min at RT. Images were acquired using a Leica STELLARIS 5 confocal microscope with HC PL APO 40 × /1.2 NA oil immersion objective.

Cell Proliferation: To measure cellular proliferation, Click-&-Go Plus EdU Cell Proliferation Kit (Click Chemistry Tools) was used. D-270 MG cells were encapsulated in hydrogels. On day 1, EdU was added to the culture medium (10 µM final concentration) and incubated with the hydrogels for 2 days. On day 3, cell-laden hydrogels were fixed and sectioned using the same method previously described for sample preparation for immunofluorescence. Following the manufacturer's instructions, EdU was stained along with the nucleus on sectioned samples. Images were acquired using a Leica STELLARIS 5 confocal microscope with HC PL APO 40 × /1.2 NA oil immersion objective. Custom script was used to quantify the %EdU positive cells from collected imaging data set.

Temozolomide Diffusion: Hydrogels were loaded with TMZ (2000 µM) and placed in PBS. PBS, along with the diffused TMZ, was collected at .5, 1, 2, 3, 5, 10, 24, and 32 h timepoints. At each collection timepoint, hydrogels were placed into fresh PBS. Using UV–vis spectroscopy, absorbance of the collected PBS samples was measured with a NanoDrop One/OneC (Thermo Scientific) at 328 nm for active TMZ. Absorbance values were converted into concentration based on a standard curve. The cumulative TMZ release was then calculated.

Imaging Collagen Network Using Confocal Reflectance Imaging: The collagen network within the different hydrogel formulations was imaged using the reflectance mode of the confocal microscopy. Samples prepared were acellular hydrogels and imaged on day 0 after hydrogel gelation to assess the initial collagen-I distribution within the matrix. Additionally, hydrogels were imaged on day 3 and day 6 to assess collagen-I distribution and retention over time. Images were acquired using a 647 nm laser light source along with Leica STELLARIS 5 confocal microscope with HC PL APO 63x/1.40 NA oil immersion objective.

Western Blot: For western blotting analysis, D-270 MG cell-encapsulated hydrogels were transferred to ice-cold 2X RIPA Lysis buffer (Millipore Sigma) containing 2X HaltTM Protease and Phosphatase inhibitor (ThermoFisher Scientific). For each group, western blot were performed with 3 biological replicates for quantitative analysis. For each individual replicate, 4 hydrogel samples were pooled together, with a total of 12 samples per group to ensure data robustness. The hydrogel samples were homogenized in the buffer and centrifuged, and the supernatant containing the lysate was collected. The protein amount in the lysate was quantified using PierceTM BCA Protein Assay Kit (ThermoFisher Scientific). 10 µg of protein from the lysate was separated by SDS-PAGE and transferred to polyvinylidene fluoride membranes. The membranes were blocked in blocking solution (5% BSA in 1X tris-buffered saline with Tween-20, TBST (Santa Cruz Biotechnology) at room temperature for 1 h. The membranes were then incubated in primary antibodies diluted in SuperBlockTM blocking buffers (ThermoFisher Scientific) overnight at 4 °C. The following primary antibodies were used at the mentioned dilutions: Nestin (EMD Millipore, ABD69, 1:25 000), CD133 (Abcam, ab19898, 1: 500), Sox2 (Cell Signaling Technology, 23064S, 1:1000), GFAP (Abcam, ab7260, 1:10 000), TRPV4 (Abcam, ab39260, 1:1000), and GAPDH (Cell Signaling Technology, 5174S, 1:50 000). Following primary antibody incubation, the membranes were washed 3 times with TBST for 5 min per wash and then incubated in HRP-conjugated secondary antibodies (goat anti-rabbit, Abcam, ab6721, 1:100 000 and donkey anti-mouse, Jackson ImmunoResearch, 715-035-151, 1:10 000) for 1 h at room temperature. The membranes were then washed thrice in TBST for 5 min per wash, developed with SuperSignal West Femto Maximum Sensitivity Chemiluminescent Substrate (ThermoFisher Scientific) for 5 min, and imaged using Invitrogen iBright CL1500 imaging system. Quantifications of band intensities were performed using ImageJ and band intensities were normalized to GAPDH as the loading control.

Calcium Imaging and Analysis: For intracellular calcium imaging, D-270 MG cells in hydrogels after day 3 of culture were incubated in D-270 MG growth media with Fura red AM (33 µM, ThermoFisher Scientific) and Fluo-3 AM (20 µM, ThermoFisher Scientific) for 1 h. The hydrogels were then washed 3 times with PBS. The intensities of the calcium dyes in the cells were captured using live-cell confocal microscopy with a Leica STELLARIS 5 confocal microscope with HC FLUOTAR L 25x/0.95 NA water immersion objective. Fluorescent intensities of Fura red and Fluo-3 were measured with excitation at 488 nm and detection at >610 nm for Fura red and between 515 and 580 nm for Fluo-3. Intracellular calcium concentration level was calculated as the ratio of Fluo-3 intensity to Fura red intensity. Custom MATLAB script was used for image processing and analysis.

Statistical Analysis: Statistical analyses were performed using GraphPad Prism Software. The statistical tests performed and corresponding p and n values are specified in the figure legends.

Supporting Information

Supporting Information is available from the Wiley Online Library or from the author.

Acknowledgements

The authors would like to acknowledge NIH R01DE024772 (F.Y.), R01AR074502 (F.Y.), and the Stanford Bio-X Interdisciplinary Initiative Program (F.Y.) for grant support. S.S. would like to thank the NIH F31 predoctoral fellowship (5F31CA246972-02) and Stanford NIH Biotechnology training program for support. M.A. would like to thank Stanford Interdisciplinary Graduate Fellowship for support. The authors would like to thank the Chaudhuri lab at Stanford University for kindly allowing the use of their lab's rheometer. S.S. would like to thank Dhiraj Indana for rheometer training, Dr. Julie Chang and Dr. Kolade Adebowale for introduction to Imaris software, Sarah Jones for assistance in ^{1}H NMR analysis, and Dr. Pranay Agrawal for assistance in image analysis. The authors also acknowledge the Stanford Cell Sciences Imaging Facility for Imaris software access and technical assistance.

Conflict of Interest

The authors declare no conflict of interest.

Data Availability Statement

The data that support the findings of this study are available from the corresponding author upon reasonable request.

Keywords

3D disease models, drug responses, glioblastoma multiforme, hydrogels, stress relaxation, viscoelasticity

Received: September 8, 2022
Revised: September 28, 2022
Published online: November 16, 2022

[1] Q. T. Ostrom, G. Cioffi, H. Gittleman, N. Patil, K. Waite, C. Kruchko, J. S. Barnholtz-Sloan, *Neuro-Oncology* **2019**, *21*, v1.
[2] W. Wu, J. L. Klockow, M. Zhang, F. Lafortune, E. Chang, L. Jin, Y. Wu, H. E. Daldrup-Link, *Pharmacol. Res.* **2021**, *171*, 105780.
[3] A. C. Tan, D. M. Ashley, G. Y. López, M. Malinzak, H. S. Friedman, M. Khasraw, *Ca-Cancer J. Clin.* **2020**, *70*, 299.
[4] A. Claes, A. J. Idema, P. Wesseling, *Acta Neuropathol.* **2007**, *114*, 443.
[5] S. Darmanis, S. A. Sloan, D. Croote, M. Mignardi, S. Chernikova, P. Samghababi, Y. Zhang, N. Neff, M. Kowarsky, C. Caneda, G. Li, S. D. Chang, I. D. Connolly, Y. Li, B. A. Barres, M. H. Gephart, S. R. Quake, *Cell Rep.* **2017**, *21*, 1399.
[6] J. D. Lathia, S. C. Mack, E. E. Mulkearns-Hubert, C. L. L. Valentim, J. N. Rich, *Genes Dev.* **2015**, *29*, 1203.
[7] J. M. Heffernan, R. W. Sirianni, *Front. Mater.* **2018**, *5*, 7.
[8] C. Wang, X. Tong, F. Yang, *Mol. Pharmaceutics* **2014**, *11*, 2115.
[9] C. Wang, S. Sinha, X. Jiang, L. Murphy, S. Fitch, C. Wilson, G. Grant, F. Yang, *Tissue Eng. Part A* **2021**, *27*, 390.
[10] C. Wang, X. Tong, X. Jiang, F. Yang, *J. Biomed. Mater. Res., Part A* **2017**, *105*, 770.
[11] L. J. Kaufman, C. P. Brangwynne, K. E. Kasza, E. Filippidi, V. D. Gordon, T. S. Deisboeck, D. A. Weitz, *Biophys. J.* **2005**, *89*, 635.
[12] O. Chaudhuri, J. Cooper-White, P. A. Janmey, D. J. Mooney, V. B. Shenoy, *Nature* **2020**, *584*, 535.
[13] O. Chaudhuri, L. Gu, D. Klumpers, M. Darnell, S. A. Bencherif, J. C. Weaver, N. Huebsch, H. P. Lee, E. Lippens, G. N. Duda, D. J. Mooney, *Nat. Mater.* **2015**, *15*, 326.
[14] D. Indana, P. Agarwal, N. Bhutani, O. Chaudhuri, D. Indana, O. Chaudhuri, P. Agarwal, N. Bhutani, *Adv. Mater.* **2021**, *33*, 2101966.
[15] C. M. Madl, B. L. LeSavage, R. E. Dewi, K. J. Lampe, S. C. Heilshorn, C. M. Madl, B. L. LeSavage, R. E. Dewi, K. J. Lampe, S. C. Heilshorn, *Adv. Sci.* **2019**, *6*, 1801716.
[16] S. Budday, T. C. Ovaert, G. A. Holzapfel, P. Steinmann, E. Kuhl, *Arch. Comput. Methods Eng.* **2019**, *27*, 1187.
[17] M. Reiss-Zimmermann, K. J. Streitberger, I. Sack, J. Braun, F. Arlt, D. Fritzsch, K. T. Hoffmann, *Clin. Neuroradiol.* **2015**, *25*, 371.
[18] K. J. Streitberger, M. Reiss-Zimmermann, F. B. Freimann, S. Bayerl, J. Guo, F. Arlt, J. Wuerfel, J. Braun, K. T. Hoffmann, I. Sack, *PLoS One* **2014**, *9*, e110588.
[19] V. L. Cross, Y. Zheng, N. Won Choi, S. S. Verbridge, B. A. Sutermaster, L. J. Bonassar, C. Fischbach, A. D. Stroock, *Biomaterials* **2010**, *31*, 8596.
[20] A. M. Rosales, K. S. Anseth, *Nat. Rev. Mater.* **2016**, *1*, 15012.
[21] D. D. McKinnon, D. W. Domaille, J. N. Cha, K. S. Anseth, *Adv. Mater.* **2014**, *26*, 865.
[22] B. M. Richardson, D. G. Wilcox, M. A. Randolph, K. S. Anseth, *Acta Biomater.* **2019**, *83*, 71.
[23] D. D. McKinnon, D. W. Domaille, T. E. Brown, K. A. Kyburz, E. Kiyotake, J. N. Cha, K. S. Anseth, *Soft Matter* **2014**, *10*, 9230.
[24] D. K. Kölmel, E. T. Kool, *Chem. Rev.* **2017**, *117*, 10358.
[25] L. S. Payne, P. H. Huang, *Mol. Cancer Res.* **2013**, *11*, 1129.
[26] I. J. Huijbers, M. Iravani, S. Popov, D. Robertson, S. Al-Sarraj, C. Jones, C. M. Isacke, *PLoS One* **2010**, *5*, e9808.
[27] K. B. Pointer, P. A. Clark, A. B. Schroeder, M. S. Salamat, K. W. Eliceiri, J. S. Kuo, *J. Neurosurg. Pediatr.* **2016**, *126*, 1812.
[28] A. Vollmann-Zwerenz, V. Leidgens, G. Feliciello, C. A. Klein, P. Hau, *Int. J. Mol. Sci.* **2020**, *21*, 1932.
[29] D. A. Lauffenburger, A. F. Horwitz, *Cell* **1996**, *84*, 359.
[30] A. J. Ridley, M. A. Schwartz, K. Burridge, R. A. Firtel, M. H. Ginsberg, G. Borisy, J. T. Parsons, A. R. Horwitz, *Science* **2003**, *302*, 1704.
[31] K. M. Joo, J. Kim, J. Jin, M. Kim, H. J. Seol, J. Muradov, H. Yang, Y. la Choi, W. Y. Park, D. S. Kong, J. il Lee, Y. H. Ko, H. G. Woo, J. Lee, S. Kim, D. H. Nam, *Cell Rep.* **2013**, *3*, 260.
[32] S. Nam, V. K. Gupta, H.-p. Lee, J. Y. Lee, K. M. Wisdom, S. Varma, E. M. Flaum, C. Davis, R. B. West, O. Chaudhuri, *Sci. Adv.* **2019**, *5*, eaaw61712.
[33] A. Armento, J. Ehlers, S. Schötterl, U. Naumann, in *Glioblastoma [Internet]*, (Ed: S. De Vleeschouwer), Codon Publications, Brisbane, Australia **2017**, Ch. 5.
[34] D. J. Aum, D. H. Kim, T. L. Beaumont, E. C. Leuthardt, G. P. Dunn, A. H. Kim, *Neurosurg. Focus* **2014**, *37*, E11.
[35] B. Ortensi, M. Setti, D. Osti, G. Pelicci, *Stem Cell Res. Ther.* **2013**, *4*, 18.
[36] A. Dirkse, A. Golebiewska, T. Buder, P. v. Nazarov, A. Muller, S. Poovathingal, N. H. C. Brons, S. Leite, N. Sauvageot, D. Sarkisjan, M. Seyfrid, S. Fritah, D. Stieber, A. Michelucci, F. Hertel, C. Herold-Mende, F. Azuaje, A. Skupin, R. Bjerkvig, A. Deutsch, A. Voss-Böhme, S. P. Niclou, *Nat. Commun.* **2019**, *10*, 1787.
[37] L. Persano, E. Rampazzo, G. Basso, G. Viola, *Biochem. Pharmacol.* **2013**, *85*, 612.
[38] C. S. Jung, C. Foerch, A. Schänzer, A. Heck, K. H. Plate, V. Seifert, H. Steinmetz, A. Raabe, M. Sitzer, *Brain* **2007**, *130*, 3336.
[39] W. Paulus, *Acta Neuropathol.* **2009**, *118*, 603.
[40] S. Y. Lee, *Genes Dis.* **2016**, *3*, 198.
[41] J. Zhang, M. F. G. Stevens, T. D. Bradshaw, *Curr. Mol. Pharmacol.* **2011**, *5*, 102.
[42] H. Calvert, H. S. Friedman, T. Kerby, *Clin. Cancer Res.* **2000**, *6*, 2585.
[43] W. P. Roos, L. F. Z. Batista, S. C. Naumann, W. Wick, M. Weller, C. F. M. Menck, B. Kaina, *Oncogene* **2006**, *26*, 186.

[44] C. Riganti, I. C. Salaroglio, V. Caldera, I. Campia, J. Kopecka, M. Mellai, L. Annovazzi, A. Bosia, D. Ghigo, D. Schiffer, *Neuro-Oncology* **2013**, *15*, 1502.
[45] D. Beier, S. Röhrl, D. R. Pillai, S. Schwarz, L. A. Kunz-Schughart, P. Leukel, M. Proescholdt, A. Brawanski, U. Bogdahn, A. Trampe-Kieslich, B. Giebel, J. Wischhusen, G. Reifenberger, P. Hau, C. P. Beier, *Cancer Res.* **2008**, *68*, 5706.
[46] D. Beier, J. B. Schulz, C. P. Beier, *Mol Cancer* **2011**, *10*, 128.
[47] J. Chen, Y. Li, T. S. Yu, R. M. McKay, D. K. Burns, S. G. Kernie, L. F. Parada, *Nature* **2012**, *488*, 522.
[48] R. C. Gimple, S. Bhargava, D. Dixit, J. N. Rich, *Genes Dev.* **2019**, *33*, 591.
[49] Z. Wang, H. Zhang, S. Xu, Z. Liu, Q. Cheng, *Signal Transduction Targeted Ther.* **2021**, *6*, 1.
[50] S. D. Fouse, J. L. Nakamura, C. D. James, S. Chang, J. F. Costello, *Neuro-Oncology* **2014**, *16*, 361.
[51] D. A. Fletcher, R. D. Mullins, *Nature* **2010**, *463*, 485.
[52] J. M. Muncie, V. M. Weaver, *Curr. Top. Dev. Biol.* **2018**, *130*, 1.
[53] J. M. Northcott, I. S. Dean, J. K. Mouw, V. M. Weaver, *Fron.t Cell Dev. Biol.* **2018**, *6*, 17.
[54] R. K. Assoian, E. A. Klein, *Trends Cell Biol.* **2008**, *18*, 347.
[55] T. A. Ulrich, E. M. d. J. Pardo, S. Kumar, *Cancer Res.* **2009**, *69*, 4167.
[56] P. P. Provenzano, P. J. Keely, *J. Cell Sci.* **2011**, *124*, 1195.
[57] M. A. Wozniak, C. S. Chen, *Nat. Rev. Mol. Cell Biol.* **2009**, *10*, 34.
[58] H.-p. Lee, R. Stowers, O. Chaudhuri, *Nat. Commun.* **2019**, *10*, 1.
[59] W. Yang, P. fei Wu, J. xing Ma, M. jun Liao, L. shan Xu, L. Yi, *Sci. Rep.* **2020**, *10*, 1.
[60] Q. Ou-yang, B. Li, M. Xu, H. Liang, *Biochem. Biophys. Res. Commun.* **2018**, *503*, 876.
[61] W. H. Lee, L. Y. Choong, N. N. Mon, S. Lu, Q. Lin, B. Pang, B. Yan, V. S. R. Krishna, H. Singh, T. Z. Tan, J. P. Thiery, C. T. Lim, P. B. O. Tan, M. Johansson, C. Harteneck, Y. P. Lim, *Sci. Rep.* **2016**, *6*, 1.
[62] X. Li, Y. Cheng, Z. Wang, J. Zhou, Y. Jia, X. He, L. Zhao, Y. Dong, Y. Fan, X. Yang, B. Shen, X. Wu, J. Wang, C. Xiong, L. Wei, X. Li, J. Wang, *Cell Death Dis.* **2020**, *11*, 1.
[63] A. Momin, S. Bahrampour, H.-K. Min, X. Chen, X. Wang, Y. Sun, X. Huang, *Trends Pharmacol. Sci.* **2021**, *42*, 367.
[64] M. Nabissi, M. B. Morelli, M. Santoni, G. Santoni, *Carcinogenesis* **2013**, *34*, 48.
[65] G. Chinigò, H. Castel, O. Chever, D. Gkika, *Front. Cell Dev. Biol.* **2021**, *9*, 617801.
[66] E. Henke, R. Nandigama, S. Ergün, *Front. Mol. Biosci.* **2020**, *6*, 160.
[67] C. Loebel, R. L. Mauck, J. A. Burdick, *Nat. Mater.* **2019**, *18*, 883.
[68] T. Sethi, R. C. Rintoul, S. M. Moore, A. C. MacKinnon, D. Salter, C. Choo, E. R. Chilvers, I. Dransfield, S. C. Donnelly, R. Strieter, C. Haslett, *Nat. Med.* **1999**, *5*, 662.
[69] A. J. Wong, J. M. Ruppert, S. H. Bigner, C. H. Grzeschik, P. A. Humphrey, D. S. Bigner, B. Vogelstein, *Proc. Natl. Acad. Sci. U. S. A.* **1992**, *89*, 2965.
[70] S. H. Bigner, P. A. Humphrey, A. J. Wong, B. Vogelstein, J. Mark, H. S. Friedman, D. D. Bigner, *Cancer Res.* **1990**, *50*, 8017.
[71] J. Chang, E. M. Pang, K. Adebowale, K. M. Wisdom, O. Chaudhuri, *Biophys. J.* **2020**, *119*, 726.

Molecular Oncology

Pericyte-secreted IGF2 promotes breast cancer brain metastasis formation

Kinga Molnár[1,2], Ádám Mészáros[1,3], Csilla Fazakas[1,4], Mihály Kozma[1,2], Fanni Győri[1,2], Zita Reisz[5], László Tiszlavicz[5], Attila E. Farkas[1,4], Ádám Nyúl-Tóth[1,6], János Haskó[1], István A. Krizbai[1,7] and Imola Wilhelm[1,7]

1 Institute of Biophysics, Biological Research Centre, Szeged, Hungary
2 Theoretical Medicine Doctoral School, University of Szeged, Szeged, Hungary
3 Doctoral School of Biology, University of Szeged, Szeged, Hungary
4 Department of Physiology, Anatomy and Neuroscience, University of Szeged, Szeged, Hungary
5 Department of Pathology, University of Szeged, Szeged, Hungary
6 Vascular Cognitive Impairment and Neurodegeneration Program, Department of Biochemistry and Molecular Biology, Reynolds Oklahoma Center on Aging/Oklahoma Center for Geroscience, University of Oklahoma Health Sciences Center, Oklahoma City, OK, USA
7 Institute of Life Sciences, Vasile Goldiş Western University of Arad, Arad, Romania

Keywords
brain metastasis; cerebral pericyte; insulin-like growth factor 2; picropodophyllin; triple-negative breast cancer

Correspondence
I. A. Krizbai and I. Wilhelm, Institute of Biophysics, Biological Research Centre, Temesvári krt. 62, Szeged 6726, Hungary
Fax: +36 62 433133
Tel: +36 62 599601
E-mails: krizbai.istvan@brc.hu (IAK); wilhelm.imola@brc.hu (IW)

(Received 24 February 2020, revised 25 May 2020, accepted 8 June 2020, available online 26 June 2020)

doi:10.1002/1878-0261.12752

Brain metastases are life-threatening complications of triple-negative breast cancer, melanoma, and a few other tumor types. Poor outcome of cerebral secondary tumors largely depends on the microenvironment formed by cells of the neurovascular unit, among which pericytes are the least characterized. By using *in vivo* and *in vitro* techniques and human samples, here we show that pericytes play crucial role in the development of metastatic brain tumors by directly influencing key steps of the development of the disease. Brain pericytes had a prompt chemoattractant effect on breast cancer cells and established direct contacts with them. By secreting high amounts of extracellular matrix proteins, pericytes enhanced adhesion of both melanoma and triple-negative cancer cells, which might be particularly important in the exclusive perivascular growth of these tumor cells. In addition, pericytes secreted insulin-like growth factor 2 (IGF2), which had a very significant pro-proliferative effect on mammary carcinoma, but not on melanoma cells. By inhibiting IGF2 signaling using silencing or picropodophyllin (PPP), we could block the proliferation-increasing effect of pericytes on breast cancer cells. Administration of PPP (a blood–brain barrier-permeable substance) significantly decreased the size of brain tumors in mice inoculated with triple-negative breast cancer cells. Taken together, our results indicate that brain pericytes have significant pro-metastatic features, especially in breast cancer. Our study underlines the importance of targeting pericytes and the IGF axis as potential strategies in brain metastatic diseases.

Abbreviations
BBB, blood–brain barrier; CEC, cerebral endothelial cell; CNS, central nervous system; EGFP, enhanced green fluorescent protein; EmGFP, emerald green fluorescent protein; EMT, epithelial-to-mesenchymal transition; EV, extracellular vesicle; FAK, focal adhesion kinase; HA, human astrocyte; HBVP, human brain vascular pericyte; IGF, insulin-like growth factor; IGF1R, type 1 insulin-like growth factor receptor; NVU, neurovascular unit; P/S, penicillin/streptomycin; PDGFRβ, platelet-derived growth factor receptor β; PM, pericyte medium; PPP, picropodophyllin; RIPA, radioimmunoprecipitation assay buffer; TNBC, triple-negative breast cancer.

Molecular Oncology **14** (2020) 2040–2057

1. Introduction

Cerebral metastases are frequent and dismal complications of a few tumor cell types, including lung cancer, breast cancer, and melanoma. In breast cancer, which is the second most frequent cause of central nervous system (CNS) metastases, brain lesions primarily occur in triple-negative (estrogen receptor-, progesterone receptor-, and Her2-negative) and Her2/neu-overexpressing subtypes. Triple-negative breast cancer (TNBC) has a particularly poor prognosis, many patients developing and eventually dying of brain metastasis [1]. Melanoma, the third most common brain metastatic tumor, represents the highest risk to spread to the CNS, and brain metastases are a leading cause of death from this disease [2].

Presence of the blood–brain barrier (BBB) [3], tumor heterogeneity and plasticity [4], and unique molecular features of brain metastatic cells [5] all contribute to the poor outcome of cerebral secondary tumors. The most important unique aspects of brain metastasis development are linked to the neurovascular unit (NVU), that is, cerebral endothelial cells (CECs), pericytes, glial cells, and neurons, with whom tumor cells form complex interactions [6]. These interactions have been extensively studied, except for pericytes.

Brain pericytes are mural cells located in the duplication of the basement membrane of microvessels, coming in close contact with cerebral endothelial and glial cells. They may act as regulators of vessel formation and stabilization [7,8], BBB permeability [9,10] and—although still debated—cerebral blood flow [11,12]. Pericytes play a crucial role in various neurological diseases, including ischemia, traumatic injury, neurodegenerative and neuro-immune conditions, and also glioblastoma [13]. However, interactions of brain pericytes with metastatic tumor cells are largely unexplored, although pericytes have recently emerged as important players in creating the premetastatic niche in peripheral organs [14]. Since microvessels of the CNS have the highest pericyte coverage in the organism [15], we hypothesized that pericyte-metastatic cell interactions might be particularly critical in the brain.

2. Materials and methods

2.1. Cell culture

2.1.1. Culture of human NVU cells

Human brain vascular pericytes (abbreviated as HBVP; obtained from ScienCell Research Laboratories, Carlsbad, CA, USA) were cultured on poly-L-lysine-coated dishes in Pericyte Medium (PM; ScienCell Research Laboratories) supplemented with 5% FBS (Sigma-Aldrich, St. Louis, MO, USA) and penicillin/streptomycin solution (P/S; ScienCell Research Laboratories) and used between passage numbers 2 and 6. Human astrocytes (HA; ScienCell Research Laboratories) were grown on poly-L-lysine-coated dishes in astrocyte medium (AM) supplemented with 5% FBS and P/S (all from ScienCell Research Laboratories) and used between passage numbers 2 and 4. Human microvascular cerebral endothelial cells (hCMEC/D3, shortly D3) were cultured on rat-tail collagen-coated dishes in endothelial cell basal medium-2 (EBM-2) with EGM-2MV kit including supplements and 2% FBS (all from Lonza, Basel, Switzerland) and used between passage numbers 30 and 40.

2.1.2. Isolation and culture of mouse NVU cells

Venus-YFP-expressing primary mouse brain endothelial cells were isolated from 6- to 8-week-old FVB/Ant: TgCAG-yfp_sb #27 mice, as described previously [16]. Murine pericytes were collected in parallel with endothelial cells after the first enzymatic digestion. Pericytes were seeded onto rat-tail collagen-coated dishes and kept in PM supplemented with 5% FBS (Sigma-Aldrich) and P/S solution. Mouse pericytes were used for experiments between passage numbers 5 and 7. Primary mouse astrocytes were isolated from brains of 1- to 3-day-old Balb/c mouse pups by mechanical trituration. Astrocytes were seeded onto poly-L-lysine-coated dishes and kept in low-glucose Dulbecco's modified Eagle's medium (DMEM; Thermo Fisher Scientific, Waltham, MA, USA) supplemented with 10% FBS (Sigma-Aldrich).

2.1.3. Culture of tumor cells

MDA-MB-231 human triple-negative breast cancer cells (shortly MDA), enhanced green fluorescent protein (EGFP)-expressing MDA-MB-231 cells (shortly MDA-EGFP); mouse triple-negative mammary carcinoma cells 4T1, 4T1-tdTomato and 4T1-EmGFP (expressing emerald GFP); A2058 human and B16/F10 (abbreviated as B16) murine melanoma cells were cultured as described previously [17]. A2058-EGFP cells were obtained by transfection with the pEGFP-C1 plasmid using TurboFect reagent (Thermo Fisher Scientific) and selection with 500 $\mu g \cdot mL^{-1}$ G418 (Thermo Fisher Scientific).

All cell lines were regularly tested for mycoplasma contamination using the MycoAlert Mycoplasma Detection Kit (Lonza). Only mycoplasma-negative cultures were used for experiments.

2.2. Preparation of conditioned media

Human and mouse cells were grown until 90% confluency in 6-cm culture dishes. Growth medium was replaced with HBVP complete medium (PM + 5% FBS + P/S) and left for 2 days. Nonconditioned complete medium was used as negative control. All media were filtered through 0.2-µm pore size syringe filters to remove cells and debris.

Extracellular vesicles (EVs) were depleted from HBVP control and conditioned media by using a serial centrifugation protocol: 700 ***g***, 5 min; 1000 ***g***, 8 min; 10 000 ***g***, 30 min and 150 000 ***g***, 90 min. Media were collected and filtered through 0.1-µm pore size syringe filters.

2.3. Experimental animal surgeries

All mice were housed and treated in accordance with widely accepted standards, and the protocols were approved by the institutional care and the Regional Animal Health and Food Control Station of Csongrád County (permit number: XVI./764/2018). Surgeries were carried out on 6- to 10-week-old female FVB/Ant:TgCAG-yfp_sb #27 mice (obtained from Institute of Experimental Medicine, Budapest, Hungary), as described previously [16]. For *ex vivo* experiments, 6- to 10-week-old female mice received 10^6 4T1-tdTomato cells in 100 µL into the right common carotid artery. For testing the effect of picropodophyllin (PPP) on tumor growth *in vivo*, animals were inoculated with 3×10^6 4T1-tdTomato cells/200 µL by intracardiac injection. The well-being of the animals was monitored daily during the postoperative period. No infection or wound dehiscence was detected, neither any signs of chronic pain. Maximum 5% of weight loss was observed, and the operation-induced mortality rate was 2–3%. On days 5 and 6 postinjection, mice received 40 $\mathrm{mg \cdot kg^{-1}}$ PPP (Alfa Aesar, Thermo Fisher Scientific) in corn oil or vehicle only, intraperitoneally. On day 8, mice were transcardially perfused. Coronary brain sections were prepared from all animals from parietal cortical regions, and the same volumes were used for imaging with a Leica SP5 microscope (Leica Biosystems, Wetzlar, Germany). Tumor-covered areas in control and PPP-treated animals were measured with FIJI software using a custom-made macro [18].

2.4. Immunofluorescence

Human triple-negative breast cancer brain metastasis and control brain samples were acquired from the Department of Pathology, University of Szeged. Human samples were collected in accordance with the permission of the Human Investigation Review Board, University of Szeged (permit number: EMLOSEB001, issued on January 31, 2017), in agreement with the Declaration of Helsinki of the World Medical Association. Surgical samples were fixed in PFA and embedded into paraffin blocks. Five-micrometer-thick slices were used for immunofluorescence staining. After deparaffinization in xylol, samples were rehydrated through a descending series of alcohol to water. Antigen retrieval was performed by boiling in 10 mM sodium citrate pH = 6 for 15 min.

After fixation, whole mouse brains were mounted onto a freezing microtome (Reichert-Jung, Leica Biosystems) and 20-µm-thick coronal brain sections were cut, which were kept in PBS with 0.05% sodium azide until further processing. Antigen retrieval was performed by incubating the sections at 80 °C for 30 min in 10 mM sodium citrate pH = 6.

All sections were permeabilized in 0.5% Triton X-100 (Sigma-Aldrich) for 20 min, then blocked with 3% BSA (VWR International, Radnor, PA, USA) in PBS containing 0.5% Triton X-100 for 1 h. Primary antibodies (Table S1) were diluted in 1% BSA with 0.5% Triton X-100, and sections were incubated overnight at 4 °C on an orbital shaker. Slides were extensively washed in PBS. Alexa Fluor 488-labeled anti-rabbit, Alexa Fluor 594-labeled anti-mouse, Alexa Fluor 647-labeled anti-goat IgG (Thermo Fisher Scientific), and STAR RED-labeled anti-rabbit IgG (Abberior, Göttingen, Germany) were used as secondary antibodies in a dilution of 1 : 300 in PBS for 60 min at room temperature in the dark. Sections were washed, counterstained with a nuclear dye (Hoechst 33342; Sigma-Aldrich) for 10 min, washed again with PBS, rinsed in water, and mounted in FluoroMount-G (SouthernBiotech, Birmingham, AL, USA).

Samples were analyzed using a Leica SP5 confocal laser scanning microscope.

2.5. Adhesion experiments

2.5.1. Adhesion in co-culture

HBVP cells were stained with CellTracker™ Red CMTPX Dye (Thermo Fisher Scientific), extensively washed, and mixed with MDA-EGFP cells in a ratio of 1 : 1. Mixed culture was seeded onto poly-L-lysine-coated dishes in complete HBVP medium and left for 3 days.

2.5.2. Cell-to-cell adhesion

D3, HBVP, or HA cells were seeded into 12-well plates (noncoated or coated with poly-L-lysine or rat-tail collagen) in a density of 2×10^4 cells/well. After 24 h, 1.5×10^4 cells/well MDA-EGFP or A2058-EGFP were seeded onto the cells and incubated for 24 h. Phase-contrast and fluorescence images were taken with a Nikon Eclipse TE2000U (Nikon, Tokyo, Japan) microscope connected to a digital camera (Spot RT KE, Diagnostic Instruments, Sterling Heights, MI, USA). Attached fluorescent cells were counted using FIJI software [18].

2.5.3. Cell-to-surface adhesion

5×10^5 tumor cells were seeded into 6-well plates in pericyte-conditioned or control media in the presence or absence of Src inhibitors (Selleck Chemicals, Munich, Germany) and left for 20 min (A2058, 4T1 and B16) or 120 min (MDA). Floating cells were collected by centrifugation, and phase-contrast images were taken from attached cells. Efficiency of cell adhesion was determined by counting the adherent cells. For further western blot analysis, attached and floating cells were mixed together in radioimmunoprecipitation assay buffer (RIPA).

In another setup, 6-well plates were pretreated with endothelial cell-, pericyte-, or astrocyte-conditioned media for 24 h. Conditioned media were removed, and 5×10^5 tumor cells were seeded into the pretreated wells in control medium.

2.6. Migration assays

2.6.1. Short-distance migration assay (wound healing)

3×10^4 MDA cells and 1.5×10^4 HBVP or 3×10^4 D3 cells were seeded into rat-tail collagen-coated silicone 3-well culture inserts (Ibidi, Graefelfing, Germany). After reaching confluency, the insert was removed and culture medium was changed to Leibovitz's L-15 medium (Sigma-Aldrich) supplemented with 1% FBS. Migration of cells was monitored for 24 h in phase-contrast.

2.6.2. Long-distance migration assay

3×10^4 HBVP cells and 6×10^4 MDA-EGFP and D3 cells were seeded into every second well of a rat-tail collagen-coated silicone 12-well culture insert (Ibidi). After reaching confluency, the insert was removed. After 5 days, phase-contrast and fluorescence images were taken from the whole area and an overview image was generated.

2.7. Proliferation assays

2.7.1. Phase-contrast imaging and cell number counting

10^4 tumor cells/well were plated into 6-well plates, and fresh medium was given every other day. For cell counting, phase-contrast images were taken every day. After 4 days, cells were collected in RIPA buffer for western blot analysis.

2.7.2. Real-time impedance monitoring

10^4 4T1 or B16/F10 cells were seeded into E-plates in control or pericyte-conditioned medium with or without 100 nM PPP. Fresh medium was provided after 48 h. Electrical impedance was measured in real-time using the xCELLigence system (ACEA Biosciences, San Diego, CA, USA).

2.8. Methanol–chloroform precipitation and western blot

Conditioned media were centrifuged to seed cell debris, and an equal volume of methanol and 1/4 volume of chloroform were added. Samples were vortexed, incubated for 5 min on ice, and centrifuged at 10 000 ***g*** for 5 min at 4 °C. After phase separation, aqueous phase was removed and protein samples were washed with ice-cold methanol. Samples were vortexed and centrifuged again, supernatants were discarded, and protein pellets were air-dried. Pellets were reconstituted in 2× Laemmli buffer and heated up to 95 °C for 5 min.

Cells were lysed in RIPA buffer. Protein concentration was determined by using bicinchoninic acid assay (Thermo Fisher Scientific). Laemmli buffer was added to the samples and incubated at 95 °C for 5 min. Samples were electrophoresed using standard denaturing SDS/PAGE and blotted on polyvinylidene difluoride (0.2 µm pore size; Bio-Rad, Hercules, CA, USA, or 0.45 µm pore size; BioTrace, Pall Corporations, Port Washington, NY, USA) or nitrocellulose membranes (0.2 µm pore size; Bio-Rad). After blocking with 3% BSA or 5% nonfat milk in Tris-buffered saline with 0.1% Tween-20 (TBS-T), membranes were incubated with primary antibodies (Table S1) overnight at 4 °C. Blots were washed in TBS-T three times for 10 min, incubated for 1 h in horseradish peroxidase-conjugated anti-rabbit IgG or anti-mouse IgG secondary antibodies (Jackson ImmunoResearch, Cambridgeshire, UK) diluted to 1 : 3000 in TBS-T, and then washed again in TBS-T.

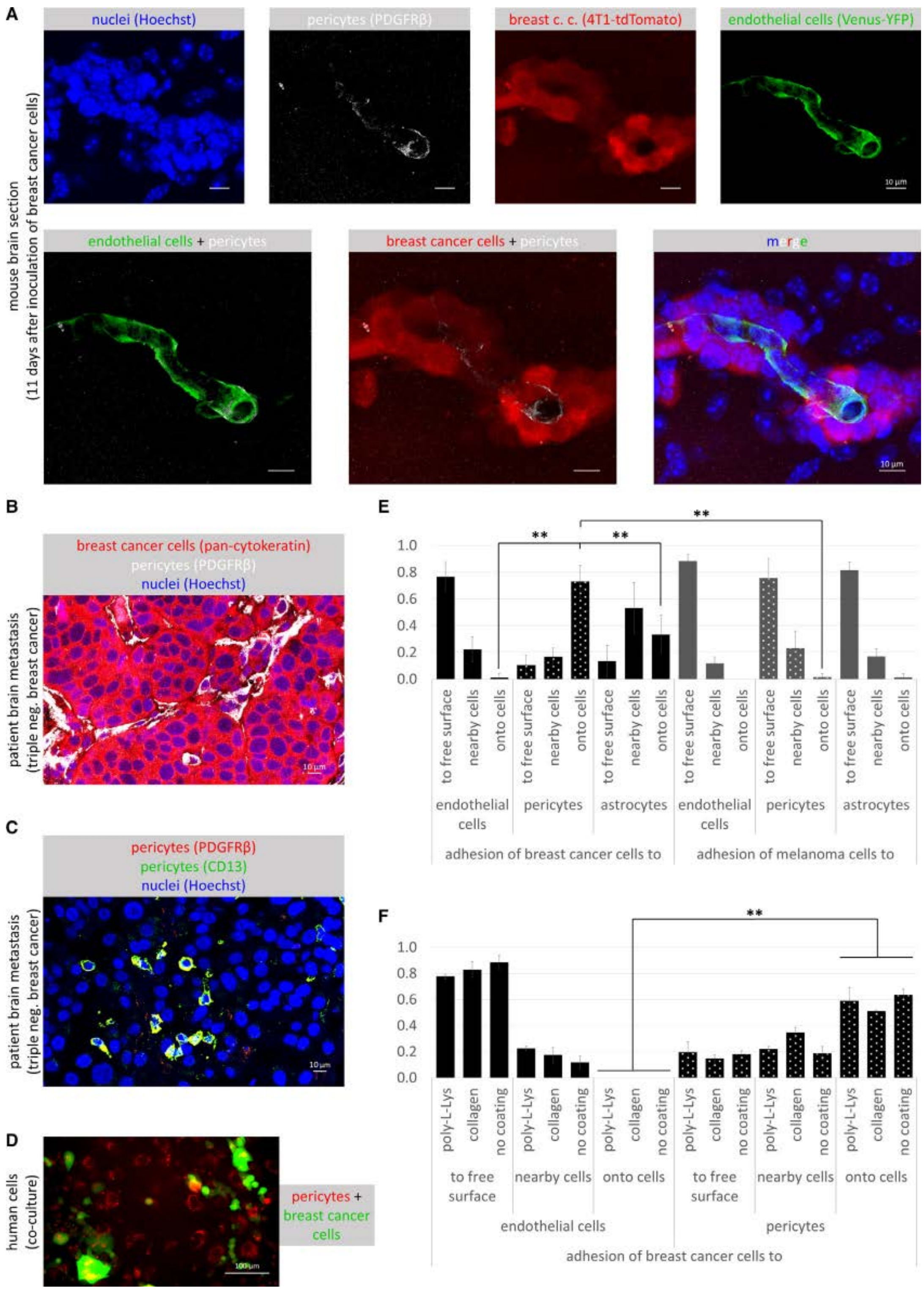
A
nuclei (Hoechst)
pericytes (PDGFRβ)
breast c. c. (4T1-tdTomato)
endothelial cells (Venus-YFP)
mouse brain section
(11 days after inoculation of breast cancer cells)
10 µm
endothelial cells + pericytes
breast cancer cells + pericytes
merge
10 µm
B
breast cancer cells (pan-cytokeratin)
pericytes (PDGFRβ)
nuclei (Hoechst)
patient brain metastasis
(triple neg. breast cancer)
10 µm
C
pericytes (PDGFRβ)
pericytes (CD13)
nuclei (Hoechst)
patient brain metastasis
(triple neg. breast cancer)
10 µm
D
human cells
(co-culture)
pericytes +
breast cancer
cells
100 µm
E
**
**
**
1.0
0.8
0.6
0.4
0.2
0.0
to free surface
nearby cells
onto cells
endothelial cells
pericytes
astrocytes
adhesion of breast cancer cells to
adhesion of melanoma cells to
F
**
1.0
0.8
0.6
0.4
0.2
0.0
poly-L-Lys
collagen
no coating
to free surface
nearby cells
onto cells
endothelial cells
pericytes
adhesion of breast cancer cells to

Fig. 1. Direct interactions of pericytes with tumor cells. (A) Brain sections of FVB/Ant:TgCAG-yfp mice 11 days after injection of 4T1-tdTomato cells showing PDGFRβ-positive pericytes localized along capillaries inside the tumor mass. Scale bars = 10 μm. (B) Human triple-negative brain metastatic tissue with PDGFRβ-positive pericytes in the stroma. Scale bar = 10 μm. (C) Human triple-negative brain metastatic tissue with PDGFRβ (red) and CD13 (green) double-positive (yellow) pericyte-like cells scattered among tumor cells. Scale bar = 10 μm. (D) Co-culture of CellTracker™ Red-stained human pericytes (HBVP cells) and human triple-negative breast cancer (MDA-EGFP) cells 3 days after seeding. Scale bar = 100 μm. (E) Quantification of tumor cell adhesion 24 h after seeding onto brain cells cultured in poly-L-lysine-coated dishes. Breast cancer cells: MDA-EGFP, melanoma cells: A2058-EGFP, endothelial cells: D3, pericytes: HBVP, astrocytes: HA. *N* = 5, average ± SD, $**P < 0.01$ (ANOVA and Bonferroni's *post hoc* test). (F) Comparison of human breast cancer cell (MDA-EGFP) adhesion to D3 and HBVP cells. *N* = 3, average ± SD, $**P < 0.01$ (ANOVA and Bonferroni's *post hoc* test).

Immunoreaction was visualized with Clarity Chemiluminescence Substrate (Bio-Rad) in a ChemiDoc MP System (Bio-Rad). Densitometry analysis was performed with the IMAGE LAB Software, version 5.2 (Bio-Rad).

2.9. RNA isolation and real-time polymerase chain reaction

Total RNA was isolated using TRIfast reagent (VWR International). Maxima First Strand cDNA Synthesis Kit (Thermo Fisher Scientific) was used to transcribe RNA into cDNA. Amplification was performed using iTaq™ Universal SYBR® Green Supermix (Bio-Rad) or Luminaris Color HiGreen qPCR Master Mix kit (Thermo Fisher Scientific) on a Bio-Rad iQ5 instrument under the following conditions: 40 cycles of 95 °C for 15 s, 56–60 °C for 30 s, 72 °C for 30 s using primers detailed in Table S2.

2.10. Enzyme-linked immunosorbent assay

After collection of conditioned media, cells were trypsinized and counted in a hemocytometer. Conditioned media were centrifuged at 1000 ***g*** for 15 min at 4 °C. Insulin-like growth factor 1 (IGF1) and IGF2 contents of conditioned media were measured using commercial ELISA kits (CSB-E04580h and CSB-E04583h, respectively; Cusabio, Wuhan, China) following the manufacturer's instructions.

2.11. Silencing of Igf2 gene

Stealth™ siRNA duplex oligoribonucleotides were designed using Invitrogen BLOCK-iT™ RNAi designer and purchased from Thermo Fisher Scientific. The following sequences were used: sense, 5′-UCGAUGCUGGUGCUUCUCACCUUCU-3′ and antisense, 5′-AGAAGGUGAGAAGCACCAGCAUCGA-3′. Cell transfection was performed with Lipofectamine 2000, as previously described [19].

2.12. Statistical analysis

Student's *t*-test and analysis of variance (ANOVA) were performed using the Excel 2016 Data Analysis plugin. For *post hoc* tests, we applied SIGMAPLOT version 12.3 (Systat Software Inc., Chicago, IL, USA).

3. Results

3.1. Direct interaction of brain metastatic tumor cells with pericytes *in vivo* and *in vitro*

We have previously shown that TNBC cells proliferate along capillaries in the mouse brain, co-opting the endothelium, but expelling astrocytes and astrocyte end-feet to the surface of the tumor [16]. Since tumor co-opted endothelial cells maintained tight junctions in the absence of astrocyte end-foot coverage, we investigated whether pericytes—another cell type involved in the induction of barrier properties of CECs [9,10]—remained in contact with the vessels, as previously described in a different metastatic model [20]. Indeed, we found that PDGFRβ (platelet-derived growth factor receptor β)-positive pericytes were localized to capillaries inside metastatic lesions in the mouse brain (Fig. 1A). In human TNBC brain metastases, PDGFRβ-positive perivascular cells were found in the stroma (Fig. 1B), in single or multiple layers, as previously shown [21]. In addition, we have also detected single pericyte-like cells expressing the specific markers PDGFRβ and CD13, scattered among the tumor cells, especially in less cell-dense areas, probably in the proximity of necrotic zones (Fig. 1C).

All these data prompted us to hypothesize that direct interactions between tumor cells and pericytes might influence brain metastasis development. Therefore, we first modeled contacts between metastatic cells and pericytes using an *in vitro* setup, by plating the tumor cells onto sparse cultures of brain pericytes and other cells of the NVU. Breast cancer cells

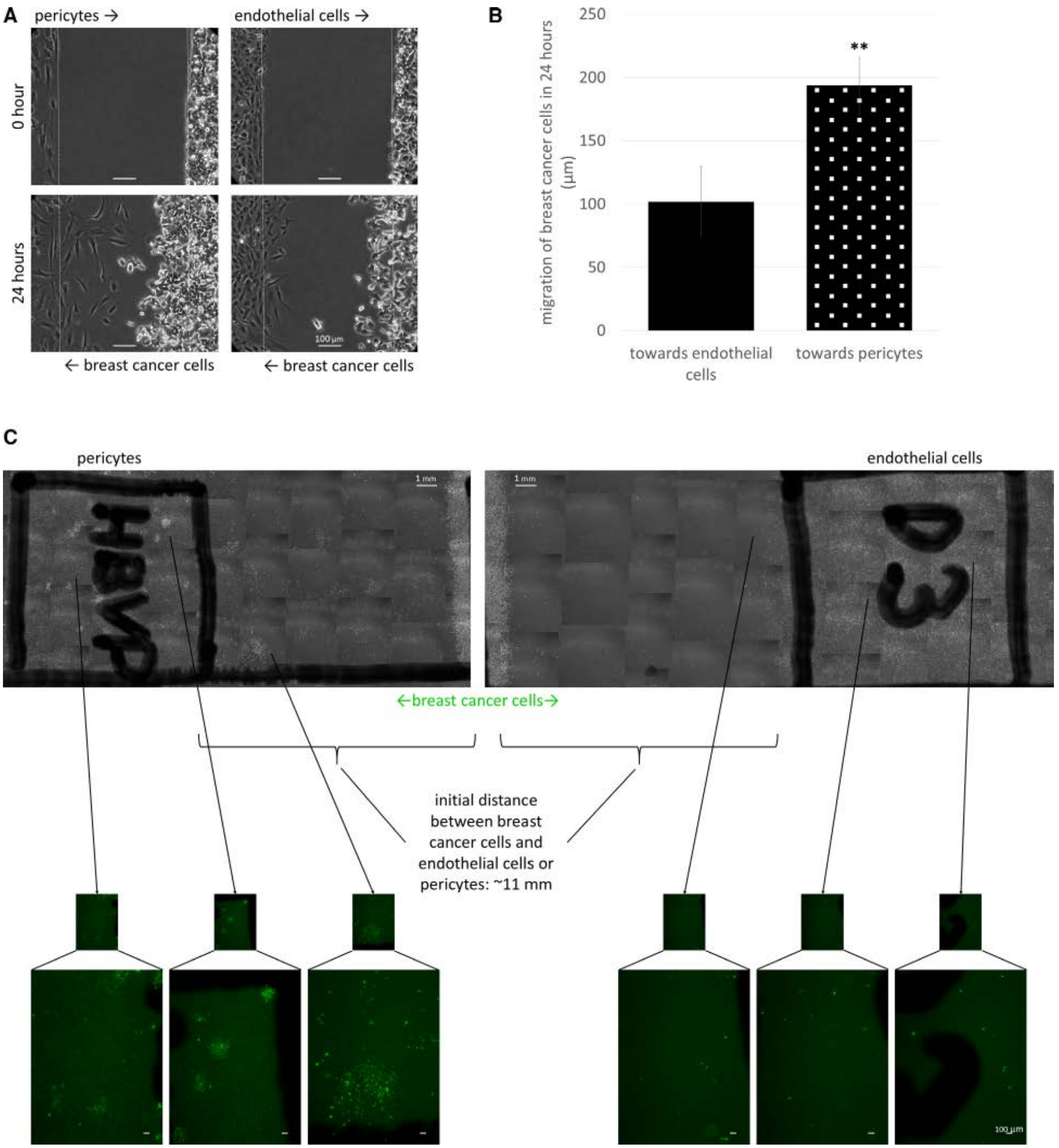

Fig. 2. Migration of breast cancer cells toward brain pericytes. (A) Representative phase-contrast images of pericyte-breast cancer cell and brain endothelial-breast cancer cell migration (short-distance invasion assay—described in Materials and methods). Scale bar = 100 µm. (B) Quantitative analysis of the short-distance wound assays at 24 h. $N = 5$, average ± SD, $^{**}P < 0.01$ (Student's *t*-test). (C) Phase-contrast and fluorescence (green insets) images of HBVP, D3, and MDA-EGFP cells after 5 days of migration in the long-distance invasion assay. Scale bars = 1 mm (top panels) and 100 µm (bottom panels).

preferentially gathered onto the top of pericytes, avoiding the cell-free culture surface (Fig. 1D,E), and this was independent of the coating of the culture dish (Fig. 1F). In contrast, when breast cancer cells were co-cultured with CECs, they seldom adhered onto endothelial cells, but rather into gaps among them. In co-culture with astrocytes, direct contacts of the tumor cells were more frequent than with endothelial cells, but less preferred than interaction with pericytes (Fig. 1E, Fig. S1). In contrast to breast cancer cells, the highest number of melanoma cells attached to free surfaces among the cells, independent of the cell type they were co-cultured with (Fig. 1E, Fig. S1).

As a next step, we aimed to explore whether breast cancer cells could actively migrate in the direction of brain pericytes. Carcinoma cells readily migrated toward pericytes, covering a significantly larger distance on their way to brain pericytes than to endothelial cells (Fig. 2A,B). When leaving a much longer distance (more than 1 cm) between tumor cells and two different brain cells (endothelial cells and pericytes, respectively), breast carcinoma cells preferentially migrated in the direction of pericytes. After a few days, several breast cancer cells were detected in the initially cell-free area between tumor cells and pericytes and large breast cancer cell colonies were formed among pericytes. On the other hand, only a few scattered mammary carcinoma cells were observed in the direction of and among endothelial cells (Fig. 2C). These results indicate that pericytes might communicate with tumor cells through secreted factors. Therefore, we conditioned culture medium on brain pericytes to characterize in details its effects on neoplastic cells.

3.2. Effects of pericytes on tumor cell adhesion

First, we seeded breast cancer and melanoma cells in control and pericyte-conditioned media and performed an adhesion assay. As shown in Fig. 3A–D, both human and mouse breast cancer and also melanoma cells attached to the culture dish surface and elongated more rapidly in pericyte-conditioned media, than in control conditions. The difference between cells seeded in control and conditioned media was very high and significant (Fig. 3C,D). Next, prior to seeding of the tumor cells, we pretreated the culture dishes with conditioned media of brain pericytes, endothelial cells, or astrocytes and performed an adhesion assay. Pericyte-conditioned medium enhanced attachment of both breast cancer and melanoma cells more effectively than endothelial-derived medium, while astrocyte-secreted factors had a more pronounced effect on breast cancer cells and were less effective on the adhesion of melanoma cells (Fig. 3E).

Adhesive substrate for the cells is provided by extracellular matrix, for example, basement membrane proteins. Therefore, we tested secretion of type IV collagen and fibronectin, two major components of the vascular basal lamina in the brain. According to our data, pericytes—similar to astrocytes—secreted high amounts of collagen type IV and fibronectin (Fig. 3F,G). These results explain the prominent adhesion enhancing effect of pericytes and astrocytes.

Cells attach to the extracellular matrix in focal adhesions, which are regulated by FAK (focal adhesion kinase), Src, and other signaling proteins [22]. Both FAK and Src phosphorylation increased in breast cancer and melanoma cells seeded in pericyte-conditioned media (Fig. S2A,B). In addition, PP2, a specific Src inhibitor—but not the structurally related negative control PP3—significantly reduced the adhesion-inducing effect of pericyte-conditioned media (Fig. S2C–E).

3.3. Effects of pericytes on tumor cell proliferation

As a next step, we aimed to understand how brain pericytes influence tumor growth. Therefore, we performed a tumor cell proliferation assay in the presence and absence of factors released by pericytes. Four days after plating, the number of breast cancer cells was substantially higher in pericyte-conditioned than in control media (Fig. 4A,B). This was clearly observed both in the human and in the mouse model. On the other hand, melanoma cells did not respond with increased proliferation to the presence of pericyte-secreted factors (Fig. 4A and Fig. S3A). In parallel, there was a significant increase in the expression of cyclin D1 in human and mouse breast cancer cells, but not in melanoma cells cultured in pericyte-conditioned media (Fig. 4C,D).

Besides soluble factors, conditioned media may contain EVs, like microvesicles and exosomes. In order to distinguish between effects of EVs and soluble factors, we prepared EV-depleted conditioned medium and compared it with complete conditioned medium in a proliferation assay. EV depletion did not influence the proliferation-increasing effect of pericyte-conditioned medium (Fig. 4E); therefore, soluble factors released by pericytes are responsible for the observed phenomenon.

Interestingly, breast cancer cells in the conditioned media, although higher in number, appeared to have fewer contact points with each other and became more dissociated (Fig. 4F). In line with this, E-cadherin expression decreased significantly in breast cancer cells being exposed to pericyte-secreted factors (Fig. 4G,H).

3.4. Insulin-like growth factor expression in cerebral pericytes

In order to identify which cerebral pericyte-secreted factors might be involved in enhancing tumor cell

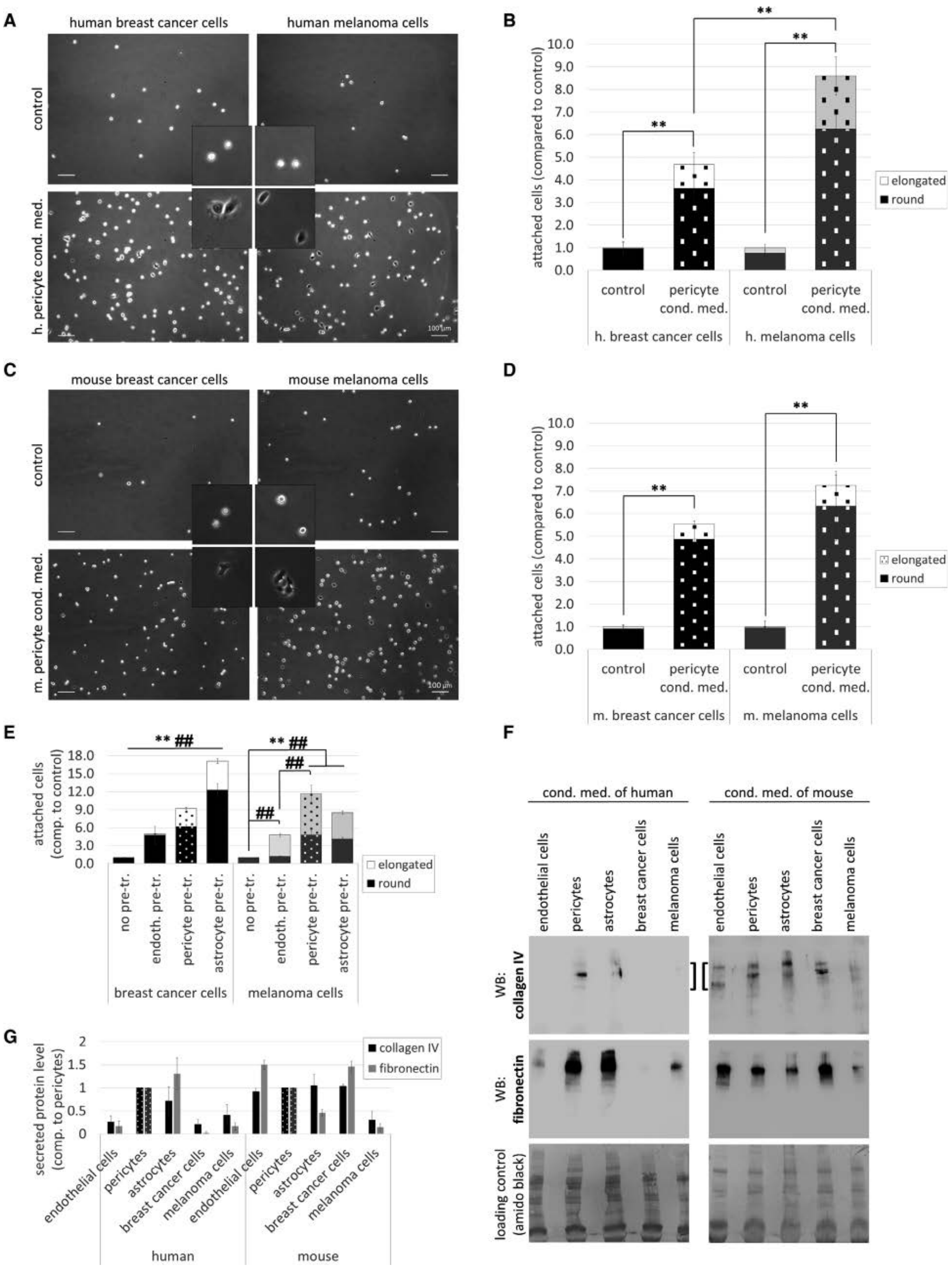
A
human breast cancer cells
human melanoma cells
control
h. pericyte cond. med.
100 µm
B
attached cells (compared to control)
10.0
9.0
8.0
7.0
6.0
5.0
4.0
3.0
2.0
1.0
0.0
**
**
**
control
pericyte cond. med.
control
pericyte cond. med.
h. breast cancer cells
h. melanoma cells
☐ elongated
■ round
C
mouse breast cancer cells
mouse melanoma cells
control
m. pericyte cond. med.
100 µm
D
attached cells (compared to control)
**
**
control
pericyte cond. med.
control
pericyte cond. med.
m. breast cancer cells
m. melanoma cells
elongated
■ round
E
attached cells (comp. to control)
18.0
15.0
12.0
9.0
6.0
3.0
0.0
** ##
** ##
##
##
no pre-tr.
endoth. pre-tr.
pericyte pre-tr.
astrocyte pre-tr.
no pre-tr.
endoth. pre-tr.
pericyte pre-tr.
astrocyte pre-tr.
breast cancer cells
melanoma cells
☐ elongated
■ round
F
cond. med. of human
cond. med. of mouse
endothelial cells
pericytes
astrocytes
breast cancer cells
melanoma cells
endothelial cells
pericytes
astrocytes
breast cancer cells
melanoma cells
WB: collagen IV
WB: fibronectin
loading control (amido black)
G
secreted protein level (comp. to pericytes)
2
1.5
1
0.5
0
■ collagen IV
■ fibronectin
endothelial cells
pericytes
astrocytes
breast cancer cells
melanoma cells
endothelial cells
pericytes
astrocytes
breast cancer cells
melanoma cells
human
mouse

Fig. 3. Role of pericyte-secreted factors in tumor cell adhesion. (A) Representative phase-contrast images of human breast cancer or melanoma cells (MDA or A2058, respectively) attached to noncoated cell culture dishes in control or pericyte-conditioned media after 120 min (MDA) or 20 min (A2058). Scale bar = 100 μm. (B) Quantification of adhesion results shown in (A). $N = 5$, average ± SD, $^{**}P < 0.01$ (ANOVA and Bonferroni's *post hoc* test). (C) Representative phase-contrast images of mouse breast cancer or melanoma cell adhesion (4T1 and B16 cells, respectively) 20 min after plating. Scale bar = 100 μm. (D) Quantification of adhesion results shown in (C). $N = 5$, average ± SD, $^{**}P < 0.01$ (ANOVA and Bonferroni's *post hoc* test). Insets in (A) and (C) show cells having typical round and elongated morphology (upper and bottom panels, respectively) (2.5 times of magnification compared to whole pictures). (E) Adhesion of MDA and A2058 cells in culture dishes pretreated for 24 h with conditioned media of D3, HBVP, or HA cells. $N = 3$, average ± SD, $^{**}P < 0.01$ (all cells), $^{\#\#}P < 0.01$ (elongated cells). Breast cancer cells: significant difference among all groups (ANOVA and Bonferroni's *post hoc* test). (F) Secretion of collagen type IV and fibronectin into culture media of brain and tumor cells (representative western blot images). (G) Quantification of collagen type IV and fibronectin western blots. $N = 3$, average ± SD (statistically not analyzed).

proliferation, we first performed a database search. In the http://betsholtzlab.org/VascularSingleCells/database.html collection [23], we found Igf2 mRNA having the highest expression in pericytes among cells of the NVU. Igf2 mRNA expression level was 487.25 times higher in pericytes than in endothelial cells, and 86.62 times more in pericytes vs. astrocytes in the mouse brain (Fig. S3B). In our human and mouse pericytes, not only Igf2, but Igf1 mRNA was also expressed (Fig. 5A,B). More Igf2 than Igf1 mRNA was found both in human and mouse pericytes; however, the ratio was higher in human cells. Mouse astrocytes expressed very low amounts of Igf1 and Igf2 mRNA, while in HAs both Igf1 and Igf2 mRNA levels were higher than in tumor cells, but still lower than in pericytes.

These data were confirmed on the protein level using ELISA. Human pericytes secreted more than 1000 pg·mL^{-1} IGF2 corresponding to almost 100 pg/100 000 cells, while in astrocytes we detected significantly less IGF2 (< 200 pg·mL^{-1}, < 40 pg/100 000 cells) (Fig. 5C). IGF1 levels in both pericyte- and astrocyte-conditioned media were below the detection limit of 1.95 ng·mL^{-1}. By using immunofluorescence, we found both IGF1 and IGF2 to be expressed in CD13-positive pericytes in the human brain (Fig. S3C, D). IGF1 was also detected in a few CD13-negative cells, probably astrocyte end-feet, while IGF2 was mainly expressed in pericytes. In human TNBC brain metastatic lesions, the expression of IGF1 and IGF2 was highly restricted to perivascular cells (Fig. 5D,E).

3.5. Role of brain pericyte-secreted IGFs in proliferation of TNBC cells

By binding to the type 1 insulin-like growth factor receptor (IGF1R), IGFs are involved in growth and survival of both normal and neoplastic cells [24]. Therefore, we next tested whether pericyte-secreted IGFs are responsible for the increased proliferation rate of breast cancer cells. For this purpose, we used a selective inhibitor of IGF1R, PPP, which efficiently blocks IGF1R without inhibiting the insulin receptor, and has low toxicity in rodents [25]. Addition of PPP to pericyte-conditioned medium reduced its proliferation-inducing effect to almost control levels both in human and mouse breast cancer cells (Fig. 6A,B).

In addition, we silenced Igf2 gene in pericytes, collected conditioned media, and performed a proliferation assay (Fig. 6C). Igf2 silencing was very efficient, and although slightly affected Igf1 mRNA expression as well (Fig. 6D), it can be considered specific, due to the much higher expression of IGF2 compared to IGF1 in brain pericytes (Fig. 5). Proliferation rate of breast cancer cells in conditioned media of Igf2-silenced pericytes was similar to control cells, or cells cultured in pericyte-conditioned media in the presence of PPP (Fig. 6C).

In line with secreted IGF2 levels, astrocyte-conditioned media had a much less pronounced effect on proliferation of breast cancer cells and no effect on melanoma cell division. PPP reversed the astrocyte-conditioned medium-induced slight increase in breast cancer cell proliferation (Fig. S4A,B).

In contrast to breast cancer cells, proliferation of melanoma cells was not affected by PPP (Fig. S4C). In order to understand the discrepancy between the effect of pericyte-derived IGFs on breast cancer and melanoma cells, we analyzed receptor expression level of the two cell types. Igf1R mRNA expression level was similar in the two cell types; however, melanoma cells expressed almost two times more Igf2R mRNA than breast cancer cells (Fig. 6E). This is in line with data from the Human Protein Atlas (https://www.proteinatlas.org/ENSG00000197081-IGF2R/pathology), which indicates a higher average mRNA and protein expression of IGF2R in melanoma than in breast cancer. This might partly explain the resistance of melanoma cells to IGFs, because IGF2R directs IGF2 to lysosomes to attenuate signaling [26].

Since PPP can cross the BBB [27], we next designed an *in vivo* setup to test the role of IGFs in breast

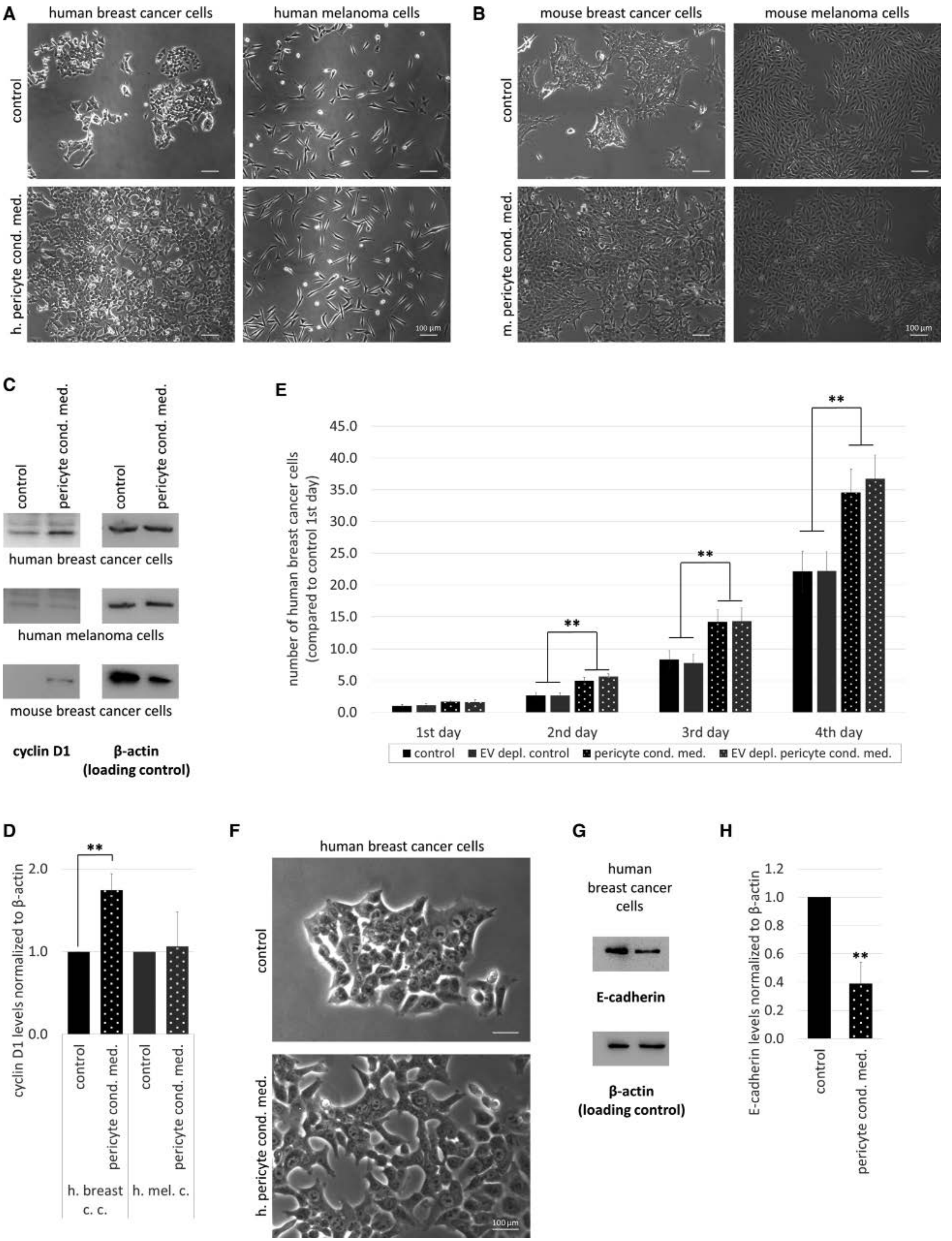
A
human breast cancer cells
human melanoma cells
control
h. pericyte cond. med.
100 µm
B
mouse breast cancer cells
mouse melanoma cells
control
m. pericyte cond. med.
100 µm
C
control
pericyte cond. med.
control
pericyte cond. med.
human breast cancer cells
human melanoma cells
mouse breast cancer cells
cyclin D1
β-actin (loading control)
E
number of human breast cancer cells (compared to control 1st day)
45.0
40.0
35.0
30.0
25.0
20.0
15.0
10.0
5.0
0.0
**
**
**
1st day
2nd day
3rd day
4th day
control
EV depl. control
pericyte cond. med.
EV depl. pericyte cond. med.
D
cyclin D1 levels normalized to β-actin
2.0
1.0
0.0
**
control
pericyte cond. med.
control
pericyte cond. med.
h. breast c. c.
h. mel. c.
F
human breast cancer cells
control
h. pericyte cond. med.
100 µm
G
human breast cancer cells
E-cadherin
β-actin (loading control)
H
E-cadherin levels normalized to β-actin
1.2
1.0
0.8
0.6
0.4
0.2
0.0
**
control
pericyte cond. med.

Fig. 4. Role of pericyte-secreted factors in tumor cell proliferation. (A, B) Representative phase-contrast images of tumor cells grown in control or pericyte-conditioned medium for 4 days. Scale bars = 100 μm. (C) Cyclin D1 expression in tumor cells grown in control or pericyte-conditioned medium for 4 days. (D) Quantification of cyclin D1 western blots. $N = 3$, average ± SD, $^{**}P < 0.01$ (ANOVA and Bonferroni's *post hoc* test). (E) Quantification of cell numbers of MDA cells grown in control, pericyte-conditioned, and EV-depleted media. $N = 4$, average ± SD, $^{**}P < 0.01$ (ANOVA and Bonferroni's *post hoc* test). (F) Representative high-magnification phase-contrast images of MDA cells grown in control or pericyte-conditioned medium for 4 days. Scale bar = 100 μm. (G) E-cadherin expression in MDA cells grown in control or pericyte-conditioned medium for 4 days. (H) Quantification of E-cadherin western blots. $N = 3$, average ± SD, $^{**}P < 0.01$ (Student's *t*-test).

cancer brain metastasis development. In order to test metastatic cell proliferation in the brain parenchyma, PPP was administered on days 5 and 6 after inoculation of tumor cells (Fig. 7A), when majority of cells have completed extravasation from cerebral capillaries [16]. Our results clearly showed that PPP inhibited proliferation of breast cancer cells in the brains of mice (Fig. 7B,C). The brain area covered by tumor cells became significantly, more than 2.5 times smaller in animals treated with the IGF1R inhibitor (Fig. 7D).

4. Discussion

Implicated in extravasation of malignant cells through the BBB and influencing their ability to survive and proliferate in the cerebral environment, cells of the NVU have been increasingly recognized as key players in brain metastasis formation. Although interactions between metastatic cells and CECs, astrocytes, or microglia are relatively well characterized [6], our knowledge about the role of pericytes is restricted to indirect effects on tumor cells, including regulation of blood–tumor barrier permeability [28] and secretion of connective tissue proteins [21]. By remodeling the perivascular niche [29], increasing angiogenesis [29], and acquiring an immunosuppressive function [31,32], pericytes have undisputed roles in promoting primary brain tumors. Therefore, we hypothesized that pericytes might facilitate progression of brain metastases as well.

By using *in vivo* and *in vitro* techniques and human samples, here we show and characterize direct interactions of brain pericytes with metastatic cells. First, others [20] and we have observed that pericytes remain attached to the vessels and are retained in metastatic lesions, while astrocytes are expelled to the border of the tumor [16]. In addition, inside the tumor mass, we found PDGFRβ and CD13 double-positive, non-perivascular pericyte-like cells, origin of which is unknown. Second, we proved direct interaction between tumor cells and pericytes *in vitro* as well, by showing that breast cancer cells preferentially attach to pericytes, avoiding free culture surfaces.

Our results point to a pronounced role of pericyte-secreted soluble factors, having chemoattractant, adhesion- and proliferation-enhancing effects mainly on triple-negative mammary carcinoma cells. We observed that pericytes secrete proteins of the extracellular matrix to enhance formation of tumor cell focal adhesions. In the brain, interaction with the vascular basement membrane is critical for the survival of metastatic cells [33,34]. Embedded in the inner, endothelial layer of the vascular basal lamina, pericytes substantially contribute to the secretion of matrix proteins [35], which might be particularly important in metastatic tumors, which tend to detach astrocytes—another major source of basal membrane proteins—from co-opted vessels. This is in line with accumulation of collagen secreted by perivascular cells observed in papillary-type human brain metastases [21].

Besides enhancing adhesion to the substrate, pericytes inhibit intercellular adhesions and expression of E-cadherin, conferring breast cancer cells a migratory, invasive phenotype, characteristic of cells undergoing epithelial-to-mesenchymal transition (EMT) [36]. In line with these results, pericytes have been shown to be

Fig. 5. Insulin-like growth factor expression in pericytes. (A, B) Igf1 and Igf2 mRNA expression in human and mouse brain and tumor cells, as assessed by qPCR with GAPDH as housekeeping gene. Results are shown as fold change in comparison with Igf1 in pericytes. Inset in (A) shows human Igf1 expression in a lower scale range. $N = 3$, average ± SD (statistically not analyzed). (C) IGF2 secretion in human brain pericytes and astrocytes, as assessed by ELISA. $N = 3$ pericytes, $N = 2$ astrocytes, average ± SD, $^{*}P < 0.05$, $^{**}P < 0.01$ (Student's *t*-test). (D) Representative immunofluorescence staining showing co-localization of IGF1 and CD13 in human TNBC brain metastatic tissue. Scale bar = 10 μm. (E) Representative immunofluorescence staining showing co-localization of IGF2 and CD13 in human TNBC brain metastatic tissue. Scale bar = 10 μm.

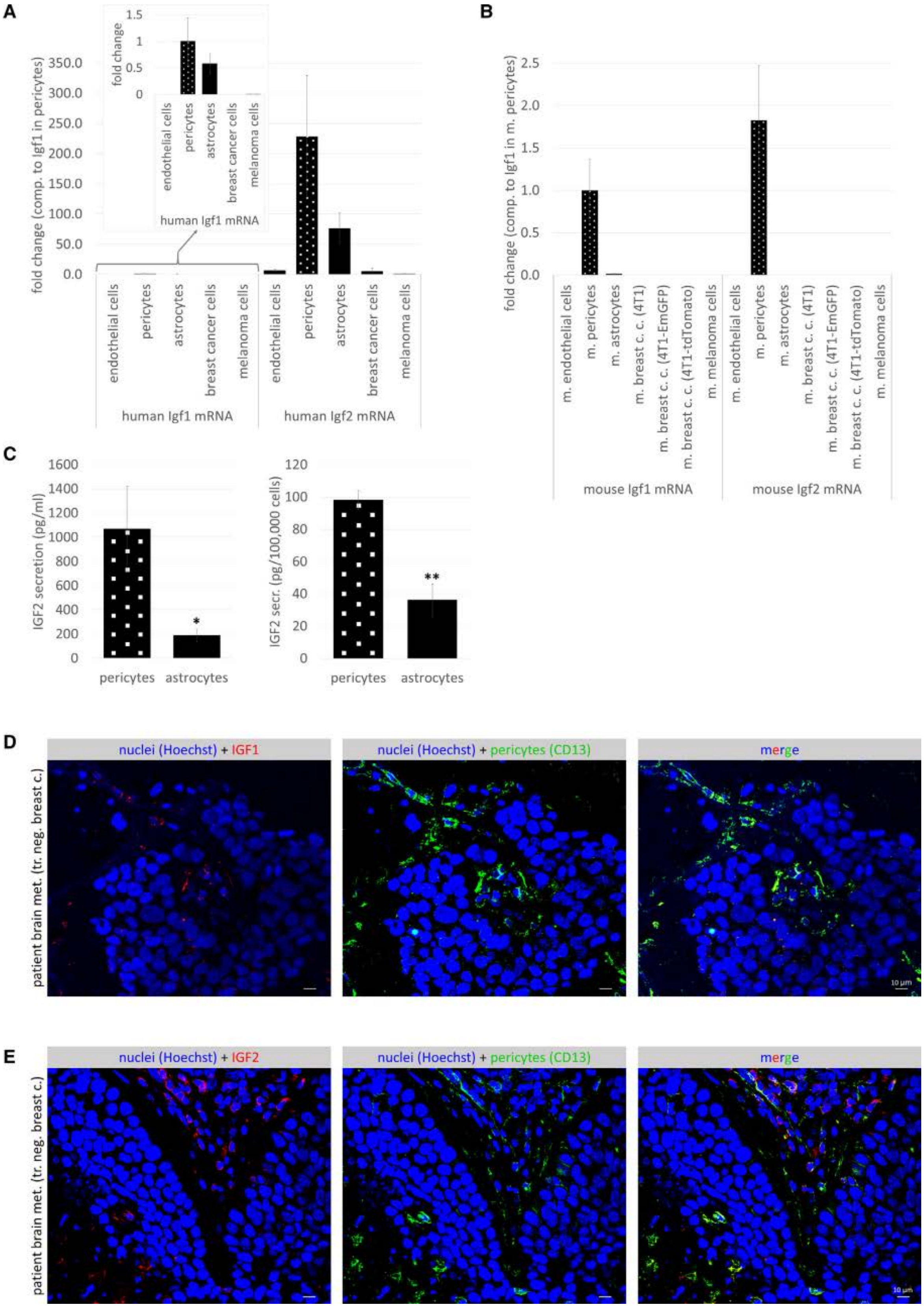
A
fold change
1.5
1
0.5
0
endothelial cells
pericytes
astrocytes
breast cancer cells
melanoma cells
human Igf1 mRNA
fold change (comp. to Igf1 in pericytes)
350.0
300.0
250.0
200.0
150.0
100.0
50.0
0.0
endothelial cells
pericytes
astrocytes
breast cancer cells
melanoma cells
endothelial cells
pericytes
astrocytes
breast cancer cells
melanoma cells
human Igf1 mRNA
human Igf2 mRNA
B
fold change (comp. to Igf1 in m. pericytes)
2.5
2.0
1.5
1.0
0.5
0.0
m. endothelial cells
m. pericytes
m. astrocytes
m. breast c. c. (4T1)
m. breast c. c. (4T1-EmGFP)
m. breast c. c. (4T1-tdTomato)
m. melanoma cells
m. endothelial cells
m. pericytes
m. astrocytes
m. breast c. c. (4T1)
m. breast c. c. (4T1-EmGFP)
m. breast c. c. (4T1-tdTomato)
m. melanoma cells
mouse Igf1 mRNA
mouse Igf2 mRNA
C
IGF2 secretion (pg/ml)
1600
1400
1200
1000
800
600
400
200
0
*
pericytes
astrocytes
IGF2 secr. (pg/100,000 cells)
120
100
80
60
40
20
0
**
pericytes
astrocytes
D
patient brain met. (tr. neg. breast c.)
nuclei (Hoechst) + IGF1
nuclei (Hoechst) + pericytes (CD13)
merge
10 µm
E
patient brain met. (tr. neg. breast c.)
nuclei (Hoechst) + IGF2
nuclei (Hoechst) + pericytes (CD13)
merge
10 µm

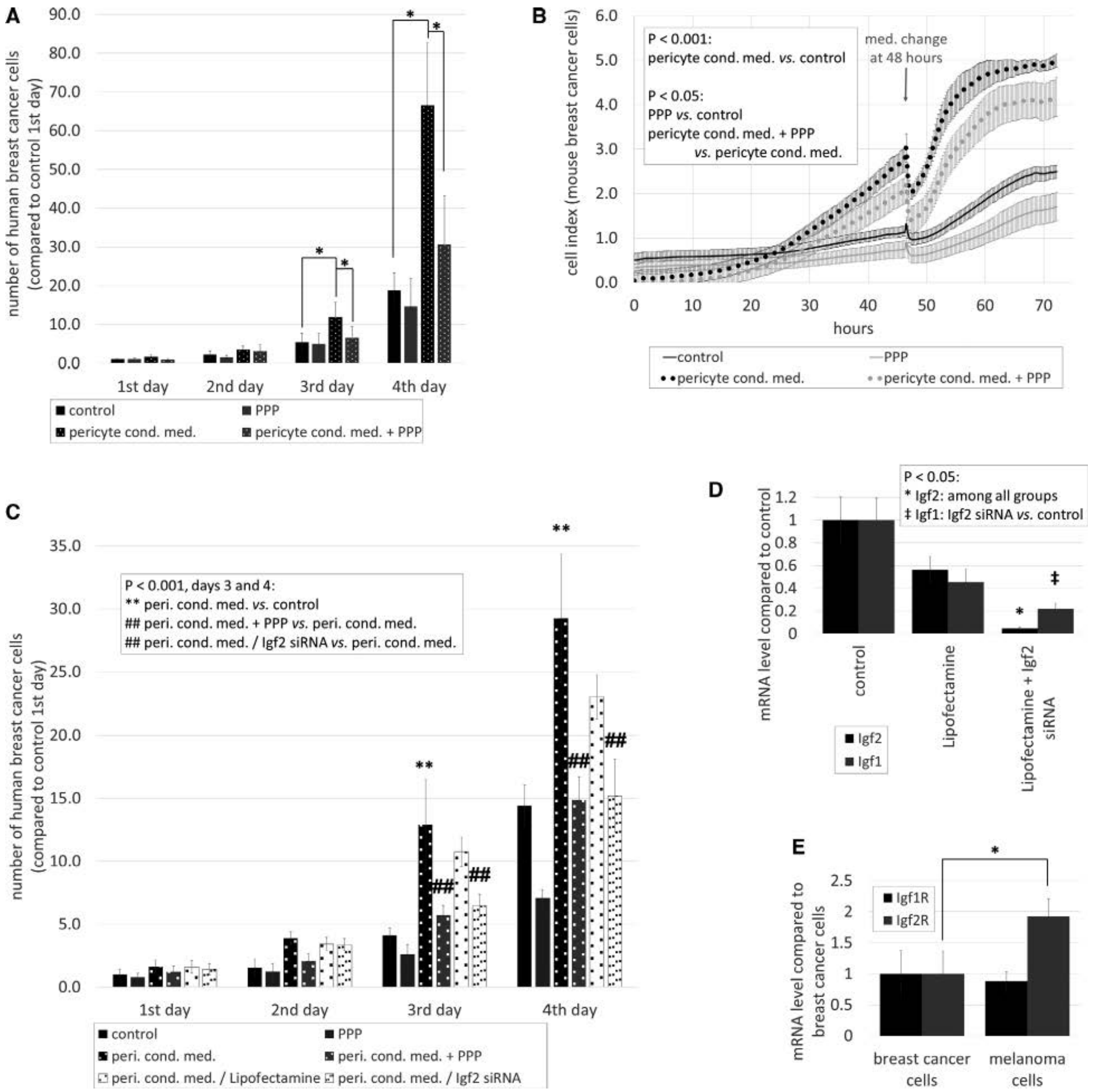

Fig. 6. Role of IGFs in breast cancer cell proliferation *in vitro*. (A) Quantification of MDA cell growth in control or pericyte-conditioned media in the presence or absence of PPP. Cells were counted in phase-contrast micrographs. $N = 5$, average ± SD, $^{*}P < 0.05$ (ANOVA and Bonferroni's *post hoc* test). (B) Growth of 4T1 cells in control or pericyte-conditioned media in the presence or absence of PPP, as assessed by impedance measurements. $N = 4$, average ± SD, $P < 0.001$ (cells cultured in pericyte-conditioned media compared to control), $P < 0.05$ (cells treated with PPP compared to control; cells cultured in pericyte-conditioned media and PPP compared to cells cultured in pericyte-conditioned media) (two-way ANOVA with repeated measures and Tukey's *post hoc* test). (C) Growth of MDA cells cultured in control or pericyte-conditioned media in the presence or absence of PPP, or in conditioned media of Lipofectamine-treated or Igf2-silenced pericytes. $N = 5$, average ± SD, $^{**}P < 0.01$ (compared to control), $^{\#\#}P < 0.01$ (compared to cells cultured in pericyte-conditioned media) (ANOVA and Bonferroni's *post hoc* test). (D) Effect of Igf2 silencing on Igf2 and Igf1 mRNA expression in HBVP cells, as assessed by qPCR with GAPDH as housekeeping gene. $N = 3$, average ± SD, $P < 0.05$ (ANOVA and Bonferroni's *post hoc* test). (E) Igf1R and Igf2R mRNA expression in human tumor cells. Results are shown as fold change in comparison with Igf1R in breast cancer cells. $N = 3$, average ± SD, $^{*}P < 0.05$ (ANOVA and Bonferroni's *post hoc* test).

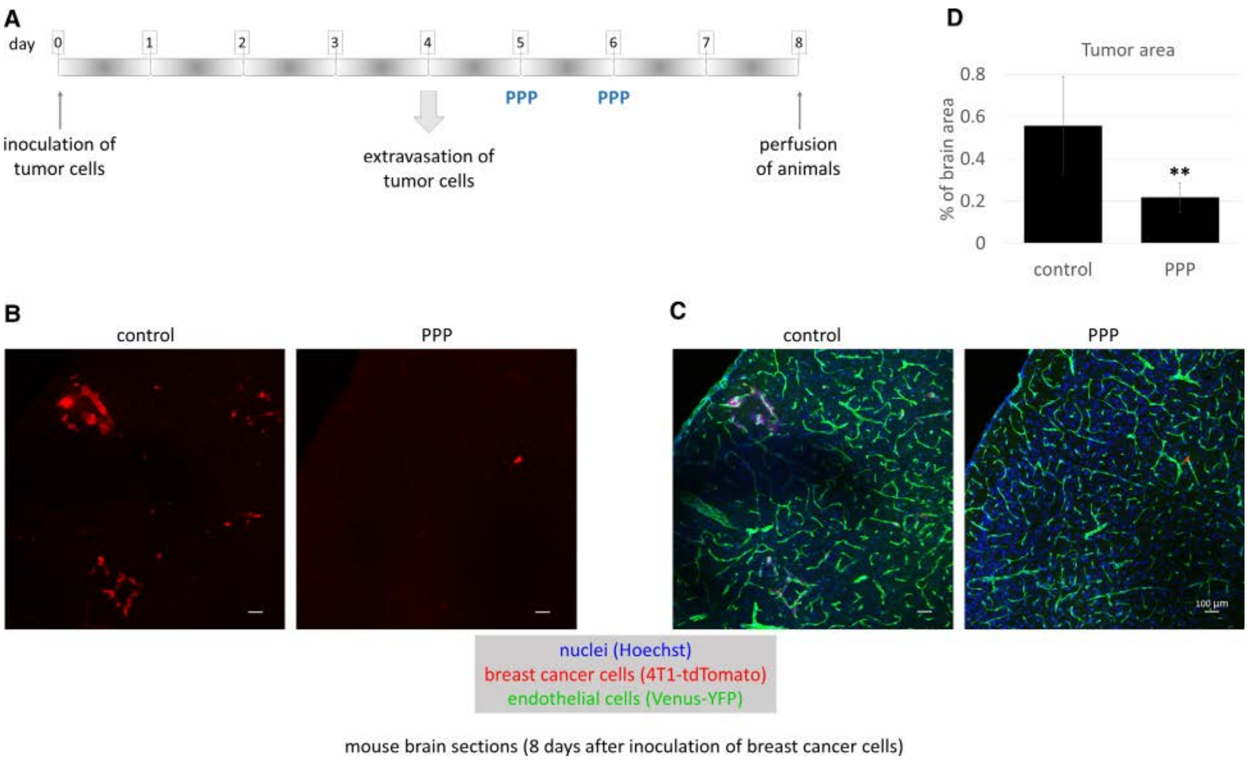

Fig. 7. Role of IGFs in breast cancer cell proliferation *in vivo*. (A) Experimental design of studying the role of IGFs in TNBC proliferation in the brains of mice. (B, C) Representative confocal micrographs of parietal brain sections of control FVB/Ant:TgCAG-yfp mice and animals treated with PPP, 8 days after inoculation of 4T1-tdTomato cells. Red channel represents tumor cells (B). In (C), the same sections are shown as in (B) in three channels: red, green (endothelium), and blue (nuclei) channels. Scale bar = 100 µm. (D) Quantification of tumor size in control and PPP-treated mice. Tumor area is presented as percentage of brain area, as calculated from 17 brain sections of three animals/treatment. Average ± SEM, $^{**}P < 0.01$ (two-way ANOVA without replication).

major sources of EMT factors in glioma [37]. We have also found that pericytes have a prompt effect on the proliferation of TNBC, but not of melanoma cells. Bioinformatics analysis, followed by experimental approaches confirmed high expression of IGFs in pericytes, contributing to breast cancer cell proliferation *in vitro* and *in vivo*. Indeed, in addition to regulating cell division, the IGF system has also been shown to promote induction of the EMT phenotype in epithelial tumors [38,39] and to play an important role in the maintenance of cancer stem cells in breast cancer [40].

Insulin-like growth factor signaling has been implicated in the growth and survival of both normal and malignant cells. IGF1R expression and activity increase in several tumor types, including breast cancer [41], resulting in enhanced proliferation rate, metastatic capacity, and resistance to chemotherapy [42]. Therefore, targeting of the IGF axis has been in the focus of therapeutic approach developments in numerous malignant diseases [43]. However, since many clinical trials have failed and further studies have been discontinued due to toxicity or low efficacy of the tested compounds, identification of predictive biomarkers is urged to define potentially responsive patient subgroups. Nevertheless, brain metastatic disease has not been specifically investigated in IGF1-targeting clinical trials, although inhibition of IGF1R has been shown to reduce breast cancer brain metastasis development in experimental models [44]. Moreover, a clinical phase I study has been completed with PPP (AXL1717) in patients with primary brain tumors, showing that the drug was well tolerated and no major side effects occurred [45].

5. Conclusions

Taken together, our results show that pericytes play crucial role in the development of brain secondary tumors by directly influencing key steps of metastatic colonization of the CNS. Secretion of soluble factors, including extracellular matrix proteins and growth factors, endows brain pericytes with significant pro-metastatic features, especially in breast cancer. Therefore, influencing pericyte functions might represent a future therapeutic opportunity in brain metastatic disease. This is in line with emerging approaches, which tend to target the more stable tumor microenvironment in addition to the very plastic cancer cells. Moreover, our study underlines the importance of IGF axis inhibition as a potential strategy in brain metastases, especially as there exists a compound (PPP/AXL1717) with high selectivity on IGF1R that not only has low toxicity, but is also BBB permeable. This is a great advantage, since the BBB represents the highest obstacle in the development of drugs targeting the CNS [46].

Acknowledgements

KM, MK, CF, and AEF are supported by the New National Excellence Program of the Ministry of Human Capacities (UNKP-19-3-SZTE-205, UNKP-19-3-SZTE-163, UNKP-19-4-SZTE-18, and UNKP-19-4-SZTE-43, respectively). CF and AEF are supported by the János Bolyai Research Fellowship of the Hungarian Academy of Sciences (BO/00213/19/8 and BO/00023/17/8, respectively). Work of CF, AEF, IAK, and IW is funded by NKFIH (National Research, Development and Innovation Office; project numbers: PD-121130, GINOP-2.3.2-15-2016-00020, GINOP-2.3.2-15-2016-00034, FK-132638, and FK-124114). Work of IW is supported by the UEFISCDI (Executive Agency for Higher Education, Research, Development and Innovation Funding) PN-III-P1-1.1-TE-2016-1352 project.

Conflict of interest

The authors declare no conflict of interest.

Author contributions

KM, IAK, and IW designed research study; KM, ÁM, CF, MK, FG, ZR, AEF, ÁN-T, and JH performed research; KM, LT, IAK, and IW analyzed the data; IW and IAK supervised research; IW drafted the manuscript; all authors approved final version.

References

1 Gabani P, Weiner AA, Hernandez-Aya LF, Khwaja S, Roach MC, Ochoa LL, Mullen D, Thomas MA, Matesa MA, Margenthaler JA *et al.* (2019) Treatment response as predictor for brain metastasis in triple negative breast cancer: a score-based model. *Breast J* **25**, 363–372.

2 Davies MA, Liu P, McIntyre S, Kim KB, Papadopoulos N, Hwu WJ, Hwu P & Bedikian A (2011) Prognostic factors for survival in melanoma patients with brain metastases. *Cancer* **117**, 1687–1696.

3 Wilhelm I, Molnar J, Fazakas C, Hasko J & Krizbai IA (2013) Role of the blood-brain barrier in the formation of brain metastases. *Int J Mol Sci* **14**, 1383–1411.

4 Han CH & Brastianos PK (2017) Genetic characterization of brain metastases in the era of targeted therapy. *Front Oncol* **7**, 230.

5 Fischer GM, Jalali A, Kircher DA, Lee WC, McQuade JL, Haydu LE, Joon AY, Reuben A, de Macedo MP, Carapeto FCL *et al.* (2019) Molecular profiling reveals unique immune and metabolic features of melanoma brain metastases. *Cancer Discov* **9**, 628–645.

6 Wilhelm I, Fazakas C, Molnar K, Vegh AG, Hasko J & Krizbai IA (2018) Foe or friend? Janus-faces of the neurovascular unit in the formation of brain metastases. *J Cereb Blood Flow Metab* **38**, 563–587.

7 von Tell D, Armulik A & Betsholtz C (2006) Pericytes and vascular stability. *Exp Cell Res* **312**, 623–629.

8 Winkler EA, Birk H, Burkhardt JK, Chen X, Yue JK, Guo D, Rutledge WC, Lasker GF, Partow C, Tihan T *et al.* (2018) Reductions in brain pericytes are associated with arteriovenous malformation vascular instability. *J Neurosurg* **129**, 1464–1474.

9 Armulik A, Genove G, Mae M, Nisancioglu MH, Wallgard E, Niaudet C, He L, Norlin J, Lindblom P, Strittmatter K *et al.* (2010) Pericytes regulate the blood-brain barrier. *Nature* **468**, 557–561.

10 Daneman R, Zhou L, Kebede AA & Barres BA (2010) Pericytes are required for blood-brain barrier integrity during embryogenesis. *Nature* **468**, 562–566.

11 Hall CN, Reynell C, Gesslein B, Hamilton NB, Mishra A, Sutherland BA, O'Farrell FM, Buchan AM, Lauritzen M & Attwell D (2014) Capillary pericytes regulate cerebral blood flow in health and disease. *Nature* **508**, 55–60.

12 Hill RA, Tong L, Yuan P, Murikinati S, Gupta S & Grutzendler J (2015) Regional blood flow in the normal and ischemic brain is controlled by arteriolar smooth muscle cell contractility and not by capillary pericytes. *Neuron* **87**, 95–110.

13 Cheng L, Huang Z, Zhou W, Wu Q, Donnola S, Liu JK, Fang X, Sloan AE, Mao Y, Lathia JD *et al.* (2013) Glioblastoma stem cells generate vascular pericytes to support vessel function and tumor growth. *Cell* **153**, 139–152.

14 Murgai M, Ju W, Eason M, Kline J, Beury DW, Kaczanowska S, Miettinen MM, Kruhlak M, Lei H, Shern JF *et al.* (2017) KLF4-dependent perivascular cell plasticity mediates pre-metastatic niche formation and metastasis. *Nat Med* **23**, 1176–1190.

15 Armulik A, Abramsson A & Betsholtz C (2005) Endothelial/pericyte interactions. *Circ Res* **97**, 512–523.

16 Hasko J, Fazakas C, Molnar K, Meszaros A, Patai R, Szabo G, Erdelyi F, Nyul-Toth A, Gyori F, Kozma M

et al. (2019) Response of the neurovascular unit to brain metastatic breast cancer cells. *Acta Neuropathol Commun* **7**, 133.

17 Herman H, Fazakas C, Hasko J, Molnar K, Meszaros A, Nyul-Toth A, Szabo G, Erdelyi F, Ardelean A, Hermenean A *et al.* (2019) Paracellular and transcellular migration of metastatic cells through the cerebral endothelium. *J Cell Mol Med* **23**, 2619–2631.

18 Schindelin J, Arganda-Carreras I, Frise E, Kaynig V, Longair M, Pietzsch T, Preibisch S, Rueden C, Saalfeld S, Schmid B *et al.* (2012) Fiji: an open-source platform for biological-image analysis. *Nature Methods* **9**, 676–682. https://doi.org/10.1038/nmeth.2019

19 Wilhelm I, Nagyoszi P, Farkas AE, Couraud PO, Romero IA, Weksler B, Fazakas C, Dung NT, Bottka S, Bauer H *et al.* (2008) Hyperosmotic stress induces Axl activation and cleavage in cerebral endothelial cells. *J Neurochem* **107**, 116–126.

20 Bugyik E, Dezso K, Reiniger L, Laszlo V, Tovari J, Timar J, Nagy P, Klepetko W, Dome B & Paku S (2011) Lack of angiogenesis in experimental brain metastases. *J Neuropathol Exp Neurol* **70**, 979–991.

21 Teglasi V, Csury DT, Dezso K, Bugyik E, Szabo V, Szallasi Z, Paku S & Reiniger L (2019) Origin and distribution of connective tissue and pericytes impacting vascularization in brain metastases with different growth patterns. *J Neuropathol Exp Neurol* **78**, 326–339.

22 Seong J, Wang N & Wang Y (2013) Mechanotransduction at focal adhesions: from physiology to cancer development. *J Cell Mol Med* **17**, 597–604.

23 Vanlandewijck M, He L, Mae MA, Andrae J, Ando K, Del Gaudio F, Nahar K, Lebouvier T, Lavina B, Gouveia L *et al.* (2018) A molecular atlas of cell types and zonation in the brain vasculature. *Nature* **554**, 475–480.

24 Ellis MJ, Jenkins S, Hanfelt J, Redington ME, Taylor M, Leek R, Siddle K & Harris A (1998) Insulin-like growth factors in human breast cancer. *Breast Cancer Res Treat* **52**, 175–184.

25 Girnita A, Girnita L, del Prete F, Bartolazzi A, Larsson O & Axelson M (2004) Cyclolignans as inhibitors of the insulin-like growth factor-1 receptor and malignant cell growth. *Can Res* **64**, 236–242.

26 Martin-Kleiner I & Gall Troselj K (2010) Mannose-6-phosphate/insulin-like growth factor 2 receptor (M6P/IGF2R) in carcinogenesis. *Cancer Lett* **289**, 11–22.

27 Yin S, Girnita A, Stromberg T, Khan Z, Andersson S, Zheng H, Ericsson C, Axelson M, Nister M, Larsson O *et al.* (2010) Targeting the insulin-like growth factor-1 receptor by picropodophyllin as a treatment option for glioblastoma. *Neuro Oncol* **12**, 19–27.

28 Lyle LT, Lockman PR, Adkins CE, Mohammad AS, Sechrest E, Hua E, Palmieri D, Liewehr DJ, Steinberg SM, Kloc W *et al.* (2016) Alterations in pericyte subpopulations are associated with elevated blood-tumor barrier permeability in experimental brain metastasis of breast cancer. *Clin Cancer Res* **22**, 5287–5299.

29 Schiffer D, Annovazzi L, Casalone C, Corona C & Mellai M (2018) Glioblastoma: microenvironment and niche concept. *Cancers* **11**, 5.

30 Krenzlin H, Behera P, Lorenz V, Passaro C, Zdioruk M, Nowicki MO, Grauwet K, Zhang H, Skubal M, Ito H *et al.* (2019) Cytomegalovirus promotes murine glioblastoma growth via pericyte recruitment and angiogenesis. *J Clin Investig* **130**, 1671–1683.

31 Valdor R, Garcia-Bernal D, Bueno C, Rodenas M, Moraleda JM, Macian F & Martinez S (2017) Glioblastoma progression is assisted by induction of immunosuppressive function of pericytes through interaction with tumor cells. *Oncotarget* **8**, 68614–68626.

32 Valdor R, Garcia-Bernal D, Riquelme D, Martinez CM, Moraleda JM, Cuervo AM, Macian F & Martinez S (2019) Glioblastoma ablates pericytes antitumor immune function through aberrant up-regulation of chaperone-mediated autophagy. *Proc Natl Acad Sci USA* **116**, 20655–20665.

33 Carbonell WS, Ansorge O, Sibson N & Muschel R (2009) The vascular basement membrane as “soil” in brain metastasis. *PLoS One* **4**, e5857.

34 Valiente M, Obenauf AC, Jin X, Chen Q, Zhang XH, Lee DJ, Chaft JE, Kris MG, Huse JT, Brogi E *et al.* (2014) Serpins promote cancer cell survival and vascular co-option in brain metastasis. *Cell* **156**, 1002–1016.

35 Thomsen MS, Routhe LJ & Moos T (2017) The vascular basement membrane in the healthy and pathological brain. *J Cereb Blood Flow Metab* **37**, 3300–3317.

36 Fedele M, Cerchia L & Chiappetta G (2017) The epithelial-to-mesenchymal transition in breast cancer: focus on basal-like carcinomas. *Cancers* **9**, 134.

37 Mader L, Blank AE, Capper D, Jansong J, Baumgarten P, Wirsik NM, Zachskorn C, Ehlers J, Seifert M, Klink B *et al.* (2018) Pericytes/vessel-associated mural cells (VAMCs) are the major source of key epithelial-mesenchymal transition (EMT) factors SLUG and TWIST in human glioma. *Oncotarget* **9**, 24041–24053.

38 Cevenini A, Orru S, Mancini A, Alfieri A, Buono P & Imperlini E (2018) Molecular signatures of the insulin-like growth factor 1-mediated epithelial-mesenchymal transition in breast, lung and gastric cancers. *Int J Mol Sci* **19**, 2411.

39 Li H, Batth IS, Qu X, Xu L, Song N, Wang R & Liu Y (2017) IGF-IR signaling in epithelial to mesenchymal transition and targeting IGF-IR therapy: overview and new insights. *Mol Cancer* **16**, 6.

40 Chang WW, Lin RJ, Yu J, Chang WY, Fu CH, Lai A, Yu JC & Yu AL (2013) The expression and significance

of insulin-like growth factor-1 receptor and its pathway on breast cancer stem/progenitors. *Breast Cancer Res* **15**, R39.

41 Yee D (2018) Anti-insulin-like growth factor therapy in breast cancer. *J Mol Endocrinol* **61**, T61–T68.

42 Yuan J, Yin Z, Tao K, Wang G & Gao J (2018) Function of insulin-like growth factor 1 receptor in cancer resistance to chemotherapy. *Oncol Lett* **15**, 41–47.

43 Osher E & Macaulay VM (2019) Therapeutic targeting of the IGF axis. *Cells* **8**, 895.

44 Saldana SM, Lee HH, Lowery FJ, Khotskaya YB, Xia W, Zhang C, Chang SS, Chou CK, Steeg PS, Yu D *et al.* (2013) Inhibition of type I insulin-like growth factor receptor signaling attenuates the development of breast cancer brain metastasis. *PLoS One* **8**, e73406.

45 Aiken R, Axelson M, Harmenberg J, Klockare M, Larsson O & Wassberg C (2017) Phase I clinical trial of AXL1717 for treatment of relapsed malignant astrocytomas: analysis of dose and response. *Oncotarget* **8**, 81501–81510.

46 Krizbai IA, Nyul-Toth A, Bauer HC, Farkas AE, Traweger A, Hasko J, Bauer H & Wilhelm I (2016) Pharmaceutical targeting of the brain. *Curr Pharm Des* **22**, 5442–5462.

Supporting information

Additional supporting information may be found online in the Supporting Information section at the end of the article.

Fig. S1. Tumor cell adhesion onto brain cells.

Fig. S2. Signaling pathways involved in pericyte-enhanced tumor cell adhesion.

Fig. S3. Tumor cell proliferation and IGF expression in the brain.

Fig. S4. Effect of IGF inhibition on tumor cell proliferation.

Table S1. Primary antibodies used for immunofluorescence (IF) and western blot (WB).

Table S2. Primers used for real-time PCR.

Received: 8 January 2021 | Revised: 23 April 2021 | Accepted: 7 June 2021

DOI: 10.1002/bit.27855

ARTICLE

BIOTECHNOLOGY BIOENGINEERING WILEY

On-chip determination of tissue-specific metastatic potential of breast cancer cells

Burcu Firatligil-Yildirir[1] | Gizem Bati-Ayaz[2] | Ismail Tahmaz[2] | Muge Bilgen[2] | Devrim Pesen-Okvur[1] | Ozden Yalcin-Ozuysal[1]

[1]Department of Molecular Biology and Genetics, Izmir Institute of Technology, Izmir, Turkey

[2]Izmir Institute of Technology, Biotechnology and Bioengineering Graduate Program, Izmir, Turkey

Correspondence

Devrim Pesen-Okvur and Ozden Yalcin-Ozuysal, İzmir Yüksek Teknoloji Enstitüsü, Moleküler Biyoloji ve Genetik Bölümü, 35430, Urla, Izmir, Turkey.
Email: devrimpesen@iyte.edu.tr and ozdenyalcin@iyte.edu.tr

Funding information

Türkiye Bilimsel ve Teknolojik Arastirma Kurumu, Grant/Award Number: 115E057

Abstract

Metastasis is one of the major obstacles for breast cancer patients. Limitations of current models demand the development of custom platforms to predict metastatic potential and homing choices of cancer cells. Here, two organ-on-chip platforms, invasion/chemotaxis (IC-chip) and extravasation (EX-chip) were used for the quantitative assessment of invasion and extravasation towards specific tissues. Lung, liver and breast microenvironments were simulated in the chips using tissue-specific cells embedded in matrigel. In the IC-chip, invasive MDA-MB-231, but not non-invasive MCF-7 breast cancer cells invaded into lung and liver microenvironments. In the EX-chip, MDA-MB-231 cells extravasated more into the lung compared to the liver and breast microenvironments. In addition, lung-specific MDA-MB-231 clone invaded and extravasated into the lung microenvironment more efficiently than the bone-specific clone. Both invasion/chemotaxis and extravasation results were in agreement with published clinical data. Collectively, our results show that IC-chip and EX-chip, simulating tissue-specific microenvironments, can distinguish different in vivo metastatic phenotypes, in vitro. Determination of tissue-specific metastatic potential of breast cancer cells is expected to improve diagnosis and help select the ideal therapy.

KEYWORDS

breast cancer, extravasation, invasion, lab-on-a-chip, metastasis

1 | INTRODUCTION

Metastasis is the main cause of breast cancer mortality among women. The latest statistics revealed that the 5-year relative survival rate for women with metastatic breast cancer is around 26% between 1975 and 2017 (Howlader et al., 2020). Breast cancer frequently metastasizes to bone, lung, liver and brain. Although the molecular and histopathological subtypes of the tumor provide information on the metastasis risk and the target organs, there is no diagnostic tool available that can accurately predict the risk and the organ preference for an individual patient's tumor. The target organ for metastasis is specified by both physiological architectures of the circulatory system and molecular determinants. It was first hypothesized by Stephan Paget in the 19th century that metastasizing tumor cells grow preferentially in specific target organs in a similar manner that a “seed” grows only in a suitable “soil” (Paget, 1889). Since then, experimental evidence has been supporting the “seed and soil” hypothesis by showing that molecular determinants on primary

---

Burcu Firatligil-Yildirir and Gizem Bati-Ayaz contributed equally to this study.

tumor and microenvironment of the target tissue are involved in the establishment of metastasis patterns (Langley & Fidler, 2011). Thus, a platform that integrates the information coming from tumor cells and the target organs would provide a diagnostic tool that can estimate the likeness of metastasis for a given tumor cell population towards specific environments.

The metastasis cascade is a complex phenomenon that includes in series, invasion, migration, intravasation and extravasation. The invasion process starts when cancer cells dissociate from their primary sites after losing cell-cell adhesion capacity and invade the surrounding stroma, while the extravasation process involves interactions between cancer cells and endothelial cells, where cancer cells pass through the endothelial layer into the target organ (Fares et al., 2020). Here, we focus on invasion and extravasation steps of the cascade to predict the metastatic potential of the cells towards different environments.

In vivo animal models have been used for the investigation of the metastatic process. However, they do not match the clinical progression, are costly, require months to reach results and are limited in throughput (Kimura et al., 2018). The Boyden chamber and transwell systems are the most favored in vitro platforms to study invasion and extravasation due to their simplicity. However, they use artificial barrier membranes that do not allow detailed visualization of cellular behavior at multiple time points. On the other hand, organ-on-chip (OoC) systems have low fabrication costs, can generate results within days, allow 3D cell culture of human cells, are compatible with various microscopy techniques and thus are well suited for spatial and temporal quantitative data analysis. OoC systems that can mimic the in vivo microenvironment present great advantages for in vitro strategies and therefore they have a huge potential to minimize animal testing in the preclinical research area (Rodrigues et al., 2020; Soscia et al., 2017; Wu et al., 2020).

In vitro OoC models were developed to investigate different factors involved in metastasis such as intravasation (Shirure et al., 2018; Song et al., 2009; Truong et al., 2016), angiogenesis (Bi et al., 2020; Shirure et al., 2018; Vickerman & Kamm, 2012) the interaction between tumor cells and endothelial cells with stromal cells and immune cells (Bi et al., 2020; Boussommier-Calleja et al., 2019; Zervantonakis et al., 2012), the interstitial flow (Polacheck et al., 2011), matrix stiffness (Pathak & Kumar, 2012), and extravasation (Bersini et al., 2014; Boussommier-Calleja et al., 2019; Chen, Whisler, et al. (2017); Jeon et al., 2015). Target tissues such as bone (Bersini et al., 2014) and lung (Bi et al., 2020; Boussommier-Calleja et al., 2019; Shirure et al., 2018) were modelled in some of OoC models. However, assessment of tissue-specific invasion and extravasation in the context of the homing choices of cancer cells has been lacking. Here, two OoC platforms, invasion/chemotaxis (IC-chip) and extravasation (EX-chip) were used for the quantitative and comparative assessment of invasion and extravasation into microenvironments simulating specific tissues relevant to the breast cancer metastasis.

2 | MATERIALS AND METHODS

2.1 | Lab-on-a-chip fabrication

Invasion-chemotaxis and extravasation lab-on-a-chip platforms (IC-chip and EX-chip) (Figure S1, Supporting Information) were either provided by Initio Biomedical Engineering (Turkey) or fabricated by soft lithography as previously described (Ozdil et al., 2014). Briefly, SU-8 polymer was spin-coated on a silicon wafer. The design of the chip was exposed through a mask to UV light. After removing the uncrosslinked SU8 polymer using the developer solution, molds were ready for polydimethylsiloxane (PDMS) casting. After PDMS polymerization, inlet and outlet holes were punched with biopsy punches. The PDMS parts were cleaned and bonded to clean microscope slides after treatment in UV/Ozone cleaner (Bioforce Nanosciences). The chips were sterilized with UV light in a laminar hood for 15 min before use. The dimensions of IC-chip: the homing matrix channel (HMC) 3 mm width × 12 mm length × 200 μm height and medium channels (MC1/MC2) 3 mm width × 12 mm length × 200 μm height; EX-chip: the HMC 3 mm width × 15 mm length × 200 μm height, endothelial monolayer channel (EMC) 3 mm width × 20 mm length × 200 μm height and medium channel (MC) 3 mm width × 10 mm length × 200 μm height.

2.2 | Chip surface modification

IC-chips were used without any surface modifications. EX-chips were first coated with either poly-L-lysine (PLL, P8920; Sigma-Aldrich) or 3-aminopropyltriethoxysilane (APTES, A3648; Sigma-Aldrich). EX-chips were incubated with PLL (0.01 mg ml^{-1}) in ultra-pure water at 37°C in a 5% CO_2 incubator overnight. The following day, EX-chips were washed with ultra-pure water three times and then kept at 80°C for 24 h to reduce hydrophobicity of the surface. For APTES modification of surfaces, APTES (2%) dissolved in acetone was loaded into the channels of EX-chips and incubated for 15 min in laminar flow cabin. Then EX-chips were washed with first PBS once and then ultra-pure autoclaved H_2O three times. At this step, EX-chips were ready to be coated with extracellular matrix proteins: laminin (LAM), type I collagen (COL) or FN. LAM (0.0125 mg ml^{-1}, L2020; Sigma-Aldrich) and FN (0.0125 mg ml^{-1}, F2006, Sigma-Aldrich) were prepared in 1X Universal Buffer (UB), while COL (0.0125 mg ml^{-1}, 354249; Corning) was diluted in serum-free DMEM (Biological Industries; 01-055-1A). Each protein solution was loaded into EX-chips and they were incubated at 37°C in a 5% CO_2 incubator for 1 h. LAM- and FN-coated EX-chips were washed first with PBS once and then with ultra-pure autoclaved H_2O three times. COL-coated EX-chips were washed first with serum-free DMEM and then ultra-pure autoclaved H_2O for three times. Any remaining H_2O was aspirated by vacuum. EX-chips were stored in vacuum desiccators at least one day before use in experiments. APTES-LAM-coated EX-chips were used in all extravasation assays (Figure S1b, Supporting Information).

2.3 | Cell lines

Human breast cancer cell lines (MDA-MB-231 and MCF-7), human normal mammary epithelial cell line (MCF-10A), human normal lung fibroblast cell line (WI-38), rat normal liver cell line (BRL-3A), and human umbilical vein endothelial cell line (HUVEC-C) were obtained from ATCC. Organ-specific metastatic clones of MDA-MB-231, MDA-MB-231 LM2 and MDA-MB-231 1833-BoM were described previously (Bos et al., 2009; Kang et al., 2005; Minn et al., 2005) and were gifts from the Joan Massagué Lab in Memorial Sloan Kettering Cancer Center. MDA-MB-231, its derivatives and MCF-7 were cultured in DMEM high glucose (11965092; Gibco) with fetal bovine serum (FBS, 10%) (A3840001; Gibco) and penicillin/streptomycin (15070063; Gibco; 1%); MCF-10A was cultured in DMEM-F12 high glucose (11330057; Gibco) with Horse Serum (04-004-1A; Biological Industries; 5%), Insulin (I9278; Sigma; 10 μg ml^{-1}), Cholera Toxin (C8052; Sigma; 100 ng ml^{-1}), EGF (E9644; Sigma; 20 ng ml^{-1}), Hydrocortisone (H0888; Sigma; 0.5 μg ml^{-1}) and penicillin/streptomycin (1%). WI-38 and BRL-3A were cultured in high glucose MEM-α (01-042-1A; Biological Industries) with FBS (10%) and penicillin/streptomycin (1%). HUVEC-C cell line was cultured in DMEM-F12K high glucose (01-095-1 A, Biological Industries) with FBS (10%), heparin (H3393; Sigma; 0.1 mg ml^{-1}), endothelial cell growth supplement (EGCS, 0.05 mg ml^{-1}) (354006; Sigma) and penicillin/streptomycin (1%). All cell lines were cultured at 37°C in a humidified incubator with 5% CO_2.

2.4 | Labelling of cell lines

MDA-MB-231, metastatic clones of MDA-MB-231 (LM2 and 1833-BoM) and MCF-7 cancer cell lines were stably labelled with a red fluorescent protein (DsRed). MSCV retroviruses expressing both DsRed and puromycin resistance genes were used for infection. The preparation of viruses and infection of cells were performed as described previously (Yalcin-Ozuysal et al., 2010; Zengin et al., 2015). 48 h after infection, the antibiotic selection was carried out with puromycin (2 µg ml^{-1}) until all of the uninfected cells died. Transient labelling of HUVEC-C cells was performed by Green Cell Tracker CMFDA (C2925; Invitrogen). The dye was dissolved in dimethyl sulfoxide to obtain stock solution (25 mM) which was then diluted with serum-free DMEM-F12K media to get working concentration (5 µM). Cells were washed with warm PBS once, and then tracker (5 µM) was added over the cells. After 30 min of incubation at 37°C, the media was removed, cells were washed with PBS once and then complete HUVEC-C growth media was added. Labelling was performed 30 min before the experimental set-up.

2.5 | Invasion assay

IC-chips were used for invasion assays (Figure S1a). For cell-free assays, growth factor reduced matrigel (GFR-matrigel, 8 mg ml^{-1}) (354230; Corning) was diluted in 1:1 ratio with pre-cooled serum-free media and loaded into the HMC of the chips. Then, chips were incubated for polymerization at 37°C in a humidified incubator with 5% CO_2 for 30 min. After polymerization of GFR-matrigel, either serum-free or serum-containing media was loaded into the media channels 1 and 2 (MC1, MC2) and chips were incubated overnight. The following day, media in MC1 and MC2 were removed, channels were washed with serum-free media twice. Then serum-free (0%) or serum-containing media (10%) was added to MC2 of the chip for the relevant conditions. DsRed labelled MDA-MB-231 cells (1×10^6 cells ml^{-1}) resuspended in serum-free media were added to MC1. The chips were incubated vertically for 3 days.

To analyze the effects of serum on invasion towards liver microenvironment, BRL-3A normal liver cells (1×10^7 cells ml^{-1}) with GFR-matrigel were loaded to HMC of the IC-chips as explained above. Then, chips were incubated overnight with culture media with (2% or 10%) or without (0%) serum at both MC1 and MC2 channels. The following day, MC2 was loaded with serum-free media after washing the channel with serum-free media twice. DsRed labelled MDA-MB-231 cells (1×10^6 cells ml^{-1}) in serum-free media, were added to the MC1 and incubated vertically for 3 days.

To analyze invasion towards specific tissues, lung, liver and breast microenvironments were modelled by tissue-specific normal cell lines WI-38, BRL-3A and MCF-10A, respectively. Two different cell densities (2.5×10^6 and 5×10^6 cells ml^{-1} for WI38; 1×10^7 and 2×10^7 cells ml^{-1} for BRL3A) were tested for gene expression of factors involved in chemoattraction (CCL5, CXCL12, and IGF1) (Supporting Information). The cell density that provided higher cytokine expression levels was used for modeling the specific homing tissues. (Figure S2a and S2b, Supporting Information). MCF10A cells did not express any of the cytokines and they were seeded at a similar density to WI-38 cells. The cells seeded at the determined cell density organized into 3D structures in GFR-matrigel (Figure S2c, Supporting Information). Each cell line (BRL-3A: 1×10^7 cells ml^{-1}, WI-38: 5×10^6 cells ml^{-1}, MCF-10A: $4{,}4 \times 10^6$ cells ml^{-1}) was mixed with GFR-matrigel and loaded into the HMC of the IC-chips. The chips were incubated overnight with serum-free media in MC1 and MC2. The following day, media in MC2 was changed with fresh serum-free media. MDA-MB-231 or MCF-7 cells (1×10^6 cells ml^{-1}) were seeded to MC1 in serum-free media. Chips were incubated vertically for 3 days. The invasion was visualized every 24 h by 3D imaging using a Leica SP8 confocal microscope.

2.6 | Analysis of invasion

Z-stack images of post-gaps of IC-chips were acquired each day with a ×10 objective and a z-step size of 7.52 µm. The analysis of the acquired images was performed by Python programming and R Studio as previously explained (Ilhan et al., 2020). Briefly, the sum projection of z-stacks was thresholded and the distance of each bright pixel to the starting line of the invasion was calculated. The invasion capacity of the cells was determined through normalization of data sets to Day 1.

2.7 | Endothelial monolayer formation

HUVEC-C cells labelled with Green Cell Tracker CMFDA were collected from culture dishes following Trypsin EDTA Solution A (0.25%, 03-050-1B; Biological Industries) treatment for 5 min. After centrifugation, they were resuspended in 450–650 kDa dextran (8%, 31392; Sigma-Aldrich) in HUVEC-C media. The HUVEC-C cells ($3.85 \times 10^6\,\mathrm{ml}^{-1}$) were loaded to EMC of APTES-LAM-coated EX-chips. EX-chips were incubated vertically at 37°C in a humidified incubator with 5% CO_2 overnight. Endothelial monolayer formation was confirmed by 3D imaging using a Leica SP8 confocal microscope with a × 10 objective and a z-step size of 7.52 μm.

2.8 | Actin staining for endothelial monolayer

Actin staining was performed to confirm the physical integrity of the endothelial cell monolayer. Cell-free GFR-matrigel (1:1 GFR-matrigel in serum-free media) was loaded to the HMC of the EX-chips. Following polymerization of matrigel, HUVEC-C cells were seeded to the EMC, culture media was loaded into the MC and chips were incubated overnight at 37°C in a humidified incubator with 5% CO_2. The following day, media within EMC and MC was removed and paraformaldehyde (4%) was added to fix the sample. Then, the chip was incubated overnight at +4°C. The following day, the EMC and MC were washed with PBS (× 1) three times. Permeabilization solution (5% BSA and 0.1% Triton-X-100 in PBS buffer) was loaded to the EMC and MC and incubated at room temperature (RT) for 15 min. Then, the EMC and MC were washed with PBS (× 1) three times. Phalloidin (1:40, Alexa Fluor™ 647) (A22287; Invitrogen) for actin-filament staining and 4′,6-diamidino-2-phenylindole (DAPI; 1:500) for nuclei staining diluted in PBS were loaded to the EMC and MC and the chip was incubated for one hour at RT in the dark. Finally, the EMC and MC were washed with PBS and then filled with anti-fading mounting media (90% glycerol, 10% PBS × 10, 0.1 M or 2% (w/v) n-propyl gallate). The chip was kept at +4°C. The next day, images were acquired by a Leica SP8 confocal microscope (Figure 4c).

2.9 | Endothelial monolayer permeability assay

Fluorescently labelled 70-kDa dextran TR (D1830, Texas Red, neutral, Thermo Fisher Scientific) (final concentration $0.1\,\mathrm{mg\,ml}^{-1}$) was used for the measurement of endothelial monolayer permeability as described previously (van Duinen et al., 2017). 70-kDa dextran TR in PBS was loaded into the EMC. The chip was imaged using a Leica SP8 confocal microscope with × 10 objective. Images were captured every 10 min for up to 2 h. Images were then processed with ImageJ/Fiji and numerical analysis was performed using Excel. Fluorescence signal intensities were measured for the regions of interest drawn in the EMC and the HMC along the post gaps. Permeability (P) was calculated according to $P = [d(I_{HMC}/I_{EMC})/dt]^{*}V_{gel}{}^{*}1/A$ where I_{HMC} and I_{EMC} are the fluorescence intensities in the HMC and EMC, respectively; V_{gel} is the volume of the gel ($10\,\mathrm{mm}^3$), A is the surface area of the post gap ($0.06\,\mathrm{mm}^2$).

2.10 | Extravasation assay

EX-chips were used for extravasation assays (Figure S1b). The same protocols for environment generation in the invasion assay and endothelial monolayer formation were followed as explained above. Once the monolayer was formed by HUVEC-C cells, DsRed labelled MDA-MB-231 cells (1×10^6 cells ml^{-1}) were seeded to the EMC in serum-free media for each condition (lung, liver and breast microenvironments) and the chips were incubated vertically for 3 days. The integrity of endothelial monolayer was confirmed by confocal microscopy immediately after addition of MDA-MB-231 cells. The extravasation of MDA-MB-231 cells to the generated lung, liver and breast microenvironments was visualized by 3D imaging using a Leica SP8 confocal microscope at × 10 magnification and a z-step size of 7.52 μm for 3 days.

2.11 | Analysis of extravasation

Z-stack images of post gaps of EX-chips were acquired each day with a 10X objective and a z-step size of 7.52 μm. The integrity of endothelial layer covering the post-gaps was confirmed by green signal for each time point. Cancer cells were marked as “extravasated” if they passed through the endothelial monolayer, or “associated” if they kept in contact with the endothelial monolayer. The efficiency of the EX-chips was quantified by the extravasation metric (EM), defined as the ratio of the number of post gaps with one or more extravasated cells to the total number of post gaps. If extravasation is observed in all ROIs, the EM will be 1. The $\chi 2$ (Chi-squared) test was used for the statistical analysis of the EM.

2.12 | Statistical analysis

For each quantification, at least 3 post-gaps were analyzed. The number of post-gaps were indicated as “*n*” in the figure legends. Results are reported mean ± *SEM* unless otherwise noted. Student's *t* test was used for statistical analysis unless otherwise noted. A *p*-value of <.05 was considered significant.

3 | RESULTS

3.1 | Effect of serum on the invasion/chemotaxis of breast cancer cells in the presence and absence of homing cells

Invasion/chemotaxis and extravasation are two crucial steps in cancer metastasis. The factors secreted from stromal cells

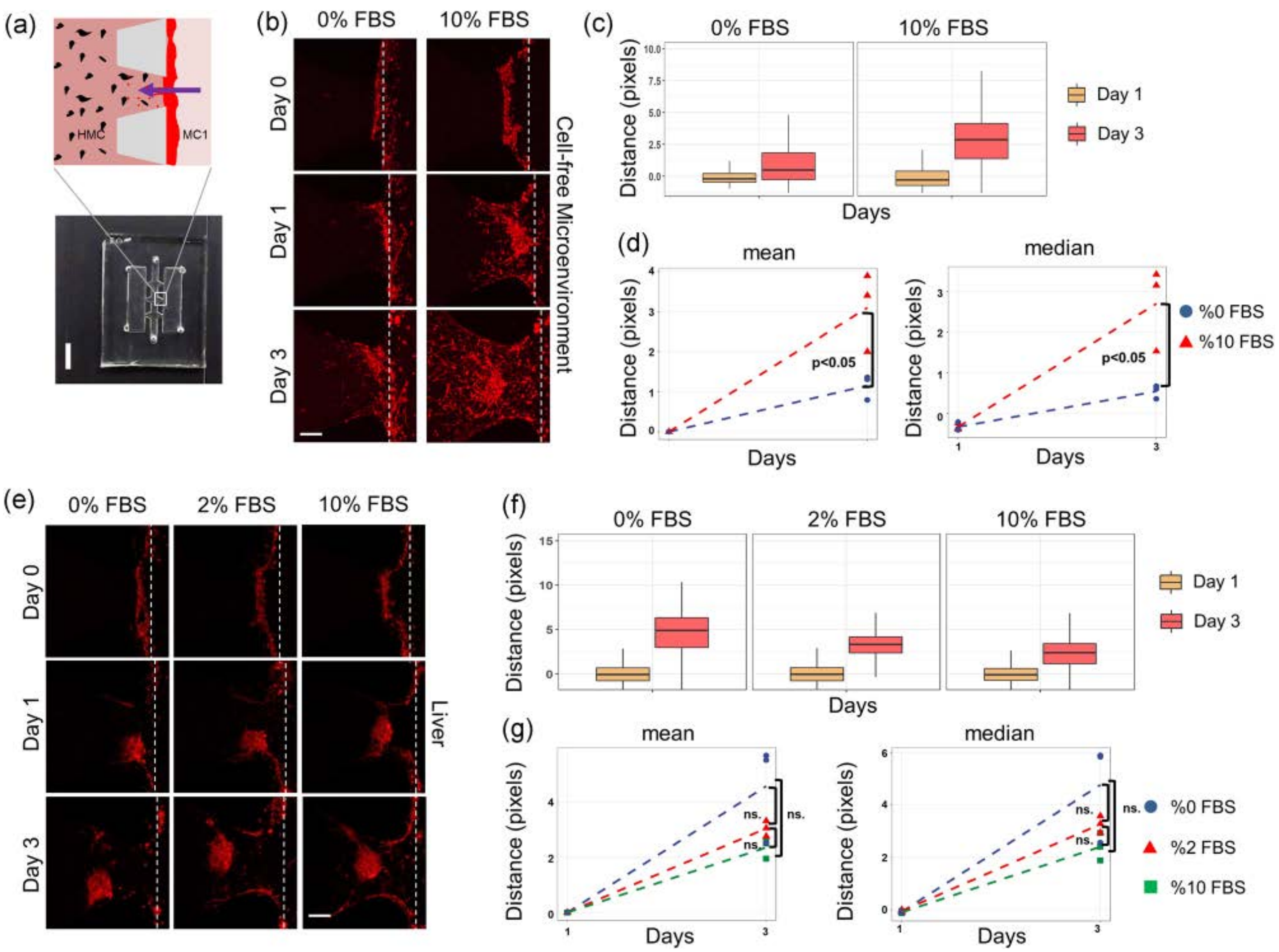

FIGURE 1 Effect of serum on the invasion/chemotaxis of breast cancer cells in the presence and absence of homing cells. (a) Schematic representation of the invasion data, where homing channel (HMC) is loaded with growth factor reduced (GFR)-matrigel including homing cells or not and medium channel (MC1) is loaded with MDA-MB-231 cells; scale bar = 5 mm. Representative Z-stack projection images showing invasion/chemotaxis of MDA-MB-231 cells (red) towards (b) cell-free GFR-matrigel in the absence or presence fetal bovine serum (FBS), and (e) liver cell-laden GFR-matrigel in the presence of 0%, 2%, and 10% FBS; scale bar = 200 μm. (c and f) Distribution of migration distances normalized to Day 1. (d and g) Mean and median values of normalized distance distributions. Data were normalized to Day 1 (*n* = 3). The dashed lines in (b) and (e) correspond to the starting line of invasion/chemotaxis

residing within target tissue microenvironments play important roles in directing tumor cells towards specific target sites (Fares et al., 2020; Guo & Deng, 2018; Roussos et al., 2011). To investigate tissue-specific invasion/chemotaxis and extravasation, two different OoC devices were used (Figure S1, Supporting Information). The invasion/chemotaxis chip (IC-chip) comprised three channels: MC1, HMC, and MC2. The IC-chip was symmetric along the long axis of HMC so that a gradient of factors in the MC2 can be realized across the HMC from MC2 to MC1. The procedure for the invasion assay on the IC-chip is shown in Figure S1a. Here, cells loaded into the MC1 were expected to show invasion and chemotaxis in response to the microenvironment in the HMC and/or the contents of the MC2.

The extravasation-chip (EX-chip) also comprised three channels: endothelial monolayer channel (EMC), HMC, MC. However, the EMC and the MC were not mirror images of each other as was the case for the MC1 and MC2 of the IC-chip. The EMC was a narrow channel designed to hold endothelial cells and intended to mimic a blood vessel. The procedure for the extravasation assay using the EX-chip is shown in Figure S1b. Here, cells loaded into the EMC after the formation of an intact endothelial monolayer were expected to show extravasation through the endothelial cells in response to the microenvironment in the HMC. In both the IC-chip and the EX-chip, the HMC was used to mimic the microenvironments of lung, liver or breast tissue, making it possible to assess tissue-specific invasion/chemotaxis and extravasation.

First, IC-chips with cell-free growth factor reduced (GFR)-matrigel in the HMC were used to examine invasion/chemotaxis of MDA-MB-231 cells using confocal fluorescence microscopy for 3 days (Figure 1a,b). Quantitative analysis of fluorescence images showed that invasion/chemotaxis increased from Day 1 to Day 3 for both 10% FBS (fetal bovine serum) and FBS-free conditions, consistent with the invasive phenotype of triple-negative MDA-MB-231 cells (Figure 1c). However, MDA-MB-231 cells showed 2.7 fold more invasion/chemotaxis towards FBS (10%) containing media than towards FBS free medium ($p < .05$), as expected (Figure 1d). A significant increase was detected in both the mean and the median distances invaded by the cells in 10% FBS condition compared to the FBS-free condition (Figure 1d). These results showed that the IC-chip can be used to quantitatively assay the invasion/chemotaxis phenotype of cells.

To optimize the invasion/chemotaxis assay towards different tissue microenvironments, the effect of serum in the presence of homing cells was tested. BRL-3A liver cells were resuspended in serum-free media, mixed with GFR-matrigel and loaded into the HMC. Medium (0%, 2% or 10% FBS) was added into the MC2. Invasion of MDA-MB-231 cells loaded into the MC1 towards the HMC was examined (Figure 1e). Quantitative image analysis showed that for all the three different FBS concentrations in the MC2, the invasion of MDA-MB-231 cells increased from Day 1 to Day 3 (Figure 1f). In addition, there were no significant differences in the invasion of MDA-MB-231 cells with 0%, 2% or 10% FBS containing medium in the MC2 when liver cells were present in the HMC (Figure 1g).

Therefore, the presence of homing cells such as BRL-3A was sufficient to induce invasion/chemotaxis of MDA-MB-231 cells. Consequently, serum-free media was used in the MC2 for all invasion experiments with cell-laden GFR-matrigel in the HMC. Altogether these results demonstrated that the IC-chip provided a robust platform for invasion/chemotaxis assays in the presence or absence of target tissue cells.

3.2 | Invasion/chemotaxis of breast cancer cells into the lung, liver and breast microenvironments

To distinguish invasion/chemotaxis to different tissues, WI-38, BRL-3A and MCF-10A cell-laden GFR-matrigel was used in the HMC of the IC-chips to simulate the lung, liver and breast microenvironments, respectively. The distance MDA-MB-231 cells invaded towards all the three (lung, liver and breast) microenvironments increased from Day 1 to Day 3 as expected due to the known metastatic phenotype of these cells (Figures 2a,b). However, the invasion of MDA-MB-231 cells to the lung and liver microenvironments was significantly 2.4 and 2.1 fold higher than that to the breast microenvironment, respectively (Figure 2c and Table S1, Supporting Information). MCF-7 cells did not significantly invade towards lung, liver or breast environments up to Day 3, as expected due to the known non-metastatic phenotype of these cells, having no preference for different homing tissues (Figures 2d–f). These data showing that MDA-MB-231 cells had a higher preference of invasion to the lung and liver microenvironments than the breast microenvironment are in agreement with published clinical data for homing choices of breast cancer (M.-T. Chen, Sun, et al., 2017; Wang et al., 2019).

3.3 | Invasion/chemotaxis of lung-specific and bone-specific metastatic breast cancer cells into the lung microenvironment

Lungs are the most common sites of breast cancer metastasis (Jin et al., 2018). Therefore, we examined the invasion/chemotaxis of organ-specific metastatic clones of MDA-MB-231 cells for lung (MDA-MB-231 LM2) and bone (MDA-MB-231 1833-BoM) (Bos et al., 2009; Kang et al., 2005; Minn et al., 2005) towards the lung microenvironment in the IC-chip. Parental and lung-specific (LM2) MDA-MB-231 cells invaded the lung microenvironment remarkably well, while bone-specific (BoM 1833) cells moved marginally towards HMC (Figure 3a,b). The distance invaded by parental and lung-specific cells were 16- and 12-fold higher than that by the bone-specific cells, respectively (Figure 3c and Table S1, Supporting Information). Taken together, these data showed that the IC-chip simulating different tissue microenvironments can successfully and quantitatively demonstrate invasion/chemotaxis and homing choices of breast cancer cells with different in vivo metastatic site preferences.

3.4 | Generation of an intact endothelial monolayer

The interior surfaces of EX-chips were chemically and biochemically modified to ensure the attachment of endothelial cells for the generation of an intact monolayer. Here, 3-aminopropyl triethoxysilane (APTES) and poly-L-lysine solution (PLL) were tested for their ability to promote FN coating. Both APTES and PLL supported FN coating and thus efficient endothelial cell monolayer formation. (Figure S3b, Supporting Information). APTES coating was preferred due to the shorter application time. To enhance formation of an intact endothelial monolayer, laminin (LAM), collagen type I (COL), and FN were tested on APTES precoated interior PDMS surfaces of EX-chips. LAM-coated surfaces provided the most appropriate surfaces for the attachment of endothelial cells that covered a larger area (Figures 4a,b). In addition, when endothelial cells were loaded into EMC, they tend to form clusters. Thus, dextran was used in the cell resuspension medium to inhibit cluster formation and ensure a homogeneous distribution of endothelial cells in the EMC (Figure S3a, Supporting Information) (Myers et al., 2012). Intact endothelial monolayer formation was confirmed by staining the cytoskeleton of endothelial cells, specifically, actin filaments (Figure 4c). Fluorescence signal coming from Green Cell Tracker labelled HUVEC-C cells was sparse. However, actin staining confirmed the confluence of the endothelial monolayer. These results suggested that the green signal obtained by transient labelling of cells by the Green Cell Tracker might not reflect the extent of HUVEC-C coverage on the surface. Intact endothelial monolayer formation was further demonstrated by measuring diffusion of fluorescent 70-kDa dextran from the EMC to the

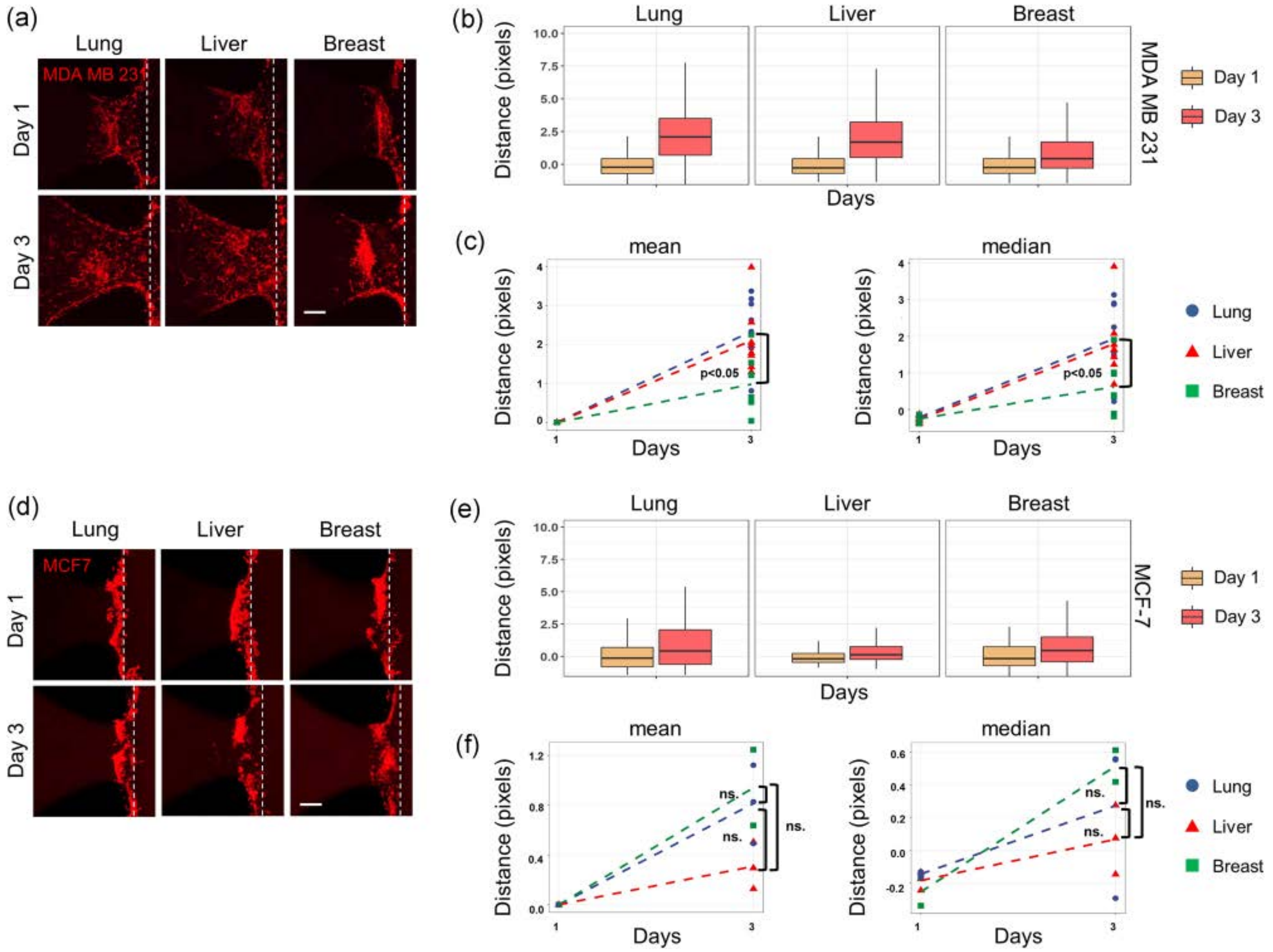

FIGURE 2 Invasion/chemotaxis of breast cancer cells into the lung, liver and breast microenvironments. Representative Z-stack projection images showing invasion/chemotaxis of (a) MDA-MB-231 cells (red) and (d) MCF7 cells (red) to the lung, liver and breast microenvironments. (b and e) Distribution of migration distances normalized to Day 1. (c and f) Mean and median values of normalized distance distributions. Data were normalized to Day 1; *n* = 6. The dashed lines in (a) and (b) correspond to the starting line of invasion/chemotaxis. Scale bar = 200 μm

HMC in the presence and absence of endothelial cells (Figure 4d,e). Permeability calculations showed that presence of an endothelial monolayer significantly reduced diffusion of fluorescent 70 kDa dextran from 3.12 ± 0.63 × 10^{-5} to 0.88 ± 0.1 × 10^{-5} cm s^{-1} (Figure 4f), in agreement with the previous studies (Frost et al., 2019; Jeon et al., 2013; van Duinen et al., 2017; Zervantonakis et al., 2012). Taken together, these results demonstrated that an intact endothelial monolayer with low permeability can be realized in EX-chips.

3.5 | Extravasation of metastatic breast cancer cells into the lung, liver and breast microenvironments

To distinguish extravasation and homing choices of breast cancer cells, the lung, liver and breast microenvironments were generated in the HMC, while an intact endothelial monolayer was realized in the EMC of the EX-chip. Extravasation was comparatively and quantitatively determined (Figures 5a,b,d). The efficiency of the EX-chips was quantified by the EM. The EM for the lung, liver and breast microenvironments were 0.89, 1 and 0.89, respectively, with no statistically significant differences between different microenvironments, showing that extravasation events were observed in almost all post gaps independent from the homing microenvironment. Cancer cells that passed through the endothelial layer were considered as extravasated, while cells that were detected within the endothelial layer were considered as associated. The number of extravasated cells were the highest in the lung, less in the liver and the lowest in the breast microenvironments. (Figure 5d and Table S1, Supporting Information). Numbers of MDA-MB-231 cells that remained associated with the endothelial monolayer were highest when the HMC contained the breast microenvironment (Figure 5d and Table S1, Supporting Information). Furthermore, the number of extravasated lung-specific MDA-MB-231 cells (LM2) were significantly higher than that of bone-specific (BoM 1833) cells towards lung microenvironment, while associated cell numbers were similar (Figure 5c,e and Table S1, Supporting Information). Taken together,

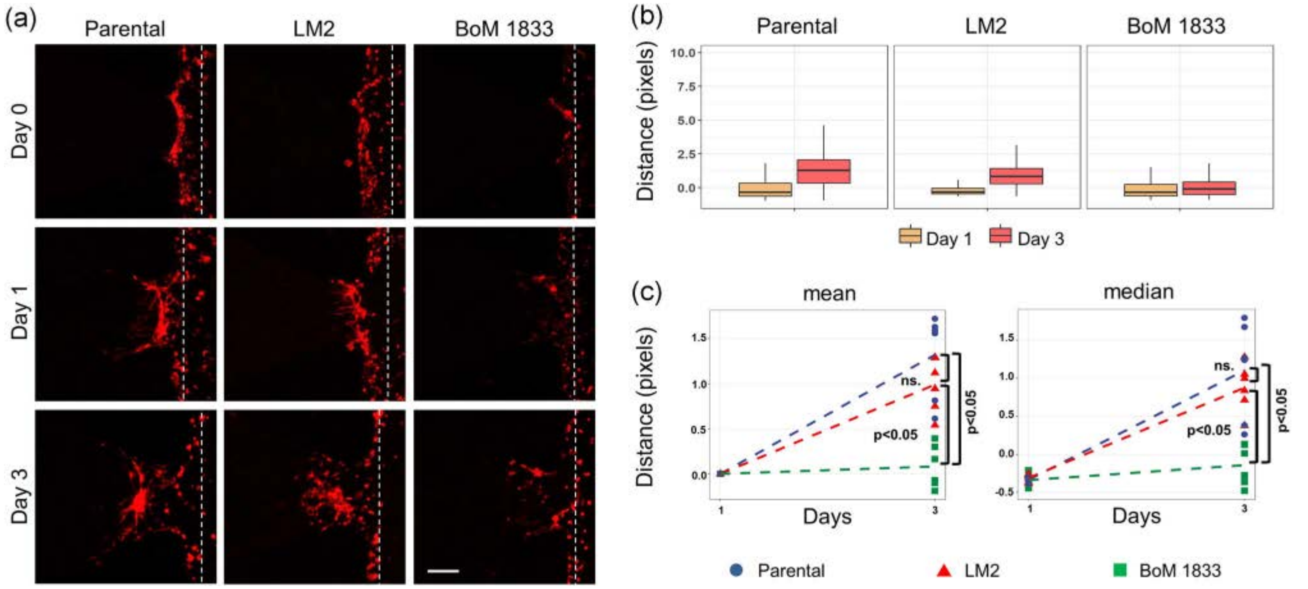

FIGURE 3 Invasion/chemotaxis of lung- and bone-specific metastatic breast cancer cells into the lung microenvironment. (a) Representative Z-stack projection images showing invasion/chemotaxis of parental, LM2 (lung-specific) and BoM 1833 (bone-specific) MDA-MB-231 cells (red) to the lung microenvironment generated by WI-38 cell line (dashed line corresponds to the starting line for invasion; scale bar = 200 μm). (b) The distance of each bright pixel to the starting line (dashed) was calculated after thresholding of Z-stack images. The data normalized to day 1 were plotted (*n* = 3). (c) Mean and median values of normalized distance distributions were plotted for Days 1 and 3 (*n* = 3)

these results showed that the EX-chip can demonstrate and quantify homing choices of the extravasating breast cancer cells.

4 | DISCUSSION

Microfluidic platforms such as OoC systems are promising tools expected to reduce and complement not only animal studies but also clinical trials (Peck et al., 2020; van Den Berg et al., 2019). Therefore, it is vital to develop OoC systems that can comparatively and quantitatively assess metastatic potential and homing choices of cancer cells. Here, we introduced two novel OoC systems that enable the visualization and quantification of tissue-specific breast cancer invasion/chemotaxis and extravasation. We generated lung, liver and breast microenvironments that simulate the well-known homing tissues for metastatic breast cancer cells and quantitatively distinguished the invasion/chemotaxis and extravasation phenotypes of different breast cancer cell lines.

Several OoC platforms using normal human lung fibroblasts were developed to model lung microenvironment and assessed intravasation, extravasation, angiogenesis, drug response and proliferation of cancer cells (Bi et al., 2020; Boussommier-Calleja et al., 2019; Shirure et al., 2018). These microenvironments included microvascular networks formed by HUVEC or cord blood-derived endothelial cells, which allowed trapping of cancer cells and physiological delivery of nutrients or drugs. Similar to a previous study that modeled bone microenvironment to assess extravasation (Bersini et al., 2014), we generated an endothelial monolayer separating cancer cells from the homing cells, where physical limitations of the capillary network are not present. The OoC platforms we used in this study reduced cost and time while increasing reproducibility. More importantly, our approach enabled quantitative differentiation of homing choices of breast cancer cells.

Currently, the OoC plattforms we present are limited by the choice of normal cell lines that can represent specific tissues. Although, the rat liver-derived cell line, BRL3A, attracted human breast cancer cells, we cannot exclude the possibility that human liver-derived cells might provide a more compatible environment for the invasion and extravasation of human cancer cells. MCF10A cells were selected to represent normal breast tissue due to their ability to form polarized acini in 3D basement membrane cultures (Debnath et al., 2003). It should be noted that MCF10A cells might develop a better environment for cancer cell attraction if supported by normal or cancer-associated fibroblasts. However, the current choice of cell lines provided the advantage of culturing with simple DMEM medium without addition of any specific growth factors to maintain the system. This allowed the IC- and EX-Chips to assess the effects of different homing cells independent of the medium components. Nevertheless, including different tissue components such as epithelial cells, fibroblasts, adipocytes, and immune cells should be further investigated to improve the microenvironment model.

Triple-negative breast cancer preferentially metastasizes to the lung and liver (Al-Mahmood et al., 2018; Chu et al., 2014). Consistent with published clinical data, invasion/chemotaxis results here showed that MDA-MB-231 cells, which are the triple-negative subtype, preferred lung and liver microenvironments over the breast

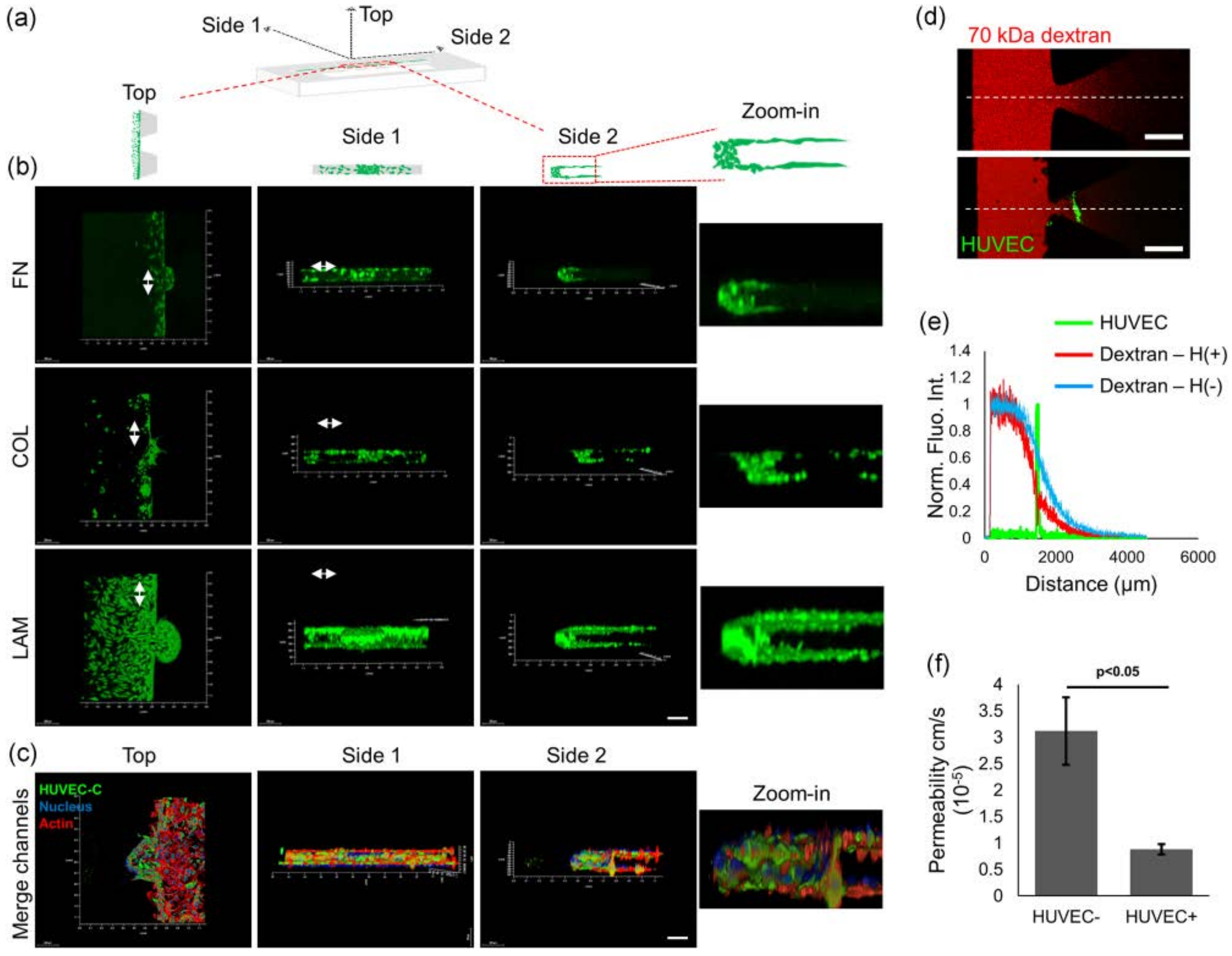

FIGURE 4 Generation of an intact endothelial monolayer. (a) Schematic of 3D Ex-chip with different views defined as Top, Side1 and Side 2. (b) Representative 3D images showing endothelial cells (green) on fibronectin (FN), collagen type I (COL), and laminin (LAM)-coated surfaces. The post gaps are marked with two-sided arrows in different views; scale bar = 200 μm. (c) Confocal images showing actin (phalloidin), nuclei (4′,6-diamidino-2-phenylindole [DAPI]), human umbilical vein endothelial cell line (HUVEC-C) (cell tracker) in red, blue, and green, respectively, from different views in APTES-LAM-coated EX-chip; scale bar = 200 μm. (d) Representative images of post-gap regions in 70 kDa fluorescent dextran (red) loaded chips in the absence (top panel) and the presence (bottom panel) of an endothelial monolayer (green); scale bar = 500 μm. (e) Normalized fluorescent intensity profiles along the dashed lines. HUVEC-C signal (green), dextran signal in the absence (blue) and presence (red) of HUVEC-C. (f) Permeability for 70 kDa dextran in the absence and presence of HUVEC-C

microenvironment. What is more, the lung metastatic subclone MDA-MB-231 LM2, showed invasion/chemotaxis preferentially to the lung microenvironment, consistent with previous in vivo studies (Minn et al., 2005). Parental MDA-MB-231 cells also showed a similar trend suggesting that the lung-specific metastatic cells could be more populated in the parental MDA-MB-231 cell line. Taken together, these results highlight the ability of the IC-chip to quantitatively determine the invasion/chemotaxis potential of cancer cells towards different target sites and to distinguish between cancer cells with different in vivo metastatic behaviors.

The generation of an intact endothelial monolayer allows mimicking the blood vessel interface (Shenoy & Lu, 2016). However, the hydrophobic nature of cured PDMS require surface modifications such as APTES and PLL coatings (Leivo et al., 2017). To optimize the formation of an intact endothelial monolayer, laminin, which is a component of the basement membrane, collagen type I, which is abundant in connective tissue and FN, a common extracellular matrix protein, were tested on the APTES pre-coated interior PDMS surfaces of EX-chips. Among the three different proteins, laminin promoted endothelial cell adhesion most. This is probably because endothelial cells in vivo exist on a basement membrane, of which laminin is a marked component.

The permeability values for in vitro networks of endothelial cells or in vivo conditions (Dreher et al., 2006; Shirure et al., 2018; Sobrino et al., 2016; Yuan et al., 2009) are one or two orders of magnitude lower than those calculated for the EX-chips in this study which are yet in agreement with previous studies using an endothelial monolayer for the extravasation interface (Frost et al., 2019; Jeon et al., 2013; van Duinen et al., 2017; Zervantonakis et al., 2012). The difference between the nature of

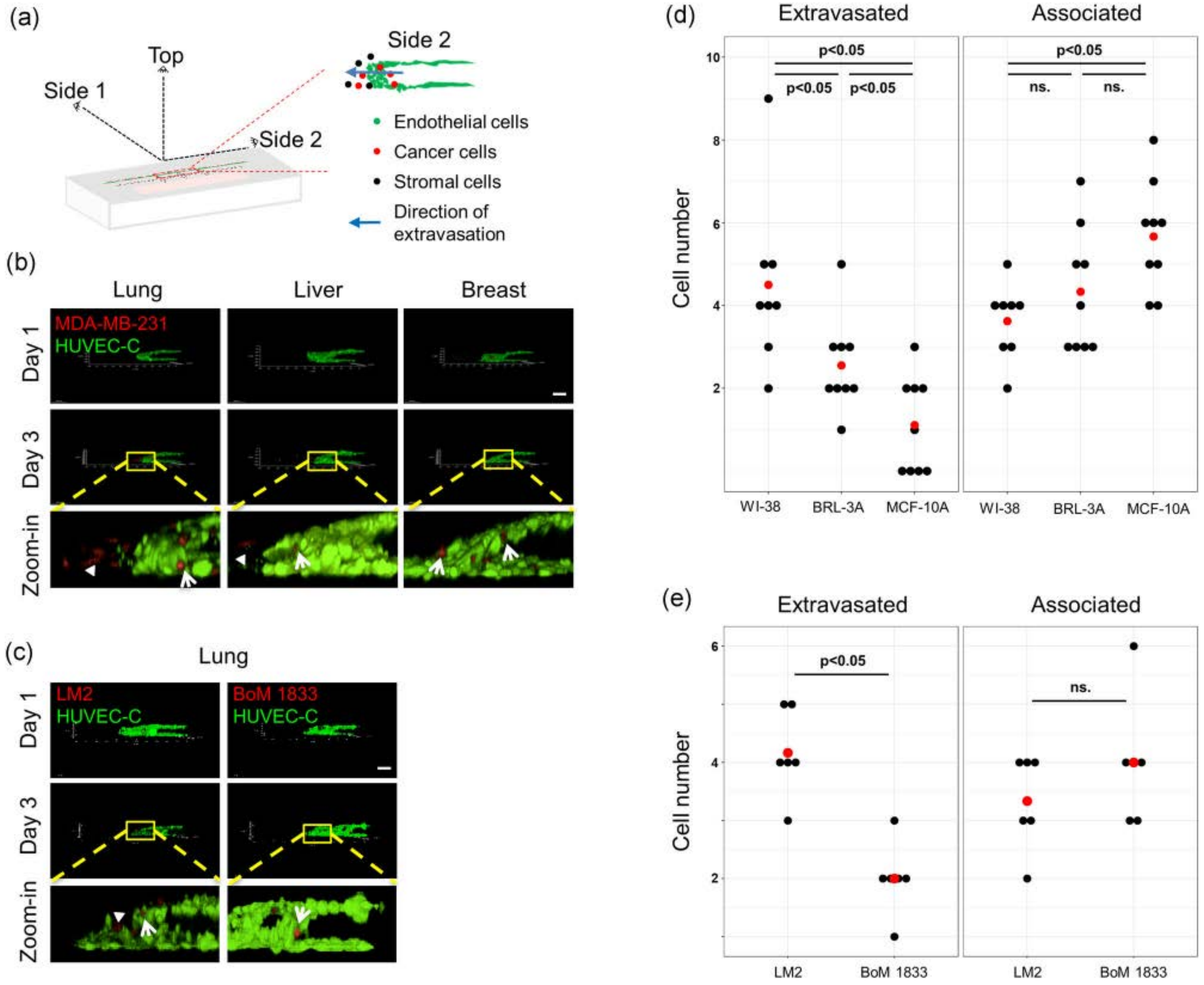

FIGURE 5 Extravasation of metastatic breast cancer cells into the lung, liver and breast microenvironments. (a) Schematic of 3D Ex-chip with different views defined as Top, Side1, Side 2 and an annotated sample Side 2 view. (b) Representative Z-stack projection images showing Side 2 views of endothelial monolayers of HUVEC-C cells (green) and extravasated (arrow head) and associated (arrow) MDA-MB-231 cells (red) into the lung, liver or breast microenvironments; scale bar = 200 μm. (c) Representative Z-stack projection images showing Side 2 views of endothelial monolayers of HUVEC-C cells (green) and extravasated (arrow head) and associated (arrow) MDA-MB-231 LM2 and BoM 1833 cells (red) into the lung microenvironment; scale bar = 200 μm. The number of extravasated and associated (d) MDA-MB-231 cells to lung, liver, and breast microenvironments (*n* = 9) and (e) MDA MB 231 LM2 and BoM 1833 to lung microenvironment (*n* = 6). Each black dot represents the cell number for one post-gap within the EX-chip, while the red dot is the average number of cells for each condition

the endothelial cell organization, that is, a network versus a monolayer is probably the reason for the difference (Offeddu et al., 2019). Nonetheless, the permeability of the EX-chips would not allow cell passage. Furthermore, since EMC contains serum-free medium, an input from, for example, growth factors or chemokines is not present to affect permeability or molecular interactions that will facilitate passage of cancer cells. However, release of chemokines from HMC to EMC might induce extravasation, which in turn is an advantage of the EX-chip set-up in terms of mimicking the in vivo conditions.

Finally, both the invasion/chemotaxis and extravasation assays showed that MDA-MB-231 cells preferred the lung microenvironment significantly more than the other target microenvironments. Although the MDA-MB-231 cells invaded towards the breast microenvironment on the IC-chip, they did not extravasate into the same microenvironment. These findings indicate that IC-chip would be useful to predict invasive behavior of the cancer cells in the primary tumor site as well as their preference for different target tissues. On the other hand, EX-chip would be more relevant and efficient for the determination of the overall metastatic potential and the homing choices of breast cancer cells.

In conclusion, we developed two OoC platforms based on the IC-chip and EX-chip, to comparatively and quantitatively determine the invasion/chemotaxis and extravasation phenotypes of different breast cancer cells to lung, liver, and breast microenvironments. Determination of tissue-specific metastatic potential of breast cancer cells is expected to improve diagnosis and help select the ideal therapy.

ACKNOWLEDGMENTS

This study was supported by the grant numbered 115E057 from Scientific and Technological Research Council of Turkey (TUBITAK). The authors thank Joan Massagué and Memorial Sloan Kettering Cancer Center for providing MDA-MB-231 LM2 and MDA-MB-231 1833-BoM cell lines.

CONFLICT OF INTERESTS

Devrim Pesen-Okvur was the co-founder and Ozden Yalcin-Ozuysal was the scientific advisor of Initio Biomedical Engineering (Turkey).

AUTHOR CONTRIBUTIONS

Burcu Firatligil-Yildirir and Gizem Bati-Ayaz: *methodology*, *formal analysis*, *investigation*, *writing-original draft*, *visualization*; Ismail Tahmaz and Muge Bilgen: *methodology*, *investigation*, *formal analysis*, *writing-original draft*; Devrim Pesen-Okvur and Ozden Yalcin-Ozuysal: *methodology*, *conceptualization*, *software*, *formal analysis*, *resources*, *writing-original draft*, *writing-review and editing*, *supervision*, *project administration*, *funding acquisition*.

DATA AVAILABILITY STATEMENT

The raw data and processed data required to reproduce these findings are available from the corresponding author upon request.

ORCID

Devrim Pesen-Okvur https://orcid.org/0000-0001-8333-4193
Ozden Yalcin-Ozuysal http://orcid.org/0000-0003-0552-368X

REFERENCES

Al-Mahmood, S., Sapiezynski, J., Garbuzenko, O. B., & Minko, T. (2018). Metastatic and triple-negative breast cancer: Challenges and treatment options. *Drug Delivery and Translational Research*, *8*(5), 1483–1507. https://doi.org/10.1007/s13346-018-0551-3

Bersini, S., Jeon, J. S., Dubini, G., Arrigoni, C., Chung, S., Charest, J. L., Moretti, M., & Kamm, R. D. (2014). A microfluidic 3D in vitro model for specificity of breast cancer metastasis to bone. *Biomaterials*, *35*(8), 2454–2461. https://doi.org/10.1016/j.biomaterials.2013.11.050

Bi, Y., Shirure, V. S., Liu, R., Cunningham, C., Ding, L., Meacham, J. M., Goedegebuure, S. P., George, S. C., & Fields, R. C. (2020). Tumor-on-a-chip platform to interrogate the role of macrophages in tumor progression. *Integrative Biology*, *12*(9), 221–232. https://doi.org/10.1093/intbio/zyaa017

Bos, P. D., Zhang, X. H., Nadal, C., Shu, W., Gomis, R. R., Nguyen, D. X., Minn, A. J., van de Vijver, M. J., Gerald, W. L., Foekens, J. A., & Massagué, J. (2009). Genes that mediate breast cancer metastasis to the brain. *Nature*, *459*(7249), 1005–1009. https://doi.org/10.1038/nature08021

Boussommier-Calleja, A., Atiyas, Y., Haase, K., Headley, M., Lewis, C., & Kamm, R. D. (2019). The effects of monocytes on tumor cell extravasation in a 3D vascularized microfluidic model. *Biomaterials*, *198*, 180–193. https://doi.org/10.1016/j.biomaterials.2018.03.005

Chen, M. B., Whisler, J. A., Fröse, J., Yu, C., Shin, Y., & Kamm, R. D. (2017). On-chip human microvasculature assay for visualization and quantification of tumor cell extravasation dynamics. *Nature Protocols*, *12*(5), 865–880. https://doi.org/10.1038/nprot.2017.018

Chen, M.-T., Sun, H.-F., Zhao, Y., Fu, W.-Y., Yang, L.-P., Gao, S.-P., Li, L.-D., Jiang, H.-l., & Jin, W. (2017). Comparison of patterns and prognosis among distant metastatic breast cancer patients by age groups: a SEER population-based analysis. *Scientific Reports*, *7*, (1). https://doi.org/10.1038/s41598-017-10166-8

Chu, J. E., Xia, Y., Chin-Yee, B., Goodale, D., Croker, A. K., & Allan, A. L. (2014). Lung-derived factors mediate breast cancer cell migration through CD44 receptor-ligand interactions in a novel ex vivo system for analysis of organ-specific soluble proteins. *Neoplasia*, *16*(2), 180–191. https://doi.org/10.1593/neo.132076

Debnath, J., Muthuswamy, S. K., & Brugge, J. S. (2003). Morphogenesis and oncogenesis of MCF-10A mammary epithelial acini grown in three-dimensional basement membrane cultures. *Methods*, *30*(3), 256–268. https://doi.org/10.1016/s1046-2023(03)00032-x

Dreher, M. R., Liu, W. G., Michelich, C. R., Dewhirst, M. W., Yuan, F., & Chilkoti, A. (2006). Tumor vascular permeability, accumulation, and penetration of macromolecular drug carriers. *Journal of the National Cancer Institute*, *98*(5), 335–344. https://doi.org/10.1093/jnci/djj070

Fares, J., Fares, M. Y., Khachfe, H. H., Salhab, H. A., & Fares, Y. (2020). Molecular principles of metastasis: A hallmark of cancer revisited. *Signal Transduction and Targeted Therapy*, *5*(1), 28. https://doi.org/10.1038/s41392-020-0134-x

Frost, T. S., Jiang, L., Lynch, R. M., & Zohar, Y. (2019). Permeability of epithelial/endothelial barriers in transwells and microfluidic bilayer devices. *Micromachines*, *10*(8). https://doi.org/10.3390/mi10080533

Guo, S., & Deng, C. X. (2018). Effect of stromal cells in tumor microenvironment on metastasis initiation. *International Journal of Biological Sciences*, *14*(14), 2083–2093. https://doi.org/10.7150/ijbs.25720

Howlader, N. N. A., Krapcho, M., Miller, D., Brest, A., Yu, M., Ruhl, J., Tatalovich, Z., Mariotto, A., Lewis, D. R., Chen, H. S., Feuer, E. J., & Cronin, K. A. (2020). Cancer of the female breast (invasive): 5-year relative and period survival by race, diagnosis year, age and stage at diagnosis. *SEER Cancer Statistics Review*. Retrieved from https://seer.cancer.gov/csr/1975_2017/

Ilhan, M., Kucukkose, C., Efe, E., Gunyuz, Z. E., Firatligil, B., Dogan, H., Ozuysal, M., & Yalcin-Ozuysal, O. (2020). Pro-metastatic functions of Notch signaling is mediated by CYR61 in breast cells. *European Journal of Cell Biology*, *99*(2-3), 151070. https://doi.org/10.1016/j.ejcb.2020.151070

Jeon, J. S., Bersini, S., Gilardi, M., Dubini, G., Charest, J. L., Moretti, M., & Kamm, R. D. (2015). Human 3D vascularized organotypic microfluidic assays to study breast cancer cell extravasation. *Proceedings of the National Academy of Sciences*, *112*(1), 214–219. https://doi.org/10.1073/pnas.1417115112

Jeon, J. S., Zervantonakis, I. K., Chung, S., Kamm, R. D., & Charest, J. L. (2013). In vitro model of tumor cell extravasation. *PLOS One*, *8*(2), e56910. https://doi.org/10.1371/journal.pone.0056910

Jin, L., Han, B., Siegel, E., Cui, Y., Giuliano, A., & Cui, X. (2018). Breast cancer lung metastasis: Molecular biology and therapeutic implications. *Cancer Biology & Therapy*, *19*(10), 858–868. https://doi.org/10.1080/15384047.2018.1456599

Kang, Y., He, W., Tulley, S., Gupta, G. P., Serganova, I., Chen, C.-R., Manova-Todorova, K., Blasberg, R., Gerald, W. L., & Massagué, J. (2005). Breast cancer bone metastasis mediated by the Smad tumor suppressor pathway. *Proceedings of the National Academy of Sciences of the United States of America*, *102*(39), 13909–13914. https://doi.org/10.1073/pnas.0506517102

Kimura, H., Sakai, Y., & Fujii, T. (2018). Organ/body-on-a-chip based on microfluidic technology for drug discovery. *Drug Metabolism and Pharmacokinetics*, *33*(1), 43–48. https://doi.org/10.1016/j.dmpk.2017.11.003

Langley, R. R., & Fidler, I. J. (2011). The seed and soil hypothesis revisited--the role of tumor-stroma interactions in metastasis to different organs. *International Journal of Cancer*, *128*(11), 2527–2535. https://doi.org/10.1002/ijc.26031

Leivo, J., Virjula, S., Vanhatupa, S., Kartasalo, K., Kreutzer, J., Miettinen, S., & Kallio, P. (2017). A durable and biocompatible ascorbic acid-based covalent coating method of polydimethylsiloxane for dynamic cell culture. *Journal of the Royal Society, Interface*, *14*(132). https://doi.org/10.1098/rsif.2017.0318

Minn, A. J., Gupta, G. P., Siegel, P. M., Bos, P. D., Shu, W., Giri, D. D., Viale, A., Olshen, A. B., Gerald, W. L., & Massagué, J. (2005). Genes that mediate breast cancer metastasis to lung. *Nature*, *436*(7050), 518–524. https://doi.org/10.1038/nature03799

Myers, D. R., Sakurai, Y., Tran, R., Ahn, B., Hardy, E. T., Mannino, R., Kita, A., Tsai, M., & Lam, W. A. (2012). Endothelialized microfluidics for studying microvascular interactions in hematologic diseases. *Journal of Visualized Experiments*, *64*, 3958. https://doi.org/10.3791/3958

Offeddu, G. S., Haase, K., Gillrie, M. R., Li, R., Morozova, O., Hickman, D., Knutson, C. G., & Kamm, R. D. (2019). An on-chip model of protein paracellular and transcellular permeability in the microcirculation. *Biomaterials*, *212*, 115–125. https://doi.org/10.1016/j.biomaterials.2019.05.022

Ozdil, B., Onal, S., Oruç, T., & Pesen Okvur, D. (2014). Fabrication of 3D controlled in vitro microenvironments. *Methods*, *1*, 60–66. https://doi.org/10.1016/j.mex.2014.06.003

Paget, S. (1889). The distribution of secondary growths in cancer of the breast. *The Lancet*, *133*(3421), 571–573. https://doi.org/10.1016/S0140-6736(00)49915-0

Pathak, A., & Kumar, S. (2012). Independent regulation of tumor cell migration by matrix stiffness and confinement. *Proceedings of the National Academy of Sciences of the United States of America*, *109*(26), 10334–10339. https://doi.org/10.1073/pnas.1118073109

Peck, R. W., Hinojosa, C. D., & Hamilton, G. A. (2020). Organs-on-chips in clinical pharmacology: Putting the patient into the center of treatment selection and drug development. *Clinical Pharmacology & Therapeutics*, *107*(1), 181–185. https://doi.org/10.1002/cpt.1688

Polacheck, W. J., Charest, J. L., & Kamm, R. D. (2011). Interstitial flow influences direction of tumor cell migration through competing mechanisms. *Proceedings of the National Academy of Sciences of the United States of America*, *108*(27), 11115–11120. https://doi.org/10.1073/pnas.1103581108

Rodrigues, R. O., Sousa, P. C., Gaspar, J., Bañobre-López, M., Lima, R., & Minas, G. (2020). Organ-on-a-chip: A preclinical microfluidic platform for the progress of nanomedicine. *Small*, *16*(51), 2003517. https://doi.org/10.1002/smll.202003517

Roussos, E. T., Condeelis, J. S., & Patsialou, A. (2011). Chemotaxis in cancer. *Nature Reviews Cancer*, *11*(8), 573–587. https://doi.org/10.1038/nrc3078

Shenoy, A. K., & Lu, J. (2016). Cancer cells remodel themselves and vasculature to overcome the endothelial barrier. *Cancer Letters*, *380*(2), 534–544. https://doi.org/10.1016/j.canlet.2014.10.031

Shirure, V. S., Bi, Y., Curtis, M. B., Lezia, A., Goedegebuure, M. M., Goedegebuure, S. P., Aft, R., Fields, R. C., & George, S. C. (2018). Tumor-on-a-chip platform to investigate progression and drug sensitivity in cell lines and patient-derived organoids. *Lab on a Chip*, *18*(23), 3687–3702. https://doi.org/10.1039/c8lc00596f

Sobrino, A., Phan, D. T., Datta, R., Wang, X., Hachey, S. J., Romero-López, M., Gratton, E., Lee, A. P., George, S. C., & Hughes, C. C. (2016). 3D microtumors in vitro supported by perfused vascular networks. *Scientific Reports*, *6*, 6. https://doi.org/10.1038/srep31589

Song, J. W., Cavnar, S. P., Walker, A. C., Luker, K. E., Gupta, M., Tung, Y.-C., Luker, G. D., & Takayama, S. (2009). Microfluidic endothelium for studying the intravascular adhesion of metastatic breast cancer cells. *PLOS One*, *4*(6), e5756. https://doi.org/10.1371/journal.pone.0005756

Soscia, D., Belle, A., Fischer, N., Enright, H., Sales, A., Osburn, J., Benett, W., Mukerjee, E., Kulp, K., Pannu, S., & Wheeler, E. (2017). Controlled placement of multiple CNS cell populations to create complex neuronal cultures. *PLOS One*, *12*(11), e0188146. https://doi.org/10.1371/journal.pone.0188146

Truong, D., Puleo, J., Llave, A., Mouneimne, G., Kamm, R. D., & Nikkhah, M. (2016). Breast cancer cell invasion into a three dimensional tumor-stroma microenvironment. *Scientific Reports*, *6*(1), 34094. https://doi.org/10.1038/srep34094

van Den Berg, A., Mummery, C. L., Passier, R., & van der Meer, A. D. (2019). Personalised organs-on-chips: Functional testing for precision medicine. *Lab on a Chip*, *19*(2), 198–205. https://doi.org/10.1039/c8lc00827b

van Duinen, V., van den Heuvel, A., Trietsch, S. J., Lanz, H. L., van Gils, J. M., van Zonneveld, A. J., Vulto, P., & Hankemeier, T. (2017). 96 perfusable blood vessels to study vascular permeability in vitro. *Scientific Reports*, *7*(1), 18071. https://doi.org/10.1038/s41598-017-14716-y

Vickerman, V., & Kamm, R. D. (2012). Mechanism of a flow-gated angiogenesis switch: early signaling events at cell-matrix and cell–cell junctions. *Integrative Biology*, *4*(8), 863–874. https://doi.org/10.1039/c2ib00184e

Wang, R., Zhu, Y., Liu, X., Liao, X., He, J., & Niu, L. (2019). The clinicopathological features and survival outcomes of patients with different metastatic sites in stage IV breast cancer. *BMC Cancer*, *19*(1), 1091. https://doi.org/10.1186/s12885-019-6311-z

Wu, Q., Liu, J., Wang, X., Feng, L., Wu, J., Zhu, X., Wen, W., & Gong, X. (2020). Organ-on-a-chip: Recent breakthroughs and future prospects. *Biomedical Engineering Online*, *19*(1), 9. https://doi.org/10.1186/s12938-020-0752-0

Yalcin-Ozuysal, O., Fiche, M., Guitierrez, M., Wagner, K. U., Raffoul, W., & Brisken, C. (2010). Antagonistic roles of Notch and p63 in controlling mammary epithelial cell fates. *Cell Death and Differentiation*, *17*(10), 1600–1612. https://doi.org/10.1038/cdd.2010.37

Yuan, W., Lv, Y. G., Zeng, M., & Fu, B. M. (2009). Non-invasive measurement of solute permeability in cerebral microvessels of the rat. *Microvascular Research*, *77*(2), 166–173. https://doi.org/10.1016/j.mvr.2008.08.004

Zengin, T., Ekinci, B., Kucukkose, C., & Yalcin-Ozuysal, O. J. P. O. (2015). IRF6 is involved in the regulation of cell proliferation and transformation in MCF10A cells downstream of notch signaling. *PLOS One*, *10*, e0132757. https://doi.org/10.1371/journal.pone.0132757

Zervantonakis, I. K., Hughes-Alford, S. K., Charest, J. L., Condeelis, J. S., Gertler, F. B., & Kamm, R. D. (2012). Three-dimensional microfluidic model for tumor cell intravasation and endothelial barrier function. *Proceedings of the National Academy of Sciences of the United States of America*, *109*(34), 13515–13520. https://doi.org/10.1073/pnas.1210182109

SUPPORTING INFORMATION

Additional Supporting Information may be found online in the supporting information tab for this article.

How to cite this article: Firatligil-Yildirir, B., Bati-Ayaz, G., Tahmaz, I., Bilgen, M., Pesen-Okvur, D., & Yalcin-Ozuysal, O. (2021). On-chip determination of tissue-specific metastatic potential of breast cancer cells. *Biotechnology and Bioengineering*, 118, 3799–3810. https://doi.org/10.1002/bit.27855